Doctoral theses at NTNU, 2017:326

Mads Christensen

Fabrication of lead-free ferroelectric thin films based on $Bi_{0.5}Na_{0.5}TiO_3$ by aqueous chemical solution deposition

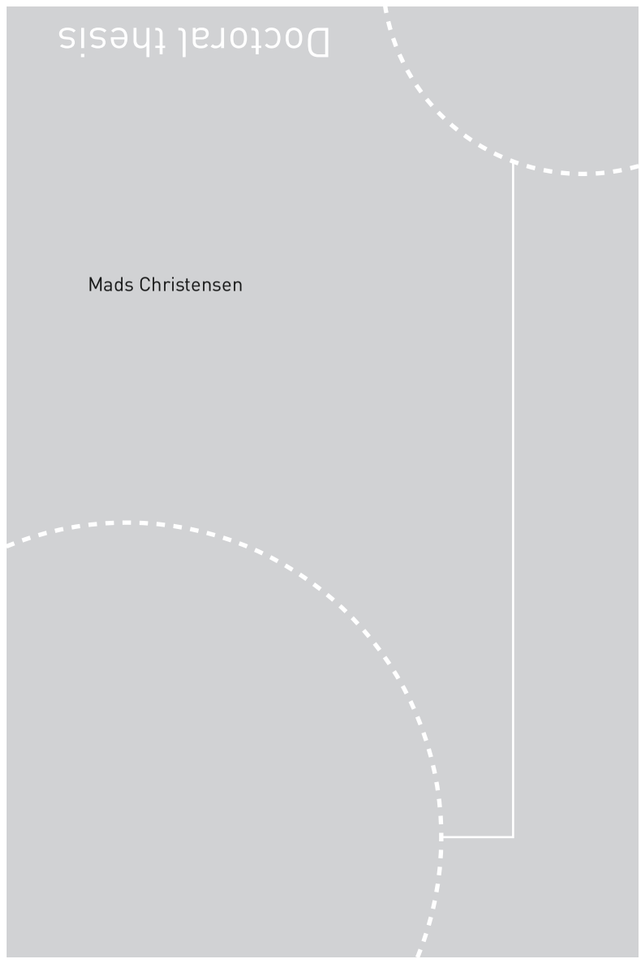

ISBN 978-82-326-2720-2 (printed ver.)
ISBN 978-82-326-2721-9 (electronic ver.)
ISSN 1503-8181

NTNU
Norwegian University of
Science and Technology

NTNU
Norwegian University of Science and Technology
Thesis for the Degree of
Philosophiae Doctor
Faculty of Natural Sciences
Department of Materials Science and
Engineering

Doctoral theses at NTNU, 2017:326

NTNU
Norwegian University of
Science and Technology

Mads Christensen

Fabrication of lead-free ferroelectric thin films based on $Bi_{0.5}Na_{0.5}TiO_3$ by aqueous chemical solution deposition

Thesis for the Degree of Philosophiae Doctor

Trondheim, November 2017

Norwegian University of Science and Technology
Faculty of Natural Sciences
Department of Materials Science and Engineering

NTNU
Norwegian University of
Science and Technology

NTNU
Norwegian University of Science and Technology

Thesis for the Degree of Philosophiae Doctor

Faculty of Natural Sciences
Department of Materials Science and Engineering

ISBN 978-82-326-2720-2 (printed ver.)
ISBN 978-82-326-2721-9 (electronic ver.)
ISSN 1503-8181

Doctoral theses at NTNU, 2017:326

Printed by NTNU Grafisk senter

Preface

This thesis has been submitted NTNU, the Norwegian University of Science and Technology, in partial fulfillment of the requirements for the academic degree of Philosophiae Doctor.

The work described here has been conducted at the Inorganic Materials and Ceramics Research Group at the Department of Materials Science and Engineering from August 2014 to September 2017. Supervising the work were Professor Tor Grande and Professor Mari-Ann Einarsrud (co-supervisor).

Funding for the work has been received from the Research Council of Norway through the project "Beat the Human Eye" (grant number 235210) and via NTNU NanoLab through the Norwegian Micro- and Nano-Fabrication Facility, NorFab (197411/V30).

The author has conducted all of the experimental work and prepared all unreferenced figures and illustrations. The author has been the main contributor to the published and unpublished work.

Results and discussion of this work are organized as papers. Papers 1-4 are included as Chapters 4-7.

1. Christensen M., Einarsrud M.-A., and Grande T., *Fabrication of Lead-Free $Bi_{0.5}Na_{0.5}TiO_3$ Thin Films by Aqueous Chemical Solution Deposition.* Materials, 2017. **10**(3) 213 doi: 10.3390/ma10020213.
2. Christensen M., Einarsrud M.-A., and Grande T., *Aqueous chemical solution deposition of phase pure Ba doped $Bi_{0.5}Na_{0.5}TiO_3$ thin films.* Manuscript not submitted.
3. Christensen M., Einarsrud M.-A., and Grande T., *Chemical modification of $Bi_{0.5}Na_{0.5}TiO_3$ thin films prepared by aqueous chemical solution deposition.* Manuscript not submitted.
4. Christensen M., Einarsrud M.-A., and Grande T., *Deposition of $B_{i0.5}Na_{0.5}TiO_3$ thin films on platinized silicon – Identification and management of a Bi-Pt reaction.* Manuscript not submitted.

Acknowledgements

First, I want to express gratitude to my main supervisor Professor Tor Grande for his guidance throughout these years. It has been a privilege working with him, and I appreciate the discussions we have had. I particularly want to acknowledge the freedom he has given me in defining the project and in following my own ideas. Despite this, he has always been able to provide encouragement and input to situations where it was needed. Second, I want to thank my co-supervisor Professor Mari-Ann Einarsrud for her insightful comments on both the science of the work and also during writing of the paper manuscripts. Furthermore, I am grateful to the people at poLight, particularly Lars Henriksen and Jon Herman Ulvensøen, for helpful feedback and for providing an exciting research project entirely without constraints or demands. I also want to thank the people at HSN for the interesting discussions we shared both in Trondheim and in Horten.

This work would not have been possible without support from the staff at the department and at NTNU NanoLab. I would particularly like to thank Kristin Høydalsvik Wells, jools, Mark Chiappa and Svenn Ove Linde for your technical support and dedication. Moreover, Vidar Broholm, Solveig Jonassen, Elin Kaasen, and others have helped me with countless non-scientific endeavors. The scientific community at our department is the perfect environment for interesting and helpful discussions and feedback. Particularly the weekly meetings in the ferrogroup have been an inspiring arena, and I appreciate our discussions. I was lucky enough to act as co-supervisor for Kim Lorentzen, and I want to thank him and Trygve Ræder for our scientific and practical discussions and collaboration. During my master thesis, I was co-supervised by Espen Wefring, and I learned a lot from him that have benefited me during the PhD as well.

Next, the colleagues and friends at the department and in the Inorganic Materials and Ceramics Research Group have helped make the everyday life as good as it has been. Of course, I am grateful to my office-mates Antoine, Laura, Rokas, Ingeborg (and Carlos), for our many serious and less serious moments. You have all been great companions during these years. To the rest of the people in K2 and K1, thank you for the civilized and deep discussions on politics and religion, and for helping create such an inspiring and fun environment both during and after working hours.

I want to thank my family and friends. To mom and dad, thank you for encouraging me and for allowing me to always choose my own path. To Mette, thank you for your above average enthusiasm. To the rest of my family, thank you for always being there. I have been very lucky to be a part of NTNUI Swing og Folkedans, and I am very grateful to all of you for the countless moments we have shared both on the dance floor and in other contexts. To the rest of my friends, thank you for being who you are and for helping be get to this point. Last but not least, I want to thank my dear Guro for your support and understanding throughout this busy period, and for always being there for me.

Summary

Since the discovery of piezoelectric ceramic materials in the mid-20th century, piezoelectric materials have become an important research field and is currently used in a whole range of applications such as sensors and actuators. The most important piezoelectric materials today are those based on the lead containing perovskites such as $Pb(Zr,Ti)O_3$ (PZT). However, lead is known to be toxic, and safety and environmental concerns have led the EU and other governments to encourage the replacement of lead containing materials in electronic devices. The development of lead-free piezoelectric ceramics has therefore emerged as an important research field in the last decade. The Norwegian company poLight AS has developed a tunable autofocus lens (TLens) based on a PZT actuator. The present thesis was part of a project which focused on materials and technology for the next generation TLens, and the objective of this work was to develop a synthesis route to a lead-free piezoelectric material to replace the PZT actuator. $Bi_{0.5}Na_{0.5}TiO_3$ (BNT) was chosen as the most suitable lead-free alternative due to the superior actuator properties reported for bulk BNT-based materials.

In the first part of the study, an aqueous synthesis route to BNT thin films was developed for the first time. Chemical solution deposition (CSD) based on water as the solvent was selected as the synthesis method due to the overall goal of producing non-toxic and environmentally friendly piezoelectric devices. In the sol, Ti isopropoxide was stabilized by citric acid (CA), Bi citrate was stabilized by ethanolamine, Na was added as hydroxide, and the pH of the sols was adjusted to neutral by ammonia solution. The synthesis route provided sols with no sign of aging still after two years. An alternative system based on Bi and Na nitrates with low pH to avoid Bi precipitation did not provide sols with sufficient stability, and was therefore not pursued further. BNT thin films were deposited on $SrTiO_3$ (ST) and platinized silicon (SiPt) substrates by spin-coating, and the films were pyrolized and annealed by rapid thermal processing in O_2. The BNT perovskite phase was observed to form after calcination at 450 °C by X-ray diffraction, while thermal decomposition of the gel was shown to be completed at 550 °C by thermogravimetric analysis. The microstructures of the thin films were shown by electron microscopy to be homogeneous and dense at 550 °C. Decomposition of the gel was thoroughly investigated, and the conditions to obtain phase pure materials were identified. The main challenge of the CSD route was related to transient reduction of Bi^{3+} into metallic Bi during pyrolysis, which resulted in formation of a Bi-rich pyrochlore secondary phase. Re-oxidation of Bi occurred above 450 °C, and phase pure BNT thin films could be obtained by pyrolysis at 550 °C for 5 min, while pyrolysis at 500 °C required additional thermal annealing.

The second part of the work was devoted to incorporation of Ba doping in the BNT synthesis route. Large strain in bulk BNT is only obtained upon compositional engineering, and Ba is the most common dopant. Successful stabilization of the sols with Ba was obtained by using Ba nitrate stabilized by EDTA and CA. It was demonstrated that the presence of Ba promoted the formation of the pyrochlore phase, and that Ba-rich BNT compositions required heat treatment at 800 °C to obtain phase purity. Alternatively, phase pure as-pyrolized thin films were obtained by adding 10 % Na excess to the sols. Thin films of both BNT and BNT doped with 6 % Ba deposited on Nb-doped ST were demonstrated to be ferroelectric, with leakage current characteristics comparable to state of the art BNT thin films.

Further efforts to optimize the microstructures of BNT thin films were carried out. Films deposited on SiPt were homogeneous, dense, and defect free using a heating rate of 40 °C/s in the pyrolysis step, while thin films deposited on ST required lower heating rate of 1.67 °C/s to 450 °C and 40 °C/s in the interval 450-550 °C. Slow heating rate during the entire pyrolysis event caused porous films, while rapid heating resulted in thin films with defects formed due to gas evolution during thermal decomposition of the gels.

The synthesis route was further developed to incorporate more complex BNT compositions, including the cations K, Li, Sr, and Nb in addition to Ba. These dopants are also known to cause large strain response in bulk BNT. Hydroxides were used as alkali cation precursors, Sr nitrate was stabilized by EDTA and CA, while Nb was added as Nb ammonium oxalate ($NH_4NbO(C_2O_4)_2$). It was demonstrated that the complex compositions of the sols promoted formation of the pyrochlore secondary phase in the thin films. The first layers were phase pure, but an increasing pyrochlore content appeared with additional layers. Also in this case, Na excess was demonstrated to promote phase purity and more efficient perovskite formation, while equal amounts of Bi and Na excess did not sufficiently suppress the formation of the pyrochlore. Thin films of approximately 800 nm thickness (15 layers) were predominantly phase pure after annealing at 700 °C. Ferroelectric properties of the thin films were demonstrated, and leakage current and tolerance to high fields were comparable to state of the art BNT thin films. Compositional dependence of the ferroelectric performance could not be determined due to clamping of the substrate and leakage contributions. These dopants comprise a representative selection of the most common modifications to BNT, demonstrating that the synthesis framework developed in this study is robust and able to accommodate the most significant BNT based compositions.

The fabrication of BNT thin films on SiPt substrates is contained in the final part of the study. SiPt may be considered the industry standard for deposition of piezoelectric thin films. It consists of a single crystal Si wafer coated with SiO_2, TiO_x and a Pt electrode. It was found that a high reactivity of Pt and Bi from the BNT film caused a detrimental weakening of the TiO_x-Pt interface. This led to delamination of the films as they reached approximately 300 nm thickness. A $BaTiO_3$ (BT) protective layer was introduced to spatially separate the BNT layer from Pt, leading to thicker achievable BNT films before delamination occurred. The microstructure and morphology of the BT protective layer was improved by adjusting the number of depositions and heat treatment procedure, but a sufficiently dense BT film was not achieved, and reaction between Bi and Pt was not completely eliminated. The films delaminated at a thinner critical thickness than what can be predicted from evaluating the stress due to thermal expansion mismatch of Si and BNT. Nevertheless, the feasibility of applying a protective BT layer for deposition of BNT on SiPt was demonstrated, and its potential was established.

In summary, the content of this work was the successful development of a novel aqueous BNT CSD method with implementation of the relevant dopants. Challenges related to transient Bi reduction, formation of the pyrochlore secondary phase, and Pt-Bi reaction were the main aspects requiring in-depth investigation.

Table of contents

List of acronyms and terms

See also an overview of electromechanical parameters in Table 2.2 on page 14.

2-MOE	2-methoxyethanol
BCZT	$Ba_xCa_{1-x}Zr_yTi_{1-y}O_3$
BF	$BiFeO_3$
BiCit	Bi (III) citrate, $BiC_3H_5O(COO)_3$
BKT	$Bi_{0.5}K_{0.5}TiO_3$
BNT	$Bi_{0.5}Na_{0.5}TiO_3$
BNT-*x*Ba	$(Bi_{0.5}Na_{0.5})_{1-x/100}Ba_{x/100}TiO_3$
BT	$BaTiO_3$
CA	Citric acid, $C_3H_5O(COOH)_3$
CSD	Chemical solution deposition
d	Piezoelectric coefficient (strain-field and surface charge-stress)
d^*	Large-signal coefficient ($d^* = S_{max}/E_{max}$)
d_{31}	Transverse strain
d_{33}	Longitudinal strain
D	Displacement or surface charge density
e	Piezoelectric coefficient (surface charge-strain stress-field)
E	Electric field
E_c	Coercive field (switching field)
EA	Ethanolamine, $H_2N(CH_2)_2OH$
EDTA	Ethylenediaminetetraacetic acid, $C_{10}H_{16}N_2O_8$
ER	Ergodic relaxor
k	Electromechanical coupling coefficient
KNN	$K_xNa_{1-x}NbO_3$ (most commonly $x \approx 0.5$)
MEMS	Micro electromechanical system
MPB	Morphotropic phase boundary
NAmOx	Nb ammonium oxalate, $NH_4NbO(C_2O_4)_2$
NR	Nonergodic relaxor
p	Dipole moment
P	Polarization
P_r	Remnant polarization
P_s	Spontaneous polarization
P_{sat}	Saturation polarization
pc	Pseudocubic
PLZT	$Pb_xLa_{1-x}Zr_yTi_{1-y}O_3$
PMN	$PbMg_{1/3}Nb_{2/3}O_3$
PNR	Polar nano region
PPT	Polymorphic phase transition
PT	$PbTiO_3$
PZ	$PbZrO_3$
PZT	$PbZr_xTi_{1-x}O_3$
Q_m	Mechanical quality factor

s	Mechanical compliance (s = 1/Youngs modulus)
S	Strain
SiPt	Platinized silicon: $Si_{100}\|(SiO_2)\|TiO_x\|Pt_{111}$
ST	$SrTiO_3$ (often as a single crystal substrate)
T	Temperature
T_B	Burns temperature
T_C	Curie temperature
T_d	Depoling temperature
T_f	Freezing temperature of PNRs
$T_{V\text{-}F}$	Vogel-Fulcher temperature. Same as T_f
T_m	Temperature of maximum permittivity
TIP	Ti isopropoxide, $Ti(OCH(CH_3)_2)_4$
TLens	Tunable Lens
ε	Dielectric permittivity
ε_0	Permittivity of vacuum
ε_r	Relative permittivity (to that of vacuum)
σ	Stress
χ	Dielectric susceptibility

Chapter 1

Background

1.1 Introduction to piezoelectric materials

Piezoelectrics are materials which develop an electrical signal as a response to mechanical pressure. The name is derived from the Greek word *piezein*, meaning to press. The effect is reversible, implying that applying a voltage will cause the material to deform. The piezoelectric effect is illustrated in Figure 1.1. Rochelle salt was the first material to demonstrate piezoelectric properties in 1824, and the electromechanical coupling was demonstrated in 1880. During the second world war, several countries independently developed sonar technology based on the piezoelectric ceramic $BaTiO_3$. $Pb(Zr,Ti)O_3$ (PZT) was discovered in the mid 50's, and after more than 60 years of development, PZT and related materials have achieved the role of state of the art piezoelectrics. [1]

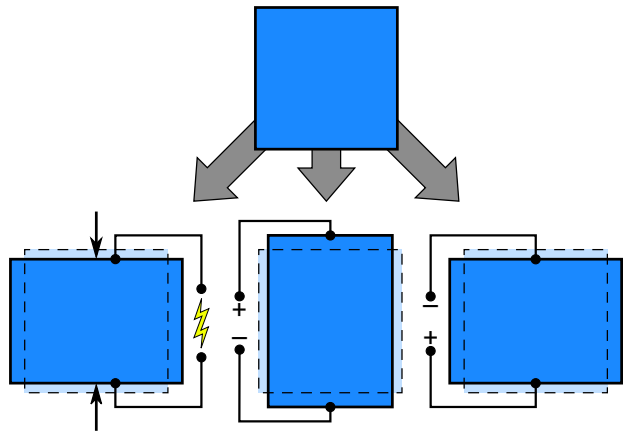

Figure 1.1: Piezoelectric response. Top: starting material. Left: electrical output from mechanical stimulus. Middle/right: mechanical output from electrical stimulus.

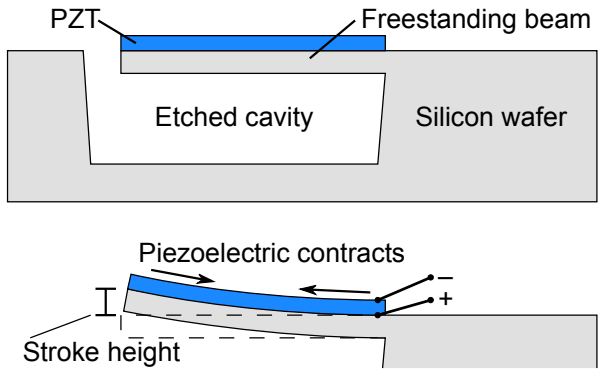

Figure 1.2: Illustration of a cantilever bending actuator on silicon wafer. The typical unit footprint is 10×10 μm^2 to 500×500 μm^2.

Piezoelectric materials are relevant for a range of applications, and PZT and other piezoelectric materials are currently employed in a number of devices. For example, PZT can be found in pressure sensors, balances, accelerometers, transducers, ultrasonic imaging devices, and high accuracy micro-positioners such as the Hubble space telescope and fuel injection dies in combustion engines. Another important application of PZT materials is in capacitors, as the dielectric permittivity of piezoelectric materials is inherently large. For this reason, PZT and related materials may be found in nearly all categories of electronic devices. [1, 2]

When PZT is deposited as a thin film on top of a cantilever beam, the cooperative bending gives rise to actuators with much larger stroke lengths than what can be achieved for bulk piezoelectrics. Figure 1.2 illustrates how contraction in the piezoelectric layer causes bending in a bimorph cantilever. Silicon wafer technology is mature, and fabrication facilities and single crystal wafers are readily available. Furthermore, there is a range of techniques available for deposition of additional functional layers and controlled removal of silicon by etching techniques. Preparing structures such as the one depicted in Figure 1.2 is therefore trivial, and every wafer may consist of thousands of these units. Devices, both actuators and sensors, fabricated used the silicon wafer processing framework are known by the term *micro electromechanical systems* (MEMS). [3]

The widespread use of PZT in electronic devices is not without concern due to the well-known toxicity of lead. In principle, no more than 0.1 % of lead is allowed in any homogeneous material in electronic devices, according to the EU-directive “Restriction of the use of certain Hazardous Substances in electrical and electronic equipment” (RoHS). [2] PZT contains about 60 wt% lead, and should for this reason not be allowed. At this point in time, however, lead-free alternative material systems are not as developed, and despite more than a decade of significant research into lead-free piezoelectrics, replacing PZT in all usage areas is not feasible. Lead containing piezoelectric materials are therefore explicitly exempt from the RoHS until alternative material systems are developed. One of the most appealing features of the PZT materials is that the properties may be adapted by modifying the composition, making it ideal for all kinds of applications. Lead-free alternatives, on the other hand, appear to be more limited to specific uses, requiring a combination of materials in order to replace

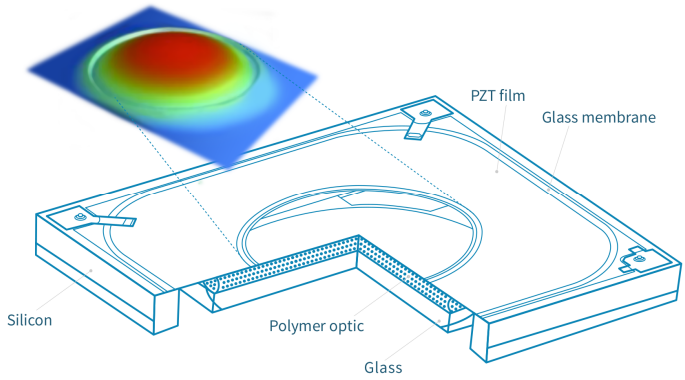

Figure 1.3 Illustration of the TLens. Reprinted with permission from [6].

PZT across the market. For some specific applications, lead-free alternatives are now emerging. [4]

1.2 The TLens

TLens, short for tunable lens, is an autofocus lens commercialized by the Norwegian company poLight AS. In contrast to traditional voice coil motor (VCM) lenses, where change of focus is achieved by moving solid glass lenses back and forth, the TLens relies on a soft lens which is deformed to change curvature and focal length. The size of the first generation TLens is $3.2\times3.2\times0.4$ mm^3, making it the autofocus lens with the smallest footprint available. With the emergence of dual camera set-ups in recent mobile devices, a selling point of the TLens is the electrical mode of operation which, unlike the magnetically driven VCM lenses, does not suffer from interference by closely placed devices. Moreover, because there is only minimal movement compared to the offsetting of glass lenses in alternative setups, autofocus can be achieved almost instantaneously, giving the most rapid autofocus of any competing technology. The soft lens itself consists of a patented high refractive index polymer gel [5], which is bonded to a thin glass membrane in the front. This glass membrane is in turn coated with a piezoelectric PZT film resulting in a 3-dimensional version of the bending mode actuator described in Figure 1.2. The PZT film is only present around the edges of the lens, leaving a transparent aperture in the center as shown in Figure 1.3. [6]

The main figure of merit for changing the focal length is the curvature of the face of the lens, which in turn is determined by the stroke length of the bimorph piezoelectric actuator. Therefore, the most critical property of the piezoelectric layer is achievable strain in the in-plane direction. Moreover, the film must be dense, homogeneous, and the correct thickness to properly match the mechanical properties of the film with properties of the glass membrane. If the film is too thin, it will not deliver sufficient force to bend the glass and deform the polymer, while if it is too thick, its own bending resistance will constrict the stroke height. For the current TLens with a PZT actuator, the ideal thickness is on the order of 2 µm.

There are primarily two alternative electrode designs often used for MEMS devices: top and bottom, and interdigitated. [7] As can be seen in Figure 1.4, the former makes use of the

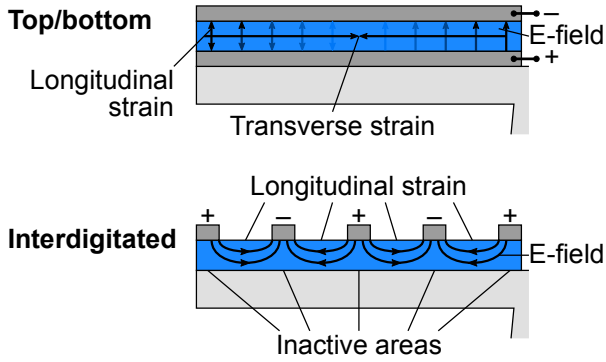

Figure 1.4 Different MEMS electrode designs.

transverse strain, while the latter makes use of longitudinal strain. Typically, longitudinal strain is larger in magnitude than transverse strain, but interdigitated electrodes leave portions of the piezoelectric material inactive. Furthermore, transverse strain is most often contractive, and longitudinal elongating. The TLens currently employs top and bottom electrodes, and this design is the technologically easiest to achieve, but depending on the properties of the piezoelectric, it would also be possible to make use of the interdigitated design. In the case of elongating strain, the piezoelectric would have to be placed underneath the glass membrane, which is gives a more complicated production, but is still viable.

Regardless of electrode design, the electrode material must be compatible with the piezoelectric material. This means that nucleation and growth of the PZT film must be promoted on top of the bottom electrode, and that the electrode itself must be able to withstand the conditions during synthesis of the piezoelectric material. For perovskite materials such as PZT and other piezoelectrics, thin film annealing is often conducted at 700-800 °C under oxidizing conditions, meaning that the electrode must be either an oxide or a noble metal which will not be oxidized. For PZT, the limiting aspect is the relative nobility of lead. During synthesis, too reducing conditions will cause reduction of lead, which must be avoided. Other piezoelectric materials may be more stable, allowing for less oxidizing conditions and use of less noble electrodes. Platinum is stable at oxidizing processing conditions, and have been found to be an excellent seed layer for deposition of perovskites. Therefore, the so-called platinized silicon has become the standard substrate for deposition of electronic oxides in silicon wafer technology. [8] Platinized silicon stacks consist of a single crystal silicon wafer in the (100) direction, ~1 µm SiO_2, ~20 nm partially oxidized titanium (TiO_x), and finally a ~40 nm thick platinum bottom electrode textured in the (111) direction. Even though some lead-free materials could potentially use cheaper and otherwise preferred electrode materials, the fact that platinized silicon is the industry standard results in most research on lead-free materials to employ it as well. The TLens is currently produced using a modified platinized silicon substrate.

1.3 Motivation

The motivation of this work was simply to replace PZT in the TLens with another suitable lead-free alternative due to the environmental, health, and legislative concerns surrounding lead containing materials. As discussed above, the most promising lead-free piezoelectric materials are still not mature enough for implementation, and as such, the goal is not to produce a TLens version 2, but rather to address some of the currently unsolved challenges. A replacement material would need appropriate properties for use in the TLens, it would need to be synthesized in sufficient quality and thickness, and it would need to be compatible with current silicon wafer batch processing for large scale production at a competitive cost. The material system chosen for this task is the one based on $Bi_{0.5}Na_{0.5}TiO_3$ (BNT) because of its excellent strain properties and due to considerable recent efforts to develop BNT materials.

Other well-known lead-free material systems under investigation for replacement of PZT are $(K,Na)NbO_3$ (KNN), $BaTiO_3$ (BT), and $(Ba,Ca)(Zr,Ti)O_3$ (BCZT). [4] The material systems are characterized by different advantages and disadvantages. For example, KNN exhibits a relatively large small-signal piezoelectric coefficient, meaning that a large response is achieved at a small applied voltage. Furthermore, the Curie temperature is high, meaning that high-temperature applications is possible. This makes KNN ideal for transducer applications, but a moderate achievable absolute value of strain limits the applicability when large stroke lengths is key. [4] Similarly, BT is limited by the maximum operation temperature, but excels in dielectric permittivity, making it interesting for capacitor applications. [4] BCZT, on the other hand, possesses excellent actuator properties, albeit with a significant temperature dependency. It is therefore primarily interesting for room temperature applications. [4] A camera module in a mobile device must be expected to operate at any temperature between −10 and 80 °C, and the temperature stability and large strain of BNT based materials render it ideal for use in the TLens. [9, 10] For a more comprehensive treatment of relevant properties of the materials, the reader is referred to Section 2.2.2 Lead-free alternatives.

For production of electronic oxide thin-films such as PZT in the TLens, chemical solution deposition (CSD) combined with spin-coating is the industrially most relevant method. [11] Compared to alternative thin-film deposition methods, CSD can be adapted for deposition on wafers of varying sizes. This allows for high throughput batch level production of devices in established production facilities. With respect to research and development, CSD has the advantage of the simple procedure for preparing precursor solutions, allowing rapid investigation of chemical modifications to the oxide film, and simple production of a range of compositions. Finally, CSD is ideal for production of films approximately 2 µm thick, the optimal thickness of the actuator in the TLens. Further discussion on deposition methods is provided in Section 2.4: Thin film synthesis.

1.4 Aim of the work

Most of the literature on BNT involves preparation of bulk BNT ceramics and their piezoelectric properties. The fundamental understanding of the properties of bulk BNT have been intensively studied recently (see Section 2.3 BNT), including the compositional dependence of the properties. For this reason, the primary focus was to establish a BNT thin-film synthesis route compatible with silicon wafer technology.

Currently, the majority of perovskite thin-film deposition uses either physical deposition methods or CSD methods based on 2-methoxyethanol (2-MOE) or other organic solvents. [12] The methods based on 2-MOE are mature, but the toxicity of 2-MOE is a concern. CSD based on other organic solvent are generally sensitive to aging with resulting poor reproducibility. [11, 12] Furthermore, since the overall goal of the project was to make the TLens more environmentally friendly and less toxic, avoiding harmful substances during synthesis was also desirable. The present research group has solid experience in chemical solution methods using water as the solvent, and preparing BNT thin-films by an aqueous method was therefore the ideal choice. The primary goal of the work was to develop a robust and up-scalable aqueous chemical solution deposition framework for the BNT material system. Spin-coating was selected as the deposition method, and the resulting wet layer was dried and pyrolized by rapid thermal processing before repeating the process for increasing the thickness of the final thin films. Different precursor chemistries were investigated with respect to stability, aging, and phase purity of the final films. Powder samples were prepared to investigate the chemistry of the process, the thermal decomposition of the inorganic-organic network, and the crystallization of the BNT perovskite.

Superior piezoelectric properties of BNT are obtained upon chemical modification with other cation dopants. Solid solutions of $Bi_{0.5}Na_{0.5}TiO_3$-$BaTiO_3$ (BNT-Ba) are the most commonly reported BNT materials in literature, and enhanced piezoelectric properties have been seen at the morphotropic phase boundary (MPB) at 6 % Ba. [13] The second aim of the work was therefore to adapt the BNT synthesis framework for addition of Ba. Other commonly added dopants yielding promising compositions include K, Sr, Li, and Nb [9, 10, 14, 15], and substitution of these elements was therefore also investigated with focus on the phase purity of the samples and the sol behavior. Finally, electrical properties of the chemically modified thin films were characterized, establishing the ferroelectric nature of the thin-film materials.

Substrates on which perovskites are deposited vary, but the most commonly used are platinized silicon (SiPt) and single crystal oxides such as $SrTiO_3$ (ST). SiPt is the industry standard for use in MEMS devices, and is highly relevant for the TLens. ST is similar to BNT, with the same crystal structure and closely matched mechanical properties. Furthermore, ST is inert and provides excellent seeding conditions. For this reason, ST was used as a reference substrate throughout this work. SiPt, on the other hand, represents challenges due to difference in thermal expansion coefficients and reactivity of the different layers and interfaces. Adapting the BNT synthesis framework for use on SiPt substrates was the final aim of this work. The major challenge in this regard was reactivity of Bi from BNT and Pt which, coupled with thermal expansion mismatch, led to film delamination. Bi-Pt reactivity was shown to be a persistent problem when coating BNT directly on top of Pt, and improved thin-film quality was pursued by introduction of a $BaTiO_3$ intermediate protective layer.

Chapter 2

Literature review

2.1 Piezoelectricity

2.1.1 Classifications

Only few material classes are piezoelectric. First, the material must be a so-called *dielectric* material (insulating). An electrically conductive material has mobile charges which will counteract any internal polarizations. Central to the piezoelectric response is unequal movement of ions of opposite charge. Due to different electronegativity of the elements, even covalently bonded materials are ionic to some extent as long as the material does not contain only one type of element. Even for ionic dielectric materials, however, piezoelectricity is not guaranteed.

The microscopic origin of piezoelectricity lies in the symmetry of the crystal. [1] Imagine first the well-known sodium chloride structure shown in Figure 2.1. This 2-dimensional representation illustrates that applying a force to the material will displace positive and negative charges the same magnitude and therefore not influence internal polarization. Conversely, by exposing NaCl to an electric field, even though Na^+ and Cl^- will be oppositely displaced, the overall repeating unit will not change dimensions. The structure symmetry condition dictating this lack of piezoelectric properties lies in the fact that NaCl is centrosymmetric. [2] Each repeating unit is symmetric through the center, rendering different response of positive and negative charges (i.e. piezoelectricity) impossible.

Imagine next a material which is not centrosymmetric, as shown in Figure 2.2. Here, applying an external force will cause dissimilar offset of positive and negative charges. In this example, positive charges are offset by d downwards, and negative charges are offset by d upwards. Multiplied by the charge, q, the electric dipole moment, p, for each repeating unit is obtained. For illustrative purposes, the vertical bond lengths are assumed constant. This assumption is supported by imagining that the bond lengths are more rigid than the bond

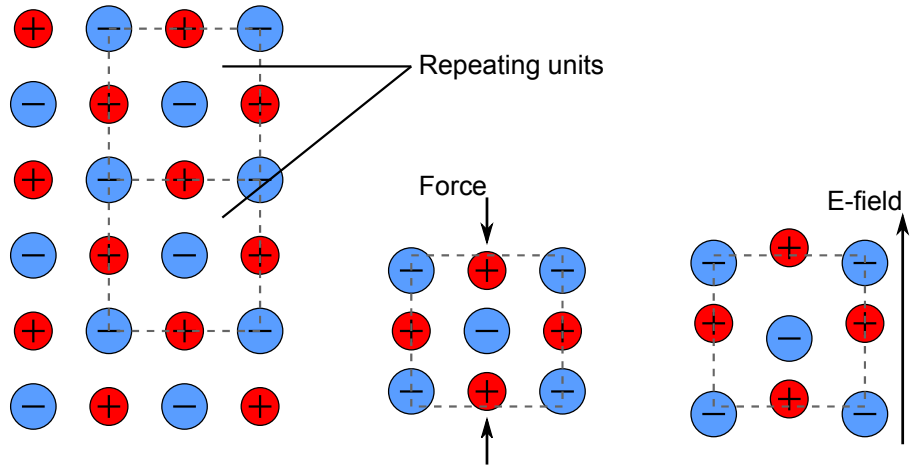

Figure 2.1 2-dimensional illustration of how a centrosymmetric material reacts to external mechanical and electrical stimuli. It is shown that applying a force does not cause dipole moments, and that applying a field does not strain the material.

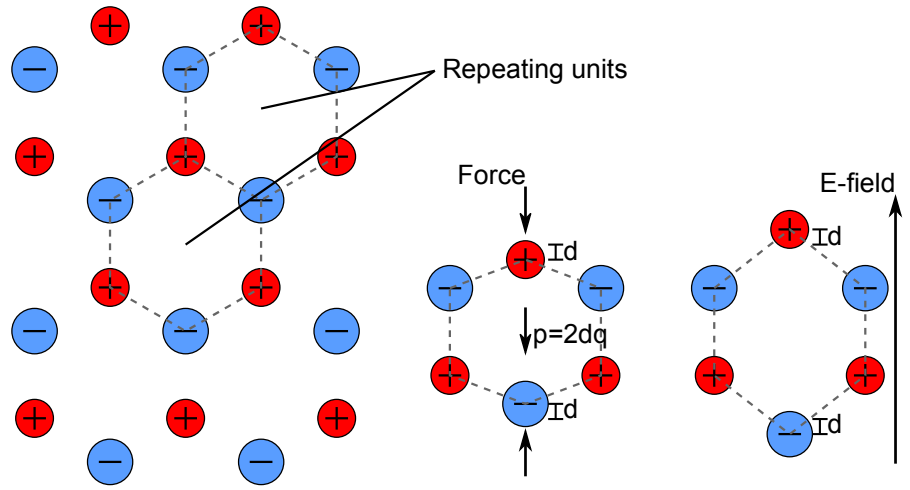

Figure 2.2 Illustration of how a non-centrosymmetric and non-polar material reacts to electrical and mechanical stimuli. Applying a force causes a dipole moment by offsetting opposite charges in opposite directions. An external field causes an elongation of the repeating unit, and accumulated strain.

angles. By considering the empty volume in the center the illustrated response becomes apparent. In a real material, the vertical bonds would be somewhat compressed, contributing to a small reduction in net achieved dipole moment. An external mechanical stimulus resulting in polarization is known as the *(direct) piezoelectric effect*. The *converse* or *indirect piezoelectric effect* describes when an external electric field causes elongation of the repeating units, resulting in a net strain in the bulk material.

In crystallographic terms, the requirement for piezoelectricity is that the point group of the structure must be non-centrosymmetric. In the structure depicted in Figure 2.2, each repeating unit contains 3 positive and 3 negative ions, but they are all shared between 3

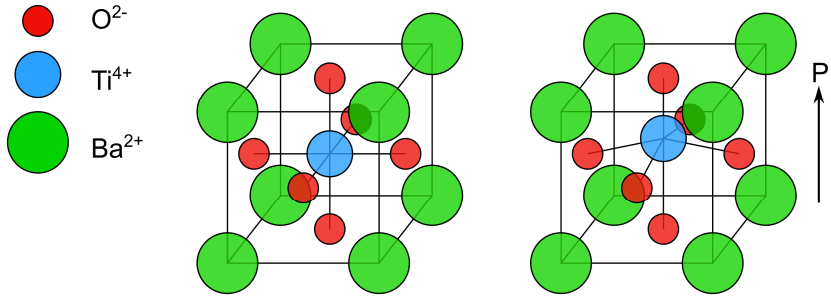

Figure 2.3 Illustration of cubic and polar/tetragonal perovskite $BaTiO_3$.

adjacent units. In crystallography, a lattice point contains exactly one unit formula (ex. A^+B^-), and unit cells containing one lattice point are called *primitive unit cells*. [16] The point group describes the symmetry of each lattice point, and the requirement for piezoelectricity is therefore contained in the primitive unit cell. To account for only one unit formula for each primitive unit cell, the *electric dipole moment*, p [Cm], of two ions is treated. The dipole moments of the other ions must be assigned to the adjacent primitive unit cells. The volume density of these dipole moments is called *polarization*, P [Cm^{-2}].

Figure 2.2 illustrates a piezoelectric material which is not spontaneously polar. In 3-dimensional space, there are 32 distinct point groups. 11 of these are centrosymmetric, while 21 are not. 20 point groups are piezoelectric. A sub-group of piezoelectric materials are the 10 spontaneously polar point groups. The best-known examples of polar piezoelectric materials are the tetragonal perovskites $BaTiO_3$ (BT) and $PbTiO_3$ (PT), [1] and the BT structure is illustrated in Figure 2.3. The unit cell to the left is the prototype cubic perovskite, while the one to the right demonstrates that the central Ti-atom is displaced upwards, giving a dipole moment and polarization in the same direction. Both BT and PT are tetragonal, but while Ti^{4+} is displaced in BT, Pb^{2+} offset is equally important in PT. For $BaTiO_3$ and $PbTiO_3$, this dipole moment is spontaneous at room temperature, making the materials piezoelectric at the unit cell level (macroscopic piezoelectricity is discussed in Section 2.1.3). In polar materials, this *spontaneous polarization*, P_s, is an important material parameter. As the temperature is increased from room temperature, P_s decreases, and at the *Curie temperature*, T_C, the materials undergo a phase transition to a high-temperature *paraelectric* (non-piezoelectric) polymorph. For BT, T_C is 120 °C, and for PT it is 490 °C. [1] The Curie temperature is related to the magnitude of the spontaneous polarization. Stronger dipole moments represent a more stable polar phase, implicating that the extent of this phase will be greater also with respect to other parameters such as temperature. For example, in BT (low T_C), the ion displacement is 0.132 Å, while in PT (high T_C), it is 0.299 Å. [17] The main reason for the different spontaneous polarization values for these materials is the $6s^2$ electron *lone pair* of Pb^{2+}. Because the ions in BT may be assumed to be spherical, the dipole moment may be accurately described by geometrical considerations. For PT, the ion sizes are comparable to BT, but the electron lone pair in the outer band of Pb^{2+} causes a partial covalent bond to O^{2-}, causing an increased dipole moment. [2] BT is for many applications limited by its low Curie temperature, and the superior dipole moment in PZT translates to a higher Curie temperature, and is in part the reason why it is the technologically most successful piezoelectric ceramic.

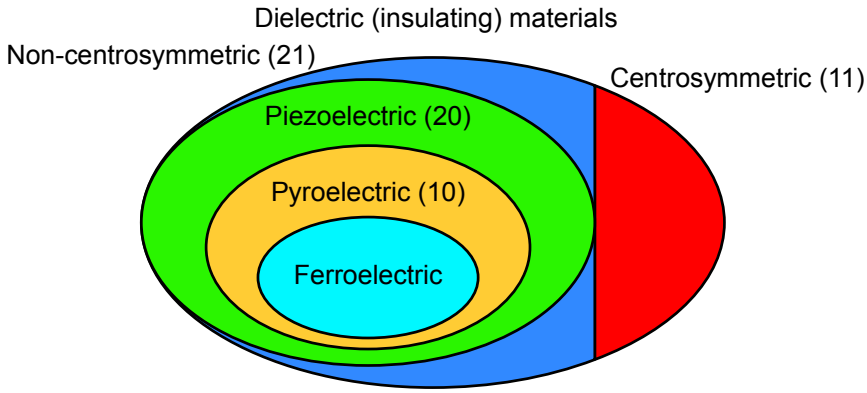

Figure 2.4 Illustration of the sub-group relationships of properties. All dielectric materials are either centrosymmetric or not, while all piezoelectric materials are non-centrosymmetric. The number of point groups are given in parenthesis. Ferroelectricity is not defined by symmetry.

The piezoelectric hierarchy of properties, shown in Figure 2.4, is now emerging. 20 of 32 crystallographic point groups are piezoelectric. Of these, 10 groups are spontaneously polarized. Spontaneously polarized materials express a particular property: they are *pyroelectric*. When a permanent polarization exists, the magnitude of this will be coupled to the dimensions of the crystal lattice. When the lattice expands or contracts due to thermal expansion, the polarization will vary, and a change in temperature may be measured by the developed voltage. It is this coupling of temperature and polarization that defines pyroelectric materials. Yet another sub group of pyroelectric materials are the *ferroelectric* materials. In crystallographic terms there is no point group difference distinguishing pyroelectric and ferroelectric materials. The word *ferro* is adapted from ferromagnets, as the behavior of these materials is similar. Ferromagnets are spontaneously magnetically polar, and this polarization direction may be switched by application of an external magnetic field. The same situation is true for ferroelectric materials. The electrical polarization direction of ferroelectric materials may be switched by application of an external electric field. In the case of the tetragonal perovskite illustrated in Figure 2.3, the possible polarization directions are along the unit cell axes; the Ti atom may be displaced toward any of the six oxygen ions. These directions are energetically equivalent, only distinguished by the switching energy barrier separating the six states. Other perovskite ferroelectric materials may be distorted in another manner than tetragonal. Tetragonal perovskites are polarized in one of the <100> directions, rhombohedral perovskites along <111>, orthorhombic perovskites along <110>, while monoclinic (<hk0>) and triclinic (<hkl>) perovskites are more arbitrarily polarized. [2]

$Pb(Zr,Ti)O_3$ (PZT) is a solid solution system of the two end members $PbTiO_3$ (PT) and $PbZrO_3$ (PZ). While PT is a tetragonal ferroelectric, PZ is *antiferroelectric*. Antiferroelectric materials contain dipole moments, but every adjacent unit is oppositely oriented, rendering the net polarization zero. Thus, these materials are not piezoelectric. The dipoles are present, however, and antiferroelectrics behave different than paraelectric materials. For example, application of an external field may reorient the dipoles, causing an electric field induced phase transition to a ferroelectric state, associated with a large strain. [1] When the field is

removed, however, the material will return to the antiferroelectric state. The phase diagram of PZ-PT will be further discussed in Section 2.1.3.

Electrostriction is a property related to piezoelectricity. The situation described in Figure 2.1 is not completely accurate, as even centrosymmetric dielectric (insulating) materials will react somewhat to external electric fields. [18] More specific, in the NaCl example application of an external field will cause a slight accumulated elongation of the bulk material. All dielectric materials, even non-ionic materials, exhibit electrostriction. Electrostriction applies only to the converse situation, meaning that a field gives resulting strain. On the other side, non-piezoelectric materials will not develop internal polarization due to mechanical stimulus. While fundamental piezoelectricity expresses a linear relationship between electric field and strain, electrostrictive strain is proportional to the square of the electric field. Furthermore, electrostriction is typically smaller in magnitude, and may only be elongating, while piezoelectricity may be contractive.

2.1.2 Mathematical description

Piezoelectric materials are characterized by the coupling of mechanical and electrical properties. The mechanical input/output is often expressed as either strain, S [%], or stress, σ [Pa]. Electrical state is expressed as electric field, E [V/m], surface charge density/displacement, D [Cm^{-2}], or polarization, P [Cm^{-2}]. The general equations relating basic electrical properties of materials and vacuum are given by

$$D = P + \varepsilon_0 E = \varepsilon E \tag{2.1}$$

$$P = D - \varepsilon_0 E = \varepsilon_0 \chi E \tag{2.2}$$

$$\varepsilon = \varepsilon_0 \varepsilon_r \tag{2.3}$$

$$\varepsilon_r = 1 + \chi \tag{2.4}$$

where relative permittivity, ε_r, absolute permittivity, ε, and electric susceptibility, χ, are material parameters, and ε_0 is the permittivity of vacuum. It can be seen that the polarization of a material is the materials intrinsic response, not including the response of vacuum, $\varepsilon_0 E$, while displacement, D, is the net macroscopic response. For piezoelectric materials, the response of vacuum is often negligible, and D and P represent the same fundamental response.

Electrostrictive strain is given by

$$S = mE^2 \tag{2.5}$$

$$S = QP^2 \tag{2.6}$$

where S is strain, E is electric field, P is polarization, and m and Q are the electrostrictive coefficients with respect to electric field and polarization, respectively. [1]

For the converse piezoelectric effect, strain is given by

$$S_i = d_{ji} E_j \tag{2.7}$$

where d, is *the piezoelectric coefficient* and i and j represents crystallographic directions. By convention, the polar direction in a material is assigned the z-direction, and most commonly the electric field is applied along the polarization direction, meaning that $j = 3$ (z-direction).

Strain is then typically measured either along the applied field, termed *longitudinal strain* ($i = 3$), or perpendicular to the field, termed *transverse strain* ($i = 1$). Thus, the piezoelectric coefficients of interest are most commonly d_{31} (transverse) and d_{33} (longitudinal). Complete mathematical treatment should relate the second rank tensor strain with the electric field vector, making d a third-rank tensor. For the scope of most technological applications however, neglecting shear stresses and strains is reasonable, reducing d to a second-rank tensor. [19]

For the direct effect, displacement, D, is given by

$$D_i = d_{ji}\sigma_j \tag{2.8}$$

where the mechanical stress is given by σ. The unit of d is pC/N or pm/V for the converse and direct effect, respectively. It can be deduced that the piezoelectric coefficients are fundamentally the same variables for the direct and converse effects. [19] The units are equal when reduced to the primitive SI units, and the magnitude of d is also equal for the direct and converse effects.

Equations (2.5) through (2.8) assumes that the material not is clamped, but is free to respond unconstricted. For the direct effect, an unclamped situation means that no electric field is influencing the achieved polarization (the two sides are electrically connected to allow neutralization of the surfaces). For the converse effect, it means that no mechanical force is applied to the material when considering the achieved strain. If the material is entirely clamped, the strain will be zero, but stress will develop according to

$$\sigma = eE \tag{2.9}$$

where e is another piezoelectric coefficient. In the case of bimorph cantilever actuators, e_{31} (out-of-plane electric field, in-plane stress) is an important parameter, as it relates the applied field to the in-plane force delivered by the piezoelectric film. In many cases, the assumption of unconstricted response is not valid, and one must consider simultaneous mechanical and electrical stimuli as well as electrostriction, yielding total strain response of:

$$S_i = d_{ji}E_j + m_{ji}E_j^{\,2} + s_{j'i}\sigma_{j'} \tag{2.10}$$

where s is the mechanical compliance (inverse of Young's modulus), and $\sigma_{j'}$ is stress (in a direction not necessarily equal to j). In a partially clamped system, the last term will be negative. Similarly, total displacement is given by

$$D_i = d_{ji}\sigma_j + \varepsilon_{j'i}E_{j'} \tag{2.11}$$

where ε is dielectric permittivity. In actuator applications, Equation (2.10) relates the most important operating parameters, strain/stroke length, electric field, and stress/force exerted by the actuator. It will be shown throughout the rest of this chapter, however, that the input/output relationship is not as straight forward, particularly due to non-constant piezoelectric coefficients upon ferroelectric switching of polarization direction.

Another commonly reported figure of merit is the electromechanical coupling coefficient, k. The square of the coupling coefficient, k^2, defines the ratio of stored mechanical energy to input electrical energy in a clamped material exposed to an electric field. When allowing the material to deform, additional energy will be lost due to friction processes, and k^2 represents the theoretical maximum conversion of electrical energy to mechanical energy

Table 2.1 Electromechanical relationships.

Output \ Input	**Strain**	**Stress**	**Electric field**	**Displacement**
Strain		$S = s\sigma$	$S = dE$	$S = gD$
Stress	$\sigma = YS$		$\sigma = eE$	$\sigma = hD$
Electric field	$E = hS$	$E = g\sigma$	(Converse effect)	$E = \frac{1}{\varepsilon}D$
Displacement (surface charge d.)	$D = eS$	$D = d\sigma$	$D = \varepsilon E$	
Strain (electrostriction)	(Direct effect)		$S = mE^2$	$S = QP^2$

without losses. Some energy is also stored electrically accounting for the non-converted energy, and is reobtained when the field is removed. [4]

For sensor applications, obtained electric field due to input stress

$$E = g\sigma \tag{2.12}$$

is an important figure of merit. g is a piezoelectric coefficient, and $d \cdot g$ defines the successfulness of non-resonant transducers.

The most relevant and commonly discussed piezoelectric relationships are presented in the preceding text. However, there are a range of electromechanical relationships. Piezoelectric couples are defined for all eight combinations of the two electrical parameters *field* and *displacement* and the two mechanical parameters *strain* and *stress*. In these relationships, there are 4 distinct piezoelectric coefficients, which can be reduced to two by including the permittivity of the material. Furthermore, Hooke's law defines the mechanical-mechanical relationship through Young's modulus, Y, and its inverse, mechanical compliance, s. The electrical relationship corresponding to Hooke's law, connects electric field and displacement through the permittivity. Both as a tool for reference, and for completeness, all electromechanical couples are given in Table 2.1. Similarly, for simplified reference, the relevant parameters are defined in Table 2.2.

2.1.3 Ferroelectric domains and hysteresis loops

Large volumes of uniform polarization lead to excessive electrostatic energy stored in the material and is not favored. Rather, every single crystal divides into *domains* of different polarization directions, separated by the *domain walls*. Across the domain walls, dipole moments gradually change and the walls may be several unit cells wide. Since the dipole moments in the domain walls are not the spontaneous magnitude, the walls will also cause an increase in energy. The final domain structure represents a balance of the two opposing energies. The overall lattice is defined by the grain, but depending on the structure of the material, several discrete polarization directions are available, as described on page 10. This means that tetragonal perovskites may have domains oriented 90° or 180° with respect to each

Table 2.2 Definition of electric, mechanical, and piezoelectric parameters.

Parameter	Symbol	Unit	Order of magnitude	Notes
Strain	S	%	0.1	$S = \Delta l / l_0$
Stress	σ	Pa	100 MPa	
Electric field	E	Vm^{-1}	10 $kVcm^{-1}$	
Surface charge density	D	Cm^{-2}	0.1	Synonym: displacement
Piezoelectric coefficient	d	$CN^{-1} = mV^{-1}$	100 pCN^{-1}	
	e	$Cm^{-2} = NV^{-1}m^{-1}$	1	$e = \varepsilon h$
	h	$Vm^{-1} = NC^{-1}$	100 MVm^{-1}	$d = \varepsilon g$
	g	$VmN^{-1} = m^2C^{-1}$	1	
Electrostrictive coefficient	m	m^2V^{-2}	10^{-18}	
	Q	m^4C^{-2}	10^{-2}	
Young's modulus	Y	Pa	GPa	
Mechanical compliance	s	Pa^{-1}	GPa^{-1}	$s = 1 / Y$
Dielectric permittivity	ε	$CV^{-1}m^{-1}$	10^{-11}	$\varepsilon = \varepsilon_r\varepsilon_0$
Electric susceptibility	χ		100	$\chi = \varepsilon_r - 1$
Polarization	P	Cm^{-2}	0.1	$D = P + \varepsilon_0 E = \varepsilon E$ $P = \varepsilon_0 \chi E$
Dipole moment	p	Cm		$P = p$ / *volume*

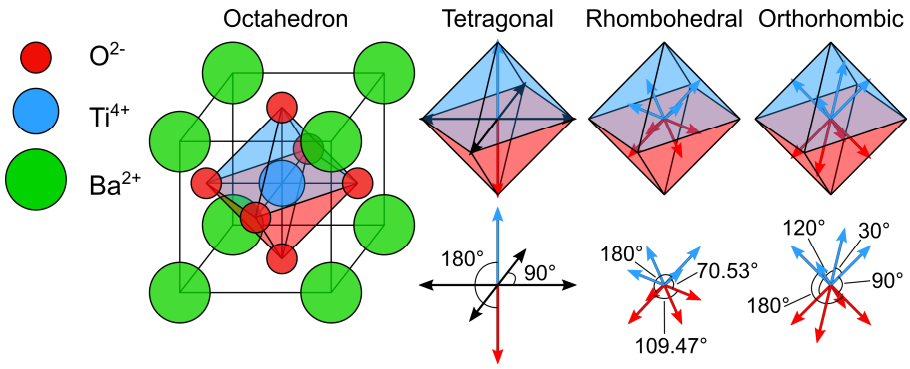

Figure 2.5 Illustration of the different polarization directions of perovskites. Tetragonal perovskites are polar towards the corners of the octahedron, rhombohedral towards the faces, and orthorhombic towards the edges. Top and bottom half of the octahedron are color coded for visibility. For clarity, the four "horizontal" polarization direction in the orthorhombic case are not shown. The grains in a material define the primary directions, but within ferroelectric domains the polarizations can be any of the energetically equivalent polarizations directions, depending on the symmetry of the structure.

other. Rhombohedral domains are oriented 70.53°, 109.47° or 180° to each other, and orthorhombic domains are oriented in 60°, 90°, 120°, and 180° intervals. Figure 2.5 illustrates the possible domain directions of perovskites with different symmetry.

In polycrystalline materials, each grain represents a specific single crystal, where the overall lattice directions are unique. Figure 2.6 illustrates a possible domain structure in a tetragonal perovskite. The net polarization is zero due to the randomly oriented domains. When applying an electric field, however, domains oriented in the proper direction will grow on the expense of neighboring domains. At a sufficiently strong field, the entire volume of the

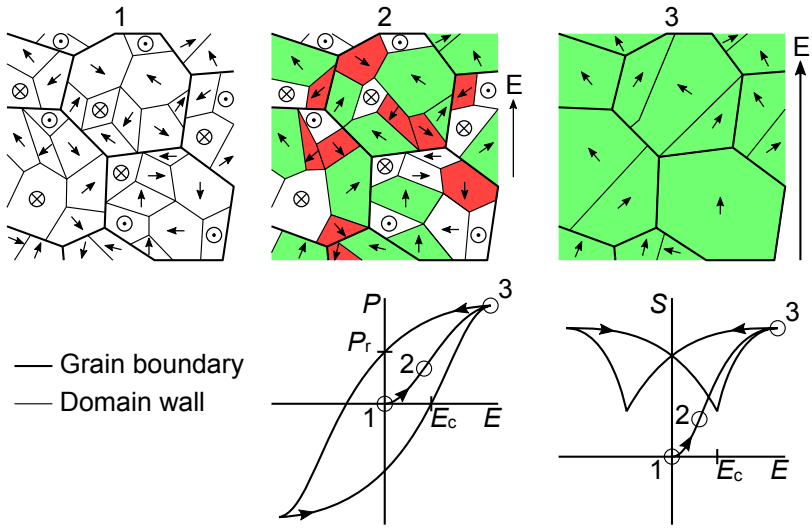

Figure 2.6 Illustration of a possible domain structure in a tetragonal (domains oriented 90° or 180° to each other) perovskite, and its response to an electric field. Green domains are energetically favorable upon applying the external field, and grow on expense of red domains. Stage 1 illustrates the virgin state before first application of an external field. At stage 2, the favored domains increase in size, and at stage 3, all domains are optimally oriented, saturating the polarization. The macroscopic polarization and strain responses are illustrated with the stages marked on the curves.

material will consist of domains oriented in almost the same direction as the field, limited only by the overall lattice of the grains. Typically, when the field is subsequently removed, a net polarization remains, rendering even polycrystalline ferroelectric materials polar. This process is known as *poling*, and is essential in modern piezoelectric technology, as most piezoelectric materials are polycrystalline ceramics. Often, poling is conducted by applying a field at elevated temperatures, and cooling down the material while maintaining the field. In the virgin state, before poling, different domains give electromechanical response in different directions, in average canceling out. The value of the polarization after returning to zero field is another important material characteristic known as the *remnant polarization*, P_r. The remnant polarization is typically stable with respect to time, but at the *depoling temperature*, T_d, the net polarization is lost. The depoling temperature is lower than T_C, effectively limiting the temperature range of application of the material. Often, poling is not feasible after implementation in a device, and heating to T_d may mean end of life for some units.

The fact that a polarization value different than zero remains at zero field means that the randomly oriented virgin state may not be re-obtained. At a sufficiently strong negative field, the domain structure is switched directly between the two directions, giving a steep slope in the field-polarization curve. The required switching field is known as the *coercive field*, E_c. After the material has been poled, the so-called *hysteresis* loop defines achievable polarization with respect to field. In Figure 2.6, the hysteresis loop is illustrated with reference to particular domain structures.

Because strain state is equal for polarizations oriented 180° to each other, the virgin material has a zero-strain state which may not be re-obtained after the initial poling, assuming

that only antiparallel electric fields are applied (Figure 2.18). Strain versus electric field is illustrated in Figure 2.6. In order to achieve the virgin zero strain, the material must be depoled, for example by thermal annealing at T_d or higher, or poled in a direction 90° to the previous state, which would enable negative transverse strain in the original poling direction. The latter option is often not viable as the electrodes in a device are fixed to a specific direction.

Microscopic piezoelectricity is a linear effect, but the switching of domains and movement of domain walls contribute with a larger, non-linear effect. The linear part is termed *intrinsic piezoelectric response* and is observed close to zero field. The intrinsic piezoelectric coefficient, d_{33}, is visible as the slope where the strain curve crosses the y-axis in Figure 2.6. Contributions from domain switching are termed *extrinsic* effects. An important piezoelectric figure of merit is the *large-signal* piezoelectric coefficient, $d^* = S_{max}/E_{max}$, expressing the average slope from zero to maximum achieved strain.

Parameters such as remnant polarization and coercive field are material specific, and may even be tailored within a material system in order to adapt to particular applications. For use in sensor or voltage generator applications, for example, it is important that the poling state is as stable as possible, because the input is mechanical, and applying a field to re-align the domains in the correct direction may not be possible. This means that the coercive field should be as high as possible, which is termed a *hard* ferroelectric. For actuator applications, however, having to apply a strong field to reach the largest strain response experienced around E_c is not ideal. Rather, E_c should be as small as possible, with a narrow hysteresis loop, termed a *soft* ferroelectric. One of the reasons why PZT has become so successful is due to its excellent tunability. In the PZT system, the so-called PZT-4 is an example of a hard ferroelectric, while one of the soft compositions is obtained at $Pb_{0.93}La_{0.07}Zr_{0.6}Ti_{0.4}O_3$ (PLZT). Figure 2.7 shows the PZ-PT-La phase diagram. Complete solid solution is obtained for up to 0-30 % La, and increasing La content decreases the Curie temperature. Most commonly, PZT materials have compositions close to the phase boundary between Zr-rich rhombohedral and Ti-rich tetragonal areas. The TLens currently employs a similar soft PZT based material. [1]

2.1.4 Morphotropic phase boundaries

PZT refers to the range of compositions from $PbZrO_3$ (PZ) to $PbTiO_3$ (PT). Figure 2.7 shows that pure PZ is antiferroelectric, and upon adding PT the structure obtained is a rhombohedral ferroelectric. Pure PT is a tetragonal ferroelectric. [8] The phase boundary between Zr-rich rhombohedral and Ti-rich tetragonal materials is located at around $PbZr_{0.6}Ti_{0.4}O_3$. This transition is more or less independent of temperature, and is termed a *morphotropic phase boundary* (MPB). [20] At the MPB, several of the piezoelectric properties are greatly enhanced, and the properties are relatively temperature independent, as seen in Figure 2.8(a). There have been suggested many explanations for the behavior at MPBs, and one relates the similar energies of the two phases to the stability of the local dipole offset. In a material where two phases are equally stable, the dipole offset of the ions are not strongly fixed to a particular position, but may more easily be affected by an external field. This translates to a stronger mechanical response to the input field, and higher piezoelectric coefficients and permittivity.

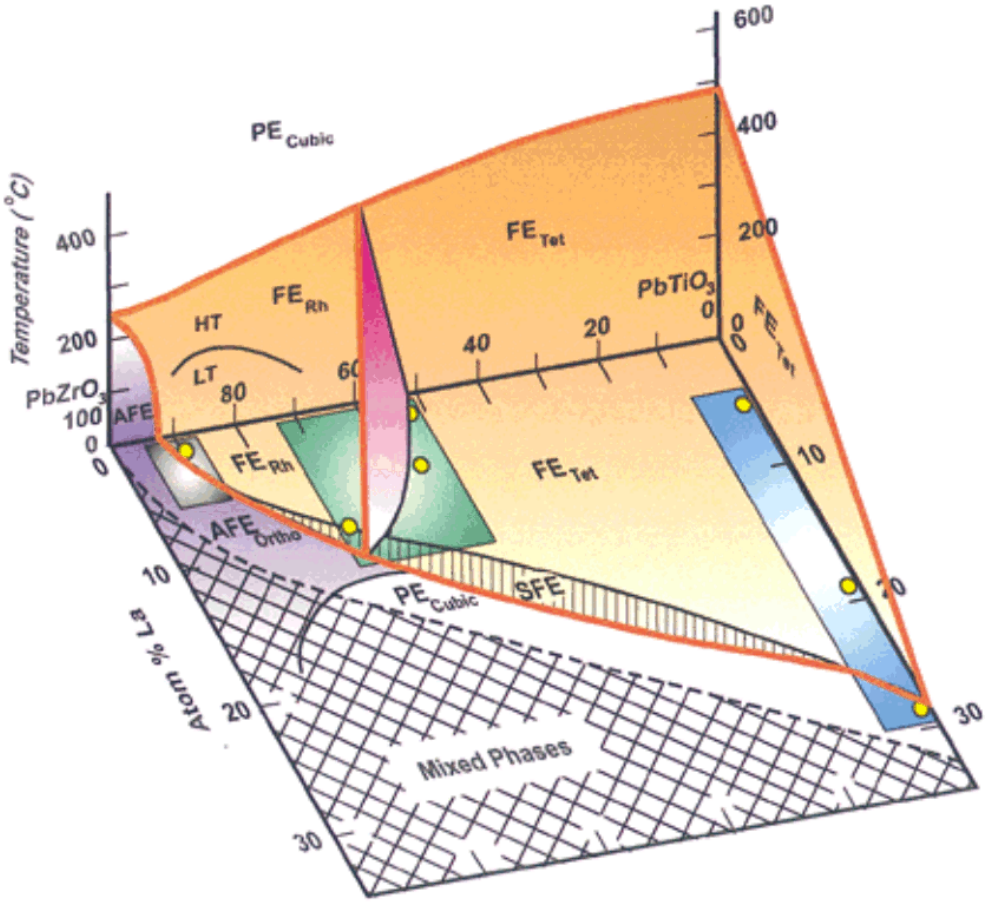

Figure 2.7 Phase diagram of PZT with La doping. Reprinted with permission from [1].

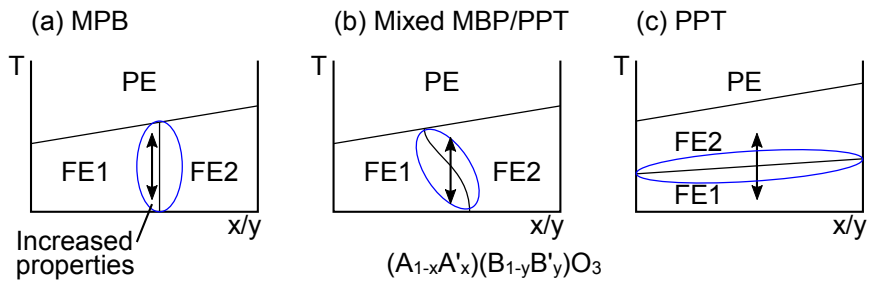

Figure 2.8 Illustration of phase diagrams with *morphotropic phase boundary* (MPB) and *polymorphic phase transition* (PPT) for the hypothetical composition $(A_{1-x}A'_x)(B_{1-y}B'_y)O_3$. Varying the temperature within the area of increased properties will cause different degrees of phase transitions and temperature-dependent performance. FE denotes ferroelectric phases, and PE denotes the high-temperature paraelectric phase.

The same trend is observed at ferroelectric to paraelectric phase transition at the Curie temperature, which is characterized by a sharp peak in permittivity. [2]

A related phenomenon is ferroelectric to ferroelectric phase transitions with respect to temperature as opposed to composition, termed *polymorphic phase transitions* (PPT). For example, the well-known lead-free piezoelectric material $K_xNa_{1-x}NbO_3$ (KNN, phase diagram in Figure 2.14) is orthorhombic at room temperature, but turns tetragonal at around 200 °C. [21] The same increase in properties may be observed at this temperature, but due to the nature of the phase transition, these properties are highly temperature dependent, as visualized in Figure 2.8c. The PPT may often be tuned to different temperatures by compositional engineering, for example chemical modifications to KNN cause the PPT to decrease to room temperature. [22] Because the maximum properties are temperature dependent, however, the uses are limited to certain applications. Furthermore, temporarily increasing the temperature across the phase transition, even during storage or handling, may cause depolarization and end of life for the device, practically limiting the devices exploiting the very best properties exactly at the transition temperature. Higher temperature stability may be achieved by designing the PPT temperature to be sufficiently different to operating temperatures, sacrificing some performance in order to avoid crossing the phase transition temperature.

In the quest for developing lead-free alternatives to PZT, a common approach has been to prepare solid solutions of different ferroelectric end member materials in the hope that an MPB with increased properties will be identified. [23] Some examples of explored combinations are $K_xNa_{1-x}NbO_3$-$BaTiO_3$ (KNN-BT), KNN-$Bi_{0.5}K_{0.5}TiO_3$ (KNN-BKT), BNT-$NaNbO_3$ (BNT-NN), BNT-$BaCu_{0.5}W_{0.5}O_3$, BNT-KNN, BNT-BT, BNT-BKT and BT-$BiFeO_3$ (BT-BF). [2] The common characteristic of these pairs is that they combine two ferroelectric perovskites of different symmetries, hoping that the phase transition composition shows enhanced properties.

2.1.5 Relaxors

Relaxors is a class of ferroelectric materials that is not yet fully understood, exhibiting superior properties in some situations. The average structure, as characterized by diffraction, is non-polar. However, relaxors behave as piezoelectrics, surpassing traditional materials in applications such as capacitors (permittivity) and actuators (hysteresis-less and large strain). Relaxors are recognized by 3 characteristic differences to regular piezoelectric materials. [24]

1. Properties at the temperature of maximum permittivity, T_m, deviates from the behavior of traditional piezoelectrics at the Curie temperature. While permittivity has a sharp maximum at T_C in regular piezoelectrics, the permittivity peak at T_m is broad in relaxors.
2. The temperature of maximum permittivity is frequency dependent. While the Curie temperature is independent on the frequency of the applied field, relaxors show increasing permittivity at decreasing T_m for decreasing frequencies (see Figure 2.9).
3. The macroscopic symmetry is not changed upon changing the temperature between high-temperature paraelectric state and low temperature relaxor/ferroelectric.

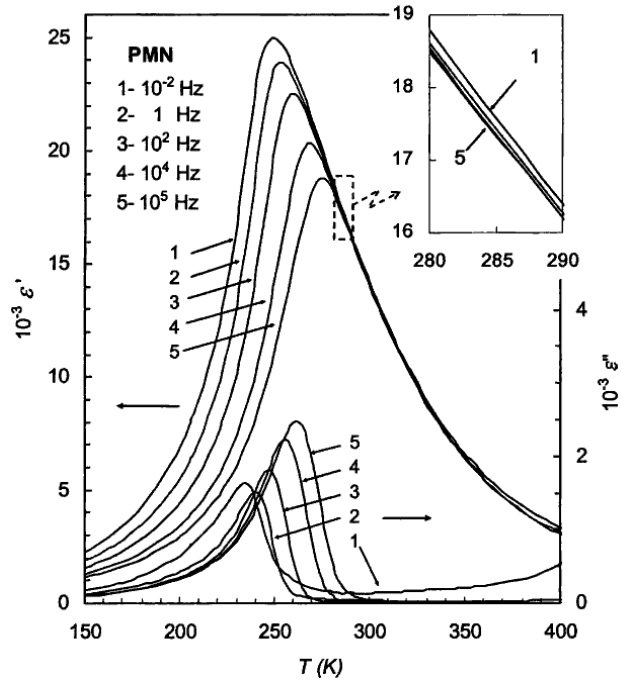

Figure 2.9 Permittivity of $PbMg_{1/3}Nb_{2/3}O_3$ (PMN) as a function of temperature. The broad maximum at a temperature varying with frequency are characteristics of relaxor materials. Reprinted with permission from [25].

Because there is no macroscopic symmetry change upon transition from relaxor to paraelectric, the Curie temperature is without meaning, and not defined. However, when cooling down, at the *Burns temperature*, T_B, the material enters the state of an *ergodic relaxor* (ER). It seems widely accepted in the literature that the microscopic cause of relaxor behavior is connected to very small polar areas in the structure, so-called *polar nano regions* (PNRs). [25] These PNRs are smaller than ordinary domains, maybe as little as a couple of unit cells large, and invisible to traditional diffraction techniques, because these probe the average macroscopic structure, which is still non-polar. The Burns temperature signifies the onset of PNRs and relaxor properties. Close to T_B, the material is ergodic, meaning that the polar areas are at an equilibrium state, and will react to infinitesimal changes in conditions. In other words, the PNRs are mobile and constantly changing. Upon further cooling, however, the PNRs will turn less dynamic, and at the freezing temperature (also known as the Vogel-Fulcher temperature, $T_{V\text{-}F}$ [26]), T_f, a nonergodic state of static PNRs will ensue. This behavior is similar to traditional glass transitions, such as the nonergodic state of dipole glasses or spin glasses. Relaxors deviate from dipole glasses, however, in that a ferroelectric state may be achieved by provoking an irreversible electric-field-induced phase transition from the nonergodic relaxor state. [25]

Analogously to the increased properties of ferroelectrics at the MPB or T_C, where ions are more easily displaced and properties are increased, relaxors also show increased properties in certain applications. For example, the dielectric permittivity may be extraordinarily high

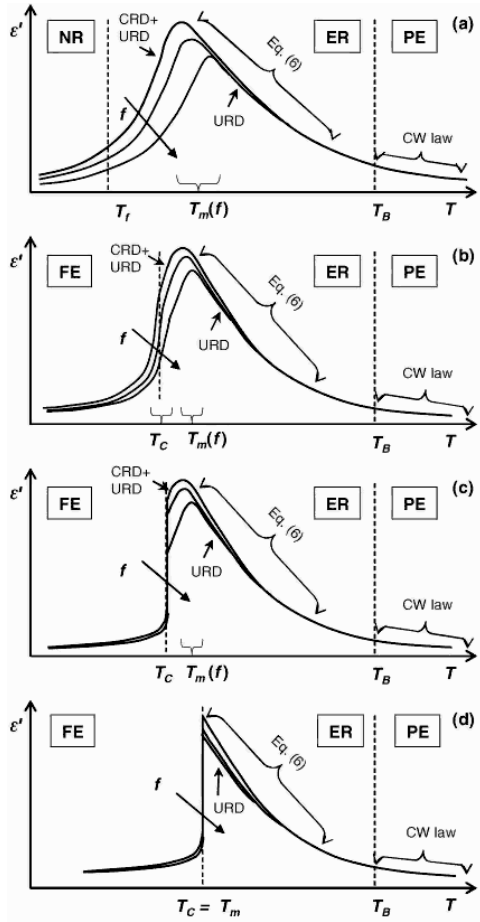

Figure 2.10 Different models of relaxor materials. (a) Canonical relaxor. (b) Relaxor with a 'diffuse' transition from ergodic relaxor to ferroelectric state. (c,d) Relaxors with exact Curie temperature, lower than, or equal to T_m, respectively. Reprinted with permission from [25].

(ε_r equal to 10 000-20 000) with larger degree of temperature stability than what could be achieved for traditional ferroelectrics at T_C. [24]

Some relaxor materials will spontaneously turn ferroelectric rather than nonergodic relaxor upon cooling, yielding an even more complicated process of characterizing and defining relaxors as a group of materials. [25] Materials exhibiting the nonergodic state are known as *canonical relaxors*. When a relaxor turns ferroelectric, either through decreasing the temperature or through applying an external field during the nonergodic relaxor state, a Curie temperature appears, signifying the return to an ergodic relaxor state upon heating. The Curie temperature is comparable to T_f. [25] Several relaxor categories are visualized in Figure 2.10.

The origin of relaxor behavior lies in the composition. $PbMg_{1/3}Nb_{2/3}O_3$ (PMN), the best known relaxor ferroelectric, contains lead at the A-site, and a mixture of magnesium and niobium at B-site. The Mg^{3+} and Nb^{5+} are not ordered in the B sub-lattice, but are randomly distributed, giving heterogeneous composition on a very short (nm) length scale. This

inhomogeneous cation ordering is central in all models describing the relaxor behavior. [24] Similarly, relaxor behavior is only observed in materials where several cations occupy the same sub-lattice, such as PMN, $Pb(Sc_{0.5}Ta_{0.5})O_3$ (PST), $(Sr_xBa_{1-x})Nb_2O_6$ (SBN), $Ba(Ti_{1-x}Sn_x)O_3$, $Ba(Ti_{1-x}Zr_x)O_3$, as well as, in fact, PLZT.

One early model describing this property imagines that the material is composed of several regions of different Curie temperatures, rendering the permittivity maximum a statistical distribution of ferroelectric to paraelectric phase transitions. Such a *diffuse phase transition* is illustrated in Figure 2.11. This model has been widely disproven, but it still serves as a crude visualization of the origin of the properties, and it is still sometimes used to explain relaxors in literature. Several more mature and robust models have been formulated the last decades, but the exact nature of the origin of relaxor properties is still unresolved. Some other models include the *superparaelectric model*, the *dipolar glass model*, and the *random-field model*. [24]

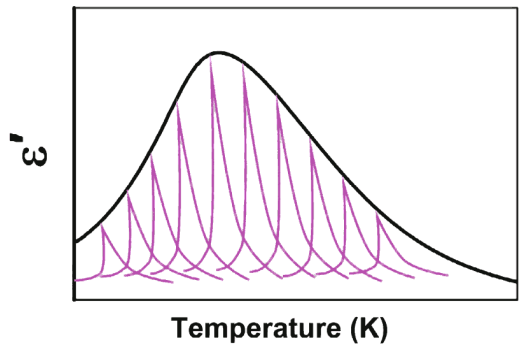

Figure 2.11 The diffuse permittivity maximum of a relaxor as a distribution of sharper traditional Curie temperature transitions. Reprinted with permission from [24].

2.2 Lead-free materials

Lead-free piezoelectric materials should be divided into two categories. The first category contains materials which are already in use due to properties outperforming the ones of PZT based materials. For example, quartz is used as an oscillator due to the temperature stability of its properties. $BaTiO_3$ is used for its high dielectric permittivity, and Bi titanate layered structures are used for high-temperature applications. Other materials such as $GaPO_4$, $LiNbO_3$, AlN, and polyvinylidene fluoride are also commonly employed in usage areas unsuitable for PZT. The other category of lead-free piezoelectrics are the materials aiming to replace PZT due to the toxicity of lead, which is the current topic of concern. [4]

2.2.1 Periodic table

Perovskite oxide materials have dominated the research field on both lead-free and lead-containing piezoelectric materials the last decades. In addition to exhibiting excellent piezoelectric properties, other electronic devices such as components in batteries, fuel cells, and touch screens are also made from perovskite materials. The perovskite oxides are thermodynamically stable, able to withstand high temperatures, and relatively tolerant to being exposed to ambient conditions. Furthermore, the structure is sufficiently simple and symmetric, rendering first principles calculations feasible. The combination of superior properties and excessive understanding of the materials accumulated from the combined global research efforts, render perovskite oxides ideal for the search for lead-free piezoelectric materials.

Looking at the periodic table, a general idea of possible perovskite materials may be obtained. The general chemical formula is ABO_3, where A is charged 1+, 2+, or 3+, with corresponding B charges of 5+, 4+, or 3+. For example, some 1-5, 2-4, and 3-3 perovskites are $(K,Na)^{+}Nb^{5+}O^{2-}{}_3$ (KNN), $Pb^{2+}(Zr,Ti)^{4+}O^{2-}{}_3$ (PZT), and $Bi^{3+}Fe^{3+}O^{2-}{}_3$ (BF), respectively. Considering toxicity and cost, only few possible cations remain as candidates to replacing PZT. Figure 2.12 shows the toxicity and cost of relevant elements. [2] The “not toxic” and “slightly toxic” categories denote substances that are at most irritant, or harmful only in direct contact. The elements that are sufficiently non-toxic and low-cost are outlined in blue. Table 2.3 shows the relevant cations sorted after valence states.

As a starting point, average A-site and B-site charge must sum up to 6. This means that alkaline metals on A-site may only be pared with Nb on B-site and vice versa. Similarly, Bi on A-site may only be pared with Fe on B-site. However, mixing Bi^{3+} and Na^{+}/K^{+} gives average A-site charge 2+, allowing for more flexibility in B-site cations, where Ti is most commonly employed (e.g. BNT, BKT, BT, PT). In perovskites, the A-site dodecahedral void is larger than the octahedral B-site, and A-site cations are consequently larger than B-site cations.

Table 2.3 Overview of low-cost low-toxicity common cations for perovskites sorted by site and valence.

A-site			**B-site**			
$\mathbf{A^{+}}$	$\mathbf{A^{2+}}$	$\mathbf{A^{3+}}$	$\mathbf{B^{2+}}$	$\mathbf{B^{3+}}$	$\mathbf{B^{4+}}$	$\mathbf{B^{5+}}$
Li, Na, K	Mg, Ca, Sr, Ba, Sn	Bi, La, Y	Zn [27]	Fe	Ti, Zr, Sn	Nb, Ta

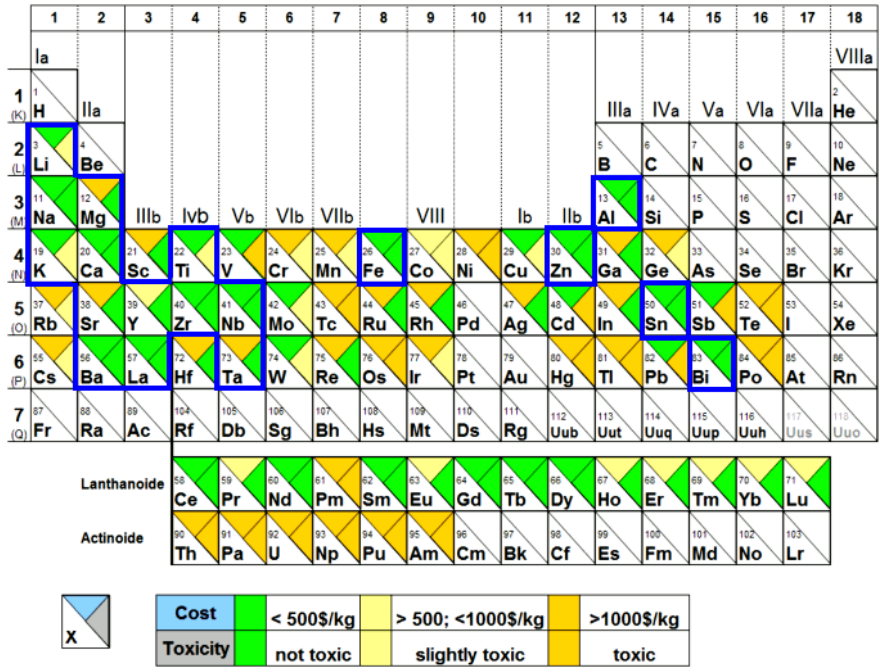

Figure 2.12 Periodic table showing the cost and toxicity of relevant elements. Adapted with permission from [2]. Blue outlines are added to illustrate the most relevant common perovskite cations.

Besides preparing stoichiometric materials, aliovalent dopants are often added in small quantities. For example, La^{3+} on A site in PLZT is a donor dopant, meaning that it has a higher charge than the cation it replaces. In order to keep electroneutrality, the increased charge on A-site is compensated by either cation vacancies or removal of oxygen vacancies. In PZT, this leads to higher resistivity and increased performance. [1]

The electronic structure of Pb^{2+} is an important factor in the success of lead based piezoelectric materials. Firstly, elements with a large number of electrons are more easily internally polarized than elements with fewer electrons. This leads to increased piezoelectric properties. As a consequence, Pb^{2+} is preferred to Sn^{2+}, and Bi^{3+} is preferred to Sb^{3+}, despite their similar electronic structure in the outer orbitals. Secondly, the electron lone pair of Pb causes increased piezoelectric response. Pb^{2+} has electronic structure [Xe] $4f^{14}$ $5d^{10}$ $6s^2$, and the $6s^2$ lone pair is easily attracted to the oxygen ions, causing stronger polarization and piezoelectric properties. Other cations exhibiting the exact electronic structure are Tl^+ and Bi^{3+}. Tl^+ is even more toxic than lead, however, and is therefore not of interest for lead-free piezoelectrics. Other cations with a lone pair are Sb^{3+} and Te^{4+} ([Kr] $4d^{10}$ $5s^2$), but these are not as polarizable as elements with larger atomic number, and they are both toxic. [2]

It is clear why most lead-free perovskite materials are based on either Bi^{3+} on A-site, or Nb^{5+} on B-site, as Nb is the only (low-cost) 5+ cation, while Bi^{3+} is the only non-toxic cation with similar electronic structure to Pb^{2+}.

2.2.2 Lead-free alternatives

Barium titanate, $BaTiO_3$ (BT), was the first ceramic material in which piezoelectric properties were demonstrated. In the 1940s, several countries independently developed $BaTiO_3$ as a high-dielectric-permittivity material for capacitors, and it was later shown that the high dielectric permittivity was due to its ferroelectric nature. [1] BT is used in capacitors due to a relative permittivity reaching as high as 10^6 for single crystals. [28] Piezoelectric properties are moderate, but a d_{33} as high as 460 pC/N has been reported in samples of very high quality. [29] The primary limitation of BT-based piezoelectric materials is the low Curie temperature of only 120 °C. Considering that the depolarization temperature, T_d, is lower, even devices for room temperature applications may suffer from temperature variable properties or even permanent loss of performance due to temporary temperature fluctuations. Common values of piezoelectric properties are coupling coefficient, k_{33}, of 0.5, and piezoelectric coefficient, d_{33}, of 190 pC/N. BT is an archetypical material, and one of the very best understood piezoelectric materials and perovskites. The structure is cubic above 120-135 °C, tetragonal at RT, orthorhombic below 5 °C, and rhombohedral below −90 °C. Although pure BT is not a likely successor to PZT based ceramics, it is an important material system for fundamental understanding, as well as in solid solutions with other materials forming MPB compositions. [23, 30, 31] For example, 6 % BT in either BNT or KNN leads to an MPB. For KNN, an additional MPB may be found at 20 % BT. [31] With respect to strain, BT is one of the best piezoelectric materials currently known. It has a very low remnant strain, yielding a useable unipolar strain of almost 0.3 % at relatively small fields (26 kV/cm, $d^*_{33} = S_{max}/E_{max}$ = 594 pm/V), but the practical application of these properties is limited by the low T_C. [32]

Barium calcium zirconium titanate, $(Ba,Ca)(Zr,Ti)O_3$ (BCZT) is a very promising material system for piezoelectric applications. It is based on BT, but with varying levels of isovalent doping on both A-site and B-site. The best-known composition is $Ba_{0.85}Ca_{0.15}Ti_{0.9}Zr_{0.1}O_3$, where a high piezoelectric coefficient, d_{33}, of 620 pC/N has been demonstrated. [23] This composition is located close to a triple point between rhombohedral and tetragonal ferroelectric phases, as well as the high-temperature cubic phase. While the piezoelectric properties including strain (d^* = 1140 pm/V [4]) are enhanced for this composition at room temperature, the inherent low Curie temperature (T_C = 93 °C) limits its use in non-ambient conditions. This materials system is difficult to prepare, as solid state synthesis requires high sintering temperatures (more than 1400 °C), resulting in too large grains. The Pechini method has been adapted to BCZT, yielding small particles after calcination, but still requiring in excess of 1200 °C for sintering. [23] Figure 2.13 shows the phase diagram of BZT-BCT, illustrating that the phase transition is in the form of PPT, not MPB. [4, 30]

Potassium sodium niobate, $K_xNa_{1-x}NbO_3$ (KNN). KNN is often considered the catalyst material fueling the quest for development of lead-free piezoelectrics, due to a very frequently cited article by Saito et al. in 2004. [33] There, piezoelectric properties comparable to that of PZT were demonstrated. This was the first account of a lead-free material exhibiting such a high piezoelectric coefficient (d_{33} = 416 pC/N). Key to the increased properties was the texturing of the material, causing attainable strain values to approach single crystal values. [34] Coupled with the appearance of legislation aiming to out-phase lead-based piezoelectric

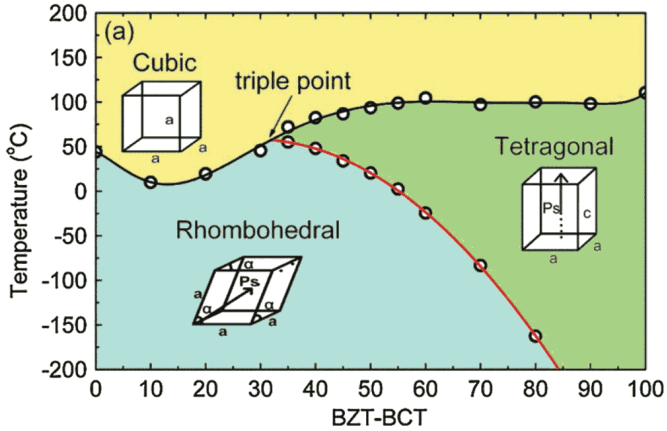

Figure 2.13 Phase diagram of $Ba(Zr_{0.2}Ti_{0.8})$-$(Ba_{0.7}Ca_{0.3})TiO_3$. Reprinted with permission from [37]. BCZT compositions are typically close to the triple point, combining the effect of the PPT/MPB and the Curie temperature.

materials, formulated and put into effect early in the 2000s (RoHS and WEEE) [35, 36], the number of yearly publications treating lead-free materials increased multiple-fold, from only a few to several hundred in the following years. [32] For use in the TLens the large-signal strain is more important than d_{33}, which is defined as the slope at zero field and strain. The strain achievable for KNN is limited by its high remnant strain of 0.13 %, which is subtracted from the poling strain of 0.19 % to obtain the useable unipolar repeatable strain. This means that while KNN is promising for high-temperature sensors and ultrasonic devices, for high stroke applications it is not competitive. [4, 32]

KNN is a solid solution of the end members $NaNbO_3$ (NN) and $KNbO_3$ (KN). NN is antiferroelectric at room temperature, while KN is ferroelectric. Only small amounts of K doping turns NN ferroelectric, and further increasing K to Na ratio leads to several orthorhombic-orthorhombic phase transitions, as seen in the KNN phase diagram in Figure 2.14. The most common KNN compositions are at or close to $K_{0.5}Na_{0.5}NbO_3$, where enhanced properties are observed. Moreover, dopants such as Li, Ca, Sr, Ta, Sb, or W, are often included. [23] The nature of the relationship between properties and composition in KNN has been a subject of debate. Early works indicated that addition of Li, Ta, and Sb caused the appearance of an MPB [33], while it was later argued that the effect of these dopants was in fact shifting of the orthorhombic-tetragonal phase boundary towards room temperature, causing the PPT effect to be dominant. [38] The influence of chemical modifications on the phase transition temperatures in KNN is shown in Figure 2.15. Specifically, Li doping is known to lower $T_{O\text{-}T}$. [38] Another important aspect of the KNN material system lies in the processing of the materials. The structure and properties are very sensitive to sintering conditions, leading to poor reproducibility and confusing conclusions, as enhanced properties are just as likely a result of higher quality samples than the composition itself. [38] KNN forms an MPB with BNT at 6-7 % KNN, yielding significantly higher strain. On the KNN rich end of the scale, an MPB appears at 2-3 % BNT, yielding a high piezoelectric coefficient of 195 pC/N. [31]

Bismuth potassium titanate, $Bi_{0.5}K_{0.5}TiO_3$ (BKT), is chemically similar to BNT, and comparing the two is therefore natural. The detailed treatment of BNT follows in Section 2.3.

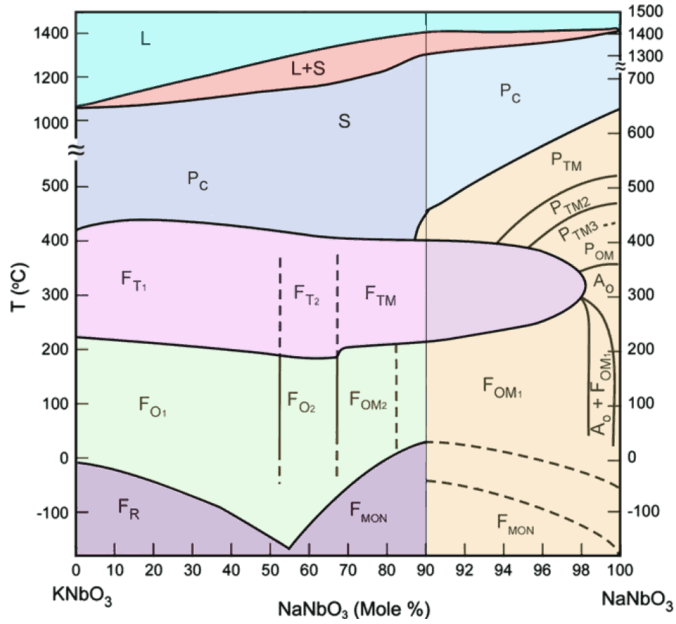

Figure 2.14 Phase diagram of KN-NN. Reprinted with permission from [38].

BKT and many other similar piezoelectric ceramics were first reported in the 50's. [30] The room temperature symmetry of BKT is tetragonal while BNT is rhombohedral. The depolarization temperature, T_d, is significantly higher for BKT (270 °C) than for BNT (187 °C), theoretically allowing for high-temperature applications. However, since the piezoelectric coefficient is only moderate (d_{33} = 101 pC/N), BKT has seen limited attention as a replacement to PZT. Moreover, it has been proven difficult to prepare dense samples. [31] It is used, however, in solid solutions for formation of MPB. For example, it forms an MPB with BNT at 16-22 % BKT. In these materials, due to the large amount of volatile cations such as Na, Bi, and K, sintering conditions significantly influences the properties. [31]

Bismuth ferrite, $BiFeO_3$ (BF), has attracted much attention due to its multiferroicity. It is simultaneously ferroelectric and antiferromagnetic, which could be relevant for development of multiferroic materials in applications such as data storage. A coupled electric and magnetic behavior could lead to a new type of hard drive which would drastically improve performance. Moreover, the Curie temperature is much higher than most comparable piezoelectric materials, at 830 °C, making it interesting for high-temperature applications. [39] The high-temperature piezoelectric performance has been characterized and d_{33} was found to reach ~120 pm/V at ~250 °C. [40] The high Curie temperature is related to the strong spontaneous polarization, which for single crystal samples have been demonstrated as high as 100 μC/cm^2. [31] In Sm doped BF thin films, a piezoelectric coefficient of d_{33} = 110 pm/V has been achieved. [31]

For application in large strain devices there are typically three alternative material systems considered. [34] BCZT exhibits high strain and low coercive field, but the properties are inherently very temperature dependent. KNN exhibits moderate strain, but it may be used at high temperatures and compositions with temperature stability are achievable. BNT is the selected material system for this work and will be treated in detail in the following.

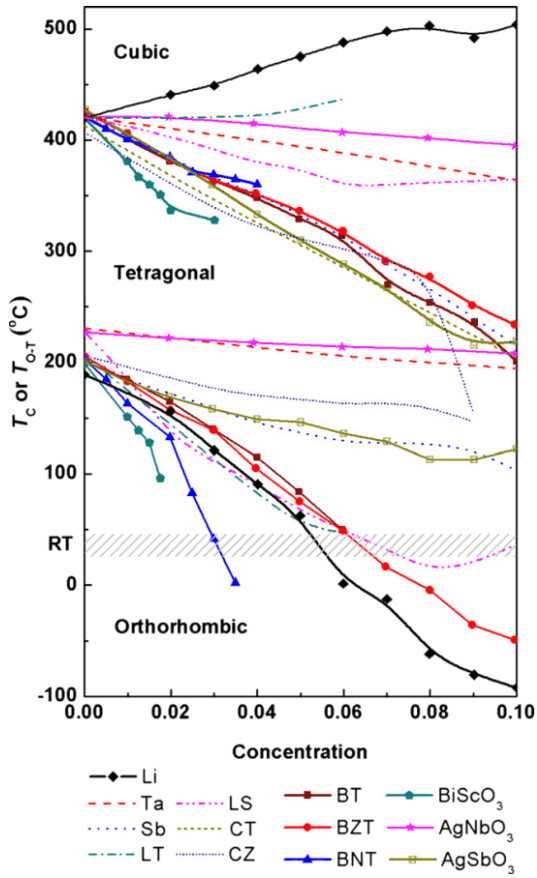

Figure 2.15 The effect of chemical modification in KNN on phase transition temperatures. [38]

2.3 BNT

2.3.1 BNT

Bismuth sodium titanate, $Bi_{0.5}Na_{0.5}TiO_3$ (BNT), was first developed by Smolenskii et al. in 1960 [41], but it did not attain much interest until the 1990's, where the number of publications became significant. Figure 2.16 shows the yearly publications on BNT compared to the total number of articles on piezoelectric materials with a focus on the topic *lead-free*. It can be seen that the significant research effort on BNT started around year 2000, with fewer than 50 total publications before 2000. The first reports of values of piezoelectric properties originated in the 1990s, and in 2002 the room temperature symmetry was assigned as rhombohedral (R3c) and the piezoelectric coefficient was measured to be moderate at 73 pC/N. [31, 42] BNT has a high initial strain value of 0.4 %, but an equally large remnant strain (0.23 %) limits the useable strain. Moreover, the required switching field, the coercive field, is uncommonly high at 80 kV/cm. [32] Figure 2.17 shows the strain of pure BNT compared to that of BT and KNN. Notice that BNT and KNN suffer from a large remnant strain, illustrated in Figure 2.18. Notice, also, that there is a remnant volume change after the initial poling cycle in BNT. This suggests that there is an irreversible phase transition occurring during the first field cycle, as simply switching domains should return the volume back to the initial stage. [32]

For use as a poled piezoelectric, the depolarization temperature, T_d, is a limiting feature, and for BNT it is as low as 187 °C. [31] When operated at increasing temperatures, the polarization-field hysteresis curves will be increasingly pinched, turning antiferroelectric-like above T_d. Naturally, crossing T_d will cause depoling, and could destroy devices that cannot be re-poled due to technical limitations. Chemical modifications to BNT are typically employed on A-site, and may include K and Li. Some researchers have developed a BNT based middle

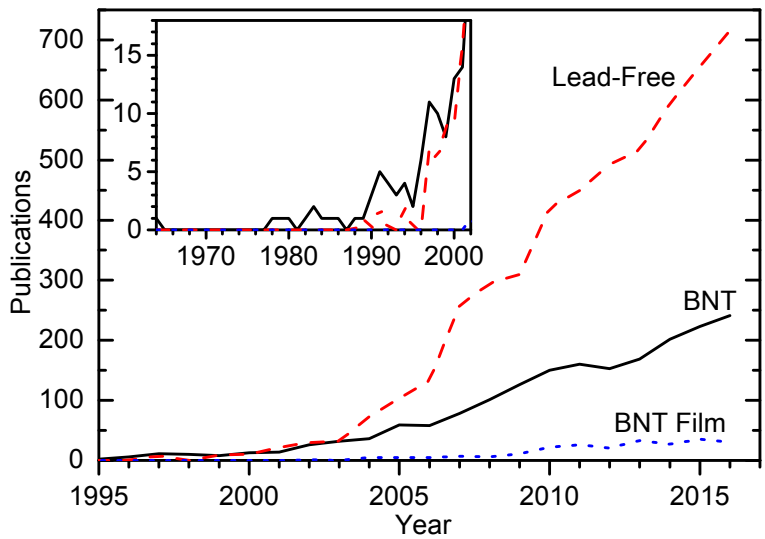

Figure 2.16 Annual number of publication on BNT compared to other lead-free piezoelectric materials. Data was compiled by performing searches in Web of Knowledge, http://apps.webofknowledge.com/, October 30th 2017.

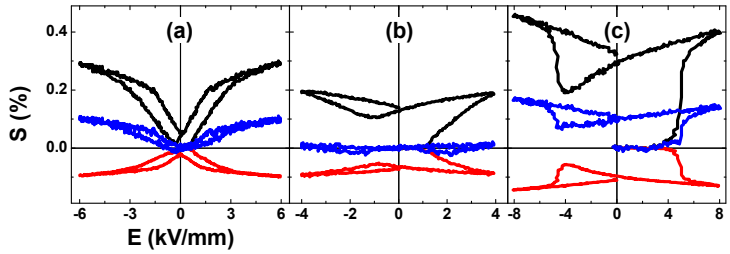

Figure 2.17 The initial strain curves of (a) BT, (b) KNN, and (c) BNT. Longitudinal strain is shown in black, transverse strain in red, and volume change in blue. Reprinted with permission from [32].

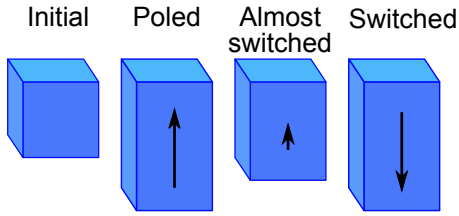

Figure 2.18 Bulk dimensions of a ferroelectric during initial polarization and subsequent polarization reversals. Arrows indicate polarization direction, which may be both positive and negative. Strain, however, consists of intrinsic piezoelectricity which may be negative, but the larger extrinsic (domain reorientation) piezoelectric effect causes strain to be exclusively positive relative to the initial state.

frequency filter with properties comparable to that of Pb-based piezoelectric materials. [31, 43] Alkali cation doping increased d_{33} to 230 pC/N, and simultaneously reduced the coercive field. In general, doping of BNT is most commonly applied to A-site. Monovalent alkaline metals replace Na, while divalent cations such as Ba and Sr replace equal amounts of Bi and Na, retaining the total A-site charge. The most common B-site dopant is Nb^{5+}, often in combination with K for Bi. Thus, when an acceptor or donor doping stoichiometry is introduced influencing the oxygen sub-lattice, it is specifically mentioned.

Pure BNT has been argued to in fact be a relaxor material. [44] This was supported by Jo et al. (Figure 2.17), and seems to be accepted in literature the last years. BNT does behave as a ferroelectric, however, since the first field cycle induces an irreversible transition to a ferroelectric metastable phase (with accompanying lost strain potential).

2.3.2 Incipient piezoelectric materials

BNT as a piezoelectric material should be divided into two categories. The first category contains the so-called *traditional* piezoelectric materials where d_{33} is an important figure of merit, T_d is a limitation, and the material is pre-poled and employed for both the direct and converse piezoelectric effects. The other category surfaced in 2007 when Zhang et al. reported what they termed a *giant strain* of more than 0.4 % in BNT-6BT-2KNN, surpassing even state of the art lead-based materials. [15]

The term *incipient* was introduced by Jo et al. in 2012 [32], meaning something that starts. In this case, it refers to the fact that BNT-6BT-2KNN is initially an unpoled relaxor with $d_{33} = 0$, and the piezoelectricity starts due to the electric field. The small-signal

piezoelectric response is zero, but upon application of a sufficient field, an electric field induced phase transition to the ferroelectric state occurs. It is this feature that defines the second category of BNT: a reversible phase transition causes the ferroelectric state to appear and diminish once during every electric-field cycle.

Compared to undoped BNT, where the remnant strain represents a lost potential for stroke length, incipient piezoelectrics have per definition zero remnant strain, and has higher repeatable/useable strain values. Thus, these materials are very interesting for high strain applications. The traditional figure of merit for piezoelectric materials, d_{33}, loses its significance, as it is defined at zero field where incipient piezoelectrics are not piezoelectric at all. In fact, ceramic incipient piezoelectric materials cannot be utilized for the direct piezoelectric effect, as poling is impossible. Rather, the most important figures of merit for incipient BNT is the strain value itself, as well as the large signal piezoelectric coefficient, $d_{33}^* = S_{max}/E_{max}$. Moreover, the strain hysteresis loops contain significant useful information not necessarily translatable to traditional constant figures of merit, such as the development of the slope, and the squareness and area of the hysteresis loop (translating to heating of the device). Incipient BNT compositions is the focus this work, and in the following it will be implied that the desired characteristics are those of incipient piezoelectrics. In other words, the reader should keep in mind that small-signal properties are of limited interest, while the sought-after properties are those of high strain, low coercive field, temperature stability, high blocking force etc.

2.3.3 Nomenclature

One of the most commonly reported BNT compositions is the solid solution with 6 % $BaTiO_3$ and 2 % KNN, often denoted BNT-6BT-2KNN. Different research groups employ different notation schemes, and they are often not easily comparable. For that reason, in the present work an alternative notation is used for BNT-rich compositions. Rather than specifying the ratios of mixed material end systems, every cation is specifically denoted. BNT-6BT-2KNN corresponds to $Bi_{0.46}Na_{0.47}Ba_{0.06}K_{0.01}Ti_{0.98}Nb_{0.02}O_3$, and is here written as BNT-6Ba-1K-2Nb (or in short form: 6Ba-1K-2Nb). With this notation, the relative difference to the undoped BNT reference is written, and adjustment of Bi, Na, and Ti is automatically implied to obtain charge balance and $A_1B_1O_3$ total nominal stoichiometry. This notation scheme is reasonable when BNT is the main constituent of the solid solutions, and it renders comparison of different compositions clearer. Consider, for example, the following compositions from literature:

1. $0.85Bi_{0.5}Na_{0.5(1-x)}Li_{0.5x}TiO_3$-$0.11Bi_{0.5}K_{0.5}TiO_3$-$0.04BaTiO_3$ ($x = 0.10$) [9]
2. $0.96[\{Bi_{0.5}(Na_{0.84}K_{0.16})_{0.5}\}_{1-x}Li_x(Ti_{1-y}Nb_y)O_3]$-$0.04SrTiO_3$ (x,$y = 0.020$) [10]

These compositions are approximately equal to

1. $Bi_{0.48}Na_{0.36}Ba_{0.04}K_{0.06}Li_{0.06}TiO_3$
2. $Bi_{0.47}Na_{0.39}K_{0.08}Li_{0.02}Sr_{0.04}Ti_{0.98}Nb_{0.02}O_3$

and will here be written as

1. (BNT-)4Ba-6K-6Li
2. (BNT-)8K-4Sr-2Li-2Nb

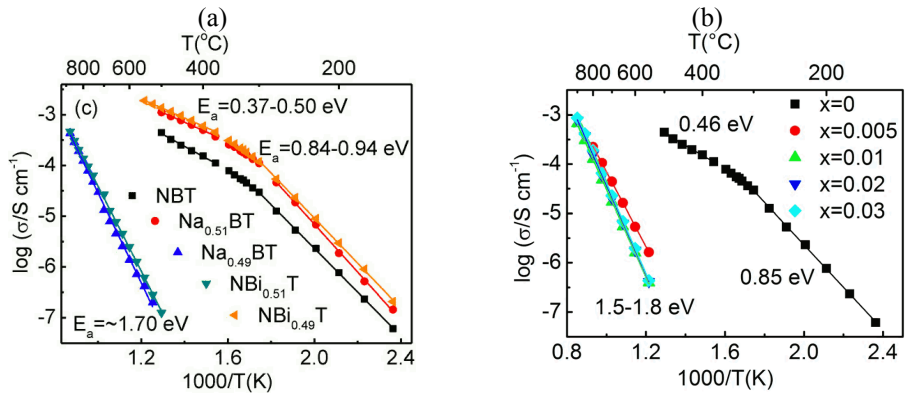

Figure 2.19 (a) Conductivity of BNT with different levels of non-stoichiometry. Bi excess and Na deficiency yields much lower conductivity than nominal stoichiometric and Bi poor/Na excess samples. Reprinted with permission from [46]. Copyright 2017 American Chemical Society. (b) Conductivity of BNT as a function of Nb doping. $Bi_{0.5}Na_{0.5}Ti_{1-x}Nb_xO_3$. From [47], free to redistribute through Creative Commons License (CC-BY).

2.3.4 Conductivity of BNT

Undoped BNT suffers from a high leakage current. Li et al. recently demonstrated that BNT possesses a high oxygen ion conductivity given the proper minor non-stoichiometry. Samples poor in bismuth or rich in sodium express conductivity several orders of magnitude greater than samples with excess bismuth or sodium deficiency (see Figure 2.19). [45, 46] The real A to B ratio may be different to the nominal stoichiometry. A site deficiency is most common, due to evaporation of Bi or Na, or due to wet precursor powders (Na precursors are more hygroscopic than for example TiO_2). This will lead to oxygen vacancies according to

$$2Na_{Na}^{\times} + O_O^{\times} \xrightarrow{BNT} 2V'_{Na} + V_O^{\bullet\bullet} + 2Na(g) + \tfrac{1}{2}O_2(g) \tag{2.13}$$

$$2Bi_{Bi}^{\times} + 3O_O^{\times} \xrightarrow{BNT} 2V'''_{Bi} + 3V_O^{\bullet\bullet} + Bi_2O_3(g) \tag{2.14}$$

In Kröger-Vink notation, V denotes vacancies, subscripts denote lattice site, and $^{\times}$, $^{\bullet}$, and $'$ denote neutral, positive, and negative charges relative to the lattice site, respectively.

In the opposite case, with A-site excess, the perovskite will not be able to accommodate interstitial oxygen or B-site vacancies. Rather sodium-rich or bismuth-rich phases were identified by Li et al. [45, 46] The result is therefore simply shifting Equations (2.13) and (2.14) to the left, reducing the concentration of oxygen vacancies.

In the case of Na to Bi non-stoichiometry, however, the effect of aliovalent doping must be considered. For example, a nominal composition of $Bi_{0.5}Na_{0.51}TiO_3$ is in fact richer in oxygen vacancies despite pushing equation (2.13) toward the left. This is due to the Na-Bi ratio, and effective acceptor doping in the form of

$$Na_2O + 2Bi_{Bi}^{\times} + 2O_O^{\times} \xrightarrow{BNT} 2Na''_{Bi} + 2V_O^{\bullet\bullet} + Bi_2O_3 \tag{2.15}$$

In the opposite situation, deficiency of Na is compensated by formation of Ti-rich secondary phase, and actually leads to lower oxygen vacancy concentration. Na deficient compositions may be viewed as excess of Bi and Ti:

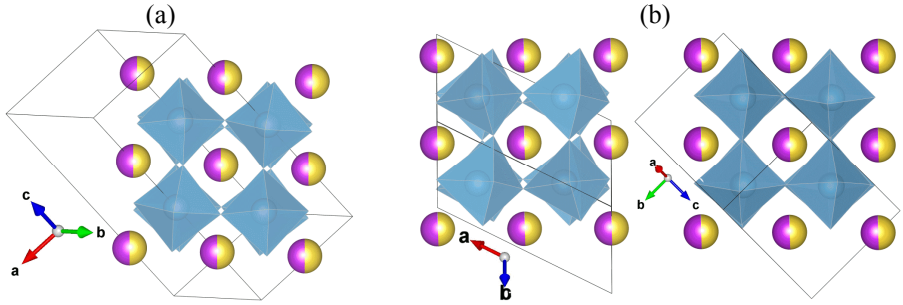

Figure 2.20 Pseudocubic representation of the crystal structure of BNT. The boundary lines correspond to the unit cell in accordance with the symmetry. Purple/yellow spheres are Bi/Na, and the octahedra represent TiO_6. (a) Hexagonal R3c structure with data from [42]. (b) Cc structure visualized along $[100]_{pc}$ (left) and $[010]_{pc}$ (right), with data from [48]. Produced in [61].

$$Bi_2O_3 + 2TiO_2 + V_O^{\bullet\bullet} \xrightarrow{BNT} Bi_{Bi}^{\times} + Bi_{Na}^{\bullet\bullet} + 2Ti_{Ti}^{\times} + 7O_O^{\times} \quad (2.16)$$

It was shown by ^{18}O tracer diffusion that the charge carrier was in fact oxygen vacancies. Thus, the relatively high conductivity of BNT bulk samples is understood, and may be manipulated by controlling the oxygen vacancy concentration. For example, Li et al showed that small levels of Nb donor doping on B-site has the same effect on conductivity as having a Bi to Na ratio greater than one (Figure 2.19b). [47]

2.3.5 Crystal structure of BNT

The crystal structure of undoped and compositionally engineered BNT is a topic that has experienced significant attention in the literature. [42, 48-60] Despite this, recent review articles (Villafuerte-Castrejón et al. 2016 and Reichmann et al. 2015) still report the exact structure to remain undecided. [23, 34] Several research groups have suggested coexistence of phases or that the history of electrical characterization influences the perovskite symmetry. For example, a monoclinic structure has been reported to exist only prior to the initial poling cycle, after which the structure remains purely rhombohedral. [60] Moreover, several authors have speculated in the nature of local symmetry as opposed to average symmetry. Inherent to relaxors and the polar nano regions, the local structure may deviate significantly from what may be seen by diffraction techniques. [34]

The most commonly reported space groups of room temperature undoped BNT are the rhombohedral R3c [34, 44] and the monoclinic Cc [48, 49, 52, 58], and the two are visualized in Figure 2.20. R3c symmetry corresponds to a pseudocubic perovskite where the unit cell has been elongated in the $[111]_{pc}$ direction (pseudocubic body diagonal). Furthermore, the octahedra are rotated the same magnitude in alternating directions around x, y, and z pseudocubic directions ($a^-a^-a^-$ according to Glazer tilt system notation). In the monoclinic structure, the tilt is still alternating on adjacent planes, but the magnitude of tilt around $[001]_{pc}$ is dissimilar to the tilt around $[100]_{pc}$, yielding the Cc space group with corresponding $a^-a^-c^-$ octahedral tilting. It should be noted that R3c and Cc symmetries are both rhombohedral-like, and referring to BNT as R3c is sufficiently accurate for the scope of this work. R3c is also the most broadly accepted symmetry in literature. [44]

The room temperature crystal structure of BNT extends down to at least 5 K, showing only a continuous change in magnitude of lattice parameters, octahedral tilt, and octahedral strain. [42] With increasing temperature, however, diverging reports emerge. From the depolarization temperature, a range of various structures and phase transitions are suggested. [34] The Curie temperature is now generally accepted to lie in the temperature range 520-540 °C, and this first order phase transition yields a paraelectric cubic Pm−3m phase. [34, 42] T_C has earlier been suggested to be as low as 325 °C, however. [31] The room temperature phase extends up to approximately 200-300 °C where the polarization is lost and a maximum permittivity is observed, but diffraction studies do not detect any symmetry change. [34, 42, 48] In the temperature range 200 to ~500 °C, a range of different symmetries has been suggested, including tetragonal P4bm [42], orthorhombic Pnma in coexistence with R3c [62, 63], and a matrix of $P4_2/mnm$ and P4/mbm [64]. The reader is referred to an excellent review article for a more thorough treatment on the symmetry of BNT polymorphs. [34]

2.3.6 Barium doping

Even before the discovery of *giant strain* in 2007, several researchers investigated BNT mixed with BT, and the morphotropic phase boundary at 6 % Ba was identified already in 1991. [65] On the BT side, a tetragonal P4mm phase exists [15, 55], while in BNT-rich compositions the pure BNT symmetry is assumed to be R3c. In Rietveld refinement of BNT-4Ba samples, Usher et al. was not able to properly describe the diffraction pattern by neither pure Cc nor pure R3c. [58] Simply refining versus a number of reasonable phase combinations did not result in increased quality of fit. Adding, however, an aristotype perovskite Pm−3m contribution, significantly improved the fit. This serves as evidence for the presence of polar nanoregions, as the true symmetry of these would not show in the XRD patterns. Rather, many regions of different orientations would average as a perfect cubic perovskite. Note that the true symmetry of the nano regions are not observable by XRD, and could for example be Cc, R3c, or P4bm.

Furthermore, the origin of the large strain in BNT-6Ba has been established as a relaxor to ferroelectric transition, which is consistent with polar nano regions as discussed above. [32] However, it should be noted that BNT-6Ba behaves ferroelectric rather than relaxor like. This is due to slow kinetics of polarization reversal. As with other relaxors, an external electric field influences the thermodynamically stable domain structure, causing polar nano regions to grow into regular sized domains. In the case of BNT-6Ba, the kinetics of returning to the relaxor state are too slow, causing a metastable ferroelectric state after the first application of external field. [32]

Electric field-temperature phase diagrams for compositions around the MPB were measured by Sapper et al., and are shown in Figure 2.21. [26] At temperatures below T_d, only one current peak is visible during increase of electric field (positive or negative). This is equal to the behavior of traditional piezoelectric materials. From T_d, however, polarization reversal took place in two steps, and the distance between these steps increased with increasing temperature. Sufficiently far from T_d, polarization is returned to zero before returning to zero field, while the oppositely directed polarization occurred at even higher negative fields. Note that the coercive field (which is equal to the field for transition to the ferroelectric state) was

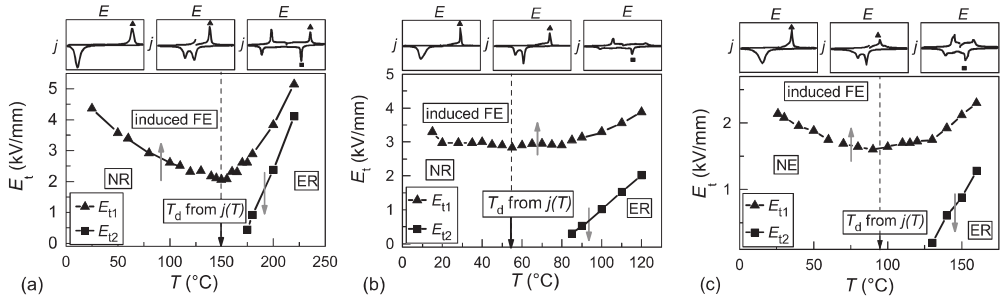

Figure 2.21 Electric field-temperature phase diagram of BNT-3Ba (a), BNT-6Ba (b) and BNT-9Ba (c). The diagrams were constructed by means of current-field measurements for identification of transitions, and small-signal piezoelectric measurements for identification of the specific phases. It can be seen that the ergodic relaxor state existed at lower temperatures for BNT-6Ba than the other compositions. NE = NR = Nonergodic relaxor, ER = Ergodic relaxor, FE = Ferroelectric. Adapted with permission from [26].

lowest at T_d. Note also that the ergodic relaxor state only existed above T_d, and that T_d was significantly lower for the MPB composition. Remember that it is the access to the ergodic relaxor state upon removal of the field that defines incipient piezoelectric materials, and it is key for the large strain response in BNT. Later it was found that the exact MPB composition is a function of electric field. At zero electric field, the MPB lies at 6-7 % Ba, while for 6 kV/mm the MPB is broad at 6-11 %. [14]

Piezoelectric properties of BNT-3.6Ba and BNT-6.3Ba single crystals were recently investigated. [55] In Figure 2.22a, it is shown that strain response in the R3c phase (BNT-3.6Ba) is small along <001> (pseudocubic notation is implied), intermediate for <110>, and large for <111> field directions. This is as expected as polarization and strain in rhombohedral perovskites are only possible along <111>. Any macroscopic response along <001> or <110> directions is a result of the projection of the field onto <111>, and causes a multidomain structure with average strain perpendicular to the field.

The piezoelectric response in the MPB composition (BNT-6.3Ba) shown in Figure 2.22b is remarkable. An unusually large strain response is measured for the <001> direction. Already at less than 3 kV/mm, the strain saturates at ~0.7 %, which corresponds to a normalized large-signal piezoelectric coefficient, d_{33}*, of 1886 pm/V. [55] The authors explain this by considering that both R3c (BNT-rich) and P4mm (BT-rich) phases may exist at this composition, and as a field is applied along <001>, the tetragonal direction of polarization is stabilized. Thus, the result of applying a field is first a relaxor to rhombohedral ferroelectric transition, then a rhombohedral to tetragonal transition. Both transitions facilitate a significant strain. [55] Strain response along <110> and <111> in the relaxor is fundamentally similar to that of the BNT-rich non-MPB composition, which can be explained by assuming the polar nanoregions are R3c in nature. Notice, however, that the required external field is significantly lower for the MPB material in agreement with the discussion in Section 2.1.4.

It is clear from the orientation dependent piezoelectric properties described above that any epitaxy or texture in the films may have a significant impact on properties. It seems that both the achievable total strain, and the dynamics of strain reversal is superior in <001> oriented MPB samples. In the case of <110> texture, the properties will likely be worse than

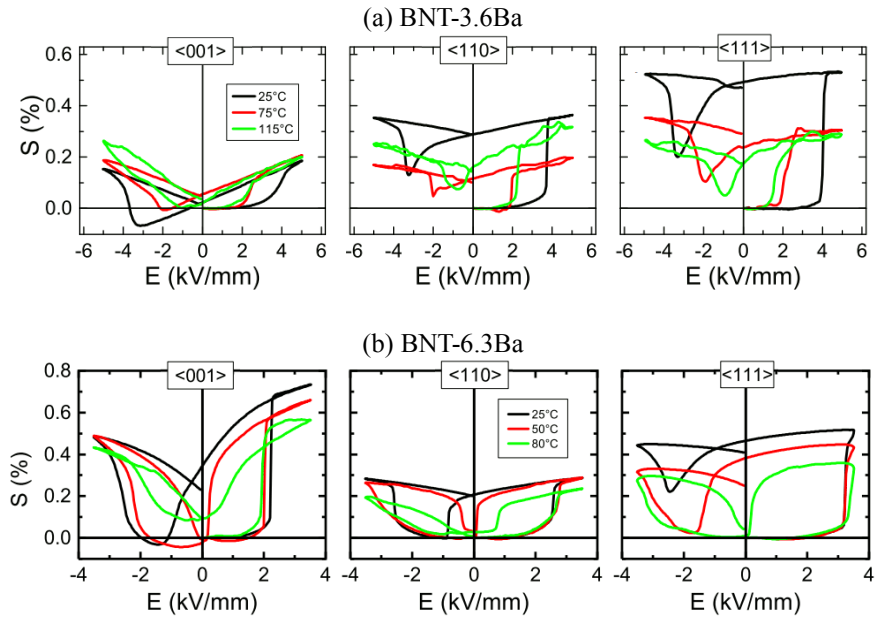

Figure 2.22 Strain in single crystal BNT along specific crystallographic directions. Adapted with permission from [55].

that of random grain orientations. <111> oriented films would show qualitatively similar behavior to that of bulk random grain samples, albeit with stronger ferroelectric behavior with more abrupt strain changes at specific field values.

2.3.7 Further compositional engineering

There are a large number of publications treating the effects of chemical modifications to BNT. In fact, it seems to be a common strategy in the search for lead-free piezoelectrics to simply take known ferroelectric materials, and map the property changes as a function of added dopants or solid solution with other piezoelectric material systems. It was mixing of the two MPB compositions BNT-6Ba and KNN-6Ba that drove Zhang et al. [15] to investigate the 6Ba-1K-2Nb composition, while the discovery of a whole new class of high-strain materials (incipient piezoelectrics) was not expected. [32] The remainder of this section treats some selected examples of chemical modifications to BNT.

Perhaps the best treated compositions of BNT are those close to 6Ba-1K-2Nb. The effect of Ba addition was shown in the previous section, while the additional KNN primarily serves to decrease the depolarization temperature and the ergodic to nonergodic temperature. In 2009, the nature of the incipient piezoelectric behavior was unraveled. It was found that 6Ba-1K-2Nb is an ergodic relaxor, rather than antiferroelectric, as previously suggested. [66] In 2012, five years after the initial discovery of this material system, Jo et al., belonging to the same research group in Darmstadt, released a comprehensive review on the origin of the properties. [32] Still it remains one of the most important articles concerning BNT, as it mapped the electromechanical properties related to temperature, Ba content, and KNN content. Furthermore, the large strain response was attributed to ergodic reversal to the

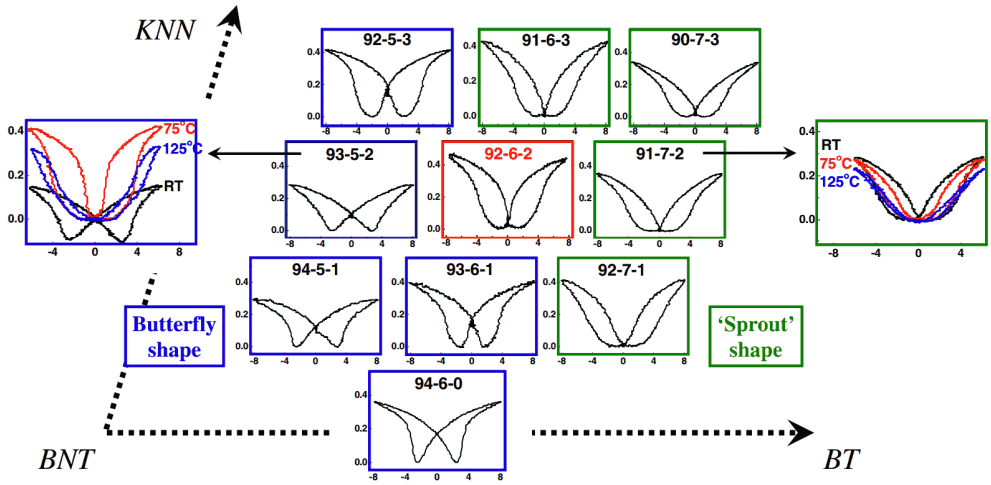

Figure 2.23 Strain vs field for different levels of BT, KNN and temperatures. The blue squares denote the *butterfly* shape, characteristic for traditional piezoelectric. The green squares denote samples with the characteristic *sprout* shape, signifying the incipient piezoelectric behavior. The composition in the red square is has the ideal composition, as strain is maximized, while S_{rem} is still zero. Reprinted with permission from [32].

zero-strain un-poled relaxor state. Moreover, the blocking force was shown to be superior to that of PZT, and the strain was still relatively unaffected after 10^6 bipolar cycles. Figure 2.23 nicely summarizes the effect of KNN addition to the BNT-Ba system. It can be seen that the effect of KNN addition is similar to that of increasing the temperature, showing that the incipient piezoelectric materials rely on the low depolarization temperature (freezing temperature) which is widely regarded as a constraint in traditional piezoelectrics.

Yin et al. substituted Li for Na in a composition already modified with 6K-4Ba. [9] They found that for up to approximately 5 % Li on A-site, the remnant strain was larger than zero, yielding a lost strain potential in the case of uniaxial fields. For approximately 6 % Li, however, they observed the same strain behavior as seen for 6Ba-1K-2Nb or BNT-5Ba at elevated temperatures (Figure 2.23). Thus, they identified a useable composition for room temperature *giant strain* without modification at the B-site. Furthermore, they showed that the strain response is practically independent on temperature up to at least 80 °C, and only slowly decreasing until 160 °C. The achieved strain was comparable to BNT state of the art, with almost 0.4 % at 65 kV/cm. Figure 2.24 shows the strain and polarization as a function of field and temperature. It can also be seen that the strain is still not saturated, possibly allowing for larger response with stronger fields. Furthermore, the area of the hysteresis is relatively small, meaning that the self-heating of the device will be limited. This composition is particularly promising for actuator applications, and is one of the compositions selected for thin film synthesis in this work.

Malik et al. added $LiNbO_3$ to a composition already containing BKT and ST, yielding approximately 8K-4Sr-*x*Li-*x*Nb, where *x* was varied from 0 to 3 %. [10] They found that increasing levels of $LiNbO_3$ gave increasing degree of ergodicity and return to the relaxor state. The best properties were found for 8K-4Sr-2Li-2Nb, where P_r, E_c, and d_{33} were all small, while P_{sat} was still large. At this composition, the strain at room temperature was 0.4 % at

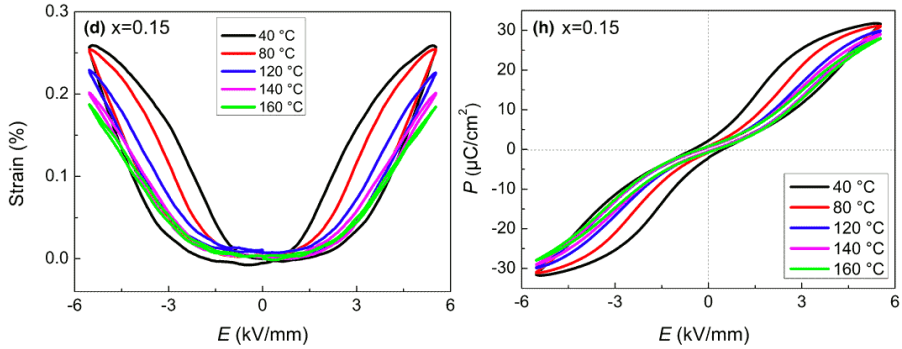

Figure 2.24 Strain and polarization in BNT-4Ba-6K-6Li. Adapted with permission from [9].

5 kV/mm, and the properties were not significantly altered up to 100 °C. This composition is particularly promising for actuator applications, and is selected for synthesis in this work.

Several authors have reported on the effect of Bi to Na stoichiometry. Prasertpalichat et al. showed that Na excess in BNT-*x*Ba gives rhombohedral distortion. Furthermore, it was shown that BNT generally expresses better piezoelectric properties when donor doped rather than acceptor doped. Sodium excess was shown to give a hardening effect of BNT. [67] Alonso-Sanjose et al. made BNT thin films by a CSD method, and found that Na excess was efficient in reducing the amount of pyrochlore secondary phase, but samples with only Na excess were more conductive than those with both Bi and Na excess. [13] Naderer et al. also found that Ti excess simply leads to TiO_2 secondary phase without much influence on properties. [68]

Aksel et al. substituted La into A-site. [69] They found that room temperature polarization and strain were not significantly influenced, but the depolarization temperature decreased from 170 °C for pure BNT to 110 °C for BNT-1.5La.

Glaum et al. introduced Zr on B-site in a BNT-BT composition, and found that only small levels of substitution lead to a core-shell structure with R3c domains in a P4bm nanodomain matrix. Further increasing Zr content towards 1 % lead to increasing volume fraction of R3c. The domains formed were coarser than what is common for BNT-BT materials. [70]

Groh et al. tried to decrease the coercive field of BNT-6Ba-*x*KNN by preparing a composite of the incipient BNT as the matrix, with inclusions of permanent ferroelectric BNT-7Ba onto which the ferroelectric phase could seed during cycling. [71, 72] They tested 2, 3, 4, and 6 % KNN, with 0, 10, 20, 30, 50, and 100 % seed phase, and found that addition of the seed phase efficiently both reduced the coercive field, and reduced the area of the hysteresis. Compositions with higher KNN content than 2 % did not outperform the well-known 6Ba-1K-2Nb. The best results were found for 10 % seed phase.

Sumang et al. substituted K and Li for Na (BNT-BKT-Li), and found an MPB at BNT-10K-1.5Li, yielding 0.36 % strain at 5kV/mm. Increasing the Li content generally led to a pinching effect of the hysteresis, but it also reduced the maximum achieved polarization. Increasing K content above 9 % in a composition containing 5 % Li also resulted in hysteresis pinching. [73]

2.4 Thin film synthesis

2.4.1 Chemical Solution Deposition

This section borrows heavily from an excellent review by Schwartz et al., and unless otherwise noted, provided details are cited from this work. [11]

Sol-gel type synthesis of oxide materials initially dates back about 70 years. [74] First, the process was used for coating of glass with SiO_2 and TiO_2. [75] The first chemical solution deposition (CSD) of electronic oxide thin films was reported in the 1980s. One of the first perovskite material systems to be synthesized in thin film format by both sol-gel [76] and metal-organic decomposition [77] was, in fact, PZT. Following this, numerous related materials have been prepared by CSD methods, such as [11]

- Perovskites: PT, BT, ST, $(Ba,Sr)TiO_3$, $Sr(Zr,Ti)O_3$, $Ba(Zr,Ti)O_3$, $Pb(Sc,Ta)O_3$, PMN
- Layered perovskites: $SrBi_2Ta_2O_9$, $SrBi_2Nb_2O_9$, $(Bi_{1-x}La_x)_4Ti_3O_{12}$
- Semiconducting perovskites: $(La,Sr)CoO_3$, $(La,Sr)MnO_3$
- Superconductors: $YBa_2Cu_3O_{7-\delta}$ (YBCO)

There are several advantages with the CSD processes. [78] CSD processes are the cheapest methods for obtaining high quality films with complex chemistry and thickness in the order of 50-10 000 nm. Compared to solid-state methods, where *particles* of individual precursor cations are mixed, in CSD the precursors are mixed at an *atomic* level. For solid-state methods, the diffusion length is therefore on the order of the particle size, ranging from 50 nm to tens of µm. For CSD, the diffusion lengths vary from Å range to a few nm. This means that CSD processes typically require significantly lower synthesis temperatures and holding times. For films thicker than several µm, CSD processes require too many steps to be viable, while solid state methods typically are not able to produce films thinner than tens of µm. Physical methods such as rf-magnetron sputtering or pulsed laser deposition (PLD), on the other side, are typically much more expensive, and limited to smaller batches than for CSD. [12] Typical drawbacks of CSD processes are crack formation and delamination. There may be large fractions of solvent and organic parts that need to be eliminated from the deposited gel film, and this volume loss leads to in-plane tensile stresses in the film. [20]

A typical CSD process consists of several key constituents and steps. The solvent and precursors chosen are central. Identifying suitable combinations are not straight forward, but there are now several families of synthesis routes with respect to chemistry. Typically, the precursors are some metal-organic molecules or salts, such as alkoxides. Then, one combines the precursors according to the proper stoichiometry, and during subsequent reactions the proper phase will form. Optionally, other additives may be introduced to alter the behavior of the solution or sol, such as to change the viscosity, wetting properties, or stability. The precursors and additives are chosen so that any unwanted compounds will burn off during heat treatment steps before achieving the final material. [11]

After obtaining a solution or sol, it is deposited in the wet form onto a substrate by one of the three most often used methods: *spin-coating*, *dip-coating*, or *spray-coating*. The wet or partly dried film is then dried, pyrolyzed, crystallized, and sometimes further annealed. It is common to repeat the coating and pyrolysis steps several times in order to achieve the target

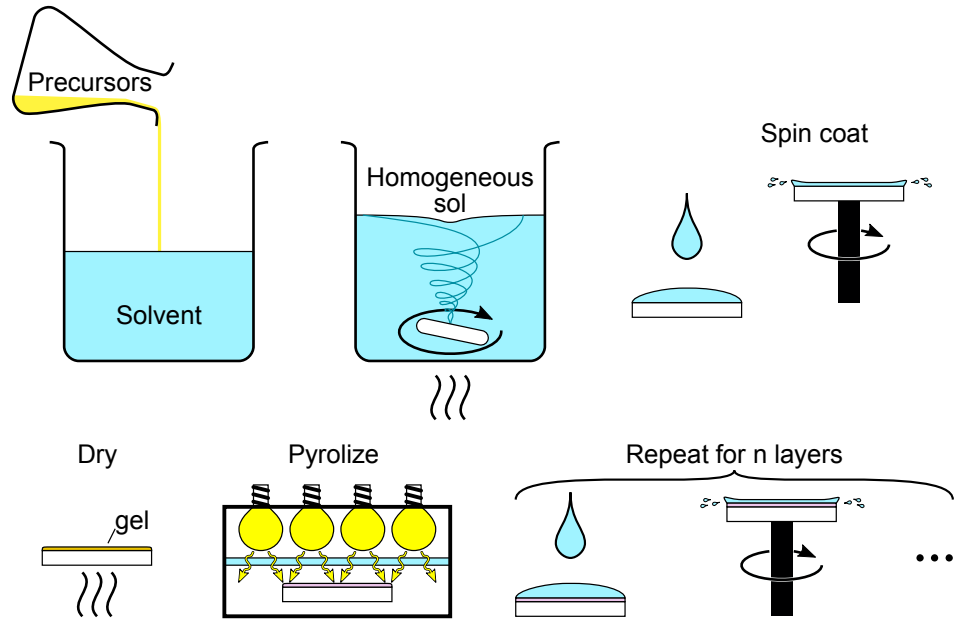

Figure 2.25 Illustration of a typical CSD synthesis route. In this example, spin coating is selected as the coating technique, and crystallization takes place in the pyrolysis step.

thickness of the film. [79] The successfulness of a CSD process depends on some key aspects [11]:

- Solubility of precursors (feasibility of sol)
- Reproducible sol characteristics (stability of sol)
- Precursors containing only combustible elements in addition to the target ions
- No segregation of constituent ions upon drying or pyrolysis. There should be no precipitation or crystallization of non-stoichiometric compounds. (Homogeneity on the *atomic level.*)
- Sufficient wetting of the substrate
- Proper viscosity/rheology of the sol
- No macroscopic defects (e.g. cracks) should form during drying or pyrolysis
- Substrate integrity. It should not react, diffuse, or degrade in contact with the film.

An illustration of the steps in a typical CSD thin film synthesis route is given in Figure 2.25.

Precursors

The precursors applied are typically one of few categories: carboxylates, alkoxides, β-diketonates, mixed ligand precursors, or mixed metal precursors. [11, 80]

Carboxylates are salts of carboxylic acids, such as acetic acid. [81] The acids are in the form R-COOH, where R can be any alkyl group. For example, a common carboxylate is barium acetate, $Ba(CH_3COO)_2$. The carboxylates are bound ionically to the Ba^{2+} cation, and for short alkyl groups the salts are highly soluble in water and other polar solvents. For longer chains the corresponding acid may be used as a solvent. Many high valent carboxylates are,

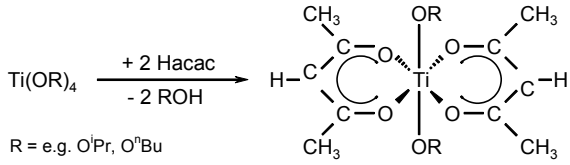

Figure 2.26 Stabilization of Ti by the *β*-diketone acetylacetate. Adapted with permission from [11].

while being soluble in water, not stable with respect to water. [11] For low valent cations such as Ba^{2+}, Sr^{2+}, and Ba^{2+}, carboxylates are often employed.

Alkoxides are similar to carboxylates, but contain an alcohol group instead of the acid group. The general formula is R-OH, and they form compounds with metals: $M(OR)_x$. Metal alkoxides are typically very reactive with water, yielding hydrolysis

$$\text{M-OR} + \text{H}_2\text{O} \longrightarrow \text{M-OH} + \text{R-OH} \tag{2.17}$$

This can lead to further condensation reactions and precipitation of the metal hydroxide or oxide. This reaction is often controlled by access to water, and *oligomers* (chains or clusters of a few monomers) are intentionally formed. Stabilization of the cation may be achieved by adding organic molecules with polar groups attracted to the cation, causing complexation and steric hindrance. *Chelating agents* are molecules that are connected with several functional groups to the same cation. Organic molecules with several polar groups are for example 1,3-propanediol ($HO\text{-}(CH_2)_3\text{-}OH$) [82, 83] or 2-methoxyethanol ($H_3C\text{-}O\text{-}(CH_2)_2\text{-}OH$) (2-MOE). [84, 85] An example of a frequently employed alkoxide is titanium isopropoxide, $Ti\text{-}(OCH(CH_3)_2)_4$ (TIP). [86]

β-diketones have two ketone groups separated by a methylene group. Due to electron sharing and proton exchange forming an alcohol group, these molecules can form connections to metal cations in the same manner as alkoxides. Figure 2.26 shows how acetylacetone (Hacac) can bond to Ti^{4+}, yielding a strong stabilizing chelating effect. Suitable solvents are alcohols, ketones, and esters. [87]

Mixed ligand precursors are, as the name suggests, precursors with several types of organic ligands. [85] This is often done to modify/reduce the reactivity of the precursor. For example, Figure 2.26 shows how Ti is bound to both acetylacetate and its original alkoxide anion. This gives a more stable precursor with respect to hydrolysis, because the two O-Ti connections on each acetylacetate sterically prevents water access to the Ti ion. [11] In the case of Ti, obtaining an octahedral environment, with six connections to Ti, is also significantly more stable than the four-coordinated TIP. [86]

Mixed metal precursors are the phenomenologically opposite of mixed ligand precursors. Different cations are bound to the same ligands or in the same oligomers. [88, 89] The motivation for preparing mixed metal precursors is to have a more rigid connection between the constituent cations, causing greater control of stoichiometry and homogeneity prior to the crystallization step. Maintaining homogeneous cation distribution not only on a molecular level, but also within the precursor molecules themselves, could potentially result in fewer secondary phases formed, as well as lower synthesis temperatures required. In practice, however, not many researchers have been successful in achieving the proper stoichiometry within the oligomers. [11]

Chemistry

Chemical solution deposition (CSD) is an umbrella term, including all forms of film synthesis starting from a true solution or colloid system. Recently, one may find authors using the term *sol-gel* when referring to any CSD process, but historically the sol-gel process follows a given sequence of steps and reactions. [80] In sol-gel, precursors used are alkoxides which are hydrolyzed, followed by controlled condensation. [11] The hydrolysis reaction is given in Equation (2.17), and depending on the access to water, only a limited number of the initial ligands are hydrolyzed. For TIP, for example, there are four alkoxide ligands, and any number of them may be replaced by the OH-group. Following hydrolysis, condensation can take place in one of two forms

$$2(\mathrm{RO})_3\text{-Ti-OH} \longrightarrow (\mathrm{RO})_3\text{-Ti-O-Ti-}(\mathrm{OR})_2\mathrm{OH} + \mathrm{ROH} \tag{2.18}$$

$$2(\mathrm{RO})_3\text{-Ti-OH} \longrightarrow (\mathrm{RO})_3\text{-Ti-O-Ti-}(\mathrm{OR})_3 + \mathrm{H_2O} \tag{2.19}$$

termed *alcohol elimination* and *water elimination*, respectively. [80] In alcohol elimination, an OH-group reacts with an alkoxide group, eliminating the alcohol corresponding to the alkoxide ligand. For water elimination, two OH-groups formed during hydrolysis reacts to eliminate a water molecule. The pH also influences the above reactions, and different microstructures in the films are achieved for basic and acidic conditions. [90]

One way to further control or reduce the hydrolyzation reaction is by using a suitable solvent. When using 2-MOE ($\mathrm{HO(CH_2)_2}$-O-OH) as the solvent, for example, alcohol exchange may take place,

$$\text{-M-OR} + \mathrm{HO(CH_2)_2\text{-}O\text{-}CH_3} \longrightarrow \text{-M-O}(\mathrm{CH_2})_2\text{-O-}\mathrm{CH_3} + \mathrm{HOR} \tag{2.20}$$

resulting in a chelating effect and slower hydrolysis. [90] For PZT, refluxing Pb carboxylates in 2-MOE yields a soluble and stable lead precursor with 2-MOE ligands. [85] After adding the other precursors, the sol is then intentionally hydrolyzed and promptly coated onto the substrate. [11] The toxicity of 2-MOE is a significant concern, limiting its largescale application to PZT thin films despite the high degree of control in processes employing it. [11]

In classical sol-gel, the *sol* is defined as the colloid system containing the oligomeric compounds prior to coating. Upon drying, further hydrolysis and condensation may take place, and the oligomers will come in contact due to removal of the solvent alone. [11] The resultant metal-organic porous network formed is termed the *gel*. As previously mentioned, the term sol-gel has now been adapted by other researchers for similar processes, and the current definitions of *sol* and *gel* are more dynamic. Often, sol is used to describe the coating solution regardless if it is a true solution or a colloid system. The gel is then any dry film, where the most important characteristic is that it is amorphous and that the cations are homogeneously distributed on the atomic scale. In general, the term sol-gel seems to most often refer to the idea of having the homogeneous inorganic-organic gel, which needs to be pyrolyzed.

Metal-organic decomposition (MOD) are synthesis routes without significant hydrolyzation/condensation reactions prior to coating. Perovskite materials are produced by MOD to a considerable extent. The precursors used are typically carboxylates or β-diketonates. [91] There are two major drawbacks of MOD synthesis systems. First, the

ligands used are so large that the high fraction of organic content may cause cracking during pyrolysis. [92] Second, since the precursors are so stable it is difficult to alter the chemistry for enhanced properties, such as wetting or rheology. [11] Alternative shorter ligands may be employed for reduced problems with film shrinkage. [81] Synthesis is relatively primitive and easy to master, but the sols created are more sensitive to aging than for traditional sol-gel, however, due to esterification of the precursors with alcohol solvents. [11]

Hybrid processes (also known as *chelate* processes) are those that employ both carboxylic and alkoxide precursors. [93, 94] In this case, short chain carboxylates are used for low-valent A-site precursors, while alkoxides are used for B-site cations. The solvent may then be the corresponding carboxylic acid, which forms oligomers with the B-site precursors. It will be shown in Chapter 2.5 that the hybrid method employing A-site acetates and B-site alkoxides is the most common BNT CSD method. Carboxylic acids with more than one acid group chelate the B-site cation, or connects to different cations, creating oligomers. Moreover, it protects the cation sterically from water access, stabilizing the solution. Other additives such as acetylacetone may be added for the same reason. Hybrid synthesis of BT [95] and PZT [96] are extensively studied, and it is found that only B-site cations are included in the formed oligomers, while A-site cations are located outside of the oligomers. Hybrid methods are easier to manage than traditional sol-gel processes, but possesses less control of the reactions and sol properties. [97] The sols are also more sensitive to aging effects, because the system is still sensitive to water, simply at a much lower rate than for sol-gel (hydrolyzation-condensation processes). [11]

Another increasingly known synthesis method is the *Pechini method*, first submitted as a patent in 1962. [98] In the Pechini method, the precursors are nitrates stabilized by citric acid. Citric acid, $HOC(COOH)(CH_2COOH)_2$, contains three carboxylic acid groups, and has a large potential for forming ligands, chelating, and crosslinking. [99] After complex ions are formed, a polyhydroxyalcohol such as ethylene glycol is added, forming ester connections as shown in Figure 2.27. The size of the oligomers can be tuned by the citric acid to polyhydroxyalcohol ratio. [100] The related *citrate method* employs citric acid to chelate and stabilize the cations, but no esterification step is employed, and the solution is simply coated as is. [101]

Several groups have also employed the chelating effect of citric acid, other carboxylic acids, or ethanediamine with water as the solvent. [102, 103] This has the obvious advantages of being less toxic than organic solvents, and less sensitive to water from the ambient atmosphere. $(Bi_{1-x}La_x)_4Ti_3O_{12}$, $SrBi_2Ta_2O_9$, and PZT have been synthesized in this fashion. [102, 103]

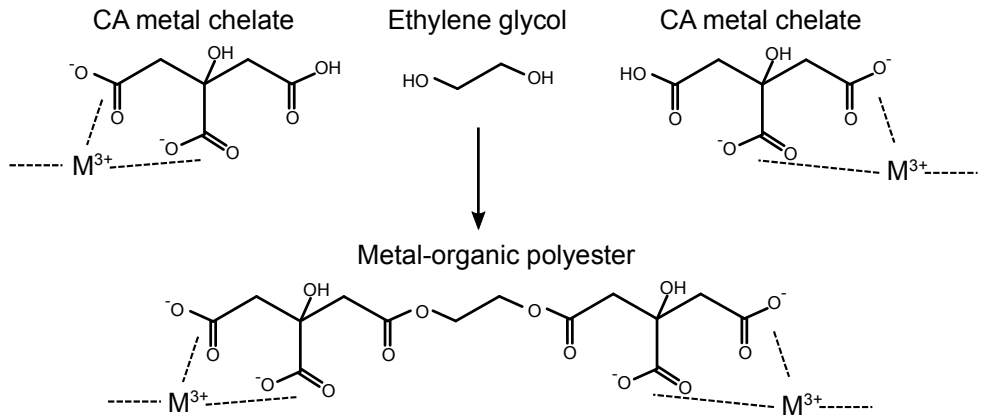

Figure 2.27 Illustration of the esterification in the Pechini process.

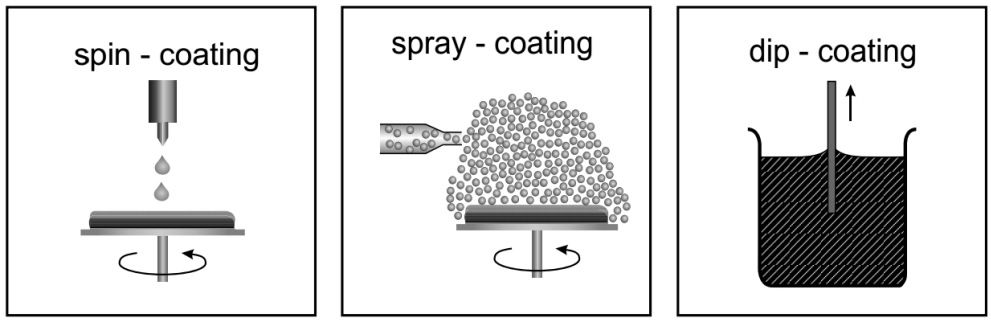

Figure 2.28 CSD coating methods. Reprinted with permission from [11].

Coating

Regardless of the chemistry of the precursor solution, a wet layer is deposited onto a substrate. The three most common deposition methods are *spin coating*, *dip coating*, and *spray coating*, as visualized in Figure 2.28. [11]

Spin coating can be applied to flat substrates of varying sizes and shapes. Most common are circular silicon wafers or smaller square cutouts of either silicon or some single crystal oxide substrate. The substrate is attached by vacuum to a chuck, and the sol is supplied either while the substrate is stationary, or during low rpm spinning. When the substrate is sufficiently wetted, the spin speed is ramped up to 1000-8000 rpm. The thickness of the wet film is given by viscosity, spin speed, spin duration, and substrate size and shape, and the resultant dry film thickness is influenced by the sol concentration. [104, 105]

During spinning, the centripetal force causes the sol to be pushed towards and off of the edges, yielding a film with homogeneous thickness in the center of the substrate. [105] At the edges and corners, however, the surface tension of the sol will cause a thicker layer to remain. On most of the surface, an iridescence color is visible, changing in color as the film gradually thins. At the end of spinning, the homogeneity of the thickness is apparent by the color of the film.

Different defects such as striation patterns may result due to spinning conditions. [104, 105] For volatile solvents, for example, evaporation of solvent prior to or during spinning can cause local variations in concentration and rheology, which can cause inhomogeneous thickness of the dry gel film. For that reason, moisture and flow of the atmosphere surrounding the substrate can have a large effect on the film quality. [106] Similarly, holding time before spinning can influence the concentration of the sol. The shape of the substrate can also have an influence on the film quality. A circular substrate does not cause much turbulence, but the corners of a square substrate may cause local air flows influencing the final film.

Dip coating is subject to many of the same influences and parameters as spin coating. As the name implies, however, the sol is deposited by submerging the substrate into the sol, and pulling it back up in a controlled manner. The process may be either continuous or batch type. In either case, the withdraw speed and angle, wetting angle, and evaporation rate are important. For the batch process, the immersion, start speed, and drainage as the substrate leaves the bath are other important aspects. [107]

Spray coating deviates from the previous methods as it is feasible to coat arbitrarily shaped substrates with larger success. The sol must be of lower viscosity in order to achieve sufficiently small droplets as the sol is *atomized*. A *mist* is created by spraying the sol through a nozzle or ultrasonic nebulizer. With a *Venturi* nozzle, droplets down to 100 nm may be achieved. The mist is transferred to the substrate by a carrier gas, and settles on the surface by gravitational pull or electrostatically. The thickness homogeneity is poorer than for the other methods, but as little as 20 % thickness variation may be obtained. [108, 109]

Drying or gelling

After coating, the film is dried resulting in the *gel* film. Because the wet film is very thin with a large area, drying is very rapid. Volatile solvents may in some cases evaporate entirely within seconds after, or even during, coating. [105] In other cases, volatile solvents may be trapped within the gel network, and it is common to apply a drying step, for example on a hot plate.

Depending on the chemistry of the sol system, the *gel* may be one of several types. *Chemical* gels experience chemical bonding between molecules or oligomers upon drying, obtaining polymeric networks. These reactions are irreversible, and the gel films may not be re-dissolved. [80] *Physical* films do not react chemically during gelling, but are formed simply due to solvent evaporation. The oligomers or precursor ions are attracted due to physical forces such as electrostatic attraction, van der Waals forces, or steric interaction. [80] Finally, *non-gelling* films remain truly wet until pyrolysis is initiated at higher temperatures. [78] The nature of the gel, particularly its density, may influence final film properties. Since the solvent evaporation rate can significantly influence the final film quality, the choice of solvent is important not only for sol stability, wetting, and viscosity, but also for proper volatility and drying properties. [105]

Pyrolysis and crystallization

Pyrolysis or *thermolysis* is the process of removing the unwanted components of the sol or gel to obtain, most commonly, an amorphous phase containing only the desired cations. [97] It is typically conducted between 400-800 °C (Table 2.4, Chapter 2.5). The term pyrolysis refers to Greek *pyro* meaning fire, due to the fact that the organic parts of the sol often reacts with oxygen to form typical combustion products such as CO_x, NO_x, and H_2O. [12] Sometimes,

pyrolysis occurs in an atmosphere without oxygen, and in that case some authors prefer the term thermolysis. [11]

Pyrolysis can occasionally be carried out on a hot plate [110], but it is most common to use a furnace, or a so-called *rapid thermal processing* oven (RTP). [12, 84] An RTP has only a small chamber size, and is designed for very high ramp rates and accurately controlled temperatures for wafers-sized samples. Some RTP equipment can reach heating rates of 200 °C/s with temperature control close to ±1 °C. [13] Cooling rates are not equally rapid, but can nevertheless be significantly faster than for conventional furnaces, due to the small volume of sample and substrate treated and because the chamber walls are water cooled. Furthermore, the atmosphere in the RTP can be controlled, ranging from pure oxygen, via vacuum, to reducing atmospheres such as N_2 or even H_2. [111]

Lead containing materials typically produce properly amorphous M-O-M oxide networks during pyrolysis [112], but material systems such as BT, ST and BST often show intermediate carbonate phases before all organic constituents are eliminated [113]. The reactions and bonds created during pyrolysis are versatile, complicated, and difficult to probe. [85] For PZT, a fluorite or pyrochlore intermediate phase is often observed when heat treated at intermediate temperatures. [12, 114] The different properties of various precursors, such as carboxylates, alkoxides, chelated, oligomers etc., lead to decomposition occurring at different temperatures. [115] For a BT process, for example, the Ti-precursor decomposed before the Ba-precursor. [113] Formation of intermediate non-stoichiometric phases can influence the final perovskite formation process and temperature. [12]

Annealing and crystallization

The nature of nucleation for the specific system has a profound influence on final microstructure. If for example nuclei are formed homogeneously throughout the film, randomly oriented grains will ensue. If, however, nuclei are more easily formed on the film-substrate interface, the resultant microstructure will typically contain oriented columnar grains extending through the entire thickness of the film. [11]

Gibbs free energy of the amorphous oxide phase compared to the energy of the crystalline perovskite phase defines the driving force for nucleation. [116] The difference in energy, ΔG_v, decreases with increasing temperature until the melting temperature where the liquid phase will be favored to the perovskite. [11] The energy barrier for nucleation is different for homogeneous nucleation (in bulk) and heterogeneous nucleation (on interfaces)

$$\Delta G^*_{homo} = \frac{16\pi\gamma^3}{3(\Delta G_v)^2} \tag{2.21}$$

$$\Delta G^*_{hetero} = \frac{16\pi\gamma^3}{3(\Delta G_v)^2} f(\theta) \tag{2.22}$$

where γ is the interface energy, $f(\theta)$ is the contribution from the interface, depending on the contact angle, θ. $f(\theta)$ leads to nucleation energy being less for interfaces than in bulk. If, however, the driving force for perovskite formation, ΔG_v, is large, both types of nucleation will occur simultaneously. Because ΔG_v is decreasing with increasing temperature, the degree of homogeneous nucleation is comparatively larger for low temperature annealing (pyrolysis

if crystallization occurs at that stage). [11] A higher degree of columnar grains or epitaxy is therefore expected with higher temperature crystallization.

Naturally, the ramp rate becomes significant when considering nucleation. If slow ramping is used, a larger degree of low temperature crystallization is allowed to take place during heating, and the microstructure will be influenced. The holding temperature, besides influencing the nucleation rates, also controls the mobility of the ions. Higher diffusion at higher temperatures generally leads to more grain growth and larger grains in a denser film.

Intermediate phases also play a significant role. Formation of transient crystalline phases influences the driving force for perovskite formation, ΔG_v. Rather than the amorphous phase, one has to consider the difference between the free energies of the intermediate phase and the perovskite. Because the intermediate phase was previously preferred to the amorphous state, this is naturally lower, and for otherwise similar systems, those with intermediate phases will show a larger degree of heterogeneous nucleation. This can for example be seen for PZT and BT, where PZT are more columnar in nature, due to its fluorite/pyrochlore intermediate phase. [114]

Texture and epitaxy can also be achieved with CSD methods. Epitaxy can be achieved when the lattice mismatch of substrate and film is small enough. [117] Seed layers may also be deposited, supplying low energy nucleation sites, driving epitaxial or highly oriented (textured) films. [118] For PZT, for example, $(100)_{pc}$ oriented films can be obtained by using PT or PbO seed layers, while $(111)_{pc}$ texture is achieved for TiO_x layers. [12] Presence of a liquid phase during sintering, can also drive epitaxy, as it promotes diffusion to more energetically favorable grains. [119] Finally, epitaxy, or heterogeneous nucleation is promoted by coating diluted solutions, shown for BNT. [118] For smaller thicknesses of gel, the probability of significant homogeneous nucleation decreases.

Today, although many CSD synthesis methods have been developed, the majority of PZT CSD processing is based on one of two methods. [97] Traditional sol-gel synthesis (hydrolysis-condensation) was developed by Budd et al. in the 80s, and still represents the foundation recent synthesis is based upon. [76, 80] This has the advantages of good process control and reproducibility, but the disadvantage of complicated synthesis. The other method is a hybrid one, developed in 1988 [94], and further modified in 1993 [120].

2.4.2 Alternative thin-film methods

Thin films are also routinely prepared by physical methods and other chemical approaches.

Sputtering is a well-established process for thin film deposition. Metallic materials can utilize direct current (DC) sputtering, while insulating materials employ radio frequency (RF) magnetron sputtering. [20, 121] PZT has been prepared by both methods. In DC sputtering, either separate Ti, Zr, and Pb metallic targets are used, or a composite single target. [122] For RF sputtering, composite targets containing PbO, TiO_2, and ZrO_2 were employed. [20] In both cases, excess of lead is used due to its volatility. Generally, precise stoichiometry control is challenging, and one has to optimize the process parameters in order to obtain the target composition. For example, when a $Pb_{1.1}Zr_{0.6}Ti_{0.4}O_3$ target was used, substrate temperatures of 475-550 °C were shown to yield perovskite films. [123] Both lower and higher temperatures gave a pyrochlore phase. At lower temperatures, the pyrochlore is similar to the intermediate

phase seen for several other synthesis methods, while at higher temperatures, it is due to excessive Pb evaporation without sufficient excess for loss compensation in the target. [123] The chamber gas also influences the result, where a mixture of argon and oxygen is typically used. The Ar pressure has a considerable influence on the microstructure of the deposited film, while O_2 partial pressure influences the stoichiometry. [20, 124] Typical advantages of sputtering techniques are high deposition rates, homogeneous thickness, possibility of large coating surfaces, and few remaining impurities. The main disadvantage is the poor composition and stoichiometry control. [20]

Pulsed laser deposition (PLD) is similar to sputtering in that it uses a composite target from which the material is evaporated before it condenses on the substrate. For PLD, however, a laser is used to heat up the target. [125] Typically, lasers with wavelength 200-300 nm are operated for 10-25 ns bursts at 10-20 Hz. [126] Since the energy source (laser) is positioned outside of the chamber, impurities due to resistive heater units may be avoided. [20] Compared to sputtering, the substrate may be colder in PLD, leading to better stoichiometry control with less evaporation of volatile species. [20] In general, exact composition transfer from the target to the substrate is obtained, leading to excellent compositional control, limited only to the target production. [20] Furthermore, the chamber gas can be high in oxygen, giving increased control of volatility and elimination of oxygen vacancies. [127] For PZT, the vapor pressure of Pb (g) is higher than for PbO (g), and by maintaining a high O_2 pressure PbO (g) is promoted, resulting in lower levels of lead loss. [128] Some notable drawbacks of PLD thin film deposition are high price, ablated particles deposited on the substrate, defects due to the same particles hitting the substrate, and inhomogeneous films for larger deposition surfaces. [20]

Metal-organic chemical vapor deposition (MOCVD) uses precursor solutions that are transferred to a gaseous state and carried into the deposition chamber. [129] The precursors can for example be alkoxides as in CSD processing. There are two main methods of transferring the precursors to the gaseous phase. The first is by bubbling a carrier gas such as N_2 through the solution [130], and the other is by vaporizing the solution itself [131]. The stoichiometry is then controlled by adjusting the flow of each individual precursor gas. In the deposition reactor, the substrate is kept at ~500 °C, allowing the perovskite to grow as the organic parts are decomposed. [132] CVD boasts high deposition rates, homogeneous thickness, deposition on large areas, and excellent step coverage and ability to coat three-dimensional structures. [20] The main challenges of CVD are composition and microstructure control, as deposition rates is dependent on process parameters. For example, not only the flow rates, but also the substrate temperature is important for stoichiometry control. [20]

Molecular beam epitaxy (MBE) has been used extensively for thin film synthesis the last couple of decades. [133] As the name implies, epitaxial films are formed. The deposition rates are very low, promoting epitaxy. [133] Moreover, composition can be accurately controlled with accuracy of monolayers. However, MBE has generally been applied for semiconductors, rather than oxides, due to the very high vacuum discouraging oxidation. [20] Despite this, PT has been prepared by means of MBE, supplying oxygen either by using ozone gas at ~10^{-5} Torr [134] or by H_2O_2 at 5×10^{-5} Torr [135]. PZT has been produced in MBE by using

Zr tetrabutoxide as a metal-organic precursor. [136] Typically, the perovskite films formed in MBE are on the order of 50 nm thick. [20]

The *hydrothermal method* may be utilized for production of perovskite thin films. In hydrothermal synthesis, a chemical solution containing precursors is brought to elevated temperatures and pressures. [137] Typically, an autoclave is employed where a steel vessel with a Teflon inner cup is tightly sealed. This is placed in a furnace, and the temperature increase and evaporation of the solvent causes the increase in pressure. One of the main advantages of this method is the low temperatures required, as perovskites may be formed already at 100-200 °C. [20] Furthermore, relatively thick films, up to tens of microns, may be formed, and substrates of complicated geometries may be used. [138] Moreover, due to the low temperatures and high pressures, volatility of elements such as Pb in PZT and Na/Bi in BNT is reduced. An important drawback, however, is the lack of monitorability, as the steel autoclave is impervious to most characterization techniques. Therefore, a higher degree of trial and error may be needed in order to identify the proper fabrication parameters. There are recent methods developed for in-situ characterization of hydrothermal synthesis. [139, 140] Furthermore, simultaneously as films deposition occurs, product powders will also form freely in the solution. Moreover, due to the nature of sample loading, high throughput production is relatively poor. For PZT, hydrothermal synthesis has the additional advantage of occurring below the Curie temperature, T_C, circumventing volume-changing texture-inducing phase transitions upon cooling. Typically, to achieve phase pure PZT, the synthesis temperature is 150-220 °C, and for lower temperatures secondary phases like PbO, TiO_2, PT, and $Pb_2Ti_2O_6$ have been observed. [20, 141] The precursors used can be chlorides, oxychlorides, nitrates, acetates, oxides, hydroxides, and alkoxides. Moreover, KOH is added as a mineralizer, driving the formation of PZT according to [142]

$$Pb^{2+} + xTiO_2 + (1-x)ZrO_2 + 2OH^- \longrightarrow PbTi_xZr_{1-x}O_3 + H_2O \qquad (2.23)$$

2.5 Synthesis of BNT thin films

In the current section, recent research efforts into CSD processing for BNT will be reviewed. The focus lies on the production of the films, while thin-film properties are treated briefly in Section 2.6. As shown by Figure 2.16, research on thin-film BNT is increasing, with close to 30 publications in 2016, and the accumulated number of articles is approximately 200. The most common BNT thin-film production method is that of CSD by spin coating. In fact, the methods, precursors, and general chemistry discussed in Section 2.4.1 and described by Schwartz et al. [11] for PZT in 2004 can largely be recognized in the BNT literature. In the following, the most important strategies for BNT thin film production are summarized, and a more detailed overview of process parameters is provided in Table 2.4.

2-MOE

As discussed above, hydrolyzation-condensation processes or *traditional* sol-gel processes provide excellent control of the thin-film deposition with a high degree of reproducibility. In general, these synthesis routes employ 2-MOE and acetic acid as a co-solvent with A-site acetates and a Ti alkoxide such as Ti isopropoxide or Ti butoxide. For these processes, refluxing and intentional aging of the sol system is required. [143]

Remondiere et al. thoroughly covered the decomposition pathway of BNT by CSD based on 2-MOE. [144] They tested three different approaches. The first approach employed the A-site acetates and Ti butoxide prepared in separate precursor solutions. Acetates were dissolved in an acetic acid/2-MOE mixture, and refluxed at 124 °C for 1 h. Ti butoxide was dissolved in 2-MOE/acetylacetone, before mixed with the other precursors and refluxed once more. In the second approach, A and B site precursors were added directly to 2-MOE and refluxed. In the third approach, vacuum was exerted on the system, lowering the reflux temperature to 30 °C. Films were spin coated and dried in a conventional manner, and pyrolized/crystallized on a hot-plate at 460 °C for 5 min.

TGA measurements demonstrated that organic decomposition and mass loss had finished at approximately 500 °C, with less than 30 % weight loss. [144] XRD measurements conducted on powder samples showed that the perovskite forms at 400-500 °C. At temperatures below 500 °C, intermediate pyrochlore and fluorite structures were observed for approach 1 and 3. The thin film samples showed the same behavior, and approach 2 gave phase pure perovskite films already when pyrolyzing below 500 °C at the hot-plate. This was explained by the relatively lower amount of organic species in this gel.

Recently, Zhou et al. [143] found that the pyrolization temperature had a large influence on phase purity. At 350 °C, a pyrochlore phase, stronger than perovskite in XRD intensity, was formed, and it could not be removed by further heat treatment. For both lower and higher pyrolysis temperatures, however, pure perovskite was formed. They formulated a model describing how the pyrochlore phase forms due to presence of metallic bismuth during synthesis. This occurs when temperatures are higher than the decomposition temperature of the Bi-carboxylate, but lower than the Na-carboxylate, causing reactive bismuth without access to Na.

Peng et al. [145] investigated the influence of annealing temperature on residual stress due to thermal expansion mismatch of BNT and SiPt. Each layer was pyrolyzed at 450 °C for 5 minutes, and crystallization was conducted at 650, 700, 750, and 800 °C for every 8th

Table 2.4 Summary of selected references with BNT thin-film fabrication by CSD. Abbreviations: Acetic acid (AA), propionic acid (PA), ethylene glycol (EG), acetylacetone (acac), Ti isopropoxide (TIP), and Ti butoxide (TB).

Comp	Substrate	Thick. (nm)	Solvent/stabilizer	Precursors	Pyr. Ann. (°C)	Excess Bi Na (%)	Ref
BNT-KNN composite	SiPt	5000	2-MOE, acac	NaAcetate, BiNit, TB	650-750	2 10	[146]
*x*Al	SiPt	660	2-MOE, acac	NaAcetate, BiNit, AlNit, TB	650-750	2 10	[147]
*x*Mn	SiPt	500	2-MOE	Bi pentoxide, Na ethoxide, Mn butoxide, TIP	400 700	3 10	[148]
6.5Ba-9Sr	SiPt|$LaNiO_3$	400	2-MOE, acac, ammonia	Acetates, BiNit,TIP	700	10 10	[118]
6.5Ba-9Sr	MgO|ST| $LaAlO_3$| $LaNiO_3$	500	2-MOE, AA, acac, ammonia	Acetates, BiNit,TIP	700 750	10 10	[149]
6.5Ba-9Sr	ST:Nb	500	2-MOE, AA, acac, ammonia	Acetates, BiNit,TIP	700 750	10 10	[150]
6Ba	SiPt	400	2-MOE, AA, acac	Acetates, TIP	400 700	10 20	[143]
BNT	SiPt	200	2-MOE, (AA), acac	Acetates, TB	460	0 0	[144]
10Sr-9K-*x*La	SiPt	600	2-MOE, AA, acac	Acetates, BiNit, LaNit, TB	500 700	0 0	[151]
6Ba	SiPt	230	2-MOE, AA, acac	Acetates, TB	450 650-800	10 0	[145]
*x*Zr	Glass|$InSnO_3$	400	2-MOE, AA, acac	NaAcetate, Bi/ZrNit, TIP	500	0 0	[152]
BNT	Al_2O_3		2-MOE, AA, acac	Acetates, TB		0 0	[153]
6Ba-2K-4Nb	SiPt	400	2-MOE, AA, ethanolamine (for Ba)	Acetates, BiNit, Nb ethoxide, TIP	600 750	10 10	[110]
5K	ST:Nb	300	AA	Acetates, BiNit,TB	500-700	10 10	[154]
*x*Ba	SiPt	200	AA, acac	Acetates, BiNit, TIP	500 700	0 0	[155]
2Nb	Glass|$InSnO_3$	500	AA, EG, acac	NaAcetate, BiNit, NbEthoxide, TIP	500	0 0	[111, 156]
5.5Ba	SiPt	100	AA, 1,3-propanediol, water, ethylhexanol	Acetates, Ti di-isopropoxide bis-acetylacteonate	500-750	0 10/ 10 10	[13]
*x*Ba	SiPt	350-550	AA, 1,3-propanediol, water, PA, propionic anhydride, 2,4-pentanedione, butanol	Acetates, Ti di-isopropoxide bis-acetylacteonate, BaCarbonate, TB	650	0 0/ 10 10	[157]
*x*Ba-*x*K	SiPt		AA, isopropanol, acac, water, diethaneamine	Acetates, BiNit, KNit, TIP	450 700	0 10	[158-161]
8Ba	SiPt	250	AA, isopropanol, acac	Acetates, TIP	400 700	0 0	[162] [163]
10K-*x*Mn	SiPt		AA, PA, methanol	Acetates, TIP	325 700	8 16	[164]
11K-2.5Mg	SiPt	200	AA, PA, methanol	Acetates, TIP	300 600-700	10 20	[165]
BNT	silicon	900	Nitric acid, EG	Bi2O3, Na2CO3, TIP	700	0 0	[166, 167]

deposited layer. They found a presence of a pyrochlore secondary phase for all samples, and for the samples annealed at 650 and 800 °C, the amount of pyrochlore was significant. They explained this phenomenologically similar to PZT, by incomplete transformation of the intermediate phase at lower temperatures, and reappearance at higher temperatures due to volatility of Bi and Na. Residual stresses were measured to be 221, 85, 25, and 50 MPa for 650, 700, 750, and 800 °C, respectively.

Sakamoto et al. [148] investigated the effect of Mn doping in BNT, and it was shown to significantly reduce the conductivity of the samples. PE loops were measured up to 1400 kV/cm, but the pure BNT could only be measured at 600 kV/cm^2 due to the leakage. Adding 1 % Mn significantly reduced the leakage at higher fields, because pure BNT showed an abrupt increase in conductivity at approximately 100 kV/cm. Sui et al. showed a similar effect for ~2 % Zr doping in BNT. [152]

Many of the reports on 2-MOE based CSD of BNT reflect challenges with respect to phase purity and leakage current, but some particularly thorough works illustrate the potential and feasibility of the method. For example, the investigations by Zhou et al. [143] and Remondiere et al. [144] stand out. They showed that careful optimization and understanding of the synthesis process lead to high quality single phase films, providing an excellent foundation for further studies with focus on the piezoelectric properties as well as the purity and microstructure. A range of other authors and research groups report BNT thin film synthesis with methods similar to the above, all employing 2-MOE as a solvent. [110, 147, 149, 150, 168-174]

Other organic solvent systems

While synthesis routes employing 2-MOE are well known and developed both for BNT and other perovskites such as PZT, synthesis methods avoiding 2-MOE are also emerging. For example, Alonso-Sanjosé et al. have developed a CSD method with a sol stable in air. [13] They prepared separate BNT and BT starting solutions, using a 1,3-propanediol, acetic acid, and water co-solvent (1:1:1). Precursors were A-site acetates and Ti di-isopropoxide bis-acetylacetone (alkoxide stabilized by β-diketone, Figure 2.26). Different intermediate solutions were refluxed for 3-8 h, and some byproducts were removed by distillation. Finally, the sols were diluted to 0.2 M with 2-ethyl-1-hexanol. The decomposition process and resultant phases were thoroughly analyzed. TGA showed that most of the weight loss occurred below 350 °C, but some weight loss remained until approximately 600 °C (carbonate remainders) and 750 °C (speculated to originate from evaporation of volatile cations). The films were prepared between 600-750 °C, and at 650-700 °C phase pure perovskite was formed. Films crystallized at 600 °C showed the presence of pyrochlore secondary phase, and at 750 °C an unknown phase, suggested to originate from a Pt-Bi reaction. Because this phase was only visible by traditional XRD (Bragg-Brentano), and not with grazing incidence, they argued that it is highly textured, likely due to nucleation on the Pt film, supporting the notion of a Pt-Bi reaction. They also showed that the amount of this phase increased not only with increasing temperature, but also with increasing crystallization holding time at 650 °C. Finally, the piezoelectric properties were confirmed, and despite showing relatively high levels of leakage current, the hysteresis was illustrated up to 800 kV/cm.

Kim et al. have reported BNT CSD thin film synthesis already in 2005. [166, 167] In this work, they used a process different to the traditional sol-gel process. Bi_2O_3 and Na_2CO_3 were dissolved in nitric acid (70 %), and diluted in ethylene glycol, before adding TIP as the Ti precursor. Stirring at 60 °C for 1 h gave a transparent sol. They achieved phase pure perovskite films at 700-900 °C.

For both processes based on 2-MOE and not, A-site cations are often added in excess to counteract the volatility of Bi, Na, and K. In general, Na excess is often added in larger amounts than Bi. [143, 148, 165]

Table 2.5 Summary of selected references with BNT thin-film production by physical methods. Abbreviations: pulsed laser deposition (PLD), radio-frequency magnetron sputtering (rf-ms).

Composition	Substrate	Thickness (nm)	Method	Substrate temp (°C)	O_2 pressure (mbar)	Ref
BNT	SiPt|BT	400	PLD KrF eximer	650-750	0.3	[176]
6.5Ba	SiPt	420		750-800	0.13-0.4	[177]
4K-4Ba	ST|$SrRuO_3$	350		750	0.4	[126]
6Ba-0.5Mn	ST|$SrRuO_3$	250		600-750	0.27	[178]
4K-4Ba	ST|$SrRuO_3$	500		700-800	0.27-0.67	[179]
*x*Ba-5Mn	$LaAlO_3$|$La_{0.5}Sr_{0.5}CoO_3$	162		670	0.2	[180]
25Sr	Si|YSZ|CeO_2|$LaNiO_3$	230		700	0.4	[181]
*x*Ba	MgO|Pt	2500-3000	rf-ms	700	8×10^{-6} (Ar+O_2)	[182]
*x*Ba-2Mn	MgO|Pt	3000		700		[183]
BNT	SiPt	750		Postannealed: 675	pure Ar	[184]

Non-CSD methods

BNT thin films have also been produced by alternative methods such as pulsed laser deposition (PLD), radio frequency magnetron sputtering (rf-ms), and metal-organic chemical vapor depositions (MOCVD). A selection of the physical fabrication methods and their parameters is presented in Table 2.5. Duk et al. made BNT films on ST and $NdGaO_3$ substrates by metal-organic chemical vapor deposition (MOCVD). [175] The β-diketonate 2,2,6,6-tetramethyl-3,5-heptanedionate (thd) was used with the precursors Na(thd), $Ti(IP)_2(thd)_2$, and $Bi(thd)_3$ dissolved in toluene. The solutions were flash evaporated at 230 °C, and carried into the reaction chamber by 38 % O_2 in Ar (2.7×10^3 Pa). Substrate temperatures varied from 600 to 800 °C. They showed that by supplying 300 % Na precursor, compared to Bi, the pure perovskite was formed. For decreasing relative amount of Na, $Na_{0.5}Bi_{4.5}Ti_4O_{15}$, $Na_{0.5}Bi_{8.5}Ti_7O_{27}$, and $Bi_4Ti_3O_{12}$ phases were formed.

Summary of literature on thin-film BNT fabrication

As can be seen in the preceding, thin film synthesis of BNT has seen significant interest in the last decade. Particularly traditional CSD approaches have been frequently reported. The common denominator is use of acetate A-site precursors (nitrates are exceptionally reported) and Ti alkoxides (primarily Ti isopropoxide or Ti butoxide) in a solvent of acetic acid. Most commonly, 2-MOE and acetylacetone is added to stabilize Ti from hydrolysis. According to the classifications termed in Chapter 2.4.1, these synthesis routes may be considered so-called hybrid methods. In the next section, strategies for aqueous fabrication of BNT are treated.

2.5.1 Aqueous synthesis of BNT

Aqueous synthesis of BNT thin films

The number of reports on aqueous thin film fabrication of BNT is, to our knowledge, only two. Both articles were published by Cui et al. in 2016. [155, 185] The authors described their process as an “economical water-based solgel method” (from the abstract of [185]), but their

procedure does not fully qualify to our definition of an *aqueous* process. Na acetate, Bi nitrate, Ba acetate, and TIP were used as precursors, but significant amounts of acetic acid, isopropanol and acetylacetone were used in the solvent system. In fact, this method is similar to that reported for PZT in 1988. [94] Distilled water was subsequently added to the mixture, but less than 50 vol.% was added, maintaining acetic acid as the primary solvent. In [155], they label their method a "water-based sol-gel process", but water was actually not mentioned in the experimental section at all. Thus, to the best of our knowledge, aqueous fabrication of BNT thin films has still not been reported in literature.

Aqueous synthesis of BNT *powders*

There is a small selection of reports in literature on aqueous synthesis of BNT powders relevant for production of thin films by aqueous CSD.

West and Payne have reported synthesis of BNT-5Ba powders by an intricate "citrate-gel" method in 2003. [186] Their precursors were Na_2CO_3, Ti butoxide, $Ba(NO_3)_2$, and Bi_2O_3. Citric acid (CA), HNO_3, and ammonia were used for stabilization. Mixing was not straight forward, but intermediate precursors were prepared. Na carbonate was added to a boiled solution of CA, giving a Na precursor 0.1 M in Na and 0.2 M in CA. Ti butoxide was added to a solution 0.4 M in both CA and ammonia. The solution had been previously boiled, and was kept at 80 °C during addition, and for several subsequent hours, until the solution turned clear, yielding ~0.2 M in Ti. Ba nitrate was simply added in 0.2 M to deionized water. Bi nitrate was dissolved in 2.5 M nitric acid, and upon adding ammonia, $Bi(OH)_3$ precipitated. Finally, these precursors were mixed and stirred at elevated temperatures to produce a viscous sol promptly dried at 150 °C to obtain a char for further calcination. The samples were demonstrated by XRD to be relatively phase pure perovskite after heat treatment at 550 °C.

Kundu and Soukhojak have synthesized Ba and Zr doped BNT powders from an "alkoxyless wet chemical route" resembling that of West and Payne. [187] A bismuth precipitate was prepared by adding CA and ammonia to a solution of Bi nitrate. The nitrate-less precipitate was re-dissolved in a CA/ammonia solution. Titanium hydroxide was precipitated by adding ammonia to a Ti oxide sulfate solution. The clean precipitate was re-dissolved in a boiling CA solution. $ZrO(NO_3)_2$ was dissolved in the Ti solution, and Na carbonate and Ba nitrate were dissolved in separate CA solutions (cation/CA = 0.5). TGA showed mass loss to occur until approximately 550 °C, and XRD showed the perovskite from 500 °C. At 500-600 °C, there was an unidentified phase with the main reflection at $2\theta = 30°$, corresponding nicely to the pyrochlore phase frequently reported in literature. The main advantage of this method is the use of relatively cheap chemicals. Ti oxide sulfate may found for 18.8 EUR per mol Ti, and Bi nitrate is the cheapest common Bi precursor for CSD methods.

Xu et al. have made BNT-BT powders during 2005-2007. [188-190] They used A-site nitrates and Ti butoxide stabilized by CA. Ti butoxide was stabilized by CA and ammonia, and the nitrates were added. Stirring at 80 °C for 1 h yielded a transparent solution at pH 6. They reported that CA concentrations of 1.2-1.6 times total cation concentrations yielded successful sols. A pyrochlore secondary phase was observed up to 500 °C, while calcination at 600-650 °C gave phase pure samples, according to XRD. In the later article, the authors added Mn in the form of nitrate, maintaining the fabrication procedure. This fundamental

procedure will be attempted in Chapter 4.6.1 of the current work, but it will be shown that the produced sols are inferior to those of another method.

Mercadelli et al. [191] have produced BNT-BT powders by dissolving Ba acetate, TIP, and A-site nitrates in 65 wt% HNO_3, and CA was added at 2.5 times the concentration of cations. Hydrogen peroxide (2:1 vs Ti) was also added prior to TIP addition. Finally, urea (1.4:1 vs cations) was added to avoid precipitation as evaporation of NH_3 lowered the pH. They tested the influence of the ratio of citric acid to NO_3^- in the solution, and found that high levels of nitrate strongly promoted formation of bismuth oxide during calcination at 300-500 °C. With sufficiently high citric acid concentration, however (CA/nitrate > 0.2), relatively phase pure perovskite could be obtained at 500 °C (some pyrochlore was present).

To summarize, there are several reports on true water based chemical solution synthesis of BNT bulk samples. Common to all of them is the use of citric acid as a chelating stabilizing additive. The cation precursors are most often the same as known from organic CSD methods, but a small tendency to prefer inorganic salts rather than the carboxylates and alkoxides is observed. Thin film production of BNT from an aqueous method is still not sufficiently reported, and the reports on production of bulk BNT by chemical solution methods consistently do not provide details related to feasibility of thin-film production. For example, sol stability, concentration, rheology, and wetting properties are often not treated. Finally, there is also a trend of using complicated and time-consuming precipitation and re-dissolution processes.

Precursors from related material systems

The constituent cations of BNT are naturally parts of other material systems as well, and aqueous production of these may contain helpful knowledge for the synthesis of BNT. The following section addresses relevant precursor variants from literature not directly related to BNT.

Haugen et al. have provided details surrounding stabilization of Ti isopropoxide by CA for production of TiO_2. [192] TIP was added to a solution of CA (TIP:CA 1:3) at 90 °C while stirring. After continued stirring at 70 °C for 12 h a clear solution was obtained. Concentrations varied from 0.06 to 0.6 M.

Deng et al. have released a comprehensive study on the nature of the Ti citric acid complex ion. [99] They found that Ti is octahedrally coordinated, and that the functional groups bonding to the cation are the alkoxy and carboxyl groups located on the central position of the citrate molecule, as shown in Figure 2.29.The Ti coordination was not influenced by the pH of the solution, which was varied from 1 to 7 for precipitation of different complexes. This demonstrates that the $Ti(Cit)_3$ complex has 7 states, from 2− to 8−, depending on the number of protonated carboxyl groups. At pH 7, the complex is fully deprotonated, while at pH 1 it is fully protonated. The authors also showed that hydrogen bonding between protonated and deprotonated carboxyl groups are relatively strong, giving a polymerizing effect between the ligands.

Hardy et al. have developed precursors for aqueous preparation of $(Bi,La)_4Ti_3O_{12}$. [103, 193] The Bi precursor described consists of bismuth (III) citrate ($BiC_3H_5O(COO)_3$) stabilized by ethanolamine. Bi citrate is not soluble in water, but dissolves when ammonia is added. At this point, Bi will quickly hydrolyze, and hydroxides or oxides will precipitate. The authors found, however, that adding ethanolamine (1.5 times Bi concentration) resulted in a Bi

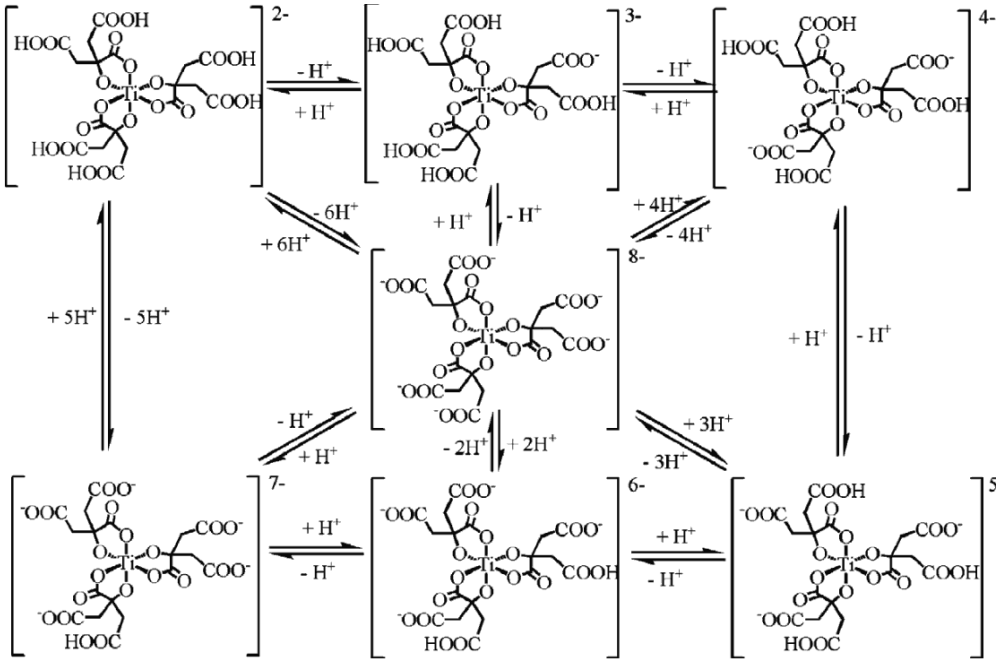

Figure 2.29 Illustration of the different levels of protonation in a $Ti(Cit)_3$ complex. Notice that the functional groups bonding to Ti are the central carboxy and alkoxy groups for all three citric acid ligands. Reprinted with permission from Elsevier [99].

solution stable at least on the order of months. Compared to alternative Bi precursors discussed in the preceding, the method described by Hardy et al. represents the simplest procedure most reliably reproduced and least sensitive to processing parameters. Moreover, bismuth citrate is readily available, and in the same price range as bismuth nitrate. TGA showed the precursor system, together with La and Ti, to decompose completely before reaching 500 °C. Later, the same authors extended the process for thin film production, and thoroughly analyzed the pyrolysis parameters and differences to bulk processing. [194] Interestingly, they found by in situ high-temperature XRD that the target Aurivillius phase formed simultaneously as a parasitic secondary pyrochlore phase at 472 °C. This pyrochlore phase could not be removed by further increasing the temperature up to 721 °C where the substrate started taking damage. With more rapid ramping to 650 °C in an RTP synthesis setup, however, the secondary pyrochlore phase was avoided.

2.5.2 Benefits of an aqueous BNT CSD method

There are many reasons for pursuing a water based CSD route. The most important reason is to avoid the solvents and stabilizing agents 2-MOE, acetylacetone, and acetic acid due to the hazards. Acetic acid and nitric acid are also considered hazardous due to the very high concentration inherent when used as the solvent itself. NaOH, KOH, and citric acid, on the other hand, would be used in a diluted aqueous solution, and are therefore not considered equally hazardous. Table 2.6 summarizes the cost and toxicity of the most common precursors and solvents in traditional CSD as well as for the aqueous method developed in this work.

Table 2.6 Comparison of common BNT precursors. Prices are compiled from selecting the cheapest product of sufficient quality from a search at http://www.sigmaaldrich.com and https://www.alfa.com/. Oxides and carbonates are shown as a solid-state synthesis reference. Price per mol is normalized against 1 cation. All prices were retrieved June 20th, 2017.

Cation	Precursor	Price (EUR/kg)	Price (EUR/mol)	Hazards	URL[2]
Na	Na acetate (anhydrous)	20	1.6	-	<alfa>A13184/
	$NaNO_3$	18.9	1.6	1	<alfa>A12327/
	NaOH	16.9	0.68	1	<sigma>mm/06203m
	Na_2CO_3	20.6	2.9	1	<alfa>A17484/
Bi	Bi acetate	1796	693	-	<alfa>017574/
	$Bi(NO_3)_3 \cdot 5H_2O$	144	70	1	<alfa>012231/
	Bi citrate	228	90	-	<sigma>aldrich/480746
	Bi_2O_3	99	23	1	<alfa>012230/
Ba	Ba acetate	82	21	1	<alfa>A10316/
	$Ba(NO_3)_2$	33	8.6	1	<alfa>A11305/
	$BaCO_3$	53	10.4	1	<alfa>A13195/
K	K acetate	17.2	1.69	-	<sigma>aldrich/w292001
	KOH	12.9	0.72	1	<alfa>A16199/
	$K_2(CO_3)$	16.1	1.1	1	<alfa>A16625/
Ti	TIP	80	22.7	1	<alfa>077115/
	Ti butoxide	94.6	32.2		<alfa>077124/
	TiO_2	40	3.2	-	<sigma>aldrich/248576
Solvent	Acetic acid (glacial)	19.1*			<alfa>033252/
	2-MOE (anhydrous)	135*			<sigma>sial/284467
	Isopropanol (anhydrous)	59*			<alfa>041463/
	HNO_3 65 %	26*			<sigma>mm/84380m
Additive	Acetylacetone	15.1	1.51		<sigma>aldrich/10916
	Citric acid	7.7	1.48	1	<sigma>aldrich/w230618
	Ethanolamine	20	1.22		<alfa>A11697/

*) EUR/liter
-) Not harmful
1) At most irritant upon contact. May be harmful if swallowed. May intensify fire. Corrosive due to pH. Hazard has limited scope with respect to time (inherent dilution or similar). Only limited safety measures required.
2) <sigma> means "http://www.sigmaaldrich.com/catalog/product/", <alfa> "https://www.alfa.com/en/catalog/".

In general, the precursors used in aqueous methods are cheaper than the acetates used with organic solvents. From Table 2.6, it is apparent that the cost of Na and K is negligible compared to that of Bi, Ti, and the solvent system. For Bi, Ba, and Ti, however, selection of the precursor type can have a considerable influence on cost. For example, Bi acetate is a factor of ten more expensive than Bi nitrate. When considering large scale commercial production, this difference may render one fabrication method preferable to the other. It should be noted that the prices reported here are compiled from a simple comparison of list prices available online. More competitive prices would likely be obtained when buying in large scale and comparing prices from different vendors. However, the trends give a general idea of the minimum cost for each type of procedure. Even the more expensive of these chemicals may be cheap enough when compared to the costs of other fabrication aspects. Nevertheless, it is encouraging to see that a water based synthesis is at least not more expensive than the current organic alternatives.

2.6 BNT thin-film properties

The electromechanical properties (piezoelectric coefficients and strain) of BNT thin films are often not the topic of investigation in literature. Rather, ferroelectric and dielectric properties are more commonly reported. This is assumed to be a result of the increased difficulty of measuring strain as compared to electrical properties. Strain measurements require more advanced equipment such as piezoresponse force microscopy (PFM), or specially prepared cantilever devices. Moreover, the clamping effect on the piezoelectric film from the substrate may be significant, and the measured property will be dominated by stress ($e_{31,f}$, Equation (2.9)) rather than strain (d_{31}). With empirical data, d_{31}/d_{33} can be estimated from $e_{31,f}$, but this requires knowledge about the Young's modulus and other parameters of the film, which are not well documented for BNT. The measured properties are therefore both difficult to obtain and do not yield a direct comparison with bulk materials. Instead, the mechanical aspect of the thin-film properties is often neglected in benefit of purely electrical properties such as polarization-field and dielectric permittivity. However, there are some reports on electromechanical properties based on methods such as PFM [118] or double-beam incidence Mach-Zehnder interferometer [195]. A selection of electromechanical and electrical properties of BNT thin films is provided in Table 2.7 and Table 2.8, respectively.

Table 2.7 Electromechanical/piezoelectric properties of BNT based thin films. S_{oop}: out-of-plain strain.

Composition	d_{33} (pm/V)	$e_{31,f}$ (C/m^2)	S_{oop} (%) @ E (kV/cm)	Notes	Prod. method	Ref
6Ba-2K-4Nb	78		0.2 @ 140		CSD	[110]
5.5Ba	40				CSD	[195]
5Ba		-8				
7Ba		-14.1		Epitaxial 100	Sputtering	[182]
10Ba		-8.1				
5K			0.38 @ 333	Epitaxial 100	CSD	[154]
			0.27 @ 333	Epitaxial 110		
			0.33 @ 333	Epitaxial 111		
6.5Ba-9Sr	210		0.32 @ 200	Epitaxial 111	CSD	[150]
	190		0.25 @ 200	Epitaxial 110		
	130		0.14 @ 200	Epitaxial 100		
6Ba-0.5Mn	120			k_p = 0.49	PLD	[178]
3Al	57				CSD	[168]
11K-5Mg			0.35 @ 500	Linear strain response	CSD	[165]
4K-4Ba		-2.25			PLD	[126]

Table 2.8 Electrical properties of BNT based thin films.

Composition	E_c (kV/cm)	P_r (μC/cm^2)	P_s (μC/cm^2) @ E (kV/cm)	ε_r	tan$d$	Prod. method	Ref
BNT				800	0.1	PLD	[176]
6Ba	100	10	35 @ 600			CSD	[143]
6Ba-2K-4Nb	40	20	60 @ 280	700-1100	0.1	CSD	[110]
BNT matrix with KNN	60-100	12-22	60 @ 600	500-1050	0.3-0.4	CSD	[146]
3.5Ba		6.7					
5.5Ba		12.3	20 @ 300	750		CSD	[195]
8Ba		6.3					
10Ba		6.4					
5Ba				750			
7Ba				1520		Sputtering	[182]
10Ba				1100			
BNT-2Nb (donor)		10.7	16 @ 700	500	0.1	CSD	[111]
6Ba	87	12	45 @ 600	550	0.05-0.1	CSD	[155]
5K				800-1180	0.02-0.05	CSD	[154]
6.5Ba-9Sr	100	10.5	25 @ 400	750	0.04	CSD	[118, 149]
6Ba-0.5Mn	200	33	80 @ 800			PLD	[178]
10K-2Mn			40 @ 800	500	0.05	CSD	[164]
3Al	300	16	40 @ 882	420	0.04	CSD	[147, 168]
11K-5Mg	50	10	50 @ 400			CSD	[165]
4K-4Ba		30		720	0.2	PLD	[126]

2.7 Platinized silicon and thermal expansion stress

Platinized silicon (SiPt) has achieved the role of a reference substrate for thin film deposition of electronic oxides in industrial processes. [3, 12] From the preceding sections on thin film deposition of perovskites, only a handful of substrates are commonly reported. Besides SiPt, the most common substrates are either those of single crystal oxides (ST, MgO, alumina), aiming to be as stable and compatible with the film as possible, or glass or simple metals, aiming to be as economical as possible. The dominant role of silicon based substrates has been achieved largely due to the substantial semiconductor industry. [3] The industry and technology of production and manipulation of electronic devices from single crystal silicon wafers is sufficiently mature, causing access to cheap single crystal substrates and fabrication facilities and methods which is unmatched by any other substrate system. [196] Perhaps the most significant advantage is the methods developed for shaping 3D free-standing structures down to even the nanometer size range. Photolithography, very high resolution deposition, and selective etching renders reliable fabrication of micro-sized beams, cantilevers, membranes etc. on a large scale possible. [3] Using silicon wafers for production of micro electromechanical systems (MEMS) devices has the additional advantage of potentially placing both the mechanical device and electronic supporting circuits on the same substrate. [97]

There are disadvantages to using silicon as the substrate for oxide film deposition, however. Silicon may be incompatible with respect to mechanical, chemical, and electrical properties. The mismatch between Si and desired electrical properties emerges when the top-and-bottom electrode layout is required for the MEMS design. Silicon is not sufficiently conductive to be utilized as a bottom electrode. For that reason, an intermediate bottom electrode needs to be deposited between the substrate and the functional film. The chemical incompatibility includes two aspects: surface nucleation and diffusivity. Because Si is relatively chemically different to perovskites, nucleation and growth of the first layer of the film may not be favored, and the target phase may be difficult to achieve. Diffusivity or chemical reactions between the elements of the film and Si may also occur. For example, sodium is known to be relatively soluble in Si, with high diffusion rates. [197]

The layers of platinized silicon

The need for a conductive layer underneath the functional layer is most easily obtained by depositing a metal bottom electrode. The selection of possible metals is heavily constrained by the chemical properties of the functional film. If considering solely perovskite films, it is natural that synthesis conditions must be sufficiently oxidizing to maintain oxides as the stable oxidation state of the cations. For PZT, for example, lead limits the selection of bottom electrodes, because it is relatively noble. The electrode material must be more noble than Pb in order to stay metallic during synthesis. Considering both the standard electrode potentials, as well other possible deteriorating reactions, platinum is an obvious candidate, despite its high cost. [198]

It is clear from the large amount of high quality films reported in literature that perovskites easily crystallize at SiPt substrates. In other words, Pt is highly chemically compatible with perovskites when it comes to nucleation of the film. When Pt is deposited to the Si|TiO_x stack, the (111) plane is thermodynamically preferred. The Pt film is not single

crystal, it consists of many grains, but all grains are highly textured, giving a mosaic microstructure with random orientation only as rotation around the direction perpendicular to the substrate. This texture has a large consequence in XRD measurements of thin film samples. [161] Because of the orientation, all Pt grains will contribute to the reflected signal when the XRD is operated in traditional Bragg-Brentano setup, and the (111) reflection of Pt at 40° 2θ is orders of magnitude stronger than the film reflections. For grazing incidence setup, however, Pt reflections are dependent on fulfilment of the Bragg criterion by applying the correct incidence angle.

Platinum does not adhere well to silicon, and for that reason a titanium layer is placed between Si and Pt. [199] This layer is subject to oxidation due to grain boundary diffusion of oxygen through the Pt layer. To obtain a more chemically stable substrate, Ti is pre-oxidized in advance of depositing the perovskite. [199] During heat treatment, Ti diffuses through Pt to form TiO_2 nucleation locations for the perovskite film. The most common diffusion protection layer is often included in the term *platinized silicon*. [12] A layer of SiO_2 is commonly grown on the Si substrate, yielding a final stack consisting of ~500 µm Si, ~1 µm SiO_2, ~20 nm TiO_x, and ~40 nm Pt. [12]

Thermal expansion mismatch

Mechanical incompatibility of film and Si substrates can arise due to difference in thermal expansion coefficients. The thermal expansion coefficient of Si, α_{Si}, is well known, and at room temperature it is 2.58×10^{-6} K^{-1}. [200] For most perovskites, however, thermal expansion is greater. BNT, PZT, and ST all have thermal expansion coefficients of approximately 9×10^{-6} K^{-1}. [56, 57, 201] This gives a thermal expansion mismatch of approximately 6.4×10^{-6} K^{-1} as a general rule for perovskites deposited on silicon substrates. Phase transitions, polarization, or other effects may enhance the mismatch further, or remedy some of it. For example, KNN has been shown to develop texture as a result of thermal expansion mismatch during cooling, as a means of relieving some of the thermal stress developed. [202]

Strain can also arise due to epitaxy coupled with different unit cell parameters. Epitaxial strain is typically reduced by lattice defects as the distance from the interface increases, however. [203] A general rule of thumb is that epitaxial strain is only significant for the first ~50 nm in a film, meaning that the force exerted by the film on the interface is not increasing further with increasing film thickness. In the case of epitaxial growth of BNT on (111) oriented Pt, one should consider the mismatch of lattice parameters. Pt is fcc, with lattice parameter a = 3.92 Å [204], which corresponds to Pt-Pt distance of 2.77 Å in a hexagonal fashion at the surface. Bi/Na-Bi/Na distance in the $(111)_{pc}$ plane of BNT varies from 5.49 to 5.51 Å, while O-O distances are 2.75-2.79 Å. [42] Due to the small lattice mismatch of BNT and ST/SiPt, epitaxial strain is expected to be minor.

The most relevant thermal expansion mismatch stresses occur during cooling. As a general rule, the thin film is crystallized at an elevated temperature, and diffusion processes relax the system during holding yielding a zero-strain state. During cooling, thermal expansion causes the film to contract more than the silicon substrate. Naturally, the ideal is that the film is bonded tightly to the substrate, and assuming that the substrate is significantly thicker than the film, the exact contraction of the substrate will be forced onto the film. Thus, at room temperature, the substrate will in practice be unstrained and unstressed, while the film

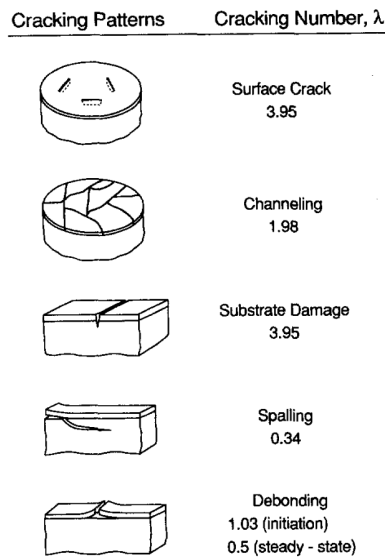

Figure 2.30 Different failure mechanisms in bonded ceramics. Reprinted with permission from Elsevier [206].

will experience a tensile strain corresponding to the thermal expansion mismatch. For cooling from 550 to 25 °C, for example, the strain in the film is 6.4×10^{-6} $K^{-1}\times525$ K = 0.336 %. The corresponding *bilateral misfit stress* of a thin film on an infinitely thick substrate is given by [205, 206]

$$\sigma = \frac{\left(\alpha_f - \alpha_s\right)\left(T_0 - T\right)E_f}{1-\nu_f} \tag{2.24}$$

where α_f and α_s are the thermal expansion coefficients of film and substrate, respectively. T_0 is the initial temperature, T is the current temperature, E_f is the Young's modulus and ν_f is the Poisson ratio.

The strain experienced by the *film* is governed exclusively by the thermal expansion of the *substrate*. As long as the thickness and stiffness of the substrate is sufficiently large, the substrate will not be influenced by the film. Away from the edges, the stress experienced in the film is independent on film thickness. Thus, increasing film thickness will lead to proportionally increasing amount of stored elastic energy in the film. This can lead to a selection of different failure mechanisms as seen in Figure 2.30. Common for all mechanisms is that they express a steady-state energy release rate during propagation. The criterion for crack propagation is then related to the interfacial fracture energy of the relevant interface. Since the stored energy increases with film thickness, there is a critical thickness, h_c, above which cracking of debonding is favored, given by

$$\frac{E\Gamma}{\left(1-\nu^2\right)h_c\sigma^2} = \lambda \tag{2.25}$$

where σ is the in-plane strain, Γ is the interfacial fracture energy, and λ is the dimensionless *cracking number* given in Figure 2.30. For debonding, the critical thickness of the film is given by

$$h_c = \frac{\Gamma E_f}{0.5(1-\nu_f)\left(\frac{(\alpha_f-\alpha_s)(T_0-T)E_f}{1-\nu_f}\right)^2} = \frac{2(1-\nu_f)\Gamma}{E_f \Delta\alpha^2 \Delta T^2} \tag{2.26}$$

for the steady-state propagation.

The main challenge of employing the theory of film failure is obtaining accurate values for the material specific parameters. For BNT, fundamental material properties, such as the Young's modulus, are lacking or varying significantly. For example, BNT-6Ba has reported values varying from 57.8 GPa at RT to 37 GPa at 150 °C. In the same work, however, the corresponding values for BNT-6Ba-1K-2Nb are 57.1 and 53.3 GPa, respectively. [207] For comparison, the Young's modulus of PZT has been reported to be 36 GPa [207], and for Si it is approximately 180 GPa. [208] The Poisson ratios of Si and BNT are 0.27 and 0.25, respectively. [34, 209] The most difficultly obtained parameters, however, are those of interfacial fracture energy for the different interfaces of potential crack propagation. For the interface of TiO_x-Pt in the SiPt stack, it is suggested to be as high as 12.36 J/m^2. [210] Applying the values to the case of debonding yields an optimistic critical BNT thickness of

$$h_c = \frac{2\cdot(1-0.25)\cdot 12.36\,\mathrm{N/m}}{57\,\mathrm{GPa}\cdot\left(6.4\times10^{-6}\,\mathrm{K^{-1}}\right)^2\cdot(525\,\mathrm{K})^2} = 28.8\,\mu\mathrm{m} \tag{2.27}$$

Summary of results

Chapter 3

This chapter contains a summary of the main findings of the thesis. The primary focus of this work was to establish an aqueous chemical solution deposition route to BNT thin films. Water-based fabrication of BNT thin films has not been previously reported in the literature, and a novel aqueous BNT chemical solution deposition method was developed for the first time. The chapter is divided in two parts. First, the chemical solution deposition method and the properties of the prepared BNT thin films are summarized. Finally, a selection of critical aspects related to the processing development is presented. The presentation of the work in this chapter do not follow the order of Chapters 4-7, and the page numbers of the original figures will be provided in each figure caption for reference.

3.1 The aqueous chemical solution deposition method

3.1.1 The aqueous sol system

The first part of the work was to develop an aqueous sol system for deposition of BNT thin films by chemical solution deposition. The sol was based on the citrate method known from literature, as discussed briefly in Chapter 2.4.1.

An illustration of the preparation procedure of the sol including the relative precursor concentrations is provided in Figure 3.1. Distilled water was used as the solvent for all individual cation precursor solutions, and the final sols were obtained by simply mixing stoichiometric amounts of the solutions containing the individual cations. The principle BNT sol was based on the combination of NaOH, Bi citrate stabilized by ethanolamine, and Ti isopropoxide stabilized by citric acid (CA). An ammonia solution was finally added to the sol to adjust the pH to neutral. The undoped BNT sols could be prepared as concentrated as 0.6 M relative to the perovskite unit, and the sols were still stable for at least two years without any constraints on the storage conditions.

Additional cation precursors were further introduced to the principle BNT sol to prepare compositionally engineered BNT. An overview of the BNT compositions prepared in the work and their abbreviations are summarized in Table 3.1. These compositions were selected based on compositions frequently reported for bulk BNT-based materials. The two compositions BNT and 6Ba were prepared for reference, while 6Ba-1K-2Nb, 4Ba-6K-6Li, and 8K-4Sr-2Li-2Nb bulk materials are reported to be so-called incipient BNT materials with an associated large and temperature stable strain response (Chapter 2.3.2). [9, 10, 15]

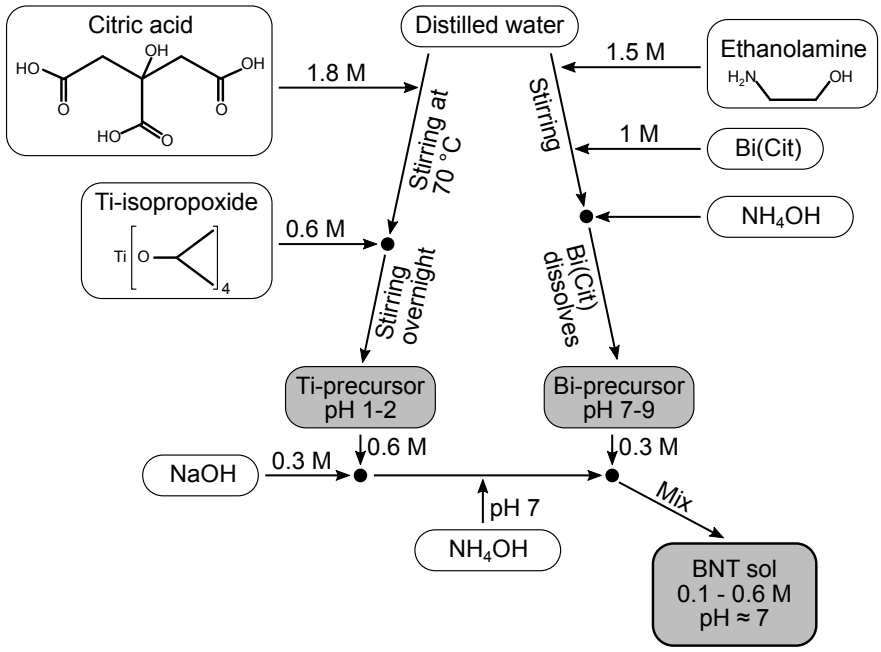

Figure 3.1 Flow chart of the BNT sol preparation procedure. (Figure 4.1, p. 83)

Table 3.1 Overview of the prepared BNT compositions.

Sample notation	Nominal composition
BNT	$Bi_{0.5}Na_{0.5}TiO_3$
6Ba	$Bi_{0.47}Na_{0.47}Ba_{0.06}TiO_3$
6Ba-1K-2Nb	$Bi_{0.46}Na_{0.47}Ba_{0.06}K_{0.01}Ti_{0.98}Nb_{0.02}O_3$
4Ba-6K-6Li	$Bi_{0.48}Na_{0.36}Ba_{0.04}K_{0.06}Li_{0.06}TiO_3$
8K-4Sr-2Li-2Nb	$Bi_{0.47}Na_{0.39}Sr_{0.04}K_{0.08}Li_{0.02}Ti_{0.98}Nb_{0.02}O_3$

The BNT sols with the complex chemical compositions (Table 3.1) were prepared from the same principle sol system as for undoped BNT, with additional introduction of other cation precursor solutions. Hydroxide solutions were used for Li and K, Ba and Sr were added as nitrates and stabilized by EDTA and CA (nitrate:EDTA:CA was 1:1:2), and ammonium niobate oxalate ($NH_4NbO(C_2O_4)_2$) was used as the Nb precursor. The sols obtained were long-term stable up to a concentration of 0.3 M without any sign of aging or deterioration after several months.

Compared to non-aqueous CSD methods, where complex fabrication routines such as refluxing or precipitation and re-dissolution are required, the aqueous CSD route was shown to requires only simple preparation steps. The chemicals employed were non-hazardous, environmentally friendly, and cheap.

3.1.2 Preparation of BNT powders

Powder samples were prepared from the sols in order to better characterize the overall gelation, gel decomposition, and crystallization processes. The powders were also used to confirm that the cation stoichiometry of the sols resulted in single phase materials. The sols were dried at 120 °C for 48 h to obtain gels, followed by calcination in air at either 550 or 800 °C for 2 h. X-ray diffraction (XRD) patterns of the gels and the crystalline BNT powders are provided in Figure 3.2. The dried gels were amorphous according to XRD, showing that the drying process occurred without segregation of the cations by precipitation of crystalline phases. The sols were prepared with either 10 % Na excess or 5 % Na and 5 % Bi (Na+Bi) excess, and XRD demonstrated formation of phase pure BNT already after calcination at 550 °C (colored graphs in Figure 3.2a).[1] A minor amount of a pyrochlore secondary phase was only observed for 4Ba-6K-6Li with Na+Bi excess (reflection at 30°, Figure 3.2a). The black diffractograms in Figure 3.2 are for powders calcined at 800 °C. All compositions were phase pure after calcination at 800 °C, and the Bragg reflections were considerably narrower due to the larger crystallite sizes.

Magnified XRD patterns of the powders calcined at 800 °C are provided in Figure 3.2 b and c. It can be seen in Figure 3.2b that the chemical modifications led to shifts in the

[1] The primary method for assessment of phase content throughout this work was that of XRD. It is noted that this method has limitations in the case of amorphous or nanocrystalline grains of secondary phases.

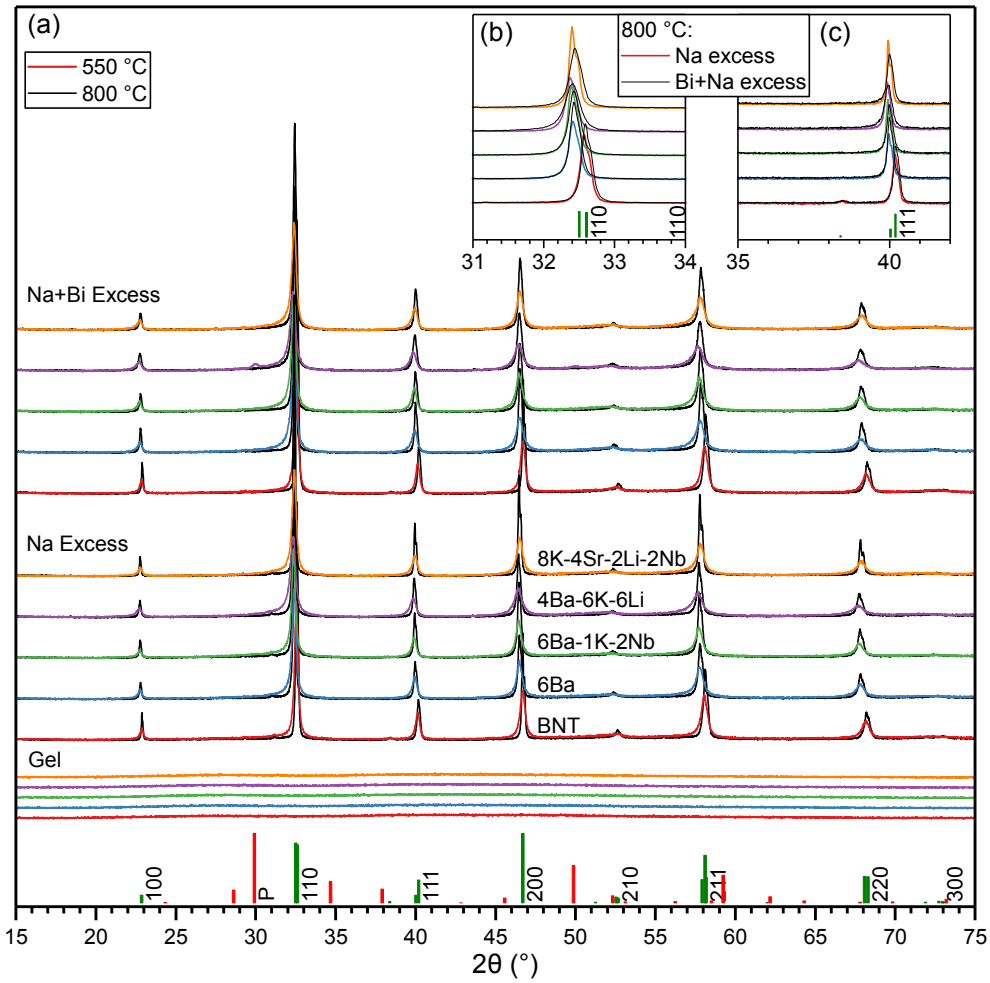

Figure 3.2 (a) XRD patterns of doped BNT powders prepared by calcination at 550 or 800 °C for 2 h in air. (b) $(110)_{pc}$ (pseudocubic Miller index) reflection of powders calcined at 800 °C. (c) $(111)_{pc}$ reflection and rhombohedral super-reflection at 38.5° (only observed for undoped BNT). Reference patterns are pyrochlore [211] and R3c BNT labeled with pseudocubic Miller indices [42]. (Figure 6.2, p. 132)

reflections due to an enlarged unit cell. Furthermore, the reflections of samples with Na excess were sharper with more pronounced splitting, demonstrating that the crystallite size of samples with Na excess were larger than for samples with Na+Bi excess. Figure 3.2c facilitates the observation of the rhombohedral super-reflection at ~38.5°, which was only observed for undoped BNT. This is in accordance with reports from the literature, as these compositions were selected for their increased properties originating from the morphotropic phase boundary (MPB). [9, 10, 15] MPB/relaxor compositions are cubic on average, rendering this reflection prohibited. [58]

Thermogravimetric analysis (TGA) and differential scanning calorimetry (DSC) during heating of the undoped BNT gel are provided in Figure 3.3. The weight loss is initiated at approximately 200 °C with an endothermic signature. The mass loss was relatively constant

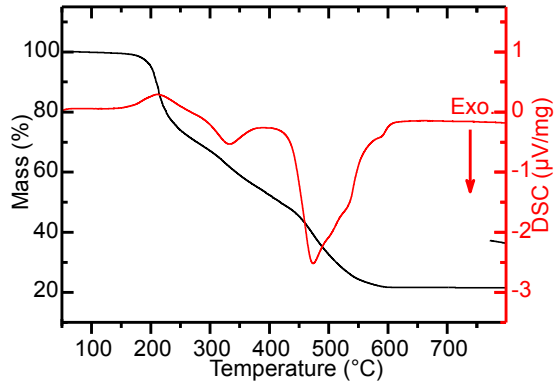

Figure 3.3 TGA and DSC of the dried BNT gel during heating. Mass loss is provided by the black curve, and DSC by the red. The experiment was conducted in synthetic air, and the heating rate was 10 °C/min. (Figure 4.5a, p. 90)

upon further heating, but two regions with exothermic character were apparent at ~300 and ~450 °C. The latter consisted of several overlapping events visible by the peak shoulders. The mass loss was completed at ~550 °C, and mass spectroscopy of the exhaust gas demonstrated signal from H_2O and CO_2. This temperature was selected as the reference temperature for pyrolysis of thin films and calcination of powders throughout this work since the mass loss had completed and the perovskite had formed at 550 °C. In general, maintaining low processing temperatures is desirable due to possible constraints in later implementation in fabrication of complex devices.

3.1.3 Phase purity of BNT thin films

Phase purity of undoped BNT thin films

Thin films of undoped BNT were deposited on single crystal $SrTiO_3$ (ST) and platinized silicon (SiPt) substrates by spin coating of the aqueous sols at 3500 rpm for 30 s. The films were dried on a hot plate at 110 °C and pyrolized at 400-550 °C for 5 min by rapid thermal processing (RTP). Deposition and pyrolysis were repeated for deposition of 5 layers before some films were further annealed in the temperature range 700-900 °C for 10 min. The effect of the pyrolysis temperature on the phase purity of the undoped BNT thin films is presented by grazing incidence XRD (GIXRD) in Figure 3.4. The crystallization of the BNT perovskite phase was significant already in the as-pyrolized films at 500 °C. The film pyrolized at 550 °C on ST (Figure 3.4a) was phase pure after the pyrolysis. Phase pure films on SiPt (Figure 3.4b) were achieved by pyrolysis at 550 °C followed by final annealing at 700 °C.

The key factor to obtain phase pure BNT thin films was a sufficiently high pyrolysis temperature, as the films pyrolized at 400 °C did not turn phase pure even after annealing at 900 °C. The secondary phase most commonly observed matched the diffraction pattern of the pyrochlore phase $Na_{0.32}Bi_{1.68}Ti_2O_{6.46}(OH)_{0.44}$. [211] The films deposited on SiPt substrates had a slightly higher content of this pyrochlore phase relative to the films deposited on ST.

BNT thin films prepared from sols with 10 % Na excess were prepared in the same manner, and the GIXRD patterns are displayed in Figure 3.4 c and d. The Na excess in the

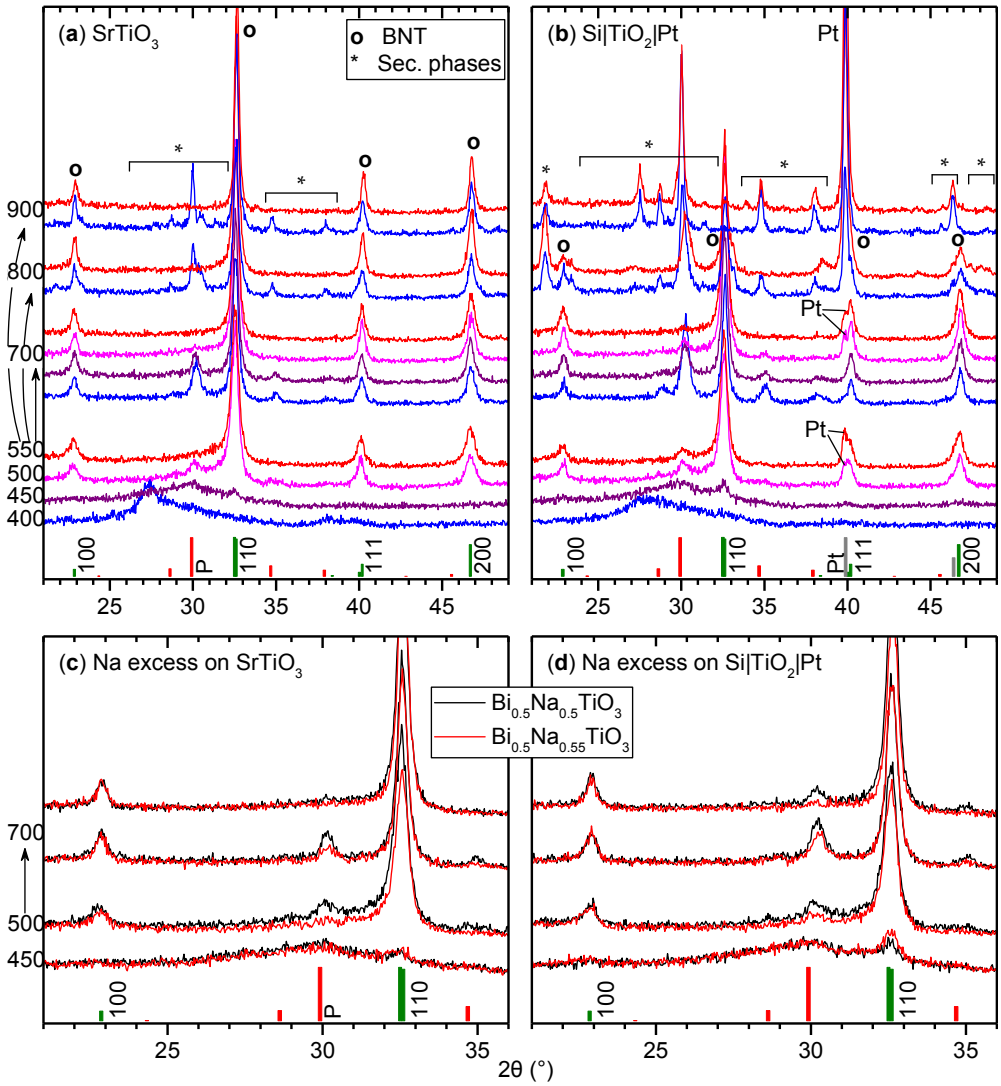

Figure 3.4 GIXRD patterns of BNT thin films deposited on ST (a) and SiPt (b). (c, d) Comparison of nominal stoichiometric and films made from sols with 10 % Na excess. Heat treatment temperatures are denoted to the left. Arrows give the pyrolysis temperature and then the final annealing temperature. (Figure 4.2, p. 87)

sols had a clear positive effect on the phase purity resulting in lower content of the pyrochlore after all heat treatments used. Phase pure BNT was obtained by pyrolysis at 500 °C in these films.

Phase purity of BNT-Ba thin films

BNT thin films doped with 0-9 % Ba were prepared using the same procedure as for undoped BNT films (5 layers pyrolized at 550 °C for 5 min, no Na excess). GIXRD patterns of the BNT-Ba thin films are shown in Figure 3.5. It can be seen that the addition of Ba resulted in an increased amount of the pyrochlore phase. Phase pure BNT-Ba films could still be obtained

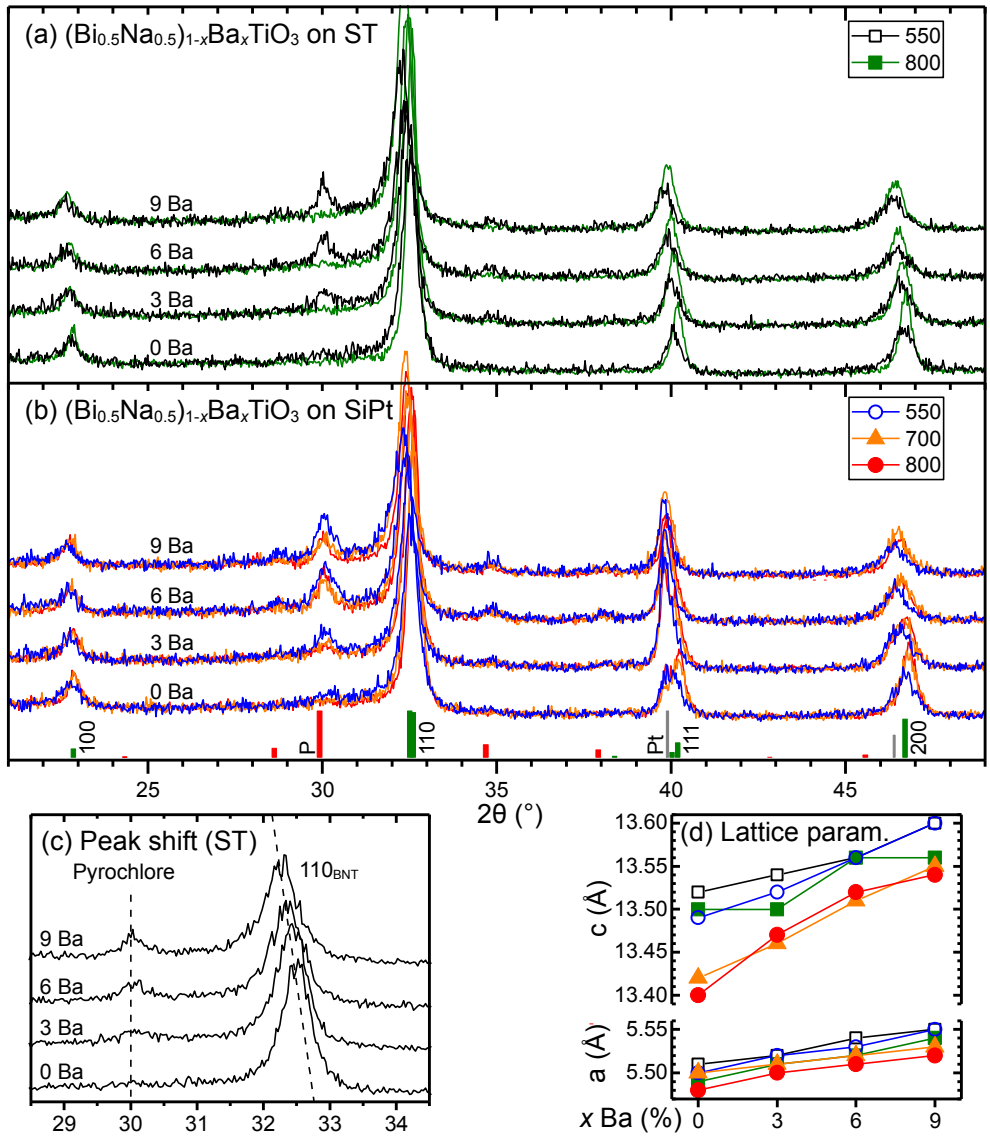

Figure 3.5 GIXRD patterns of BNT thin films with 0 to 9 % Ba doping deposited on ST (a) and SiPt (b). Films consisted of 5 layers and were pyrolized at 550 °C and annealed at 700 or 800 °C. (c) Magnified 2θ range of as-pyrolized samples on ST. (d) *a* and *c* rhombohedral lattice parameters determined by Rietveld refinement using the R3c space group. (Figure 5.3, p. 108)

by further thermal treatment, and the pyrochlore was entirely removed by final annealing at 800 °C for the films deposited on ST. The films deposited on SiPt contained a small remaining amount of pyrochlore after the corresponding thermal annealing.

A magnified 2θ range enhancing the $(110)_{pc}$ (pseudocubic) BNT reflection and the main pyrochlore reflections in the as-pyrolized films on ST are given in Figure 3.5c. The BNT reflection was shifted to smaller 2θ angles with increasing Ba content, demonstrating that Ba was incorporated in the perovskite phase resulting in an increase in the unit cell volume. The

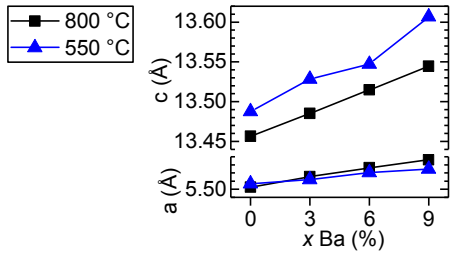

Figure 3.6 Lattice parameters of BNT-Ba powders as a function of Ba content obtained by Rietveld refinement using the R3c space group. The powders were calcined at 550 or 800 °C. The refinements were based on the XRD patterns shown in the original figure (Figure 5.4, p. 109).

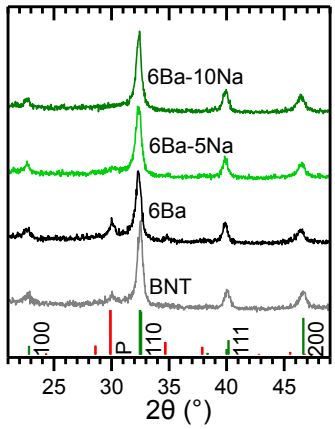

Figure 3.7 GIXRD patterns of 5-layer BNT thin films on ST with varying Na excess content. 6Ba-5Na refers to $Bi_{0.47}Na_{0.52}Ba_{0.06}TiO_3$ (approximately 10 % excess). (Figure 6.5b, p. 135)

corresponding lattice parameters obtained by Rietveld refinement of the diffraction patterns are presented in Figure 3.5d. The lattice parameters increased with increasing Ba content for all batches of the BNT-Ba thin films. Powder samples were prepared from the same BNT-Ba sols (XRD not shown), and the corresponding refined lattice parameters are shown in Figure 3.6. To the best of our knowledge, the systematic study of unit cell expansion due to Ba doping in BNT has not been previously reported. Increasing the Ba content from 0 to 9 % caused a linear increase in the *a* and *c* parameters of 0.034 Å (0.61 %) and 0.088 Å (0.65 %), respectively.

BNT thin films with 6 % Ba doping prepared from sols with Na excess yielded phase pure thin films shown by GIXRD patterns in Figure 3.7. The Na excess efficiently suppressed the pyrochlore secondary phase, resulting in phase pure as-pyrolized 6Ba films without using the high-temperature annealing necessary without Na-excess in the sol.

Phase purity of compositionally engineered BNT thin films

With the successful fabrication of the BNT-Ba thin films, preparation of BNT with further chemical modifications was carried out. The reference compositions of BNT and 6Ba as well as the incipient compositions 6Ba-1K-2Nb, 4Ba-6K-6Li, and 8K-4Sr-2Li-2Nb were prepared in thin-film form (Table 3.1). The thin films were prepared with Na excess according to

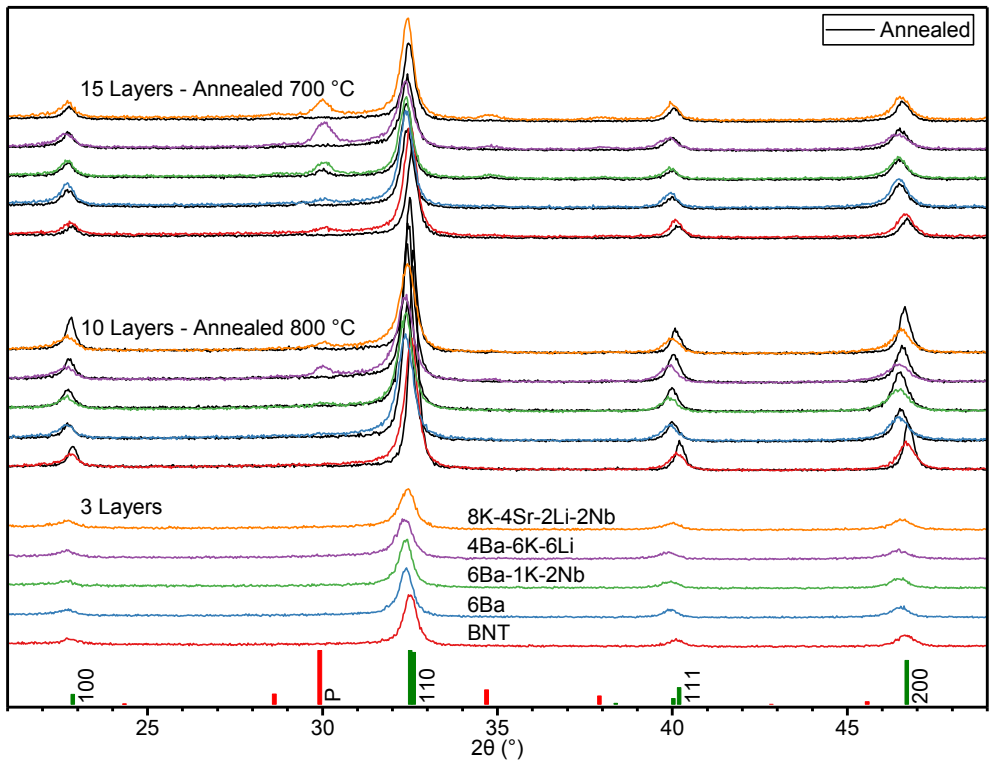

Figure 3.8 GIXRD patterns of compositionally engineered BNT thin films of different number of layers and annealing temperature. The colored graphs correspond to as-pyrolized films (550 °C for 5 min each layer), while black graphs are the corresponding annealed films (700 or 800 °C for 10 min). (Figure 6.4, p. 134)

$A_{1.05}BO_3$ nominal stoichiometry (termed 5Na in Figure 3.7), due to the beneficial effect demonstrated for undoped BNT and 6Ba. GIXRD patterns of the compositionally engineered BNT thin films are given in Figure 3.8. Three individual batches with different number of deposited layers are included in the figure. Colored and black patterns correspond to as-pyrolized and annealed films, respectively. The as-pyrolized films consisting of three layers were phase pure. Phase pure BNT was only achieved after additional annealing at 700-800 °C with increasing the number of layers. A small amount of secondary phases were observed in 6Ba and 6Ba-1K-2Nb after annealing the thin films with 15 layers at 700 °C.

3.1.4 Microstructure of BNT thin films

The deposition process of the BNT thin films was optimized, obtaining homogeneous, dense, and defect free BNT thin films on both ST and SiPt substrates. BNT films on SiPt were successfully deposited by ramping at 40 °C/s, while high quality BNT thin films were obtained on ST by ramping at 100 °C/min to 450 °C and by 40 °C/s to 550 °C. Scanning electron microscope (SEM) images of the undoped BNT thin films deposited by the optimized deposition process on ST are presented in Figure 3.9. The high density and homogeneity already in the as-pyrolized thin films were confirmed. In the SEM images, the as-pyrolized

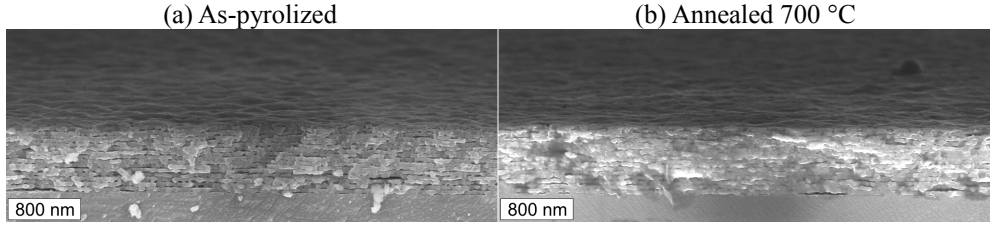

Figure 3.9 SEM images of BNT thin films with 15 depositions on Nb doped ST. (Figure 6.6a, p. 136)

thin film appeared relatively dense, while the film annealed at 700 °C appeared near 100 % dense. The thickness was approximately 780 nm after annealing, corresponding to 52 nm per deposited layer.

3.1.5 Ferroelectric properties

Thin films of the compositionally engineered BNT (Table 3.1) were prepared on Nb doped ST, and Au top electrodes were deposited for measurement of the ferroelectric properties. The films were prepared by deposition of 15 layers by the optimized pyrolysis ramp and finally annealed at 700 °C. Polarization-field hysteresis loops are shown in Figure 3.10a, demonstrating ferroelectric properties of the films comparable to state of the art BNT thin films prepared by alternative methods. [13, 143, 168] Only minimal contributions from leakage currents were observed even when cycling to fields as strong as 700 kV/cm at 500 Hz. Further cycling to 1500 kV/cm yielded well defined hysteresis loops without dielectric breakdown (shown in Chapter 6).

Leakage current measurements during stepwise increase of constant voltage are provided in Figure 3.10b. The leakage current values are on par with state of the art BNT thin films prepared by alternative methods. Often, leakage characteristics are not reported for equally strong fields. [164] Regardless, a potential for further improvement is apparent in the present thin films. The leakage current with positive bias to the top electrode was consistently orders of magnitude larger than for negative bias. Considering that known measures to decrease the conductivity in BNT, such as donor doping [47] and Mn doping [26, 156, 164, 169, 178, 179, 212-215] were not applied here, render these BNT thin films promising for further optimization.

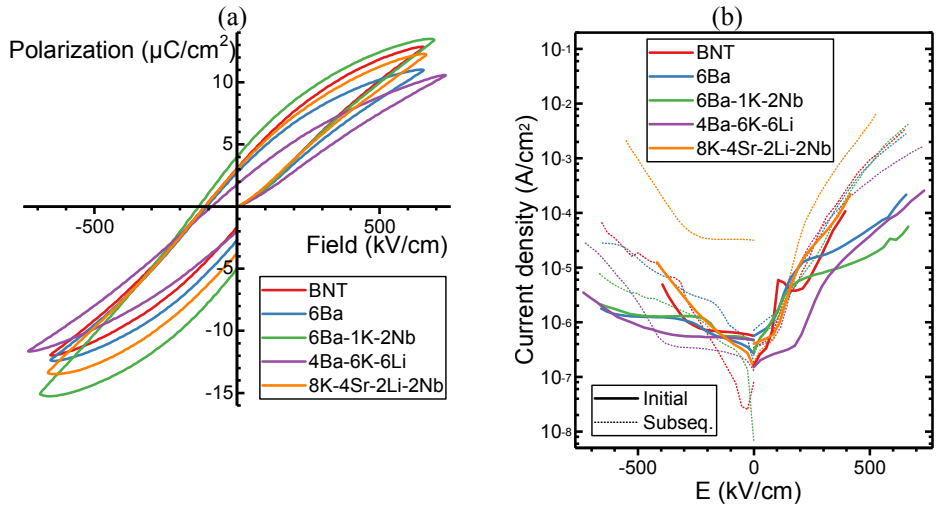

Figure 3.10 (a) Polarization-field hysteresis loops for compositionally engineered BNT thin films with 500 Hz linear cycling to 50 V. The thin films were 680-780 nm thick. (b) Initial and subsequent leakage current of the same samples measured repeatedly. Stepwise voltage increase, measuring during 1.4-1.8 s of each two-second step. (Figure 6.8f, p. 139, Figure 6.9a, p. 140)

3.2 Processing development

It was demonstrated in Section 3.1 that the aqueous CSD method developed in this work results in dense, homogeneous, and phase pure BNT thin films. BNT materials with several different chemical modifications could also be synthesized by this synthesis platform. Optimization of the thermal processing of the thin films were necessary in order to obtain phase pure BNT. Moreover, the microstructures of the thin films were also strongly influenced by the processing conditions. The key challenges in the optimization of the processes are highlighted in this chapter.

3.2.1 Reduction of Bi during decomposition

The decomposition of the inorganic-organic gels during pyrolysis was thoroughly investigated, and in the following it will be argued that transient reduction of Bi^{3+} to metallic Bi during pyrolysis was the origin of the formation of the pyrochlore secondary phase observed in thin films pyrolized at too low temperatures (Figure 3.4). In the following, results from both powders and thin films are used to explain the mechanisms relevant to phase purity of thin films.

XRD patterns of undoped BNT powders calcined in air at different temperatures are shown in Figure 3.11. The powders calcined at 300-400 °C were black, and the broad XRD reflections after calcination at 350-400 °C confirmed the presence of metallic Bi.

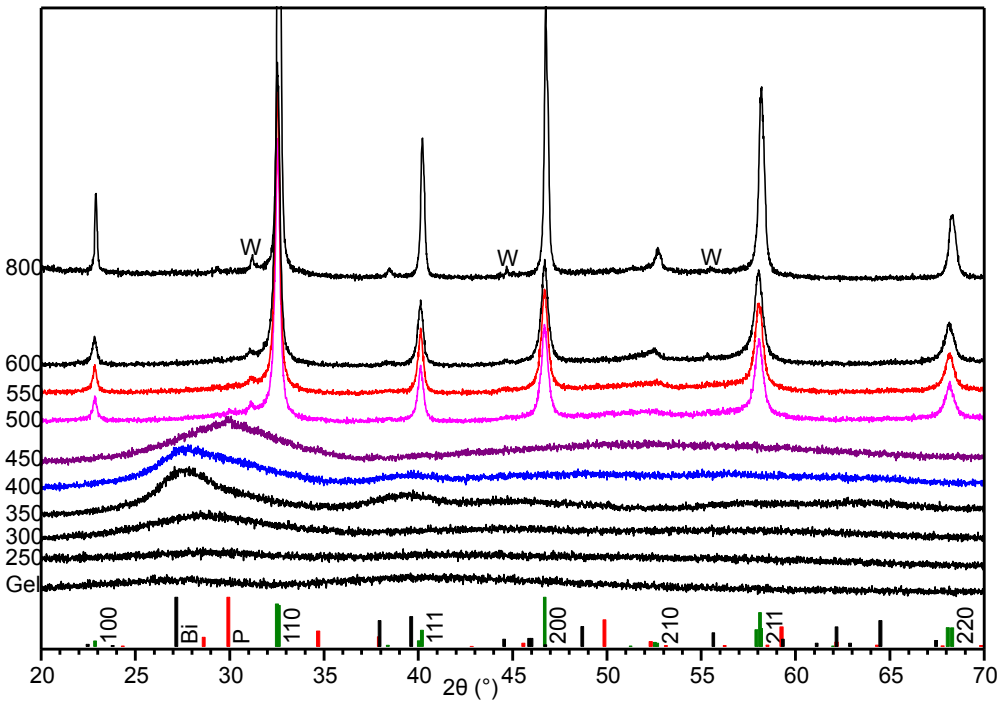

Figure 3.11 XRD patterns of BNT powders calcined for 2 h in ambient atmosphere. Reflections denoted by W were caused by tungsten Lα1 radiation from the instrument. Reference patterns are provided for BNT, pyrochlore, and metallic Bi. (Figure 4.4a, p. 89)

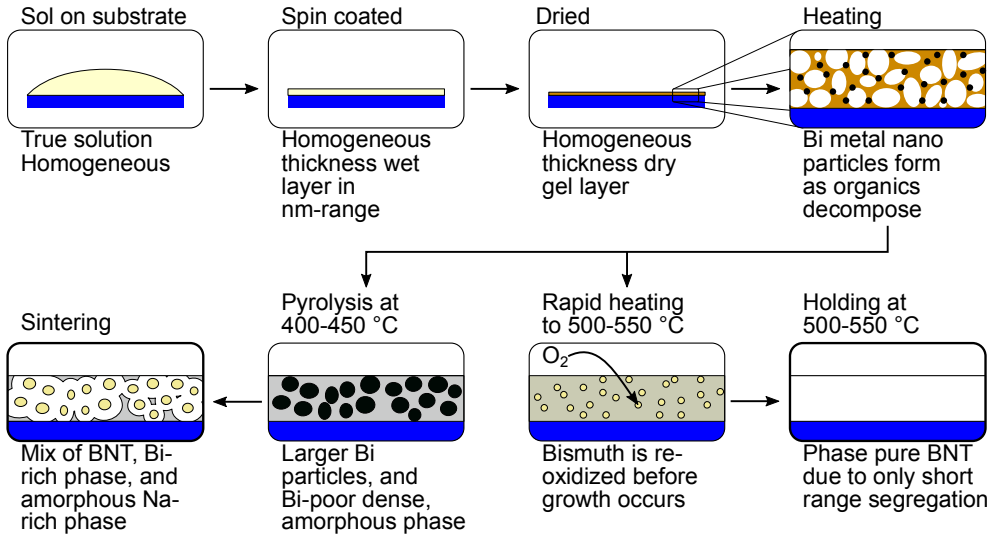

Figure 3.12 A schematic of the decomposition process of the thin films. The substrate is blue, pores and BNT are white, gel is brown, Bi rich secondary phase is yellow, and an amorphous Na/Ti rich secondary phase is drawn grey. (Figure 4.8, p. 93)

Furthermore, BNT thin films pyrolized in O_2 at 400 °C contained black areas and demonstrated characteristic GIXRD reflections of Bi at 27° and 38-40° 2θ in Figure 3.4. The observations of metallic Bi in both powders and thin films demonstrate that neither long holding time nor reducing the size of the sample to maximize the possibility for oxidation of Bi were sufficient to avoid transient reduction of Bi. Therefore, it is concluded that it was the decomposition of the organic part of the gel that caused the Bi reduction, and despite several efforts, reduction of Bi could not be circumvented.

Due to the inevitable formation of transient metallic Bi, the key to obtain phase pure perovskite BNT powders and thin films was to avoid prolonged heat treatment at temperatures where Bi remained metallic. An illustration of the proposed thermal decomposition process from gel to BNT is provided in Figure 3.12. Pyrolysis at sufficiently high temperatures caused rapid re-oxidation of the Bi droplets, yielding only small Bi_2O_3 particles which reacted further to form the perovskite during the isothermal heat treatment. Metallic Bi is liquid above 271 °C [216], leading to substantial segregation of Bi by Ostwald ripening with prolonged heat treatment at too low temperature. With subsequent annealing and Bi re-oxidation, regions of Bi-rich pyrochlore and corresponding regions of Ti/Na rich amorphous phase (undetected by XRD) resulted. Only at the interface between these regions was the perovskite obtained. These films could not be transformed to phase pure BNT films by subsequent annealing up to 900 °C (Figure 3.4) due to the severe cation segregation.

3.2.2 Pyrochlore and sodium excess

The recurring secondary phase observed in certain samples could consistently be identified by the same characteristic Bragg reflections. The thin films with the largest presence of this phase were used for phase identification, and the diffraction patterns matched the pattern

reported for the pyrochlore $Na_{0.32}Bi_{1.68}Ti_2O_{6.46}(OH)_{0.44}$. [211] An example of the characteristic pyrochlore pattern is provided by the thin film deposited on SiPt pyrolized at 400 °C and annealed at 700-800 °C in Figure 3.4b. Reflections at the same 2θ angles from Bi-rich secondary phases are often reported for BNT in literature. [13, 47, 56, 144, 155, 187, 188] As shown in the previous chapter it was repeatedly demonstrated that Na excess efficiently suppressed the formation of the pyrochlore phase (Figure 3.4 and Figure 3.7).

In PZT, a related pyrochlore phase ($Pb_2Ti_2O_6$) is poor in Pb relative to the Pb:Zr:Ti ratio in PZT of 2:1:1. For this reason, pyrochlore formation can occur due to loss of Pb. [11, 217] Drawing parallels to the PZT system, one might falsely assume that Bi loss will cause pyrochlore formation in BNT. In fact, the opposite is true, as the Bi:Na:Ti ratio in BNT is 1:1:2, and the pyrochlore phase observed in the present work is relatively rich in Bi. The pyrochlore observed in BNT in this work was as a result of Bi excess or Na loss. Addition of Na-excess to the sol therefore suppressed the formation of the pyrochlore phase.

3.2.3 Phase purity in compositionally engineered BNT

Introduction of the chemical modifications to the BNT thin films led to an increase in the amount of the pyrochlore secondary phase. Unlike for the undoped thin films pyrolized at insufficient temperatures, however, metallic Bi did not remain at the end of each pyrolysis step, and the time scale of the Ostwald ripening of Bi droplets was therefore less. In the compositionally engineered thin films, phase purity could be obtained by annealing, inferring that Bi poor and rich region had not segregated to the detrimental extent as discussed in Section 3.2.1 (Figure 3.8).

It is proposed that the reason for increased pyrochlore due to the introduction of dopants was a slight decrease in the perovskite stability, resulting in marginally suppressed BNT formation. Starting from the amorphous oxide after gel decomposition either BNT, pyrochlore, or both will form. A suppression or delay in the formation of BNT, either due to increased Gibbs energy of formation of the perovskite or due to kinetic effects, would therefore yield relatively more pyrochlore.

3.2.4 Bi-Pt reaction and delamination

SiPt substrates are widely employed and important for large scale production of devices. Compatibility of BNT and SiPt is therefore of great interest. It was found here, however, that morphological defects such as cracking and delamination of the BNT thin films were observed when BNT was deposited directly on the Pt bottom electrode. Optical microscope images comparing the morphology of BNT thin films deposited on SiPt and on SiPt protected by a coating of $BaTiO_3$ (BT) are shown in Figure 3.13. These images were captured in dark field mode (illumination from outside the lens), causing perfectly flat surfaces to appear dark and without contrast. The low contrast and lack of features in the images of BNT thin films deposited on the BT-protected SiPt are apparent. Thus, the cause of the defects in the BNT thin films deposited on unprotected SiPt was related to the direct physical contact between BNT and Pt. A $BaTiO_3$ protective coating was deposited by CSD on SiPt, employing the same precursors as for the BNT process. Further details on the BT preparation are provided in Chapter 7.

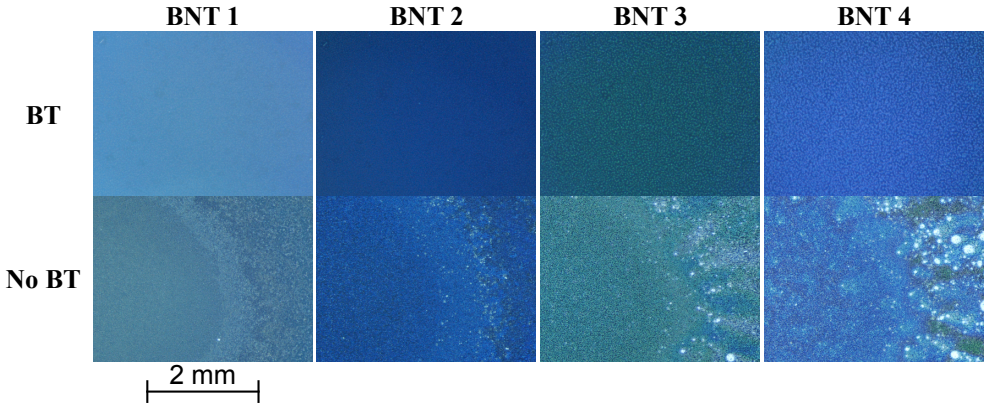

Figure 3.13 Optical microscope images of BNT thin films. Each column shows an additional deposited BNT layer on the same film. BT protected SiPt (top row) is compared to un-protected SiPt (bottom row). (Figure 7.9, p. 163)

The Bragg criterion for detection of the textured Pt electrode is not fulfilled for the pristine SiPt substrates in GIXRD (2° incidence angle). However, the appearance of the Pt reflection at ~40° 2θ in Figure 3.4 and Figure 3.5 demonstrates that Pt crystallites were reoriented during the BNT deposition. Considering that Bi and Pt are relatively reactive, forming several intermediate compounds and low melting temperature alloys [216], it is proposed that a weakening of the Pt electrode occurred due to a Bi-Pt reaction. This was likely related to or enhanced by the transient metallic state of Bi discussed in Section 3.2.1. The BT protective layer was introduced to spatially separated Pt and Bi from the BNT thin film, and its beneficial effect is clearly visible in Figure 3.13.

Introduction of the BT protective layer enabled deposition of defect free BNT thin films of 1-5 layers. However, delamination of mm-large flakes occurred at a certain critical number of BNT layers (depositions), depending on the preparation parameters of the BT layer. A delaminated portion of a film consisting of 20 BNT layers on SiPt protected by 3 BT layers is shown in Figure 3.14. The sections of Pt, BT, and BNT are clearly distinguishable both by the microstructure and by the overlaid energy dispersive X-ray spectroscopy (EDS) maps. It is apparent that the delamination occurred at the TiO_x-Pt interface of the SiPt substrate, supporting the hypothesis of a weakened Pt electrode due to the Bi-Pt contact.

In Chapter 2.7, the critical thickness for debonding of BNT thin films deposited on SiPt with respect to thermal expansion mismatch was estimated to be 28 µm. Because the thin film in Figure 3.14 delaminated at approximately 500 nm thickness (combined BT and BNT), some level of Bi diffusion through the BT layer is assumed, resulting in wakening of the Pt electrode. However, the beneficial effect of the BT layer was demonstrated, showing that BT has the potential as a protective layer for SiPt to circumvent the Bi-Pt reaction.

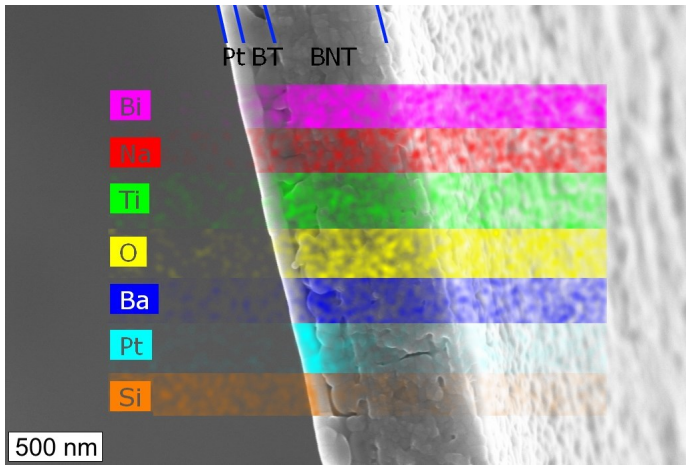

Figure 3.14 SEM image of delaminated BNT with EDS mapping overlay. Sample contained 3 layers of BT and 20 layers of BNT, and was annealed at 800 °C. The bleeding EDS signal from other sections of the film is due to fundamental limitations in EDS resolution. (Figure 7.4, p. 159)

3.2.5 Microstructure of BNT films on ST

To obtain defect free films on SiPt and ST substrates, optimization of the temperature-time program during pyrolysis was necessary. Two separate ramp rates were applied: 40 °C/s (fast) and 100 °C/min (slow). For SiPt substrates, homogeneous, dense, and defect free BNT thin films were obtained when applying the fast ramp rate from room temperature to the isotherm holding temperature of 550 °C. For ST substrates, however, the optimal film microstructures were obtained by applying the slow ramp from room temperature to 450 °C and the fast ramp from 450 to 550 °C.

When applying the fast ramp rate for BNT thin films on ST substrates, tears and inflated blisters related to gas release during organic decomposition resulted. Applying the slow ramp up to 450 °C provided a more gradual gas release, which enabled the preparation of homogeneous films. When applying the slow ramp in the interval 450-550 °C, however, the resulting microstructure was significantly porous. In Figure 3.4, the main XRD perovskite reflection is observed already after pyrolysis at 450 °C, and this temperature was selected for initiation of the fast ramp, in order to yield BNT crystallization at 550 °C rather than during the slow ramp. It can be seen by the microstructure of the film in Figure 3.9 that this hybrid ramp rate pyrolysis approach yielded defect free and dense BNT thin films on ST.

Fabrication of lead-free $Bi_{0.5}Na_{0.5}TiO_3$ thin films by aqueous chemical solution deposition

Paper 1

Mads Christensen[1], Mari-Ann Einarsrud[1] and Tor Grande [1,*]
[1] Department of Materials Science and Engineering, NTNU Norwegian University of Science and Technology, Trondheim NO-7491, Norway
mads.j.christensen@ntnu.no (M.C.); mari-ann.einarsrud@ntnu.no (M.-A.E.)
* Correspondence: tor.grande@ntnu.no; Tel.: +47-7359-4084
Academic Editor: Lorena Pardo
Received: 25 November 2016; Accepted: 16 February 2017; Published: 22 February 2017

Keywords: $Bi_{0.5}Na_{0.5}TiO_3$; bismuth sodium titanate; BNT; NBT; aqueous; sol-gel; chemical solution deposition (CSD); lead-free; thin-film; piezoelectric; phase purity

The following version of the article has been adjusted to fit the style of this thesis. Certain structural and minor/insignificant changes to content have been applied.
Original available at: *Materials* 2017, *10*, 213; doi: 10.3390/ma10020213
http://www.mdpi.com/1996-1944/10/2/213

Abstract

Piezoelectric ceramics are widely used in actuator applications, and currently the vast majority of these devices are based on $Pb(Zr,Ti)O_3$, which constitutes environmental and health hazards due to the toxicity of lead. One of the most promising lead-free material systems for actuators is $Bi_{0.5}Na_{0.5}TiO_3$ (BNT), and here we report on successful fabrication of BNT thin films by aqueous chemical solution deposition. The precursor solution used in the synthesis is based on bismuth citrate stabilized by ethanolamine, NaOH, and a Ti-citrate prepared from titanium tetraisopropoxide and citric acid. BNT thin films were deposited on $SrTiO_3$ and platinized silicon substrates by spin-coating, and the films were pyrolized and annealed by rapid thermal processing. The BNT perovskite phase was formed after calcination at 500 °C in air. The deposited thin films were single phase according to X-ray diffraction, and the microstructure of the films were shown by electron microscopy to be homogeneous and dense. Decomposition of the gel was thoroughly investigated, and the conditions resulting in phase pure materials were identified. This new aqueous deposition route is low cost, robust, and suitable for implementation of BNT in thin film actuator applications.

4.1 Introduction

Piezoelectric ceramics are widely used in actuator micro electro-mechanical systems (MEMS) such as fuel injection dies and precision positioning devices. The vast majority of these devices are based on $Pb(Zr,Ti)O_3$ (PZT) [32], which constitutes environmental and health hazards due to the toxicity of lead. [2] For this reason, considerable research efforts have focused on developing alternative lead-free piezoelectric materials. [4, 31, 218-220] One of the most promising lead-free materials for actuators is $Bi_{0.5}Na_{0.5}TiO_3$ (BNT), due to a large strain response originating from a reversible electric field induced relaxor to ferroelectric phase transition, observed at the morphotropic phase boundary at 6 mol% $BaTiO_3$ (BNT-6BT). [4, 55] The exact nature of the phase transitions in the BNT-BT system below T_C is still a matter of debate. A detailed review of the properties of BNT-based materials with regards to actuator applications has recently been published. [34]

Chemical solution deposition (CSD) is a low cost and versatile method to achieve high quality and homogeneous thin films with good stoichiometry control. [221] PZT and other oxide thin films are routinely prepared via CSD. [12] Precursor chemistries based on 2-methoxyethanol (2-MOE) or other organic solvents have achieved the role of a standard which other CSD methods are often compared to. [11, 97] Synthesis routes employing 2-MOE have been developed for, among others, PZT [97], $K_{1-x}Na_xNbO_3$ (KNN) [222], and $BaTiO_3$ (BT) [223], as well as for BNT [143-145, 148, 151-153]. However, 2-MOE and other organic solvents are both toxic and expensive, and aqueous thin film processing is therefore desirable.

Reports on aqueous chemical solution synthesis of BNT is scarce in the literature, and to our knowledge, aqueous thin film deposition has yet to be demonstrated. West et al. have reported to stabilize Ti and Na cations in solution by citric acid, while the chemistry of dissolving $Bi(OH)_3$ was not properly accounted for. [186] In this work it was assumed that stabilization of the Bi ions in the solution was related to a combined Bi-Na citrate complex. Furthermore, the stability of the sol, with a concentration of less than 0.2 M, was not reported. Xu et al. prepared a Ti-citrate solution from tetrabutyl titanate and citric acid, into which NH_4OH, $NaNO_3$, $Ba(NO_3)_2$, and $Bi(NO_3)_3 \cdot 5H_2O$ were added. [188-190, 224] A total citric acid to cation concentration ratio of 1.2-1.6 yielded a transparent homogeneous sol with pH 6, but the stability timeframe of the sol was not addressed. Aqueous synthesis of other related materials introduces different stabilization techniques for the constituent cations of BNT. $Bi_4Ti_3O_{12}$ has been synthesized from Bi-citrate by dissolving with NH_4OH and stabilizing with ethanolamine [103], and TiO_2 has been synthesized by stabilizing Ti isopropoxide by citric acid [192].

Here, we report on aqueous chemical solution deposition of BNT thin films. Two different sol systems were investigated. The first, referred to as the citrate sol, employed bismuth citrate stabilized by ethanolamine [103] and NaOH. In the second sol, the nitrate sol, $Bi(NO_3)_3 \cdot 5H_2O$ and $NaNO_3$ were used, similar to the method of Xu et al. [188] Ti isopropoxide stabilized by citric acid [192] was used as Ti precursor. The sols were compared with respect to properties of resultant oxide, and the feasibility of employing the synthesis route in production lines. Thin films were fabricated by spin-coating the sol onto single crystalline $SrTiO_3$ and platinized silicon substrates, and the thermal processing parameters governing phase purity were thoroughly investigated. Finally, BNT powders were also prepared by the two routes, providing supplementary insight into the decomposition and

crystallization processes. The main focus was devoted to the citrate route, which proved to be more successful. The findings of the nitrate method are presented in Appendix A.

4.2 Experimental

4.2.1 Sol preparation

Two different recipes to BNT sols were investigated. Both recipes used Ti(IV)-isopropoxide (>97 %, Sigma-Aldrich, SKU 87560) stabilized by citric acid (99 %, Sigma-Aldrich, SKU C0759) as titanium precursor. [192] In the first recipe, referred to as citrate method, the other precursors were Bi-citrate (99.99 %, Sigma-Aldrich, SKU 480746) stabilized by ethanolamine (>99.5 %, Sigma-Aldrich, SKU 411000) [103], NaOH solution (4.00 M, Sigma-Aldrich, SKU 35274), and finally NH_4OH solution (33 %, Sigma-Aldrich, SKU 05002) was used in order to increase pH of the final sol. The second recipe, the nitrate method, used $Bi(NO_3)_3 \cdot 5H_2O$ (>98 %, Sigma-Aldrich, SKU 383074), $NaNO_3$ (>99 %, VWR, Cnr 14493), polyvinyl alcohol (PVA, Sigma-Aldrich, SKU 341584) as surfactant, and finally HNO_3 (65 %, Merck KGaA, Pnr 1.00456) in order to decrease pH. In both cases, distilled water was used as solvent, yielding sols of varying concentration, from 0.1 M to 0.6 M. A flow-chart illustrating the preparation of citrate sol is shown in Figure 4.1.

The Ti precursor was prepared by heating 1.8 M citric acid in distilled water to 80 °C, followed by addition of Ti isopropoxide via a syringe to 0.6 M final concentration. Upon addition of Ti isopropoxide, a precipitate was immediately formed yielding a white opaque slurry. After stirring at 70 °C overnight, the solution turned clear with a yellow tint, signifying the formation of a $Ti(cit)_3$ complex as described by Deng et al. [99] Concentration was adjusted to approximately 0.6 M in Ti by diluting with distilled water or careful evaporation at 70 °C depending on the volume of the solution. Finally, the exact concentration was measured by heat treatment of three parallels of 1.00 ml solution at 1000 °C for 8 h, and

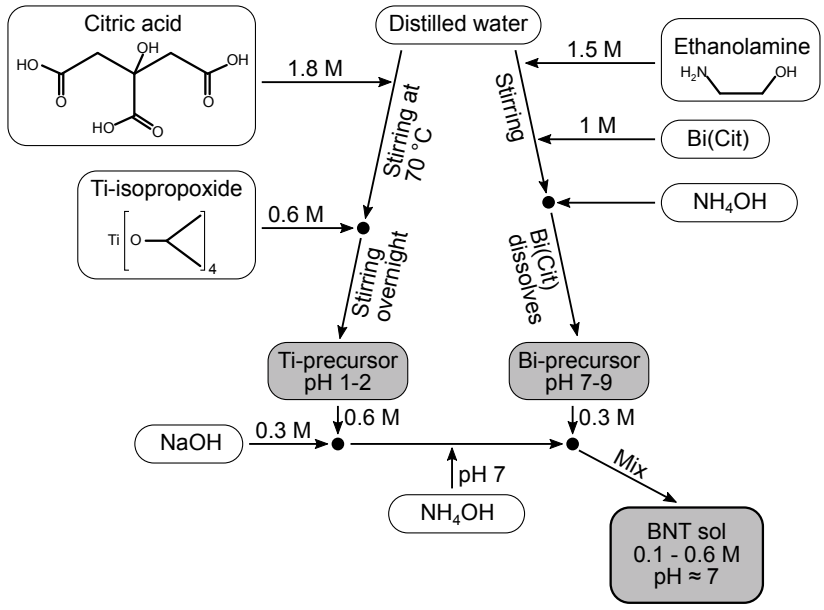

Figure 4.1 Flow-chart of the citrate method for BNT sol preparation.

measuring the mass of resultant TiO_2. The precursor had pH equal to 1, and showed no sign of ageing or precipitation even after 10 months.

For the citrate method, Bi-ethanolamine complex was formed by stirring Bi-citrate and ethanolamine in a 1:1.5 molar ratio in distilled water. To increase the solubility of Bi-citrate, NH_4OH was added to pH = 8-9, and a clear 1.0 M solution was obtained. The complete BNT sol was finally prepared by adding, in molar ratio, 1 part Ti precursor, 0.5 parts NaOH, 2 parts NH_4OH, and 0.5 parts Bi precursor, in chronological order.

The nitrate sol was prepared by adding $NaNO_3$, $Bi(NO_3)_3 \cdot 5H_2O$, HNO_3, and a PVA aqueous solution (~0.1 wt%) to the Ti precursor. As is seen in Appendix A, the order of addition had great influence on the stability of the sol.

4.2.2 Powder and film preparation

Powder samples were obtained by drying the sol at 80 °C for several hours in a Pt crucible. The citrate method also required further drying at 120 °C to obtain a porous gel. The resulting powders were crushed and calcined at 250-800 °C in alumina crucibles and ambient atmosphere for 2 h. Samples with little (<1 mm height) or much (~5 mm height) crushed gel were heat treated simultaneously, and compared.

Thin films were prepared by spin-coating the sol onto 1x1 cm^2 single crystal substrates of $SrTiO_3$ (STO) (100 oriented, Crystal GmbH, Part No 1STO 101E) and piranha etched platinized silicon (Si100|TiO_x|Pt111, MEMS Exchange, Reston, Virginia). Nitrate sol samples were only deposited on STO substrates, and wetting during spin coating was enhanced by PVA addition to the sol. To further increase wetting of the platinized Si substrates, the substrates were heated to 200 °C on a hot plate, covered with sol, and cooled to room temperature. This led to a thick gel coating, which was rinsed off with water before the substrate again was covered with sol at room temperature and left resting for 5 min. Again, the sol/gel was rinsed off with water, and the subsequent addition of two drops of sol followed by promptly spin coating, gave good wetting with homogeneous thickness, as evident by a uniform iridescence color of both wet and dry films. The films were spin coated at 3000 rpm for 30 s, and then dried on a hot plate at 200 °C for 5 min. Production of the thin films were conducted in an ISO 7 level clean room. In order to ensure that secondary phases observed in thin film samples were not due to faulty sols, small batches of powders calcined at 800 °C were prepared from all sol batches. All of these were phase pure according to XRD, demonstrating that the secondary phases were not a result of stoichiometry.

Films were pyrolized for 5 min in oxygen by rapid thermal processing (RTP), ramping at 40 °C/s to various temperatures (Jipelec Jetfirst 200 mm). A SiC coated graphite susceptor and lid surrounded the samples in order to protect the chamber from evolved gases. Spin coating and pyrolysis were repeated for each layer, in total 5 times. Finally, the samples were annealed at various temperatures for 10 min by RTP. During annealing, sacrificial powder of BNT was added to the susceptor in order to increase the vapor pressure of volatile Na and Bi, and thereby decrease the evaporative loss of these species.

4.2.3 Characterization

The phase purity and crystallinity were characterized by XRD (Bruker D8 Advance DaVinci), powders in Bragg-Brentano setup with a variable slit size, and films using grazing incidence setup with 2° incidence angle. All samples were measured with equal scan conditions, and no data manipulation other than vertical offset were applied. Rietveld refinements were carried out in Bruker AXS Topas version 5. Fundamental parameters peak shape was employed, with starting point in R3c reference unit cell parameters. [42] Background signal was refined for the most crystalline samples, and fixed to the same value for the remaining samples, where only unit cell parameters and crystallite size were refined. Powder samples were refined by the 2θ range 20-75°, and films by 21-49°.

Thermogravimetric analysis combined with mass spectroscopy (TGA-MS, Netzsch STA 449 C and Netszch QMS 403 C) was conducted in synthetic air (20 % O_2, 80 % N_2) and argon on dried sols, heating and cooling at 10 °C/min. Scanning electron images were captured on a field emission gun SEM (Zeiss Ultra 55, Limited Edition). Fourier transform infrared spectroscopy (FTIR) was done in vacuum by the attenuated total reflectance (ATR) method (Bruker Vertex 80v) on the ground calcined powders.

4.3 Results

4.3.1 Deposition of thin film using the citrate sol

BNT thin films were successfully deposited on both types of substrates, and grazing incidence XRD of the films are displayed in Figure 4.2. Phase pure BNT perovskite was achieved on $SrTiO_3$ (STO) substrates (Figure 4.2a) after pyrolysis at 550 °C, or pyrolysis at 500 °C followed by thermal processing at 700 °C. The films deposited on platinized silicon (SiPt), Figure 4.2b, were phase pure after pyrolysis at 550 °C and sintering at 700 °C, thus requiring higher thermal processing temperature than STO films. The unit cell parameters and the crystallite size obtained by Rietveld refinement for the films are summarized in Table 4.1, and crystallographic data is in reasonable agreement with literature. [42]

The pyrolysis temperature was demonstrated to be critical with respect to the phase purity of the films. The ratio of BNT to secondary phases obtained during pyrolysis is retained after annealing, irrespectively of further thermal processing. STO films pyrolized at 550 °C remains single phase BNT after thermal annealing, while the amount of secondary phases in thin films pyrolized at 400 °C was not altered after thermal annealing at 700, 800, and 900 °C. The diffraction patterns of the secondary phase are reasonably well described by a pyrochlore phase [211], although the chemical composition of the pyrochlore was affected by the thermal processing, evidenced by the shift in the position of the main diffraction lines.

Black color of the films and broad Bragg reflections, observed after pyrolysis at 400 °C, is proposed to originate from the formation of metallic bismuth. The formation of elemental Bi results in secondary phases upon re-oxidation during further thermal processing of the films. Several bismuth rich structures, such as $Na_{0.32}Bi_{1.68}Ti_2O_{6.46}(OH)_{0.44}$ [211] and $Bi_4Ti_3O_{12}$ [225], match the observed secondary phase well, suggesting that these phases grew from areas enriched in bismuth.

Thin films deposited on STO and SiPt substrates behaved similarly for heat treatments up to 700 °C, but a range of secondary phases appeared at 800-900 °C in the thin films on SiPt (Figure 4.2b). These films turned matte grey in color and appeared inhomogeneous to the naked eye. Moreover, at 900 °C, BNT formed during pyrolysis disappeared, reflecting the strong change in the visible appearance. Note also that Pt reflections became apparent for samples pyrolized at 500-550 °C, but not for samples pyrolized at 400-450 °C even after annealing at 700 °C, indicating that there is some degree of Pt recrystallization during pyrolysis, but not during further thermal processing. Platinum bottom electrodes is the industry standard for electronic oxide thin films, and compatibility towards Pt is essential. For SiPt substrates, pyrolysis at 550 °C and annealing at 700 °C yielded phase pure samples.

Thin films prepared from a sol containing 10 % sodium excess clearly reduced the amount of pyrochlore at any given heat treatment for films on both STO and SiPt substrates (Figure 4.2c,d).

Representative thin films from the heat treatment procedures yielding phase pure films were selected for investigation by scanning electron microscope (SEM). Figure 4.3 shows that the films were homogenous and fairly dense, and that the thickness is approximately 300 nm for 5 layers. At the surface (5^{th} layer) the grain size is approximately 20 nm in thin films on

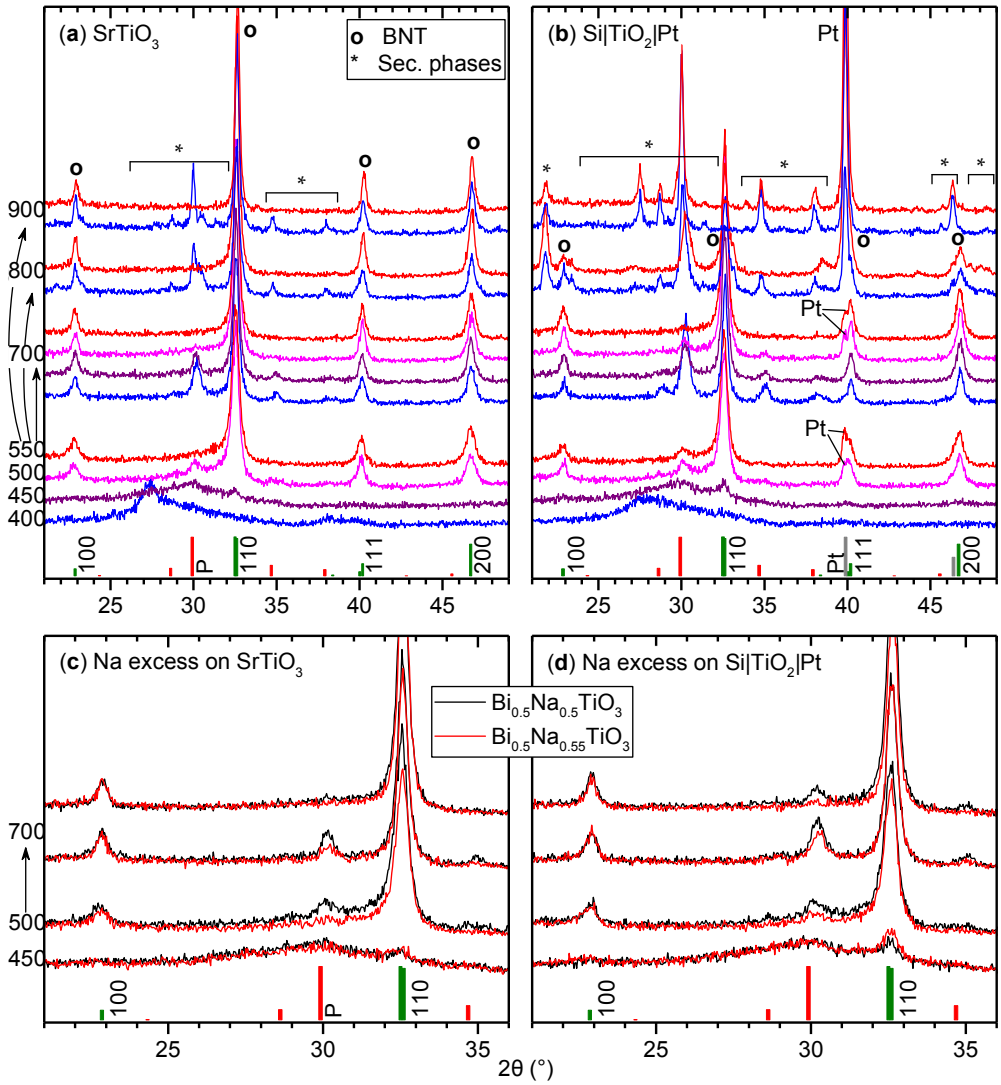

Figure 4.2 Grazing incidence XRD patterns of deposited BNT films. (a) Films deposited on STO substrates. (b) Films deposited on SiPt substrates. (c) Comparison of nominal stoichiometric and 10 % Na excess sols on STO. (d) Comparison of stoichiometric and Na excess on platinized silicon. Heat treatment temperatures are denoted to the left. Arrows indicate that samples were first pyrolized for each layer, then finally annealed at the given temperature. Color codes correspond to the pyrolysis temperatures. Reference patterns are shown for R3c BNT (pseudo cubic hkl indices) [42], a Na-poor pyrochlore phase ("P") [211] and platinum ("Pt").

STO, both before and after annealing at 700 °C, while in case of SiPt substrates, the grain size is slightly larger. Cross section images show that grain size is larger in bulk than at the surface. Sintering at 900 °C yields significantly larger grains on STO, approximately 200 nm.

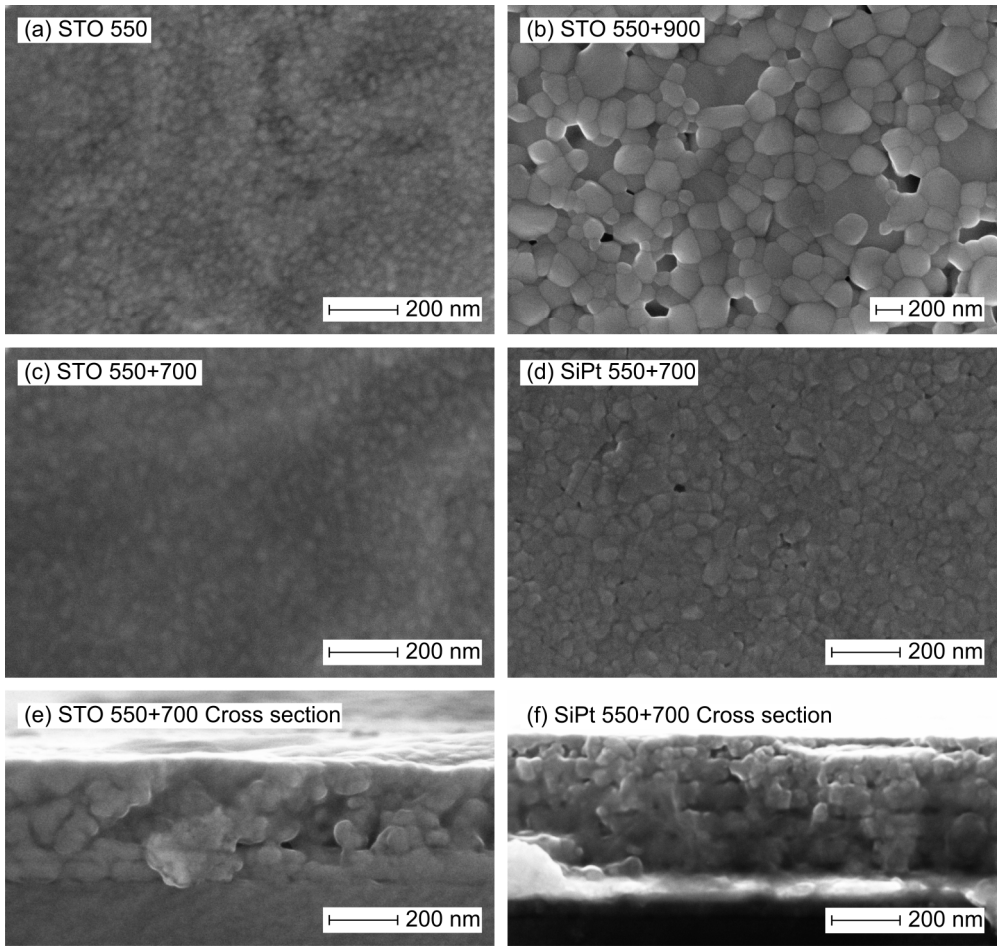

Figure 4.3 Secondary electron SEM images of phase pure BNT films prepared by the citrate sol. (a) Top view of films on STO pyrolized at 550 °C before and (b) after sintering at 900 °C. (c) Top and (e) cross section view of films on STO and (d,f) SiPt pyrolized at 550 °C and sintered at 700 °C.

4.3.2 Decomposition of gel from citrate sol

Supplementary to thin films, powder samples were prepared by drying a portion of the sols used for deposition of thin films. XRD patterns of powders heat treated at various temperatures in ambient atmosphere are shown in Figure 4.4a. From 500 to 800 °C, the samples were phase pure BNT according to XRD. The crystallinity of the powders increased by increasing the calcination temperature, and the reflection at about 52°, as well as the rhombohedral super-reflection at 38°, became more pronounced.

Heat treatment up to 250 °C yielded amorphous samples, showing that evaporation of the solvent did not lead to crystallization or precipitation, suggesting that the dried gel is homogeneous on the atomic level. At 300 to 400 °C, however, broad reflections corresponding to metallic bismuth appeared, and these samples were black. The bismuth particles were nano-sized, increasing in size with temperature, indicated by the width of the reflections.

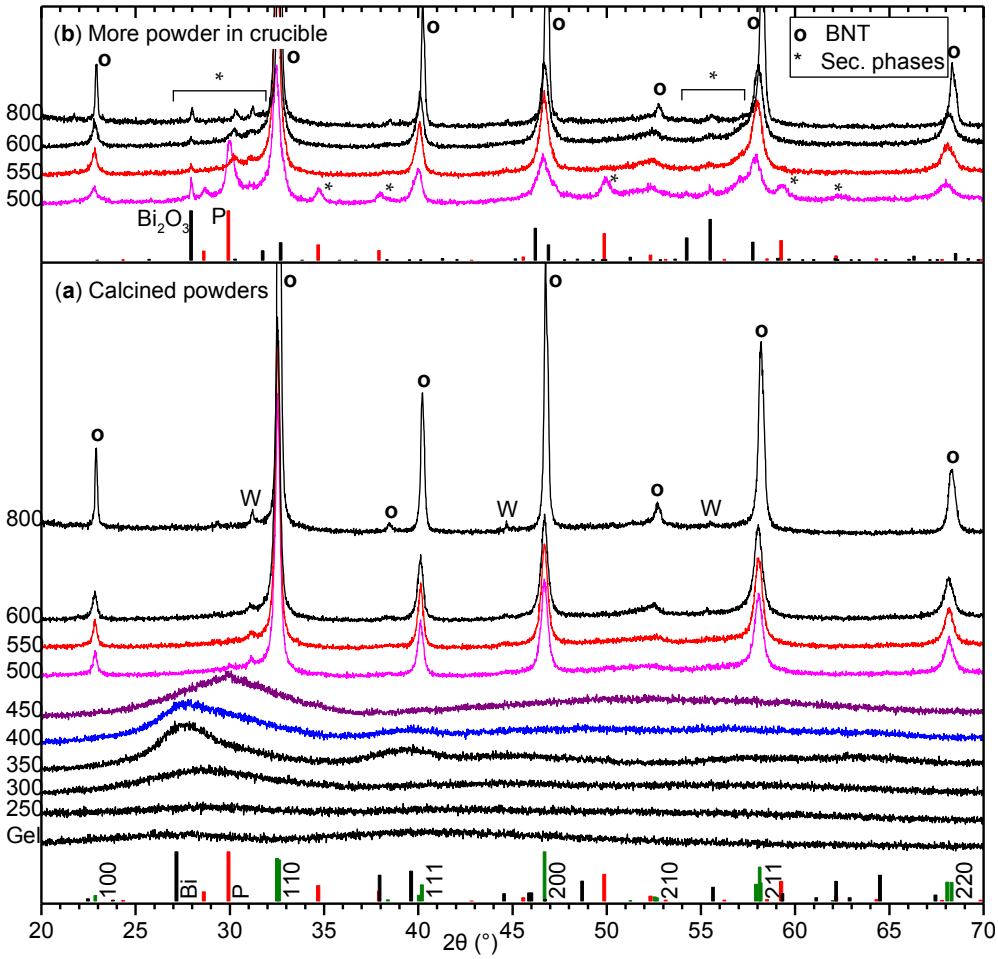

Figure 4.4 (a) XRD patterns of BNT powders calcined for 2 h in ambient atmosphere. (b) Powders calcined simultaneously as in (a), but with larger amounts of powder in the crucibles. The temperature interval 400-550 °C is color coded to augment comparisons between figures. Reference patterns are shown for R3c BNT (pseudo cubic hkl indices) [42], metallic bismuth ("Bi"), a Na-deficient pyrochlore phase ("P") [211] and Bi_2O_3 Reflections denoted by W are caused by tungsten Lα1 radiation from the instrument. Rietveld refinement of the patterns are presented in Table 4.1, showing reasonable agreement with literature data [42].

Access to oxygen was essential for obtaining phase pure samples. Figure 4.4b displays XRD patterns of samples prepared together with the samples in Figure 4.4a, but with significantly more powder in the crucibles. After calcination, these samples were inhomogeneous, as the outer layers were white, while the cores were yellow or black, and XRD confirmed the presence of secondary phases. This can be explained by the reduction of bismuth during heating, and slower bismuth re-oxidation where oxygen access is limited, allowing for Ostwald ripening and segregation of Bi and subsequent formation of secondary phases upon re-oxidation of Bi.

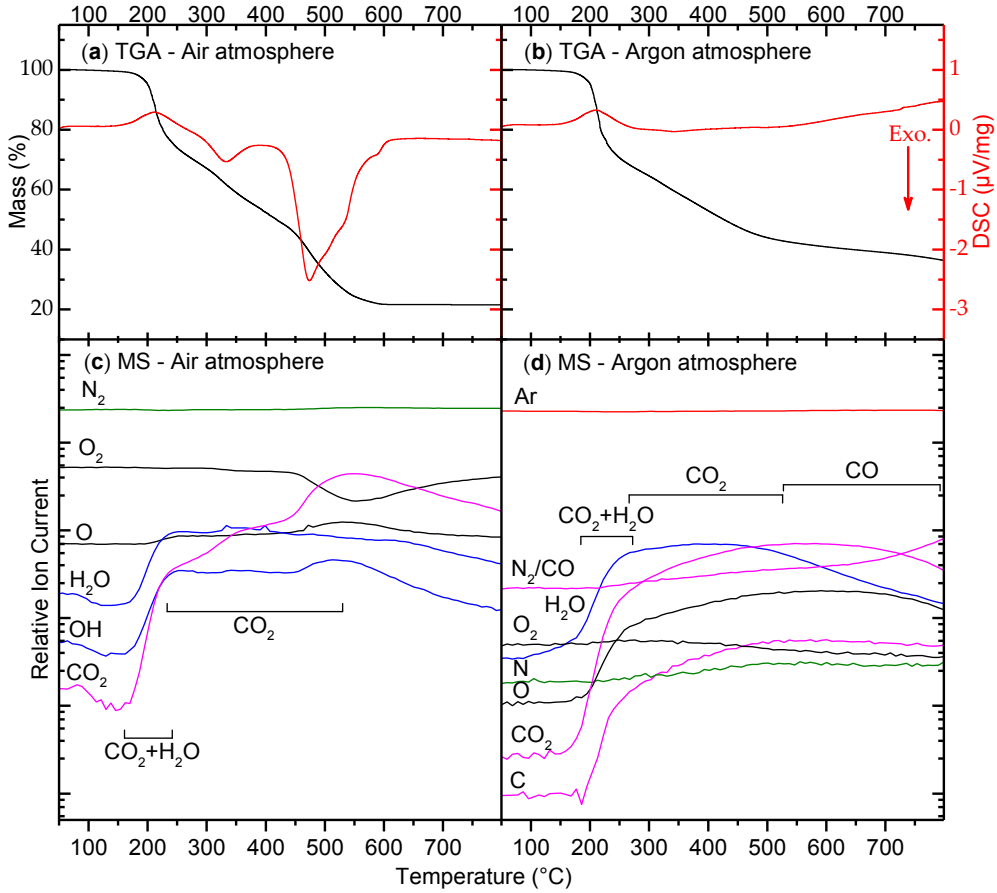

Figure 4.5 TGA-MS of dried BNT gel. (a,b) Mass loss (black, left axis) and differential scanning calorimetry (red, right axis). (c,d) In situ mass spectroscopy (MS) of TGA outlet gas. Different graphs correspond to specific m/z values, labelled with the gaseous species contributing to the m/z current. Lines are color coded: Green-nitrogen, black-oxygen, blue-water, magenta-carbon, red-argon. Dominating gaseous species for mass loss are indicated next to MS-curves. In (d) combined assessment of curves for N, C and CO_2 shows that N_2/CO signal originates from N_2 at low temperature and CO at high. 10 °C/min ramp rate.

Thermogravimetric analysis with outlet gas mass spectroscopy (TGA-MS) of the gel during heating is shown in Figure 4.5. Evaporative loss of water (endothermic) and CO_2 occurred at 200 °C. Decomposition of the gel and formation of metallic bismuth corresponds to an exothermic mass loss at 300 °C. Accompanied by a significant consumption of oxygen, several exothermic events overlapped at 450-550 °C, one of which was likely related to bismuth re-oxidation. The mass loss stabilized at 79 % at approximately 550 °C, and the sample recovered from the TGA experiment was phase pure BNT according to XRD (not shown). Figure 4.5b and d shows that the initial release of water and CO_2 was independent of oxygen access, but increasing the temperature further in argon atmosphere led to incomplete decomposition, and none of the exothermic events observed in air occurred. At 800 °C, weight

loss was still incomplete, and the recovered sample contained no perovskite phase, but primarily metallic bismuth according to XRD (not shown).

IR transmittance spectra of the powders calcined at different temperatures are shown in Figure 4.6. In accordance with XRD and TGA experiments, decomposition of the gel was complete after calcination at 550 °C, leaving only bands related to the TiO_6-octahedra in BNT. The band at 1430 cm^{-1} corresponds to a carbonate phase formed by the decomposition of the organics [226] (p. 284).

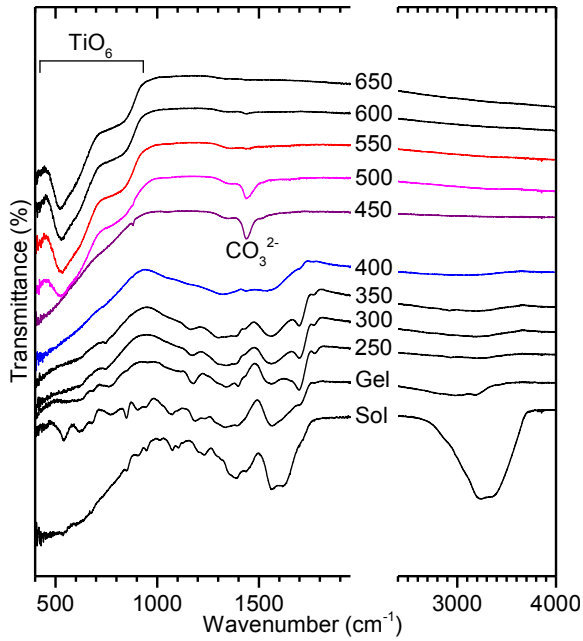

Figure 4.6 FTIR spectra of calcined citrate BNT powders. The scale is changed at wavenumber 2000 cm^{-1} in order to more clearly show the features of interest. Consecutive graphs are offset the same value.

4.4 Discussion

To the best of our knowledge, this is the first report on preparation of BNT thin films by an aqueous chemical solution deposition method. The citrate method reported here resulted in single phase, homogeneous and dense BNT thin films. Furthermore, the preparation of the sol does not require any costly, time consuming, or complicated steps, and results in a stable, pH neutral sol free of harmful or environmentally toxic chemicals. Due to the simple synthesis and robust method, the results obtained are easily reproducible and are suitable for further modification or up-scaling.

The process of decomposition of the gel into oxide powders and thin films was studied in detail. Reduction of Bi^{3+} and the growth and segregation of metallic Bi particles is the main challenge of the synthesis, potentially leading to secondary phases during re-oxidation of bismuth. A hypothesis for the decomposition process in powder samples is presented in Figure 4.7, where the various parameters controlling phase purity of the product are highlighted. During drying, the viscosity of the sol increases gradually as water and volatile species evaporate, leading to a brittle and porous gel, which is amorphous and homogeneous on the atomic level. Upon heating past 300 °C, the hybrid inorganic-organic gel decomposes, causing oxidation of organic constituents and reduction of Bi^{3+}. Bi^{3+} has previously been shown to act

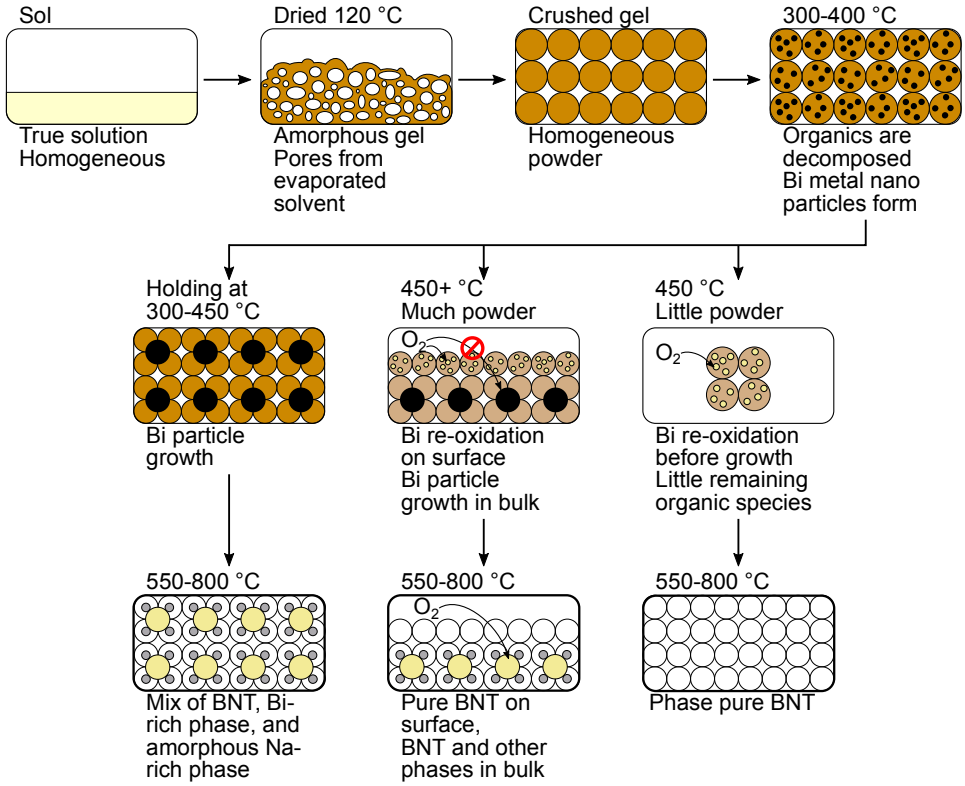

Figure 4.7 Proposed decomposition process for citrate method powders. In the bottom panels, yellow signifies a bismuth rich secondary phase (e.g. Bi_2O_3), grey signifies an amorphous sodium rich secondary phase invisible to XRD, and white signifies BNT.

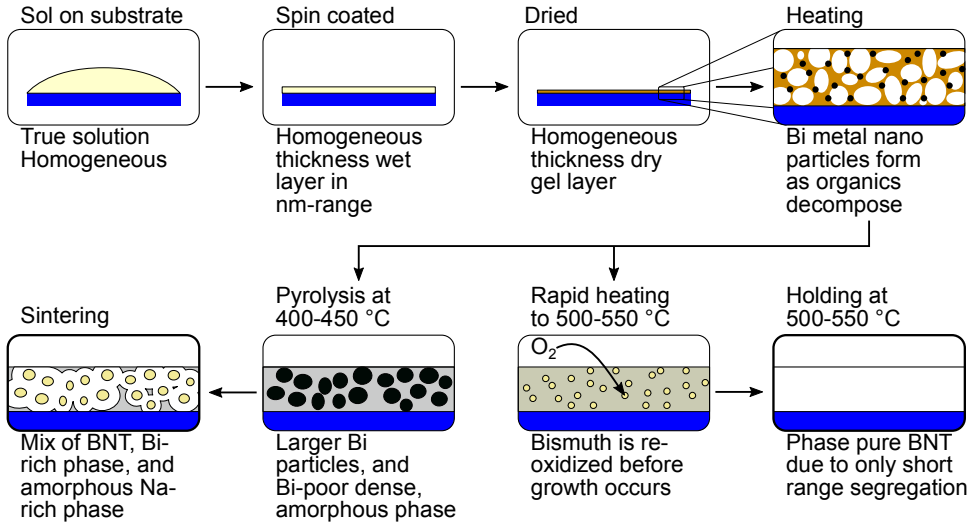

Figure 4.8 A schematic of the decomposition process of citrate method thin film samples. The substrate is drawn blue, pores and BNT are white, gel is brown, Bi rich secondary phase is yellow, and an amorphous Na rich secondary phase is drawn grey.

as an efficient oxidizing agent for benzylic, allylic and aliphatic alcohols. [227] Initially, metallic bismuth takes the form of nano-sized liquid droplets, and appears as nano-crystalline Bi in XRD patterns after cooling to ambient temperature. During further annealing at 300-450 °C, however, the bismuth droplets grow through Ostwald ripening, causing increasing levels of bismuth segregation and formation of phase pure BNT is hindered due to the segregation of Bi. The result is therefore bismuth rich secondary phases containing a varying amount of titanium and sodium, such as Bi_2O_3 and pyrochlore ($Na_{0.32}Bi_{1.68}Ti_2O_{6.46}(OH)_{0.44}$) [211]. If, however, the temperature during calcination is high enough to allow re-oxidation of Bi and crystallization of BNT perovskite, the growth of bismuth droplets and segregation is hindered, yielding phase pure BNT. The temperature limit for these two scenarios was shown to be 450-500 °C.

Even if the temperature is high enough for bismuth re-oxidation, access to oxygen may still be limiting. If the layer of powder in the crucible is too thick, re-oxidation will be diffusion controlled, and Bi growth will be allowed to occur in the core of the powder bed, again resulting in secondary phases. We therefore can conclude that in order to obtain phase pure powders, calcination should be carried out at 450-500 °C or higher, and sufficient oxygen should be present.

The thermal processing of thin films is subject to the same challenges as observed in the preparation of powders. Metallic bismuth was shown to be formed during pyrolysis at 400 °C, and a pyrochlore secondary phase was observed for several heat treatment routes. A schematic for the proposed processes involved during thermal processing of the thin films, and the influence of heat treatment parameters, is presented in Figure 4.8. First, the sol is spin-coated onto the substrate and dried, giving a thin homogeneous layer of the gel. As shown for the powder, decomposition and oxidation of the hybrid gel is accompanied with reduction of Bi^{3+}, forming metallic bismuth. Observing that formation of metallic Bi occurred in case of both

powder and thin film samples, where heating rates, holding times, and diffusion lengths are significantly different, the reduction is concluded to be a result of the local environment of Bi in the gel, and not the access to oxygen during decomposition of the gel. Thus, sufficiently high pyrolysis temperature is essential, as pyrolysis at 400-450 °C promotes Ostwald ripening of Bi(l), while pyrolysis at 500-550 °C cause rapid Bi re-oxidation, hindering segregation. It is concluded that the final phase purity is largely determined by the pyrolysis temperature. Any segregation and secondary phases formed during pyrolysis will remain after further thermal processing, independent of the thermal processing temperature. Pyrolysis of the BNT thin films at 500 °C or higher was demonstrated to be key to obtain phase pure BNT thin films.

Reduction of bismuth during chemical solution processing of oxides is known, but rarely reported. [227] For example, Nelis et al. prepared $SrBi_2Nb_2O_9$ by a similar method and report metallic bismuth after heat treatment at 400 °C. [228] Furthermore, the connection between segregation during decomposition and resultant secondary phases after subsequent heat treatment is frequently not recognized. Often, in related material systems, secondary phases are simply accredited to evaporation of volatile species, while it is likely that bismuth reduction and segregation during pyrolysis is equally important. For example, Xu et al. report a $Bi_4Ti_3O_{12}$ secondary phase (similar to the pyrochlore reported here) after heat treatment at 500-550 °C when preparing BNT-BT. [188, 189] Li et al. made BNT-BKT-BZT thin films by an organic solvent procedure, and reported a small amount of pyrochlore after pyrolysis at 400 °C and sintering at 700 °C. [229] Alonso-Sanjosé et al. also made BNT-BT thin films by organic solvent sol-gel method, and reported formation of a pyrochlore phase after heat treatment at 600 °C, but not after 650 °C. [13] Moreover, Zhou et al. prepared BNT-BT films, and observed that pyrolysis at 350 °C resulted in the presence of a pyrochlore phase after sintering at 700 °C, while pyrolysis at 400 °C did not. [143] In the latter case the authors presented a possible explanation which resembles the one presented here.

Sodium excess was shown to efficiently reduce the amount of pyrochlore secondary phase for all the heat treatment procedures used in this work. Both bismuth and sodium are known to be volatile, and adding excess Bi- or Na precursors during synthesis is common. It has been shown that the BNT material system is not able to accommodate a large amount of A to B non-stoichiometry, and less than 1 mol% variation cause formation of secondary phases (i.e. Bi_2O_3 for Bi rich, $Na_2Ti_6O_{13}$ for Na rich, and TiO_2 for Ti rich). [45, 46] However, increasing the Na to Bi ratio acts as A site acceptor doping, which is charge compensated by oxygen vacancies, leading to a conductivity increase by several orders of magnitude. [45, 46] Moreover, Na excess cause hardening of BNT-BT ferroelectrics. [67] Therefore, while sodium excess is efficient in reducing the amount of pyrochlore phase, care should be taken as it might significantly reduce the piezoelectric properties. A possible remedy for the negative effects of Na excess is addition of some donor dopant, such as Nb^{5+} on B site.

When films deposited on platinized silicon were heat treated above 700 °C, a range of secondary phases evolved due to a reaction between BNT and the platinum bottom electrode. Alonso-Sanjosé et al. report formation of a Bi-Pt secondary phase when heat treating BNT thin films on platinized silicon at 750 °C. [13] Considering the high solubility in the Bi-Pt binary system, this reaction is a likely explanation. For example, a 50-50 at% Bi-Pt alloy melts at 765 °C, and the melting point only decreases for higher Bi content. [216] For

implementation of BNT thin films on silicon wafers, where Pt has achieved the role as the standard bottom electrode, either suppressing the Pt-Bi reaction, or replacing Pt in favor of another electrode may be necessary.

Changes in the Pt bottom electrode was also observed at lower heat treatment temperatures. XRD patterns recorded in grazing incidence mode for clean substrates or samples pyrolized at 400-450 °C (Figure 4.2b) did not show Pt reflections, but Pt reflections became visible after pyrolysis at 500-550 °C. The same trends have also been reported for $Bi_{3.25}Nd_{0.75}TiO_{12}$ on platinized silicon, showing Pt reflections after annealing at 500-650 °C, but not after annealing at 400 °C. [230] Initially the Pt layer is textured with (111) orientation, and in grazing incidence mode horizontally oriented planes will not appear. Appearance of Pt reflections can be explained by recrystallization of the Pt layer, which could be induced by impurities, most likely Bi diffusion from the deposited film. We suggest that the absence of recrystallization at 400-450 °C is due to lower mobility and solubility in the Bi-Pt system at low temperature. At higher temperatures, a small amount of Bi-Pt interdiffusion takes place, causing Pt recrystallization. However, when the stable perovskite phase forms, the reactivity of Bi is reduced, explaining why no further Pt recrystallization is observed during annealing at 700 °C.

Processing of thin films was the focus of the current work, and for that reason, obtaining phase pure powders in large quantities was not investigated. However, there are clear advantages to using a chemical solution method when producing powders, such as small particle size, excellent control of stoichiometry and low heat treatment temperatures. Solid state synthesis of BNT typically requires sintering temperatures in excess of 1100 °C [23], where volatility of bismuth and sodium can give poor stoichiometry control, and where significant grain growth is difficult to avoid. Compared to the other reports on aqueous BNT processing, the citrate method developed here shows advantages such as high stability and pH neutrality of the sol, cheap precursors, and a simple process. For bulk powder production, a sufficient flow of oxygen for re-oxidation of Bi is necessary.

The most attractive piezoelectric properties of BNT based materials are found for materials with barium A site doping as well as a small amount of B site doping such as Nb or Zr [66]. Due to the robustness, low cost, and benign characteristics of the citrate sol, this method is well suited for further modifications and up-scaling.

4.5 Conclusions

Two aqueous-based synthesis routes to BNT materials were developed in this work. Preparation of phase pure BNT thin films as well as powders were demonstrated by the use of the citrate method. The thermal decomposition of the gels obtained from the aqueous sol and formation of BNT were studied in detail by thermal analysis, FTIR spectroscopy, X-ray diffraction, and electron microscopy.

The main challenge during the thermal processing of the materials was the reduction of Bi^{3+} to metallic bismuth during decomposition of the precursor gel, causing segregation of Bi and subsequent formation of a pyrochlore secondary phase. The parameters governing this effect was investigated, resulting in good control of the process yielding phase pure BNT thin films and powders. Parallels were drawn to similar synthesis routes of related materials, showing that the insight gained here may also be of value to these methods. The synthesis route was demonstrated to possess ideal properties for chemical solution deposition of BNT thin films, and is suitable for both further modifications and up-scaling for industrial applications.

Acknowledgments

Financial support from The Research Council of Norway to the project "Beat the Human Eye" (number 235210) and for the support to NTNU NanoLab through the Norwegian Micro- and Nano-Fabrication Facility, NorFab (197411/V30), is gratefully acknowledged. Support for open access publishing has been received from the open access publishing fund at NTNU.

Author contributions

All authors conceived and designed the experiments, analyzed the data, and wrote the paper; M.C. performed the experiments.

Conflicts of interest

The authors declare no conflict of interest.

4.6 Appendix A. The nitrate method

4.6.1 Synthesis by the nitrate method

XRD patterns of samples prepared from the nitrate method gel by calcination at various temperatures for 2 h in air are shown in Figure 4.9. Phase pure powders were achieved, and crystallization of BNT perovskite phase occurred already at 450 °C. However, the reduction of bismuth at 300-400 °C is more pronounced with sharper diffraction lines, signifying larger metallic Bi crystallites, showing that the oxidizing properties of NO_3^- does not influence the reduction of Bi. Remnants of the bismuth phase formed early in decomposition can be seen as a diffraction line from a secondary phase peak at approximately 30° even after calcination at 500-600 °C.

TGA measurement of the nitrate method gel is shown in Figure 4.10. In accordance with the XRD data, the mass loss terminated at approximately 450 °C, 100 °C earlier than for the citrate method.

Due to inferior stability and pH of the nitrate method sol compared to the citrate method, fabrication of thin films was not investigated thoroughly. Pyrolysis at 500 °C and annealing at 700 °C yielded significant amounts of pyrochlore secondary phase, and additional annealing only increased the pyrochlore to BNT ratio.

While phase pure powder samples could be prepared from the nitrate sol, successful films could not be achieved, and the properties of this sol are significantly inferior to those of the citrate method sol. First, the required low pH of the system represents a hazard during

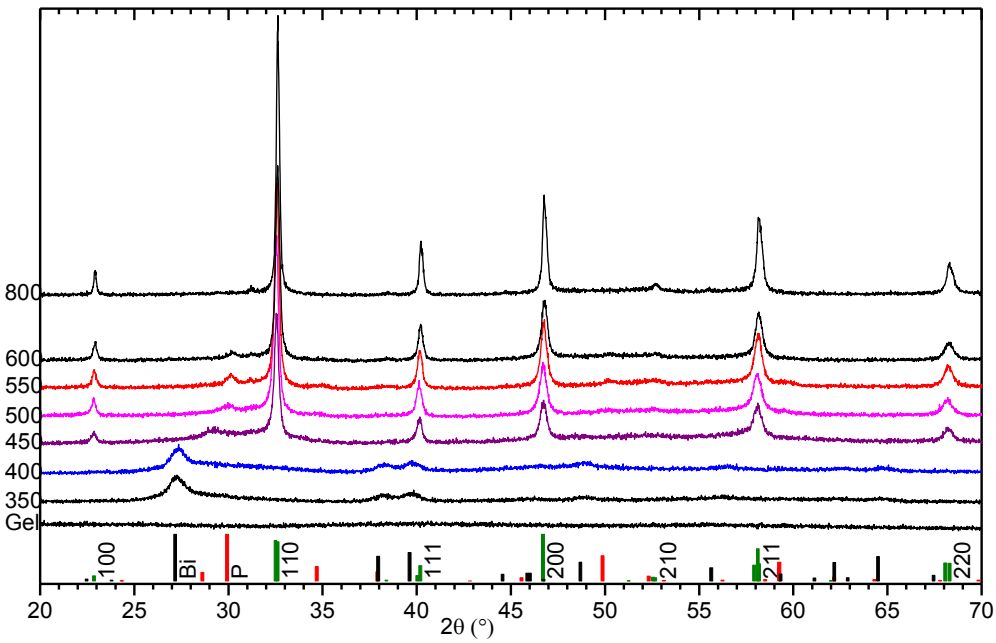

Figure 4.9 XRD patterns of calcined powders from nitrate method gel. All samples were calcined for 2 h in ambient atmosphere. Calcination temperatures are given to the left, and reference diffraction patterns for BNT [42], metallic bismuth, and pyrochlore [211] in the bottom.

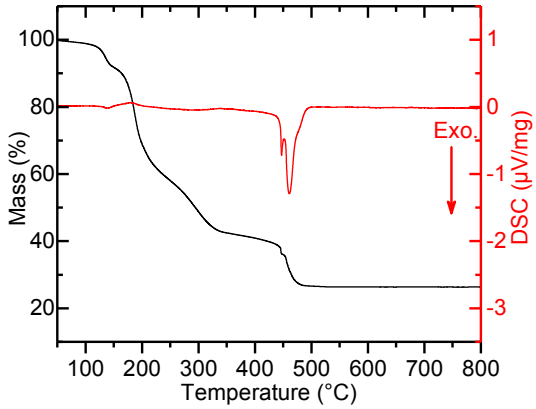

Figure 4.10 TGA measurement of BNT gel from nitrate method. 10 °C/min ramp rate, synthetic air flow.

handling, and could potentially limit the feasibility of use with pH sensitive manufacturing equipment or chemical additions such as barium to the sol. Second, while left in storage, the sol developed NO/NO_2 gases, identifiable by yellow coloration and smell, which also led to increased pressure in the containers, again posing a safety hazard. The NO/NO_2 formation may have occurred according to:

$$4HNO_3(aq) \longrightarrow 4NO_2(g) + 2H_2O + O_2(g) \tag{4.1}$$

Finally, the nitrate sol was only stable for a couple of days, limiting the practical application of the sol, and resulting in potentially uncontrolled homogeneity and reproducibility.

Some comments should be dedicated to the works of Xu et al. [188-190, 224], who prepared BNT-BT by a method very similar to the nitrate method reported here. They employed tetrabutyl titanate instead of Ti isopropoxide, but citric acid was used as complexing agent and the developed n-butanol was separated from the sol. Therefore, the resulting complex and overall Ti-precursor system should be identical to ours. They adjusted pH to neutral by addition of NH_4OH before adding $Bi(NO_3)_3 \cdot 5H_2O$. Then, the slurry was stirred for 1 h at 80 °C. In the present work, this procedure did not result in a precipitate free solution, and only when pH was kept below 1 hydrolysis and precipitation of bismuth was avoided

4.6.2 Stability of the sols

The Bi-ethanolamine precursor (1 M) showed no ageing effects after 3 months, and it has been reported to be stable for several months. [103] Mixing the Ti and Bi precursors without adding NH_4OH caused a white precipitation, likely due to too low pH for the Bi precursor, but the precipitate re-dissolved upon addition of NH_4OH. The final sols containing NaOH, Ti-precursor, Bi-precursor and NH_4OH (citrate method) was stable for months. Drying the sol resulted in gradually increasing viscosity, and finally a brittle sponge-like structure, as gas bubbles were trapped, and the sol turned into solid gel. The gel was homogeneous and amorphous, as shown by XRD in Figure 4.4.

Obtaining a stable sol proved challenging for the nitrate method. $Bi(NO_3)_3 \cdot 5H_2O$ was easily dissolved in water, but with pH above approximately 1-2, a white precipitate was

immediately formed on the nitrate surface. For this reason, HNO_3 corresponding to 1 M final concentration and PVA was added to the Ti precursor in advance of adding the cation nitrates. If the sol was to be diluted, distilled water had to be added and thoroughly mixed in advance of dissolving bismuth nitrate, as local pH values above 2 during dilution would cause precipitation which would not re-dissolve. Furthermore, as long as the Ti precursor was concentrated enough (0.6 M in Ti, 1.8 M in citric acid), the low pH from the citric acid alone was enough to properly dissolve $Bi(NO_3)_3 \cdot 5H_2O$, however, these sols were not stable for a long time. Heating and stirring the solutions only increased the level of precipitation, indicating that the sols were only stable due to slow kinetics. Properly prepared nitrate method sols were stable for 1-2 days. As with the citrate method, drying the sol produced homogeneous and amorphous gels, and spin coating could also be carried out within the stability timeframe.

4.7 Appendix B. Rietveld refinements

Table 4.1 Refined structural parameters for BNT phase in relevant samples. An asterisk (*) marks samples that are phase pure. Refinement of XRD patterns from films on SiPt required simultaneous refinement of Pt to allow BNT peaks to properly relax. Note that refinement of patterns from film samples results in too small crystallite sizes due to the inherent broad peaks obtained using grazing incidence XRD set up.

Powders				Films on STO				Films on SiPt			
Heat treatment (°C)	**a (Å)**	**c (Å)**	**Cryst. size (nm)**	**Heat treatment (°C)**	**a (Å)**	**c (Å)**	**Cryst. size (nm)**	**Heat treatment (°C)**	**a (Å)**	**c (Å)**	**Cryst. size (nm)**
Reference: R3c[42]	5.49	13.50		Stoichiometric				Stoichiometric			
Citrate				450	5.50	13.52	13	450	5.50	13.49	8
500 Little*	5.50	13.51	20	500	5.51	13.50	10	500	5.50	13.48	10
550 Little*	5.50	13.51	23	550*	5.51	13.49	11	550	5.49	13.51	13
600 Little*	5.50	13.52	22	400+700	5.50	13.49	16	400+700	5.49	13.44	19
800 Little*	5.49	13.48	52	450+700	5.50	13.48	17	450+700	5.49	13.45	16
500 much	5.51	13.49	12	500+700*	5.50	13.47	16	500+700	5.49	13.45	16
550 Much	5.50	13.52	17	550+700*	5.49	13.51	19	550+700*	5.49	13.49	16
600 Much	5.50	13.51	18	400+800	5.49	13.47	18	400+800	5.48	13.43	13
800 Much	5.48	13.46	54	550+800*	5.49	13.49	22	550+800	5.48	13.46	15
Nitrate				400+900	5.49	13.44	22	400+900	No BNT		
450	5.49	13.50	22	550+900*	5.49	13.41	30	550+900			
500	5.49	13.51	21	Na excess				Na excess			
550	5.49	13.50	26	450	5.52	13.51	6	450	5.50	13.48	8
600	5.49	13.49	28	500*	5.50	13.51	13	500	5.49	13.51	13
800*	5.49	13.47	44	450+700	5.49	13.51	20	450+700	5.48	13.50	18
				500+700*	5.49	13.50	19	500+700*	5.48	13.49	20

Aqueous chemical solution deposition of phase pure Ba doped $Bi_{0.5}Na_{0.5}TiO_3$ thin films

Paper 2

Mads Christensen, Mari-Ann Einarsrud and Tor Grande

Manuscript not yet submitted.

Abstract

Barium doped $Bi_{0.5}Na_{0.5}TiO_3$ (BNT-Ba) is one of the most promising lead-free materials for replacement of $Pb(Zr,Ti)O_3$ in actuator applications. Here, Ba doped BNT thin films were successfully prepared by a non-toxic aqueous chemical solution deposition (CSD) method. Different aspects of the synthesis route such as the thermal processing of the thin films and the sol cation stoichiometry were optimized. Phase composition was characterized by X-ray diffraction, and microstructures by scanning electron microscopy. The addition of Ba to BNT promoted formation of a Bi-rich pyrochlore secondary phase, and phase pure (according to XRD) BNT-Ba thin films were achieved by either annealing at 800 °C or by adding 10 % excess Na. Phase pure and defect free thin films with high density were obtained on SiPt substrate by employing the pyrolysis ramp rate of 40 °C/s, while films on $SrTiO_3$ substrates required 100 °C/s from room temperature to 450 °C, and 40 °C/s to 550 °C. Thin films of pure BNT and BNT-6Ba were confirmed to possess ferroelectric properties with a high tolerance for dielectric breakdown. The results demonstrate that the aqueous CSD synthesis method is robust and suitable for further compositional engineering of BNT.

5.1 Introduction

Since 2004, a strong effort has been made in the quest for lead-free piezoelectric ceramic materials. [4] Currently, $Pb(Zr,Ti)O_3$ (PZT) represents state of the art piezoelectrics, accounting for the superior market share of devices. [231] Due to the toxicity of lead, legislation in EU and other areas encourage replacement of PZT from electric devices allowing use only until sufficiently performing alternatives are developed. [35, 36]

There are currently primarily three alternative lead-free material systems for actuator applications: $(K,Na)NbO_3$ (KNN), $Bi_{0.5}Na_{0.5}TiO_3$ (BNT), and $(Ba,Ca)(Zr,Ti)O_3$ (BCZT) with breakthrough articles published in 2004, 2007, and 2009, respectively. [4, 15, 23, 30, 31, 33, 37] In devices where large strain coupled with a large operational temperature range is required, BNT currently represents the most promising alternative due to its electric field induced phase transition with accompanying strain of close to 0.5 %. [15, 32, 66] BNT has been extensively studied during the last decade, and the yearly number of publications is in the vicinity of 250 as displayed in Figure 5.1. As a result, the fundamental properties and mechanisms in bulk materials are now fairly well understood. The superior piezoelectric properties of the BNT material system is achieved upon compositional engineering. Ba addition is the most relevant and by far the most investigated dopant. [15] The solid solution of BNT and $BaTiO_3$ (BT) expresses a morphotropic phase boundary (MPB) of increased properties at 6-11 % BT. [14, 26, 190, 224] The most commonly reported composition is that of 6 at.% Ba at A-site.

The literature on fabrication and properties of BNT thin films is more limited, however, with approximately 200 total publications by the end of 2016. Chemical solution deposition (CSD) methods are the most relevant for industrial application, and with the exception of a few physical deposition methods, most literature on BNT thin films employ traditional CSD routes. Common for these routes is the application of harmful organic solvents such as 2-methoxyethanol, acetylacetone, or methanol, or very acidic conditions. [13, 143, 144, 148,

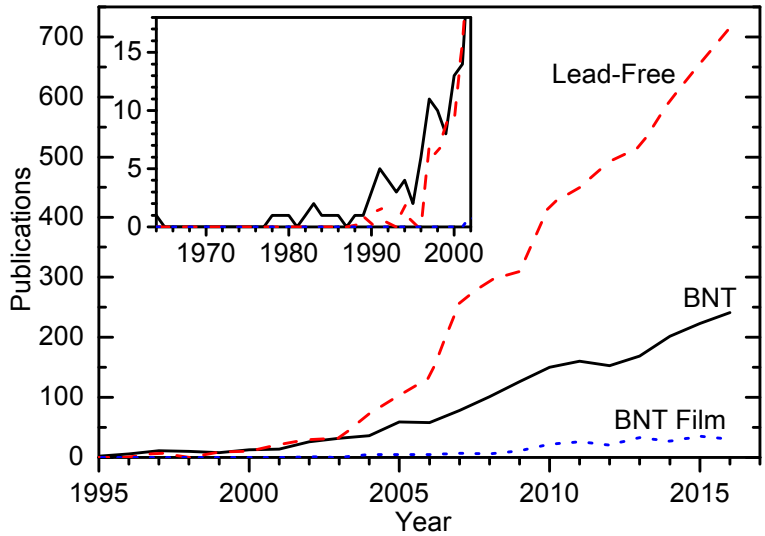

Figure 5.1 Number of yearly publications on lead-free piezoelectric materials. Data was compiled by performing searches in Web of Knowledge, http://apps.webofknowledge.com/, October 30th 2017.

151, 165, 166] To the best of our knowledge, our recent work was the first report on aqueous BNT CSD. [232] Besides the decreased working hazard and environmental impact of this synthesis route, the main advantages of the method are the stability of the sols, the simple procedure, and high reproducibility. From our previous work [232] and from literature [13, 47, 144, 187] a pyrochlore secondary phase is known to often accompany the main perovskite phase in BNT materials. XRD patterns of the pyrochlore observed in our previous work were best matched by $Na_{0.32}Bi_{1.68}Ti_2O_{6.46}(OH)_{0.44}$. [211] Related to the fact that this phase is relatively poor in sodium, we have previously shown that excess sodium in the sol resulted in the suppression of the formation of the pyrochlore phase. [232]

Here, the aqueous BNT CSD method was further developed, with focus on three individual topics in sequence. First, introduction of Ba to the aqueous BNT CSD method was treated, addressing the phase purity of thin films and powders. Second, the deposition process was optimized for obtaining thin films with superior microstructure and morphology. Finally, the electrical properties of the thin films were characterized.

5.2 Experimental

Synthesis methods

Distilled water was used as the solvent for all intermediate and final solutions, and the precursors, substrates, and abbreviations are summarized in Table 5.1. Individual precursor solutions were prepared for each cation, and all solutions remained stable after several years. A clear light yellow 0.6 M Ti precursor was prepared by adding TIP to a CA solution (1.8 M)[1] at 80 °C and stirring at 70 °C overnight. The exact Ti concentration was measured by thermogravimetric analysis of the resulting TiO_2 from three parallels of 1.00 ml heat treated at 1000 °C for 6 h. A 1.0 M solution of Bi was obtained by stirring BiCit, EA (1.5 M), and ammonia for pH 7-8 for a few minutes. The 0.2 M Ba solution was prepared by mixing Ba nitrate, CA (0.4 M), EDTA (0.2 M), and ammonia for final pH 7-8. The NaOH solution was used as Na precursor directly.

Several sols of different compositions were prepared by mixing the cation precursor solutions and adjusting the concentration by diluting with distilled water or by careful evaporation at 70 °C. Adding the undiluted NaOH solution would sometimes lead to a precipitate which re-dissolved upon stirring. Due to the large concentration of citric acid, ammonia was added to adjust the pH to neutral. The final concentration used for preparing films was 0.3 M (relative to the perovskite stoichiometric unit).

Thin film fabrication was carried out in an ISO 7 level clean room. Substrates were prepared for thin-film deposition by cleaning the surface with ethanol and ISO 5 cleanroom wipes (ThermaSeal 60, ITW Texwipe, Kernersville, USA), heat treatment in O_2 at 550 °C for 5 min, and oxygen plasma surface activation (Diener Electronics Femto Plasma cleaner, Ebhausen, Germany). The oxygen plasma treatment greatly enhanced the wetting of the sol, and was required for deposition of the initial layer. Subsequent layers wetted the oxide thin film sufficiently without the need for surface activation. The substrates were attached to the spin-coater chuck (Laurell Technologies WS-400B-6NPP-LITE/ AS, North Wales, USA) and sprayed with compressed air (cleanroom quality) in order to remove any particles and avoid

Table 5.1 Summary of chemicals and materials.

Abbr.	Name	Chem. formula	Supplier	Grade
TIP	Ti tetraisopropoxide	$Ti(OCH(CH_3)_2)_4$	Sigma-Aldrich, SKU 87560	>97 %
CA	citric acid	$C_3H_5O(COOH)_3$	Sigma-Aldrich, SKU C0759	99 %
BiCit	Bi citrate	$BiC_3H_5O(COO)_3$	Sigma-Aldrich, SKU 480746	99.99 %
EA	ethanolamine	$H_2N(CH_2)_2OH$	Sigma-Aldrich, SKU 411000	>99.5 %
ammonia	ammonia solution	NH_3 (aq)	Sigma-Aldrich, SKU 05002	(aq) 33 %
	Ba nitrate	$Ba(NO_3)_2$	Sigma-Aldrich, SKU 217581	>99 %
EDTA	ethylenediaminetetraacetic acid	$C_{10}H_{16}N_2O_8$	Sigma-Aldrich, SKU E9884	99.4-100.6 %
	Na hydroxide solution	NaOH	Sigma-Aldrich, SKU 35274	4.00 M
SiPt	platinized silicon	$Si_{100}\|TiO_{x,20nm}\|Pt_{111,40nm}$	MEMS Exchange	
ST	single crystal strontium titanate substrate	$SrTiO_3$	Crystal GmbH, Part No 1STO 101E	1×1×0.05 cm^3 (100)
ST:Nb	1 at% Nb doped ST	$SrTi_{0.99}Nb_{0.01}O_{3+\delta}$	Crystal GmbH, Part No 1STO 122E1	1×1×0.05 cm^3 (100)

[1] Molarities in parenthesis correspond to the concentration of the final solution.

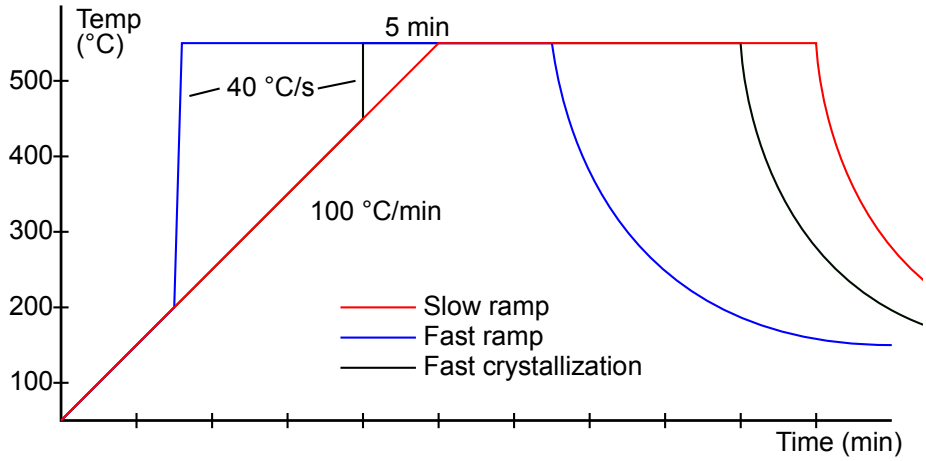

Figure 5.2 Different pyrolysis temperature ramp schemes.

so-called comet formation. A syringe with 0.2 µm filter was used for depositing 2 drops of sol, followed by promptly initiating the spin. Different spin conditions were tested. The most homogenous film thicknesses were obtained by accelerating by 1500 rpm/s to 3500 rpm for 30 s. Accelerating by 300 rpm/s to 3000 rpm occasionally led to inhomogeneous thickness, visible by different iridescence colors. After spinning, the samples were dried by hot-plate at 90-200 °C.

Pyrolysis and annealing were conducted in a rapid thermal processing (RTP) oven (Jipelec Jetfirst 200 mm, Semco Technologies, Montpellier, France). The samples were confined within a custom-made quartz glass lid placed on a Si carrier wafer in order to protect the RTP chamber from volatile Na and Bi. Three different pyrolysis temperature ramp schemes were employed in Section 5.3.2, as illustrated in Figure 5.2. In each case, the pyrolysis holding time and temperature were 5 min at 550 °C, and the cooling rate was as fast as the RTP allowed. In the other sections of this work, the *fast ramp* scheme was employed. The atmosphere in the chamber was controlled by evacuating to 10 mbar before introducing pure O_2 to ambient pressure. Spin coating and pyrolysis were repeated five times unless otherwise stated.

Electrical contacts were applied by sputtering gold top electrodes through a plastic film mask with an array of 1×1 mm^2 voids (Edwards Sputter coater s150B). The bottom surfaces of the Nb doped ST substrates were ground with SiC abrasive sheets and coated with gold in order to obtain better electrical contact.

Powder gel samples were prepared by drying portions of the sols at 120 °C for 48 h. The crushed dry gels were calcined in open alumina crucibles, ramping at 300 °C/h and holding for 2 h (Nabertherm P330, Lilienthal, Germany). The powder layer thickness was kept thinner than 1 mm in order to ensure proper access of oxygen for oxidation of Bi during the thermal decomposition of the gels.

Characterization methods

Phase content of films was characterized by grazing incidence X-ray diffraction (GIXRD) at 2° incidence angle (Bruker D8 Advance DaVinci with Lynxeye XE linear detector, Billerica, USA). Powder samples were characterized in Bragg-Brentano mode (XRD) with a variable

slit size. Lattice parameters were obtained by Rietveld refinement (Bruker AXS Topas version 5), assuming the R3c symmetry for all compositions. [42]

Microstructural images were captured by a field-emission scanning electron microscope (SEM), employing the in-lens secondary electron detector (Zeiss Ultra 55 Limited Edition, Oberkochen, Germany). Samples for cross-sectional images were fractured in a controlled manner by scribing sections of the surface, breaking, and investigating the un-scribed areas (Dynatex international DXIII, Santa Rosa, USA).

Measurements of electrical properties were conducted on the thin-film measurement setup with primitive linear bipolar 500 Hz voltage cycling (AixACCT TF 2000 FE with TFSHU_e31 extension, Aachen, Germany). No leakage current correction or data manipulation were applied. Some samples were conductive in only one direction upon the first measurement. In this case, oppositely directed unipolar cycles were stepwise ramped up to 30 V, at which point a measurement anomaly occurred, significantly reducing the leakage current in both directions for subsequent measurements. Bipolar voltage cycles up to 100 V was then applied stepwise. The reported measurements are from stepwise decreasing of voltage amplitude, finally doing the frequency dependent measurements at 50 V. Leakage current measurements were done with the same equipment, increasing the voltage stepwise with 2 V and holding for 2 s, measuring during 70-90 % of the step.

5.3 Results and discussion

Barium was successfully added to the previously reported aqueous BNT sols. [232] Despite the complex composition of the sol containing Na, Bi, Ti, and Ba cations, the prepared sols were still stable after more than a year, demonstrating that the selected methods for stabilization of the cations in water were effective. The preparation of the sol is easily adapted as only simple procedures are required. Furthermore, the sol is pH neutral, cheap, safe, and environmentally friendly. The topics phase purity, film microstructure, and electrical properties will be treated in sequence.

5.3.1 Phase purity of BNT-Ba

Phase pure BNT-Ba thin films and powders were achieved (according to XRD). The addition of Ba caused a slight increase in the tendency to form the pyrochlore secondary phase, but phase pure BNT-Ba thin films could be obtained. Strategies to ensure the phase purity will be treated in the following.

GIXRD patterns of the pyrolyzed BNT thin films doped with 0 to 9 % Ba on A-site deposited on ST are shown in Figure 5.3a. Diffraction patterns of the films both before and after annealing at 800 °C are displayed. Phase pure films up to 9 % Ba could be obtained by pyrolysis at 550 °C followed by annealing at 800 °C. In the as-pyrolized films, it is apparent that increasing amount of Ba caused an increasing amount of the pyrochlore secondary phase. In Figure 5.3c, a magnified 2θ range highlighting the primary pyrochlore reflection and the BNT $(110)_{pc}$ (pseudocubic Miller index) reflection of the as-pyrolized films is shown. The reflection of the pyrochlore phase was constant at 30° 2θ, while the $(110)_{pc}$ BNT reflection was shifted toward lower 2θ values with increasing Ba content. The shift in the BNT reflections demonstrates that Ba was incorporated into the BNT perovskite phase.

GIXRD patterns of BNT-Ba thin films deposited on SiPt substrates are shown in Figure 5.3b. The as-pyrolized films behaved equal to the films on ST with respect to pyrochlore content and phase purity. However, further annealing at either 700 or 800 °C resulted in only a reduction in the pyrochlore content in the thin films on SiPt. This is in accordance with previous work showing that BNT thin films on SiPt substrates have a slightly higher affinity to pyrochlore formation compared to films deposited on ST. [232] This could be due to diffusion of Na into the substrate, causing Na deficiency in the bottom layers of the film.

XRD patterns of BNT-Ba powders prepared from the same sols used to prepare thin films are shown in Figure 5.4a. The BNT-Ba powders were all phase pure without any trace of pyrochlore, and the corresponding shifts in reflections were observed (Figure 5.4b). Rietveld refinements are most accurate for samples with large crystallite sizes, and refinements of the powders calcined at 800 °C yielded an increase of 0.034 (0.61 %) and 0.088 (0.65 %) Å for *a* and *c* parameters, respectively, when increasing the Ba content from 0 to 9 % (Figure 5.4d). The corresponding values of ~0.54 % (*a*) and ~0.59 % (*c*) were obtained by the refinements of thin-film XRD patterns (Figure 5.3d). To the best of our knowledge, the systematic study of unit cell expansion due to Ba doping in BNT has not been previously reported. In Figure 5.4c, the rhombohedral super-reflection at 38.5° is visible only for pure BNT and for BNT-3Ba, in agreement with the literature that BNT-6Ba is at the MPB Ba concentration, suppressing the rhombohedral character with increasing Ba content. [14]

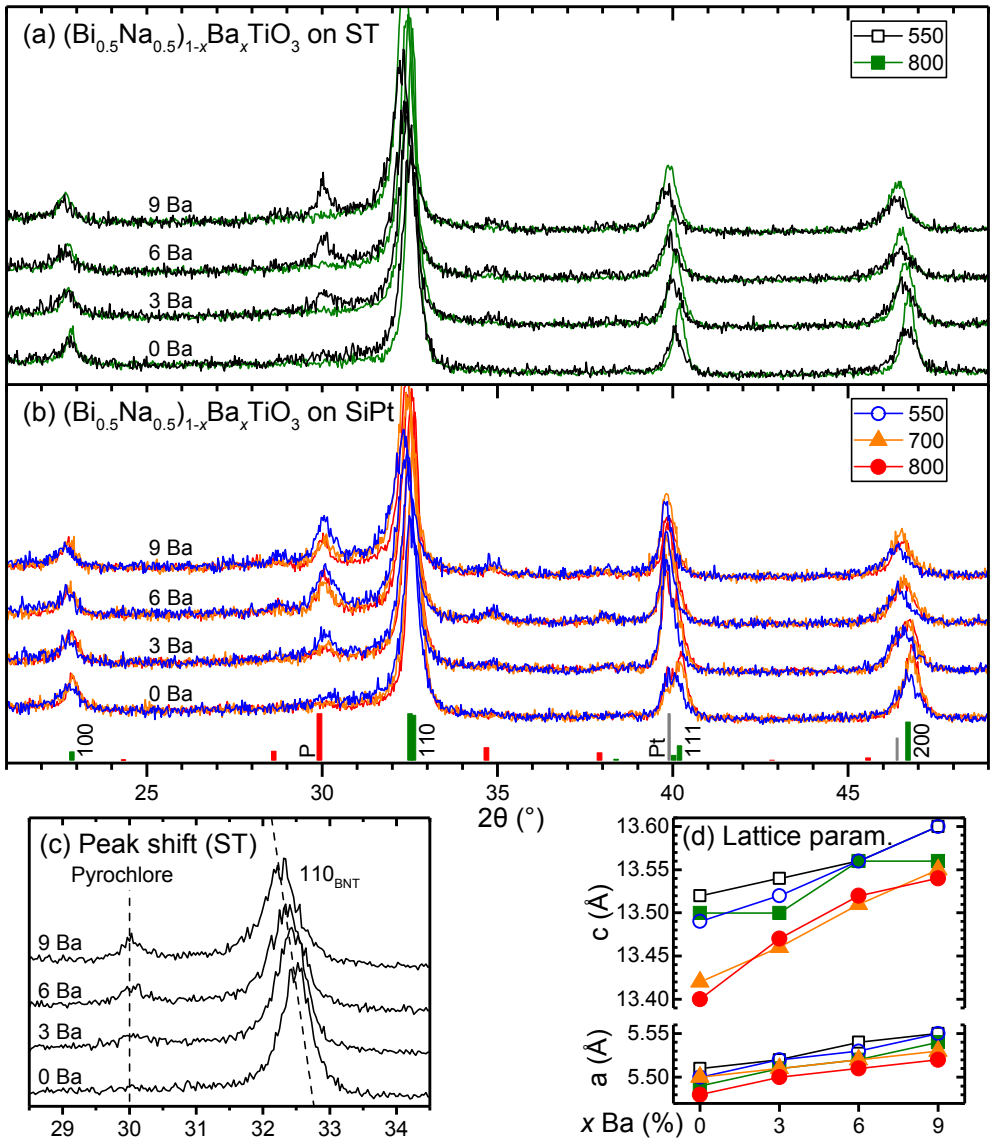

Figure 5.3 GIXRD patterns of thin films with varying Ba content from 0 to 9 % on ST (a) and SiPt (b) substrates. Films were pyrolized at 550 °C and additionally annealed at 700 or 800 °C. These samples are without any A-site excess. Red reference pattern is pyrochlore [211], green pattern is BNT with pseudocubic Miller indices [42]. (c) Magnified 2θ range of as-pyrolized samples on ST. (d) *a* and *c* rhombohedral lattice parameters determined by Rietveld refinement.

Further measures to avoid the formation of the pyrochlore secondary phase

The pyrochlore phase promoted by addition of Ba could also successfully be removed while avoiding high-temperature annealing procedures. Phase purity as a result of variations in the cation stoichiometry and heat treatment is demonstrated by the GIXRD patterns in Figure 5.5. By addition of sodium excess to the sol, phase pure samples of 6Ba were achieved already

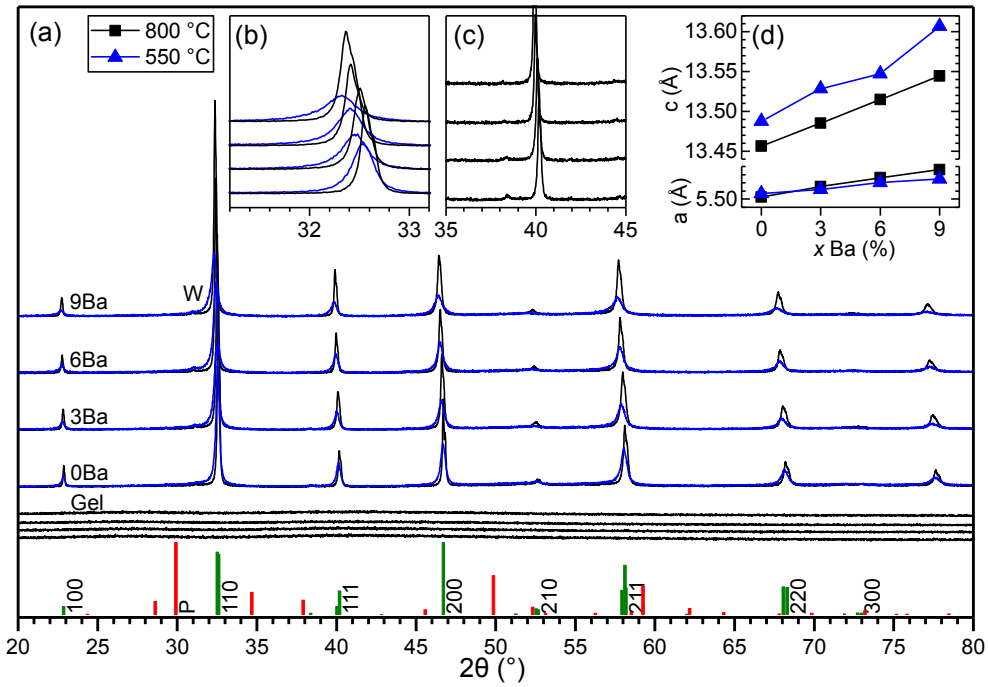

Figure 5.4 (a) XRD patterns of BNT powders heat treated for 2 h at 550 or 800 °C. (b) Magnified 2θ range showing peak shift of the $(110)_{pc}$ reflections. (c) $(111)_{pc}$ reflection and the rhombohedral super-reflection at 38.5° (visible only for 0-3 % Ba). (d) Unit cell parameters obtained by Rietveld refinement. "W" denotes the $(110)_{pc}$ reflection caused by W Lα1 radiation from the instrument.

after pyrolysis at 550 °C. A significant reduction in pyrochlore content in the nominal composition 6Ba-5Na ($Bi_{0.47}Na_{0.52}Ba_{0.06}TiO_3$) and complete removal for 6Ba-10Na is evident in Figure 5.5a. Reduction of the pyrochlore content upon adding Na excess was previously shown to occur for undoped BNT as well. [232] The general trend from all these experiments is that Ba substitution enhanced the formation of the secondary pyrochlore phase, while Na excess suppressed it.

The amount of pyrochlore could also be reduced by increasing the pyrolysis temperature from 550 to 600 °C, as seen in Figure 5.5b. Reducing the holding time to 10 s during heat treatment at 550 °C had the opposite effect (Figure 5.5c), increasing the pyrochlore content, and these samples contained black areas indicative of metallic bismuth. The same films were subsequently heat treated for an additional 10 min at 550 °C. The added heat treatment increased the intensity of the BNT reflections somewhat due to coarsening or increased crystallinity of the BNT phase, but it did not significantly influence the amount of the pyrochlore phase. The remaining pyrochlore after repeated pyrolysis for 10 s and final annealing at 550 °C for 10 min strongly contrasts the obtained phase purity by pyrolysis of a single layer for only 5 min. Thus, the process of ramping and decreasing the temperature without holding at the pyrolysis temperature for a sufficient period of time caused an irreversible stabilization of the pyrochlore secondary phase.

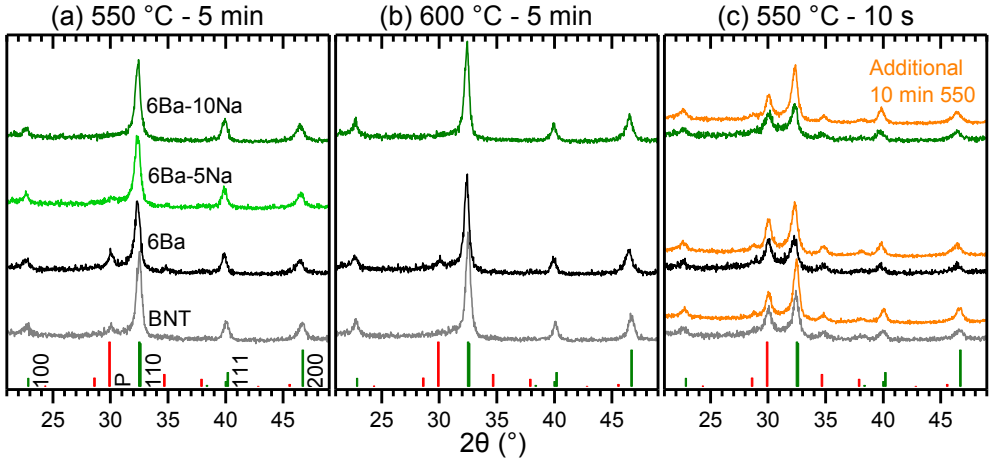

Figure 5.5 GIXRD patterns of 6Ba thin films on ST with varying Na excess content and heat treatment. (a) Reference pyrolysis of 5 min at 550 °C. (c) Increased pyrolysis temperature. (c) Shorter holding time. Patterns in the same vertical alignment are for the same stoichiometries.

Pyrochlore to perovskite reaction

In the thin films containing both BNT and pyrochlore, mass balance considerations dictate that there must be an additional secondary phase present. In samples presented here and in a previous report [232], the XRD pyrochlore pattern is best matched by $Na_{0.32}Bi_{1.68}Ti_2O_{6.46}(OH)_{0.44}$ [211]. The exact composition of the pyrochlore phase observed here cannot accurately be determined by XRD, but pyrochlore phases based on $Bi_2Ti_2O_7$ are commonly reported in BNT literature. [13, 56, 144, 155, 187, 188] In either case, compared to the perovskite, the pyrochlore phase contains larger amounts of Bi relative to Na and Ti. This means that, in addition to perovskite and pyrochlore, an undetected third phase should be rich in Na and Ti. The exact composition of this phase cannot be estimated since the composition of the pyrochlore and the level of cation loss are unknown. In Bi deficient bulk BNT, $Na_2Ti_6O_{13}$ has been detected by SEM. [45] A Na rich secondary phase has been observed in Na excess materials, while TiO_2 was previously observed in Na deficient samples. [46] In these studies, the secondary phases were not detected by XRD, and we propose that an amorphous Na/Ti rich secondary phase was present also in the films prepared here.

The reaction of pyrochlore and this amorphous Na/Ti rich phase into perovskite is thermodynamically favored at temperatures above 550 °C, evident by the increase in phase purity by annealing and by the increased pyrochlore content in samples pyrolized with shorter soaking time (Figure 5.5c). The reaction is therefore proposed to be diffusion controlled. If diffusion is limiting, morphology is important because larger grains will increase the diffusion length to obtain phase purity. Furthermore, higher annealing temperatures and longer holding times will give enhanced diffusion, but could also increase the Na loss, which would stabilize the perovskite-pyrochlore coexistence. BNT thin films have been found to contain increased amounts of pyrochlore both at low heat treatment temperatures where diffusion was too slow, and also at high temperatures where evaporation/loss caused non-stoichiometric films. [145]

The key to obtain phase pure BNT perovskite is therefore to avoid both segregation and evaporation. Segregation is avoided by applying thermal treatment promoting perovskite

nucleation and growth rather than ripening of the secondary phases such as pyrochlore. In our previous work, transient formation of metallic bismuth was observed during pyrolysis at 300-450 °C, and due to growth of the bismuth droplets, the samples could not be further reacted to phase pure perovskite by subsequent annealing at higher temperatures. [232] Bismuth was re-oxidized during subsequent heat treatment above 450 °C, but the level of segregation was too great to allow recombination of the Bi rich and deficient areas by diffusion. The phase resulting from the Bi rich areas was pyrochlore (occasionally Bi_2O_3). This large level of Bi segregation was avoided by applying pyrolysis at 500-550 °C where Bi was quickly oxidized and severe Bi metal segregation was avoided.

In the Ba substituted BNT films reported here, the amount of pyrochlore increased with increasing Ba content, while the severe segregation of Bi due to formation of metallic bismuth was not observed. In these thin films, phase purity could be obtained by annealing, which infer that Bi poor and rich region had not segregated to the detrimental extent as in our previous work. [232] Thus, while both Ba content and low pyrolysis temperatures promote the pyrochlore secondary phase, the degree of cation segregation is significantly different for the two cases.

Ba substitution may have caused increasing amount of pyrochlore by either kinetic or thermodynamic effects. Kinetic effects include reduction of diffusion rate, (minor) increase of diffusion lengths, or delayed perovskite formation due to changes to the chemistry of the decomposition process (e.g. more rapid decomposition of Bi precursor than the Na precursor). It is also possible that Ba addition influenced the Gibbs energy of the perovskite, rendering the pyrochlore phase relatively more favored. A thermodynamic destabilization of BNT due to Ba doping is supported by the observation of BaO secondary phase in BNT-Ba thin films with Na+Bi excess. [157] A destabilization of the perovskite phase would delay or suppress the BNT formation slightly, allowing a larger degree of simultaneous pyrochlore formation.

Exposure to water

Due to the strong correlation between Na stoichiometry and the occurrence of the pyrochlore secondary phase, the influence of exposing BNT thin films to deionized water was investigated. GIXRD patterns in Figure 5.6 demonstrate an increase in pyrochlore content due to extraction of Na from the crystalline BNT films during submergence in water for 5 min between deposition of the layers. The films exposed to water consistently contained a higher amount of pyrochlore. In general, films on SiPt demonstrated higher content of pyrochlore than films on ST, which could be due to a larger degree of Na diffusion into SiPt than for ST. This demonstrates that rinsing of the films or prolonged exposure to the aqueous sol prior to spin coating may promote the pyrochlore phase.

Phase pure thicker films

The thin films reported above (Figures 5.3 and 5.5) consisted of five coatings. For preparation of thicker films, the strategy of adding Na excess was employed to promote phase purity. Thin films consisting of 15 layers were prepared for BNT-5Na and 6Ba-5Na, and the GIXRD patterns are presented in Figure 5.7. Only minor amounts of the pyrochlore secondary phase could be observed in as-pyrolized films, and the pyrochlore was entirely eliminated by final annealing at 700 °C for 10 min. A small amount of an unknown secondary phase in 6Ba-5Na can be seen by the reflection at 29.5°. Compared to reports on BNT thin-film fabrication by

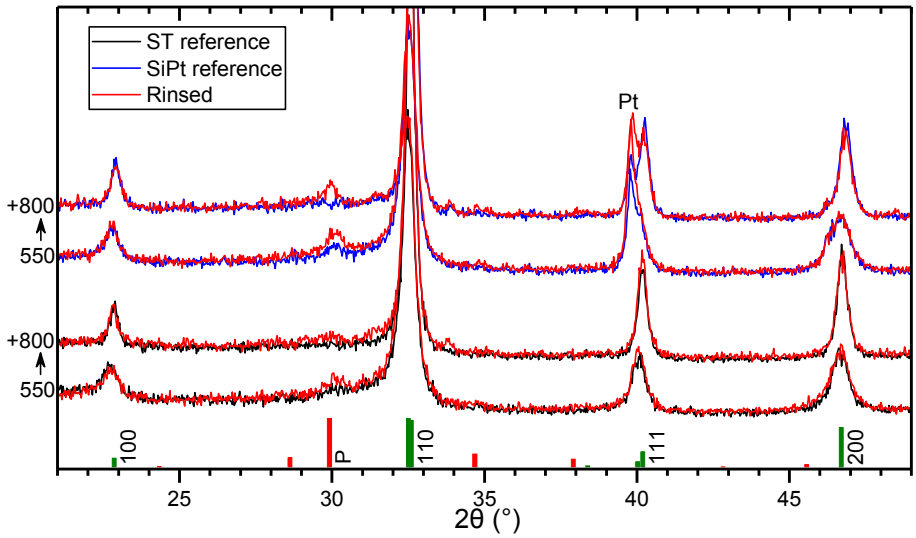

Figure 5.6 GIXRD demonstrating the effect of exposing BNT thin films to water in between deposition of layers. The samples were rinsed between each pyrolized (550 °C) layer, measured by GIXRD after 5 layers, annealed at 800 °C, then measured again. These sols did not contain Na excess.

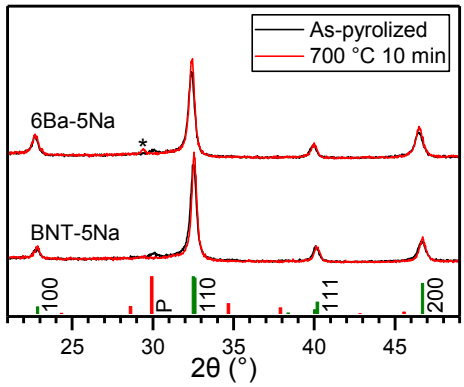

Figure 5.7 GIXRD patterns of 15-layer thick BNT-5Na and 6Ba-5Na films on Nb doped ST. The asterisk, *, denotes an unknown phase.

organic based CSD methods, the aqueous method reported here yields good control of phase purity at both low heat treatment temperatures and low levels of A-site excess. Often, more than 10 % excess is added relative to the A-site [143, 148, 165], and heat treatment temperatures of at least 700 °C are applied [13, 145, 151]. The success of Na excess was apparent, and Na excess according to $A_{1.05}BO_3$ total nominal stoichiometry was implied for the compositions in the remainder of this paper.

5.3.2 Optimization of the microstructure

SEM images of the 15-layer films of BNT and 6Ba (Na excess implied) are displayed in Figure 5.8 and Figure 5.9, respectively. The as-pyrolized films were already relatively dense, with only a small degree of porosity between the layers. Near 100 % density was achieved by

(a) BNT pyrolized 550 °C – 5 min (b) BNT annealed 700 °C – 10 min

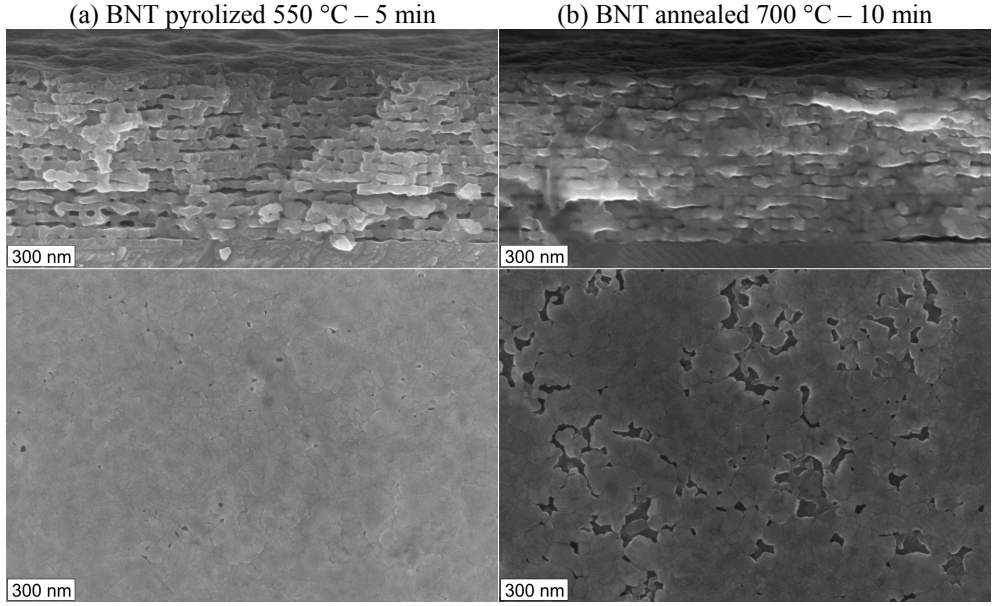

Figure 5.8 SEM images of 15-layer BNT-5Na films on ST:Nb before and after annealing at 700 °C for 10 min.

(a) 6Ba pyrolized 550 °C – 5 min (b) 6Ba annealed 700 °C – 10 min

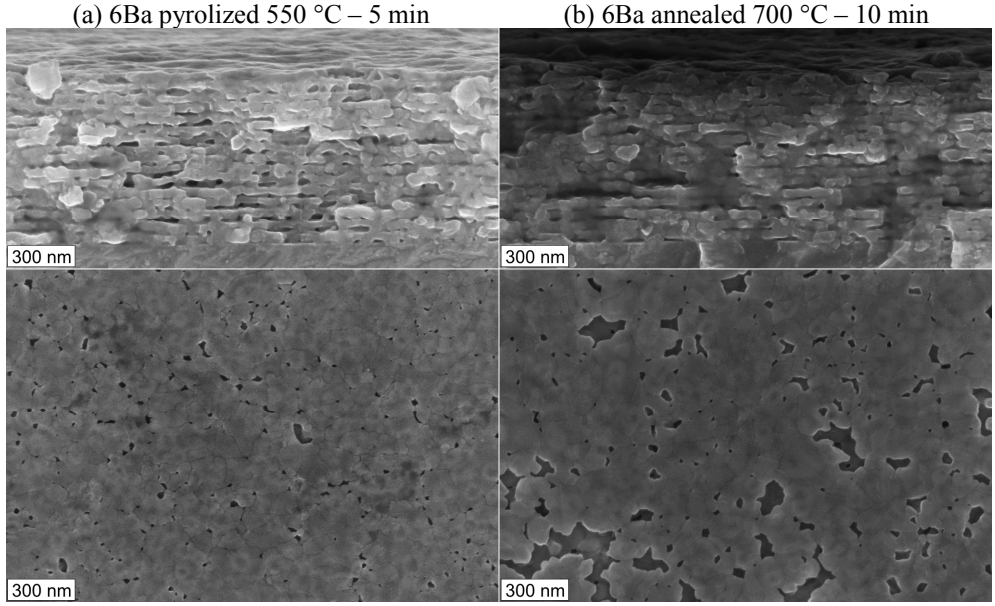

Figure 5.9 SEM images of 15-layer 6Ba films on ST:Nb before and after annealing at 700 °C for 10 min.

annealing. The films were defect free and homogeneous across the entire substrate, and the thickness was approximately 800 nm before, and 780 nm after, annealing, amounting to 52 nm per layer. Some voids were seen in the top layer after annealing, but these did not extend deep into the films.

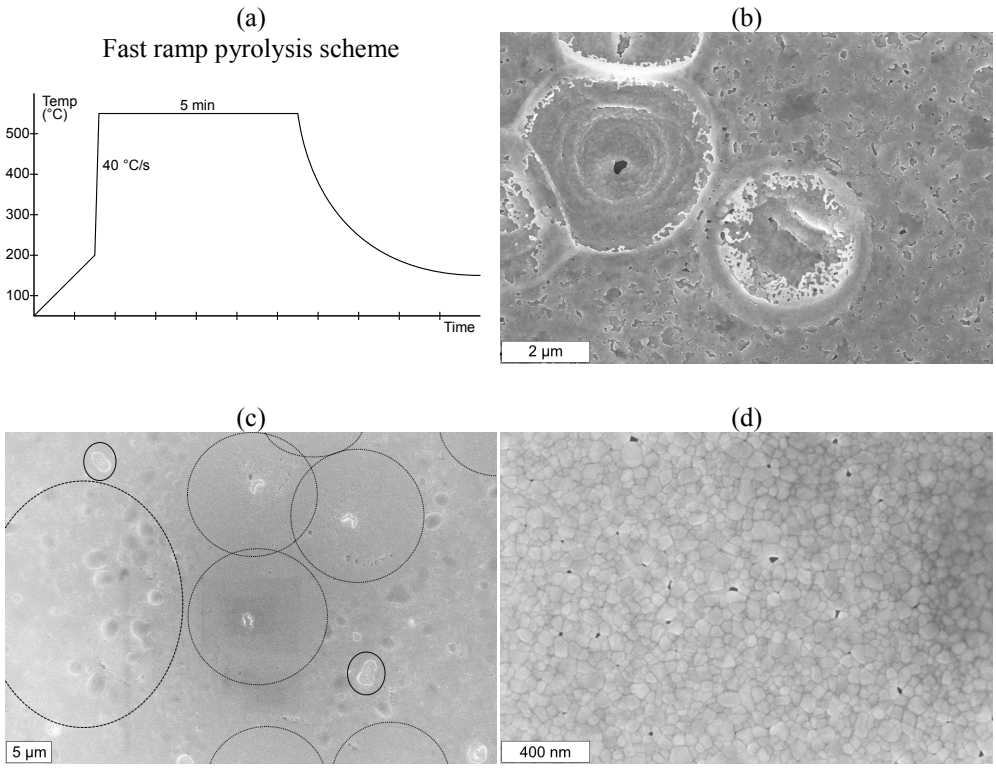

Figure 5.10 SEM images of as-pyrolized microstructure of BNT on ST resulting from *fast ramp* (40 °C/s). (b) Craters in a 10-layer film on ST:Nb. (c) Morphology on a single layer of BNT. Tears with defect-free circles (dotted lines), blisters (dashed line), and detached blisters (solid lines) are marked. (d) High magnification grain structure in c.

The microstructures of thin films on ST shown in Figures 5.8 and 5.9 were obtained by employing an optimized pyrolysis temperature ramp scheme. Thin films deposited on SiPt substrates were homogeneous and dense when applying a ramp rate of 40 °C/s (*fast ramp*) to the pyrolysis holding temperature of 550 °C. Thin films on ST, however, developed craters when the fast ramp was applied.

Pyrolysis ramp rate

In the following, the influence of pyrolysis temperature ramp rate on the microstructure of undoped thin films deposited on ST is treated. Various microstructural features of BNT thin films on ST pyrolized by the fast ramp scheme are shown in Figure 5.10. Craters were evenly distributed across the surface of a 10-layer BNT film deposited on ST:Nb (Figure 5.10b). The substrate is visible in the bottom of the craters, implying that such films will suffer from short circuit when the top electrode is deposited. The microstructure of a single layer of BNT on ST resulting from the fast ramp pyrolysis is shown in Figure 5.10c. Two types of defects related to the evolution of volatiles beneath an already densified portion of the layer were observed. ~1 µm long *tears* in the single layer of BNT were evenly distributed and surrounded by ~10 µm radius defect free circles. In between the defect free circles 2 µm *blisters* covered the entire area. Some of these were teared along the side, and some had detached leaving

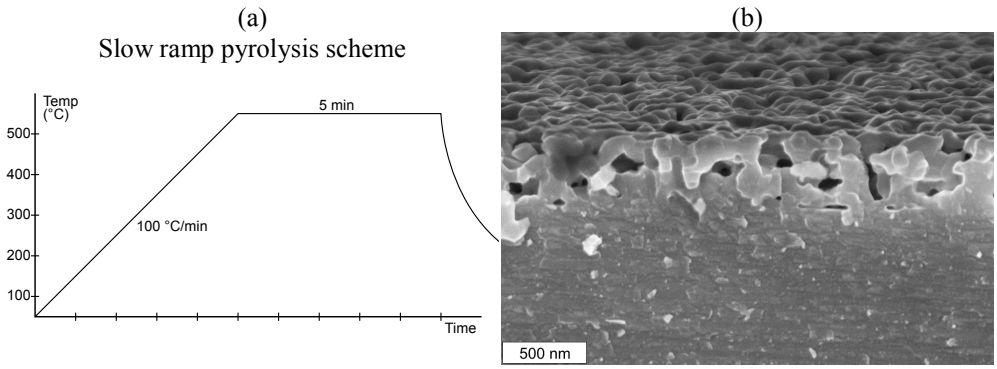

Figure 5.11 (b) SEM image of the microstructure of 10-layer BNT on ST:Nb resulting from *slow ramp* (100 °C/min).

exposed substrate. The 10-20 μm defect free circles were free of blisters, indicating that a gas release through the central tears in practice healed or protected against blister formation.

While the fast ramp pyrolysis scheme resulted in tears and blisters at a large length scale, defect-free, homogeneous, and dense microstructures were observed at high magnification (Figure 5.10d). The morphology of the developed defects suggested that they were related to trapped gas evolved during the thermal decomposition of the organic part of the gels.

In order to allow for organic decomposition prior to formation of the dense crystalline perovskite film, a *slow ramp* scheme was tested, consisting of heating by 100 °C/min. The blisters and tears observed for fast ramp were indeed avoided by the slow ramp, confirming that too rapid gas evolution was the cause of formation of the defects. However, the films prepared by the slow ramp contained significant porosity, as shown in Figure 5.11b. Porosity could be seen already after the initial layer, and after 10 layers the pores were extending through the cross-section of the film, potentially leading to short-circuit of top and bottom electrodes.

In our previous study, it was demonstrated that nucleation of the BNT perovskite phase initiates at 450 °C [232], and the *fast crystallization* temperature ramp scheme was developed to provide crystallization at 550 °C while maintaining the slow organic decomposition. The fast crystallization scheme consisted of heating by 100 °C/min to 450 °C, and by 40 °C/s to 550 °C. The microstructure of a single layer of BNT on ST resulting from the fast crystallization scheme is shown in Figure 5.12. As can be seen in the figure (and in Figure 5.8), the coarsening observed for slow ramp was efficiently circumvented, and the films were defect-free, homogeneous, and dense.

Effect of annealing on film microstructure

The effect of further heat treatment on the microstructure and porosity of 3-layer BNT thin films on ST is shown in Figure 5.13. Heat treatment up to 700 °C had only a limited effect on the density of the films. The thin films pyrolized using the fast crystallization ramp scheme were dense for all heat treatment variants. The thin films pyrolized by slow ramp, however, were equally porous after annealing. A significant coarsening with some grains exhibiting abnormal grain growth (AGG) had occurred after annealing at 800 °C, and for the slow-ramp

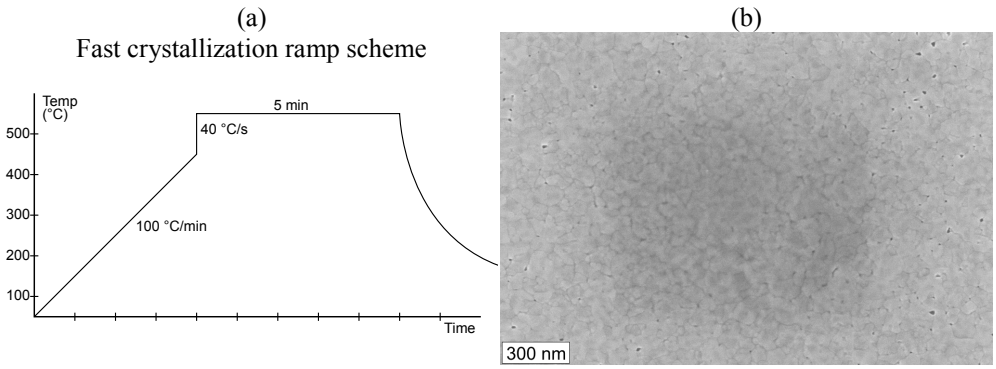

Figure 5.12 (b) SEM image of microstructure of a single layer of BNT on ST after pyrolysis using the *fast crystallization* ramp scheme

film, this caused pores with diameter on the order of the film thickness, potentially leading to short circuit when the top electrode is applied.

Some porosity appeared in the top layer of the thin film in Figure 5.13d after annealing at 700 °C, in accordance with the observation in 15-layer films (Figures 5.8 and 5.9). The same voids were not observed in films annealed at 600 °C (not shown). These pores were not detrimental to the film quality as they did not extend far into the film. It is suggested that the voids occurred as individual grains disconnected from the film, and that a slower ramp rate during annealing will suppress the effect.

From Figure 5.13 it can be seen that grain growth and coarsening did not occur to a significant degree for annealing up to 700 °C. In case of annealing at 800 °C, however, grain growth was significant. The microstructure of the thin films can therefore be controlled by careful optimization of annealing temperature in the interval 700-800 °C. Already after pyrolysis at 550 °C, the films were phase pure and dense, allowing for implementation where heat treatment temperatures are limited by the process or other aspects of the device. As-pyrolized samples had small grains, approximately 50 nm, maintaining a large potential for densification and coarsening upon further annealing.

Explanation for the formation of defects during fast ramp

In the following, a possible explanation for the formation of the gas release defects are discussed. Both the tears with defect-free circles and the blisters were only observed on ST substrates, while defect free microstructures were observed for the films deposited on SiPt with the same sol and fast ramp. An additional piece of information was obtained by the behavior of *gel* films during investigation by SEM. The electron beam caused development of defects resembling the gas release tears treated above. These defects were formed on SiPt, but not on ST substrates. Figure 5.14 shows such an area of defects forming and growing with time as the electron beam scanned over the film surface repeatedly. In the following it will be argued that ST substrates are inherently subject to higher ramp rate than SiPt during RTP, while the opposite is true during SEM investigation.

An illustration of the relevant effects during pyrolysis in the RTP is shown in Figure 5.15. The substrates are situated at a carrier Si wafer, and the temperature is controlled by a thermocouple underneath this wafer. The films are heated by visible light from above, and the

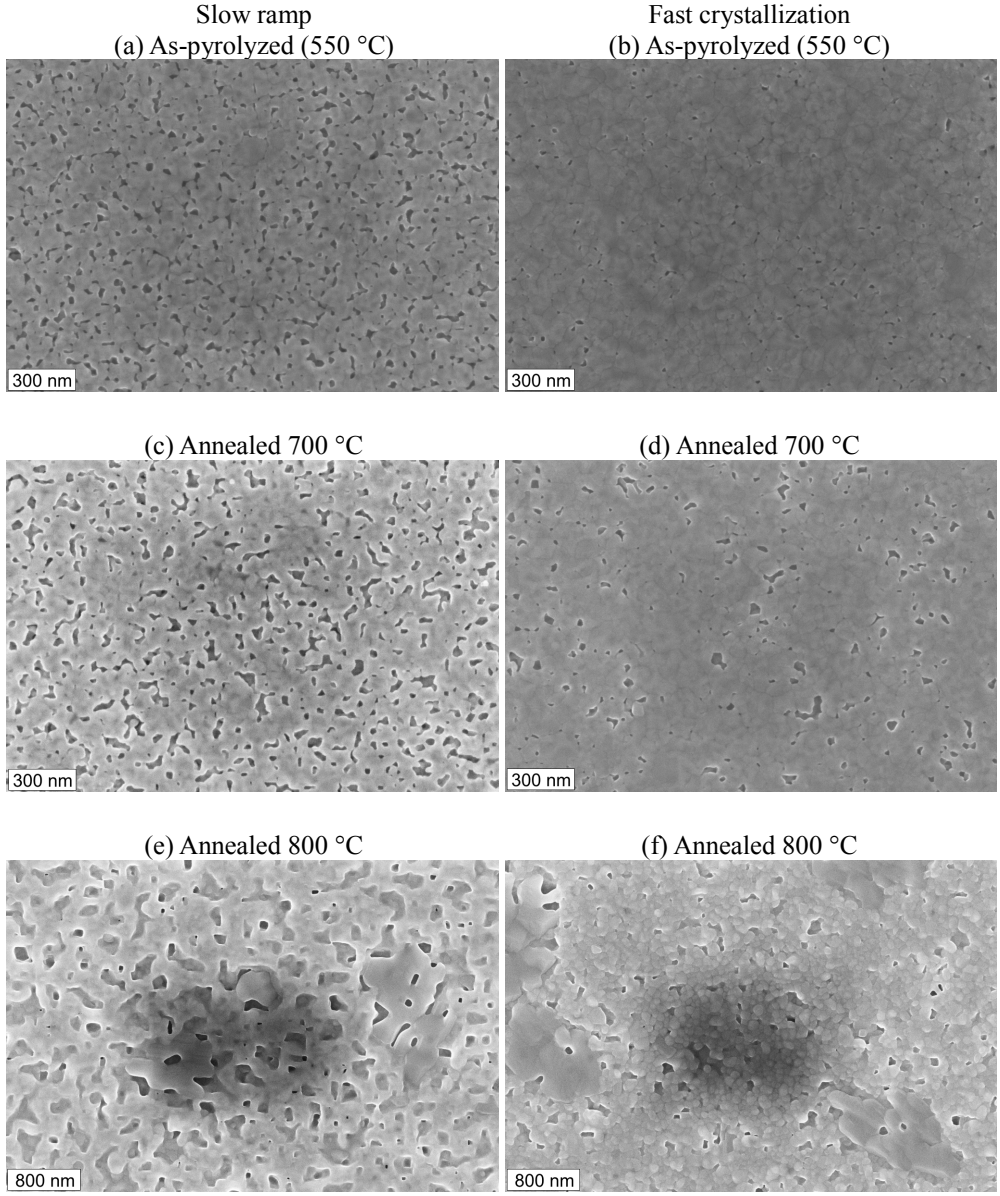

Figure 5.13 SEM images of 3-layer BNT films on ST prepared by the slow ramp and fast crystallization pyrolysis schemes. Images of 800 °C samples are less magnified.

region with the thermocouple is inherently cooler due to the water-cooled floor of the chamber. There are primarily two main differences between ST and SiPt that could lead to different ramp rates of the films despite pyrolizing the samples simultaneously or using the same temperature-time program. First, the Pt electrode on SiPt is mirror-like and reflects a large portion of the incident light compared to ST. Second, heat conduction in Si is significantly better than for ST, and since heat transport is proportional to both heat conduction and temperature difference, the temperature in a film on ST must be greater than for SiPt in

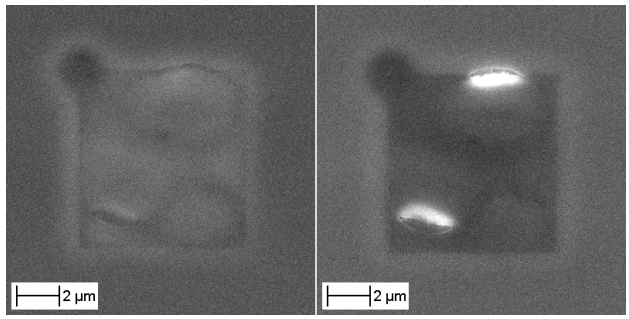

Figure 5.14 SEM images of the development of defects in BNT *gel* films (not yet pyrolized) on SiPt substrates by repeated exposure to the electron beam. The picture to the right is captured directly after the one to the left.

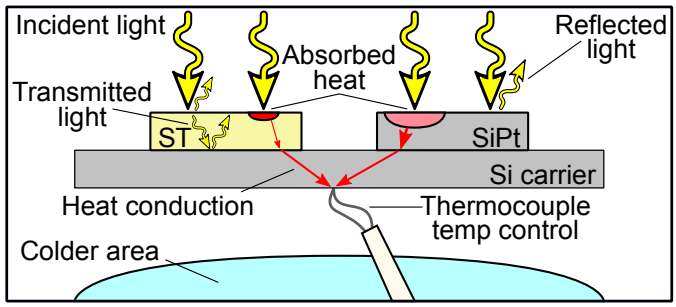

Figure 5.15 Illustration of suggested mechanisms leading to higher heating rate for ST substrates than SiPt during pyrolysis by RTP. Differences in arrow sizes and thicknesses express different heat transport magnitudes. Two independent effects are visualized. 1: greater light absorption for ST. 2: greater heat conduction away from film for SiPt.

order to yield the same response from the thermocouple. In other words, the temperature overshoot in the film and the steady-state difference between film and thermocouple are both greater for films on ST.

The apparent opposite behavior of SiPt versus ST during SEM investigation is equally explained by difference in the heating rates. When investigating insulating or semiconducting materials in SEM, charging of the sample poses a challenge, and this is more relevant for ST, both due to higher conductivity of Si than ST, but also due to the Pt electrode spreading the charge out on the surface of the SiPt substrate. The result was that local charging in ST deflected the incoming beam to a larger extent, leading to a smaller current passing through the investigated area of the film than for SiPt. The stronger current passing through the film on SiPt heated the gel significantly more than for ST.

5.3.3 Electrical properties

Electrical properties were measured for the BNT and 6Ba thin films presented in Figures 5.8, 5.9 (SEM), and 5.7 (GIXRD). The polarization-field hysteresis loops measured up to 100 V are shown in Figure 5.16 a and b. The hysteresis loops were comparable to the properties of state of the art BNT films prepared by other methods. [13, 143, 168] At fields as strong as 1400 kV/cm and 500 Hz cycling frequency, the characteristic hysteresis loops were still

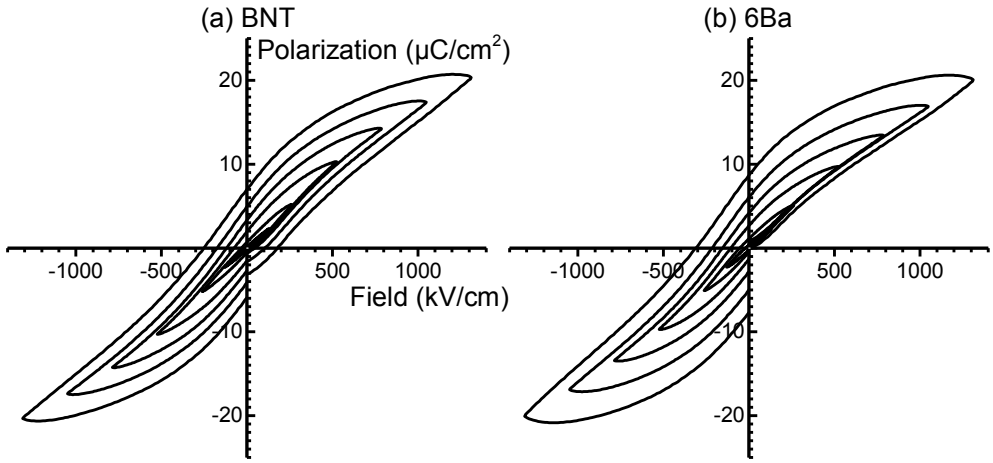

Figure 5.16 Polarization-field loops of BNT (a) and 6Ba (b). Measurements were conducted at 500 Hz with a linear increase/decrease of field.

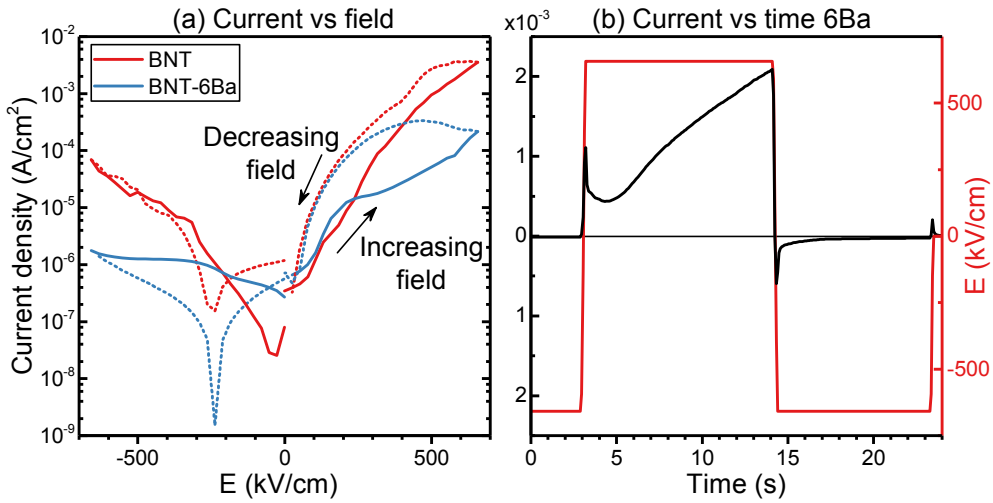

Figure 5.17 Leakage current in BNT and 6Ba. (a) Stepwise change of voltage with 2 s holding time and current measurement during 1.4-1.8 s of each step. (b) Current during holding at constant voltage for 10 s, shown for 6Ba.

obtained. Thus, little sign of leakage current was and the films were resilient towards dielectric breakdown. Saturation polarization and remnant polarization were approximately 20 and 8 μC/cm², respectively. The behavior of the two thin films were comparable, and variations within the same samples yielded larger variations than due to the Ba content. In literature, the electrical properties of BNT thin films are commonly reported for high cycling frequencies (0.1-10 kHz) exclusively. [165] In the following, the influence of the frequency on the leakage characteristics is treated.

Leakage current measurements are shown in Figure 5.17. The obtained values were comparable to what can be found in literature for BNT thin films produced by other methods.

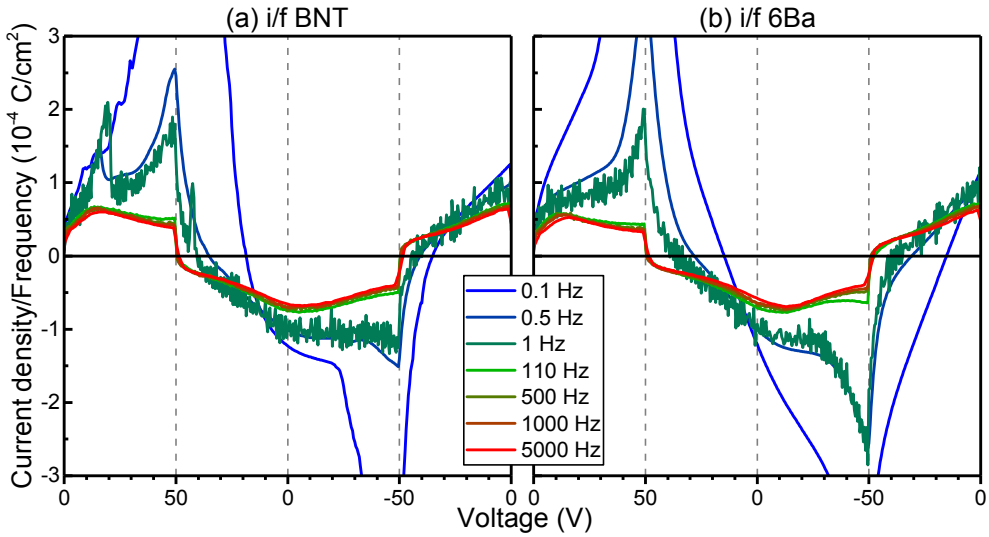

Figure 5.18 Current density over frequency versus voltage during ferroelectric switching.

[164] In general, the leakage current with positive bias to the top electrode was several orders of magnitude larger than for negative bias. Moreover, for positive bias, the current was larger during stepwise decrease of voltage than during the preceding voltage increase, while for negative bias the decreasing voltage current was smaller. This trend was confirmed by measuring current during holding at constant voltage, as seen in Figure 5.17b. For negative bias, the initial switching current peak quickly reduced into the constant leakage current level, while for positive bias the leakage current continued to increase with time. This increase in conductivity with accumulated leakage yielded highly irreproducible leakage current measurements of the sort in Figure 5.17a. The primary recurring characteristic of measurements was the asymmetry of conductivity, with current of positive bias orders of magnitude larger than for negative bias.

The influence of leakage current on the hysteresis measurements is further illustrated by plotting current density divided by frequency for polarization cycles of varying frequencies, shown in Figure 5.18. The current densities of measurements with different frequencies vary by orders of magnitude, and direct comparison of the measurements is therefore not feasible. The current density consists of two components: the ferroelectric response/capacitance and the leakage (dc) current. If one assumes that the ferroelectric response is independent of time, the surface charge density is a direct function of the electric field. For this reason, the ferroelectric component of the current density is proportional to the cycling frequency, and should normalize to the same value when dividing by frequency. Leakage current, on the other hand, is independent of frequency, and should be relatively less significant when divided by a large frequency. Converging graphs of different frequencies therefore signify that leakage current was not significant at those frequencies. Bulk BNT-6Ba samples have been shown to reach saturation switching polarization within 10^{-4} s when applying 60 kV/cm. [233] For comparison, bipolar cycling to 50 V at 1000 Hz signifies applying zero to 750 kV/cm within 2.5×10^{-4} s, rendering the assumption of time-independent ferroelectric response viable.

In Figure 5.18, the strength of the described *i*/*f*-approach is striking. The current densities of measurements from 110 to 5000 Hz are shown to be near identical when adjusting for the proportional frequency dependence. Because varying the frequency did not significantly influence *i*/*f* despite allowing ten times more time for leakage contributions for 500 Hz than for 5 kHz, it is apparent that the measurements of high frequencies were dominated by the ferroelectric response without much influence from leakage. Interestingly, the same convergence values were obtained for both BNT and BNT-6Ba, supporting the notion that ferroelectric response of these materials during these conditions (strong electric fields and clamping effects from the substrate) were practically identical. It should be noted that the switching peak at approximately ±10 V was shifted to slightly higher voltages when increasing frequency from 500 Hz to 5 kHz, demonstrating that these frequencies were on the limit of allowing full ferroelectric response in these films, in accordance with the reported switching time of 10^{-4} s. [233] Furthermore, the 500 Hz leakage current (visible as deviation from 5 kHz at high voltage) was larger for negative voltage than positive voltage in BNT-6Ba, explaining the unclosed hysteresis loops in Figure 5.16. For lower frequencies, however, the deviation from 5 kHz was larger for positive bias, reflecting the much larger (and increasing) leakage current in positive direction seen in Figure 5.17. In other words, high frequency leakage was most significant in negative direction, while low frequency leakage was strongest in positive direction.

Asymmetry of leakage current characteristics has been explained by unequal distribution of oxygen vacancies throughout the thickness of the film. [164] In general, the primary active point defects in BNT are oxygen vacancies, which can arise from either A-site deficiency due to volatile cations according to

$$2\mathrm{Na}_{\mathrm{Na}}^{\times} + \mathrm{O}_{\mathrm{O}}^{\times} \xrightarrow{\mathrm{BNT}} 2\mathrm{V}_{\mathrm{Na}}' + \mathrm{V}_{\mathrm{O}}^{\bullet\bullet} + 2\mathrm{Na(g)} + \tfrac{1}{2}\mathrm{O}_2\mathrm{(g)} \tag{5.1}$$

$$2\mathrm{Bi}_{\mathrm{Bi}}^{\times} + 3\mathrm{O}_{\mathrm{O}}^{\times} \xrightarrow{\mathrm{BNT}} 2\mathrm{V}_{\mathrm{Bi}}''' + 3\mathrm{V}_{\mathrm{O}}^{\bullet\bullet} + \mathrm{Bi}_2\mathrm{O}_3\mathrm{(g)} \tag{5.2}$$

or due to A-site non-stoichiometry:

$$\mathrm{Na}_2\mathrm{O} + 2\mathrm{Bi}_{\mathrm{Bi}}^{\times} + 2\mathrm{O}_{\mathrm{O}}^{\times} \xrightarrow{\mathrm{BNT}} 2\mathrm{Na}_{\mathrm{Bi}}'' + 2\mathrm{V}_{\mathrm{O}}^{\bullet\bullet} + \mathrm{Bi}_2\mathrm{O}_3 \tag{5.3}$$

In Kröger-Vink notation, V denotes vacancies, subscripts denote the lattice site of the species, while $^{\times}$, $^{\bullet}$, and $'$ denote neutral, positive, and negative charges relative to that site, respectively.

In fact, high oxygen ion conduction has recently been reported in BNT [45], and the conductivity in bulk BNT samples was decreased by several orders of magnitude by donor doping with either Bi on Na-site or Nb on Ti-site. [47] Donor doping decreases the oxygen vacancy concentration according to the reverse of Equation (5.3). The same approach could likely be exploited for thin films prepared by the aqueous BNT CSD. Since Na excess in general is beneficial with respect to phase purity, an inherent level of Na substitution for Bi according to Equation (5.3) poses a challenge. This can likely be overcome by donor doping of for example Nb^{5+} on B-site. Both Nb doping and O_2 annealing were shown to decrease the conductivity in BNT thin films. [111]

Another commonly reported measure to decrease the conductivity in BNT samples is by Mn substitution on Ti site. [26, 156, 164, 169, 178, 179, 212-215] Mn can have several valence states and for that reason it contributes to higher electronic Ohmic leakage current at low

fields. However, it efficiently extends the range of fields where leakage remains Ohmic, reducing the high field ionic conductivity. [164] This was explained by formation of Mn-V_O complexes reducing the mobility of oxygen vacancies.

In general, the high frequency ferroelectric properties of the BNT and BNT-6Ba thin films were comparable to state of the art BNT films produced by other means. The low frequency leakage current is not often reported, and it was here characterized to a larger extent, demonstrating that the reported 500 Hz measurements accurately described the leakage free properties of the films. The relatively good properties of the film, coupled with the inherent acceptor doping effect of the Na excess, yields a very promising foundation for further investigation with possible donor or Mn doping.

5.4 Conclusions

The Ba modified BNT aqueous chemical solution deposition method was demonstrated to yield phase pure thin films with complete control of the evolved microstructure and with electrical properties comparable to values from the literature.

In the previously reported aqueous preparation of undoped BNT thin films, phase pure films resulted from pyrolysis of nominally stoichiometric sols at 550 °C. [232] Here it was demonstrated that the Ba addition promoted a slight increase in the pyrochlore secondary phase content. Despite this, two strategies to ensure the phase purity of the BNT-Ba films were demonstrated: annealing at 800 °C, or adding 10 % Na excess.

Dense and defect-free BNT thin films were obtained on both SiPt and ST substrates. In both cases, the pyrolysis holding time and temperature of 5 min at 550 °C were employed. However, the temperature ramp rate was shown to greatly affect the microstructure and morphology of the films. Dense and defect free BNT thin films were obtained on SiPt by applying the fast ramp rate of 40 °C/s. For ST substrates, however, this led to morphologically defective films with inflation and tearing due to too rapid evolution of gaseous decomposition products. Applying the slow ramp of 100 °C/min resolved the morphological defects, but yielded a porous microstructure. The optimal pyrolysis ramp scheme for BNT thin films on ST substrates was identified as the fast crystallization, heating by 100 °C/min to 450 °C followed by rapid ramp of 40 °C/s to 550 °C. This strategy retained the slow organic decomposition, while ensuring that crystallization primarily occurred at 550 °C. Employing this heat treatment procedure yielded phase pure and dense films already after pyrolysis.

The electrical properties of BNT and BNT-6Ba were investigated and found to be comparable to that of similar compositions produced by alternative fabrication methods. The films were resilient toward dielectric breakdown, exhibiting well defined polarization-field hysteresis loops up to 1400 kV/cm. While the conductivity at 500 Hz was marginal, it was demonstrated that the level of leakage was not insignificant for lower cycling frequencies. The films showed direct current leakage on the order of 10^{-6}-10^{-3} A/cm^2 at 600 kV/cm with a strong asymmetry for positive and negative bias. These values were on par with state of the art BNT thin films, but it was proposed that conductivity can be further decreased by either donor doping or by isovalent Mn doping.

Compositionally engineered $Bi_{0.5}Na_{0.5}TiO_3$ thin films prepared by aqueous chemical solution deposition

Paper 3

Mads Christensen, Mari-Ann Einarsrud, Tor Grande

Manuscript not submitted

Abstract

$Bi_{0.5}Na_{0.5}TiO_3$ (BNT) based piezoelectric materials are promising candidates for replacement of toxic lead-containing $Pb(Zr,Ti)O_3$. BNT is commonly modified by the cations Ba, Sr, K, Li, and Nb, and compositions known for large strain response in bulk were successfully prepared in thin-film form by aqueous chemical solution deposition (CSD) in this work. Stable solutions were prepared from combinations of the precursors Bi citrate, Sr/Ba nitrate, Li/K/Na hydroxides, Ti isopropoxide, and ammonium niobate oxalate. The sols were stabilized by addition of citric acid, ethanolamine, and EDTA, and the pH was adjusted by ammonia. Phase pure BNT thin films were deposited on $SrTiO_3$ single crystal substrates, and powder samples were prepared to provide supplementary insight. The films were confirmed to be ferroelectric with properties comparable to thin films prepared by other methods. Finally, the mechanisms controlling the phase purity and factors influencing the electrical properties were thoroughly investigated. This work demonstrates that the aqueous CSD method is robust with respect to fabrication of compositionally engineered BNT thin films.

6.1 Introduction

Piezoelectric materials have many technological applications, and the majority of devices today are based on the $Pb(Zr,Ti)O_3$ (PZT) material system. [231] Due to the toxicity of lead, however, governmental regulations and environmental considerations encourage development of lead-free alternative materials. Since 2004 this research field has grown significant with excess of 600 publications annually. [4, 35, 36, 234]

The primary alternative lead-free material systems for actuator applications are currently based on $K_xNa_{x-1}NbO_3$ (KNN), $Bi_{0.5}Na_{0.5}TiO_3$ (BNT), and $(Ba,Ca)(Ti,Zr)O_3$ (BCZT). [4, 15, 23, 30, 31, 33, 37] The BNT family has advantages in applications where large strain and temperature insensitive properties are required. Undoped bulk BNT possesses only moderate piezoelectric properties, but upon doping with for example Ba, K, and Nb, a so-called incipient piezoelectric material is obtained. [32] Incipient piezoelectric materials are characterized by the lack of piezoelectric response at zero electric field with an onset piezoelectricity due to a reversible electric field induced phase transition from relaxor to the ferroelectric state. The phase transition gives rise to a repeatable unipolar strain response close to 0.5 %, which is large even when compared to PZT. [66] To achieve incipient piezoelectric properties and large strain in BNT, several alternative chemical modifications to the system have been reported. The first report on *giant strain* was for BNT modified with 6 % $BaTiO_3$ (BT) and 2 % KNN (6Ba-1K-2Nb). [15, 32, 66] Other authors have included alternative dopants such as K, Li, Sr, La, Zr, and Mn. [9, 10, 70, 73, 151, 178, 187] Certain compositions exhibiting increased temperature stability of piezoelectric properties are those of 4Ba-6K-6Li [9] and 8K-4Sr-2Li-2Nb [10]. Moreover, incorporation of Mn, Zr, or Nb have been demonstrated to reduce the leakage current. [46, 47, 178]

Chemical solution deposition (CSD) is the technologically most relevant method for deposition of perovskite thin films in industrial fabrication of devices. BNT and other similar materials are routinely prepared by CSD employing organic solvents and stabilizers, such as 2-methoxyethanol (2-MOE), acetylacetone, acetic acid, methanol, or similar. [13, 143, 144, 148, 151, 165, 166] In general, these processes are either based on hydrolysis-condensation reactions in a 2-MOE based solution, or metal-organic decomposition (MOD) with alternative solvents. [97] Hydrolysis-condensation methods yield stable sols and high reproducibility, but require chemically complicated and time-consuming processing, and employ the highly toxic solvent 2-MOE. [11] MOD fabrication employs less harmful chemicals and is easier to manage, but yields solutions sensitive to aging. [97] Fabrication of BNT thin films by an aqueous method was achieved in our previous work. [232] The aqueous CSD method did not require special accommodations such as protected atmosphere or refluxing steps, and yielded sols impervious to aging. Moreover, all employed chemicals were non-toxic, environmentally friendly, and cheap. In a second study, the method was further developed to include Ba doping, and to achieve thorough control over the microstructure by optimization of deposition and thermal processing parameters. [234]

In this work, the water based BNT CSD method was further developed to include a range of dopants, demonstrating that compositions known to possess large strain in bulk can be prepared by the CSD route. Feasible precursor and solution chemistries were selected, obtaining long term stable sols of 5 representative BNT compositions summarized in Table 3.1. BNT and 6Ba were selected as references, while 6Ba-1K-2Nb, 4Ba-6K-6Li, and

8K-4Sr-2Li-2Nb were selected due to the large and temperature insensitive strain reported for bulk materials. Thin films were deposited on single crystal $SrTiO_3$ (ST), and phase purity, microstructure, and electrical properties were characterized. Due to the requirements of sample geometry and electrode design in samples for thin-film piezoelectric measurements, this first account of fabricating chemically modified BNT focused on ferroelectric properties, while piezoelectric measurements remain a topic for further work. Finally, a thorough treatment of measures for ensuring phase purity and improved electrical properties were discussed. Powders were prepared from the sols for assessment of the BNT synthesis method without influence from thin-film related parameters.

Table 6.1 Overview of BNT compositions. The concentration of dopants in the two latter compositions were rounded to the nearest whole % for implementation in this work.

Notation	**Nominal composition**	**Ref**
BNT	$Bi_{0.5}Na_{0.5}TiO_3$	
6Ba	$Bi_{0.47}Na_{0.47}Ba_{0.06}TiO_3$	
6Ba-1K-2Nb	$Bi_{0.46}Na_{0.47}Ba_{0.06}K_{0.01}Ti_{0.98}Nb_{0.02}O_3$	[15]
4Ba-6K-6Li	$Bi_{0.48}Na_{0.36}Ba_{0.04}K_{0.06}Li_{0.06}TiO_3$	[9]
8K-4Sr-2Li-2Nb	$Bi_{0.47}Na_{0.39}Sr_{0.04}K_{0.08}Li_{0.02}Ti_{0.98}Nb_{0.02}O_3$	[10]

6.2 Experimental

Synthesis methods

The fabrication method was thoroughly treated in two previous articles. [232, 234] All precursor solutions were based on distilled water as the solvent, and the chemicals and substrates are summarized in Table 5.1. Individual precursor solutions were prepared for each cation. The Ti precursor was prepared by adding TIP (0.6 M)[1] to a solution of CA (1.8 M) at 80 °C, turning clear light yellow after stirring at 70 °C overnight. A 1.0 M solution of Bi with pH 7-8 was obtained by mixing BiCit, EA (1.5 M), and ammonia. The 0.2 M Ba and Sr solutions were prepared by mixing Ba/Sr nitrate, CA (0.4 M), EDTA (0.2 M) by stirring and adjusting pH to 7-8 by ammonia. A 0.5 M Nb precursor was prepared by dissolving NAmOx in water at 70 °C and stirring overnight. LiOH (1.0 M) was obtained by dissolution in water. The NaOH and KOH solutions were used as Na and K precursors directly. The exact concentrations of the Ti and Nb solutions were calculated from the mass of oxide resulting from thermogravimetric analysis. All precursor solutions were stable for more than one year.

Several sols of different compositions were prepared by mixing the precursor solutions and adjusting the concentration by diluting with distilled water or by careful evaporation at 90 °C. Due to the large concentration of citric acid, ammonia was added to adjust the pH to 7-10. The final sol concentration used for preparing thin films and powders was 0.3 M. Na or Na+Bi excess were added to obtain a nominal cation stoichiometry corresponding to $A_{1.05}BO_3$. For undoped BNT, this corresponds to 10 % Na excess or 5 % Na+Bi excess, while the percentage is higher for doped BNT due to the lower starting concentration of Bi/Na. Thin films were prepared with Na excess, while powders were prepared from both Bi+Na and Na excess sols.

Substrates were prepared for thin-film deposition by cleaning the surface with ethanol and cleanroom wipes (ThermaSeal 60, ITW Texwipe, Kernersville, USA), heat treatment in

Table 6.2 Summary of chemicals and substrates.

Abbr.	Name	Chem. formula	Supplier	Grade
TIP	Ti isopropoxide	$Ti(OCH(CH_3)_2)_4$	Sigma-Aldrich, SKU 87560	>97 %
CA	citric acid	$C_3H_5O(COOH)_3$	Sigma-Aldrich, SKU C0759	99 %
BiCit	Bi citrate	$BiC_3H_5O(COO)_3$	Sigma-Aldrich, SKU 480746	99.99 %
EA	ethanolamine	$H_2N(CH_2)_2OH$	Sigma-Aldrich, SKU 411000	>99.5 %
ammonia	ammonia solution	NH_3 (aq)	Sigma-Aldrich, SKU 05002	33 wt.%
	Ba nitrate	$Ba(NO_3)_2$	Sigma-Aldrich, SKU 217581	>99 %
	Sr nitrate	$Sr(NO_3)_2$	Sigma-Aldrich, SKU 243426	>99 %
EDTA	ethylenediaminetetraacetic acid	$C_{10}H_{16}N_2O_8$	Sigma-Aldrich, SKU E9884	99.4-100.6 %
	Li hydroxide	LiOH	Sigma-Aldrich, SKU 62531	>99 %
NAmOx	ammonium niobate oxalate	$NH_4NbO(C_2O_4)_2$	Aldrich, SKU 525839	99.99 %
	Na hydroxide	NaOH	Sigma-Aldrich, SKU 35274	4.00 M
	K hydroxide	KOH	Sigma-Aldrich, SKU 35113	1.00 M
ST	single crystal strontium titanate substrate	$SrTiO_3$	Crystal GmbH, Part No 1STO 101E	1×1×0.05 cm^3 (100)
ST:Nb	1 at% Nb doped ST	$SrTi_{0.99}Nb_{0.01}O_{3+\delta}$	Crystal GmbH, Part No 1STO 122E1	1×1×0.05 cm^3 (100)

[1] Molarities in parenthesis correspond to the concentration of the solution after achieving final volume.

O_2 at 550 °C for 5 min, and oxygen plasma surface activation (Diener Electronics Femto Plasma cleaner, Ebhausen, Germany). The substrates were attached to the spin-coater chuck (Laurell Technologies WS-400B-6NPP-LITE/AS, North Wales, USA), sprayed with compressed air, and 2 drops of sol was applied via a syringe with 0.2 µm filter. Next, the spin was promptly initiated, accelerating at 1500 rpm/s and spinning at 3500 rpm for 30 s. After spinning, the samples were dried on a hot plate at 110 °C.

Pyrolysis and thermal annealing was conducted in a rapid thermal processing (RTP) oven (Jipelec Jetfirst 200 mm, Semco Technologies, Montpellier, France). To protect the RTP chamber from volatile Na, K, Li, and Bi, the substrates with deposited films were confined within a custom-made quartz glass lid placed on a Si carrier wafer. Pyrolysis was conducted for each layer at 550 °C for 5 min, ramping at 100 °C/min to 450 °C, and at 40 °C/s to 550 °C, and cooling as fast as the RTP allowed. The atmosphere in the chamber was controlled by evacuation to 10 mbar before refilling with pure O_2 to ambient pressure. The thin-film preparation was conducted in an ISO 7 level clean room.

Electrical contacts were applied by sputtering gold top electrodes through a plastic film with an array of 1×1 mm^2 voids (Edwards Sputter coater s150B). The bottom of the Nb doped ST substrates were ground with abrasive sheets and coated with gold in order to obtain better electrical contact.

Gel powders were obtained by drying small portions of the sols at 120 °C for 48 h. The gels were further calcined in alumina crucibles at 550 or 800 °C for 2 h (Nabertherm P330, Lilienthal, Germany). The powder thickness was kept smaller than 1 mm to ensure access to air.

Characterization methods

Phase purity was measured by grazing incidence X-ray diffraction (GIXRD) with 0.03° step size and 7.7 s/step at 2° incidence angle (Bruker D8 Advance DaVinci with Lynxeye XE linear detector, Billerica, USA). Lattice parameters and crystallite sizes were obtained by Rietveld refinement (Bruker AXS Topas version 5), assuming the R3c symmetry for all compositions. [42] Diffraction patterns of powder samples were recorded in Bragg-Brentano mode (XRD) with 6 mm variable slit opening, 0.013° step size, and 72.96 s/step total step time.

Microstructure images were captured by a field-emission scanning electron microscope (SEM), employing in-lens secondary electron detector and 10 kV acceleration voltage (Zeiss Ultra 55 Limited Edition, Oberkochen, Germany). For investigation of cross-sections of the thin films, controlled fracture was achieved by scribing sections of the surface and examining the un-scribed areas (Dynatex international DXIII, Santa Rosa, USA).

Ferroelectric hysteresis (P-E) loops were measured on a thin-film sample measurement setup by linear bipolar 500 Hz voltage cycling (AixACCT TF 2000 FE with TFSHU_e31 extension, Aachen, Germany). Some samples were conductive in positive bias direction (relative to top electrode) upon the first measurement. In this case, oppositely directed unipolar cycles were stepwise ramped up to 30 V, at which point a measurement anomaly occurred, significantly reducing the leakage current in both directions for subsequent measurements. Bipolar voltage cycles up to 100 V was then applied stepwise. The reported P-E loops are from stepwise decrease of voltage amplitude (100-1 V). Frequency dependent measurements at 50 V were measured next. Leakage current measurements were captured after hysteresis measurements on the same samples/electrodes. The instrument leakage

current measurement mode was used, with stepwise voltage increase of 2 V, holding for 2 s and measuring current during 70-90 % of the step. Several measurements were carried out on the same electrode within 30 min.

6.3 Results

6.3.1 Sol stability and concentration limit

Sols of the selected compositions were successfully prepared, resulting in transparent and homogeneous solutions as seen in Figure 6.1. Amorphous powders were obtained from the gels by drying, demonstrating that the drying process occurred without precipitation and segregation of the constituent cations. X-ray diffraction (XRD) patterns of the gel powders demonstrating the amorphous nature are presented in Figure 6.2a.

Depending on the concentration of citric acid and ammonia, precipitation occasionally occurred after a few weeks or months in the sols of 8K-4Sr-2Li-2Nb and 6Ba-1K-2Nb. The solid precipitate could be re-dissolved by adding CA and ammonia. These compositions and undoped BNT were chosen for investigation of concentration limits, preparing sols of 0.3, 0.6, and 0.9 M. Furthermore, sols were prepared with and without 10 % CA excess relative to the CA added for stabilization of the Ti and Bi/Sr precursors. pH was adjusted to 9 by ammonia.

The resulting timeframe of stability is summarized in Table 6.3. All sols were successfully prepared with 0.9 M concentration, and the CA excess sol for undoped BNT was stable for two months. Sols of 0.3 M (0.6 M for undoped BNT) were still stable after 6 months. The effect of excess citric acid in the 0.9 M sols was significant. Viscosity similar to water was obtained by CA excess, while the sols without CA excess were significantly more viscous. The picture in Figure 6.1 was captured 3 weeks after preparation of the sols. The yellow coloration was due to the Ti-CA precursor.

6.3.2 Phase purity and crystal structure

Powders

XRD patterns of powders calcined for 2 h at 550 or 800 °C are presented in Figure 6.2a. The powders were predominantly phase pure (as detectable by XRD), but a secondary phase was observed for 4Ba-6K-6Li with Na+Bi excess. Even in this case, phase purity was achieved at 800 °C or by omitting Bi excess. The dopants resulted in an expansion of the unit cell, seen as shift in the reflections shown in Figure 6.2b. Moreover, the rhombohedral super-reflection at 38° was only observed for undoped BNT (Figure 6.2c), confirming a change in symmetry for the compositions in the vicinity of the MPB.

Table 6.3 Summary of stability timeframes of sols with different compositions and concentrations. “CA” denotes that 10 % CA excess was added. “Stable” refers to sols free of precipitation after 6 months.

Composition	0.3 M	CA	0.6 M	CA	0.9 M	CA
BNT	stable	stable	stable	stable	1 week	2 months
6Ba-1K-2Nb	stable	stable	2 weeks	2weeks	1 week	1 week
8K-4Sr-2Li-2Nb	stable	stable	2 days	2 days	2 days	2 days

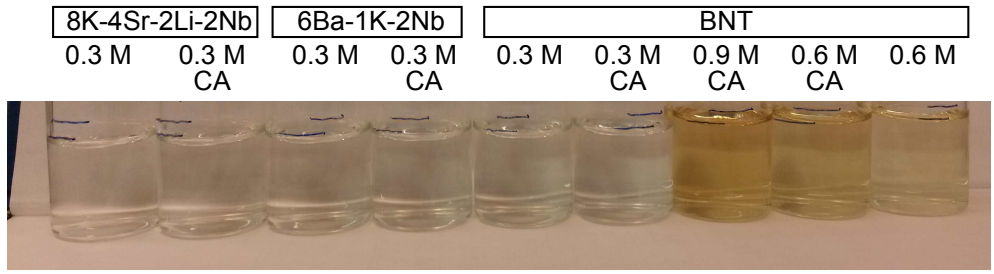

Figure 6.1 Stable sols 3 weeks after preparation. CA denotes that 10 % excess citric acid was added.

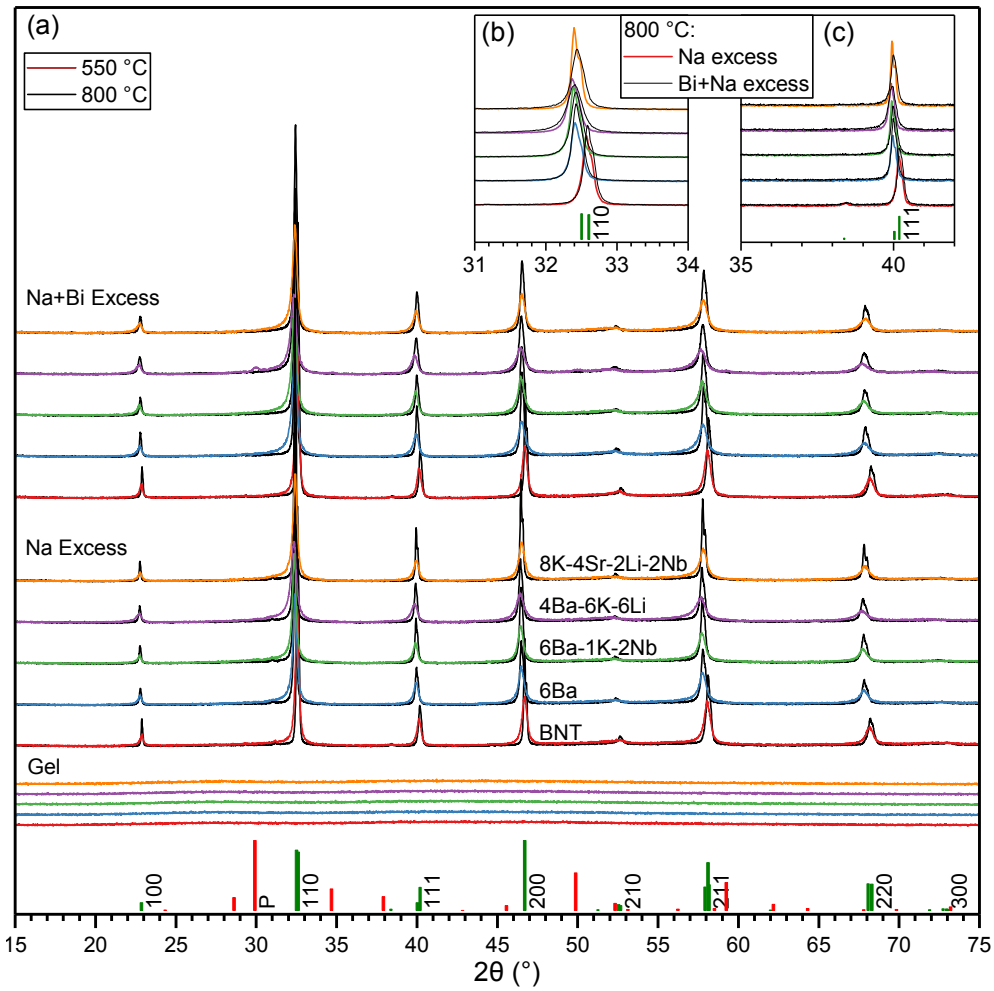

Figure 6.2 (a) XRD patterns of doped BNT powders calcined at 550 (colored) or 800 (black) °C for 2 h. (b, c) Magnified 2θ ranges of powders calcined at 800 °C, facilitating viewing of the $(110)_{pc}$ (pseudocubic Miller index) reflection (b) and the $(111)_{pc}$ reflection as well as the rhombohedral super-reflection at 38.5° (c). Reference patterns are shown for pyrochlore [211] and R3c BNT labeled with pseudocubic Miller indices [42].

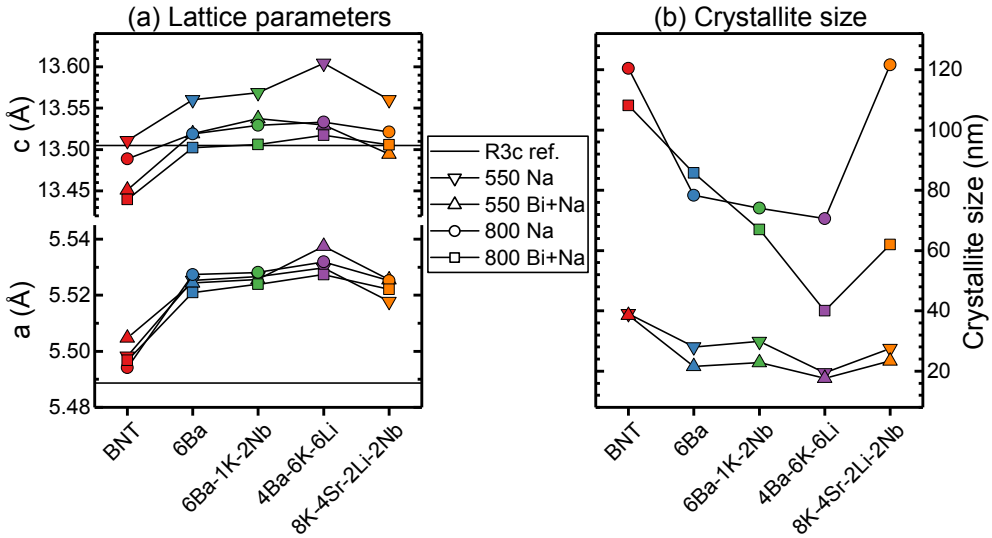

Figure 6.3 Lattice parameters and crystallite sizes of powders obtained by Rietveld refinements. Legend notations indicate the A-site excess and the calcination temperature. R3c lattice parameters for bulk BNT are shown for reference. [42]

Changes in unit cell parameters and crystallite sizes due to compositional engineering are presented in Figure 6.3. Within the different batches, the same trends of the crystal structure change due to composition were observed. The chemical modifications clearly led to expansion of the unit cell relative to undoped BNT. The expansion was largest for 4Ba-6K-6Li, followed by 6Ba-1K-2Nb and 6Ba, and marginally smaller for 8K-4Sr-2Li-2Nb. Crystallite sizes obtained from the same refinements are shown in Figure 6.3b. The calcination temperature naturally had a large effect on the crystallite sizes, but a trend due to composition is also visible. In general, the compositions with larger lattice parameters possessed smaller crystallites.

Thin films

Grazing incidence XRD (GIXRD) patterns of thin films with varying number of depositions and annealing temperatures are presented in Figure 6.4. Thin films prepared by 3 layers were phase pure already after pyrolysis. Phase purity was additionally achieved for nearly all films with a larger number of layers. The films with 10 layers were phase pure perovskite after annealing at 800 °C for 10 min, while the 15 layer thick films annealed at 700 °C were phase pure for BNT, 4Ba-6K-6Li, and 8K-4Sr-2Li-2Nb. A small amount of an unidentified phase was observed in 6Ba by the XRD reflection at 29°, while a small amount of pyrochlore was still present in 6Ba-1K-2Nb after annealing. The 700 °C annealing temperature was selected due to the significant coarsening when annealing at 800 relative to 700 °C. [234]

Formation of pyrochlore occurred in the as-pyrolized thin films with a larger number of layers. This was most pronounced for 4Ba-6K-6Li followed by 8K-4Sr-2Li-2Nb and, to some extent, 6Ba-1K-2Nb. 4Ba-6K-6Li was the only composition where pyrochlore was observed in powders, and consequently the highest pyrochlore content was observed in films of this composition.

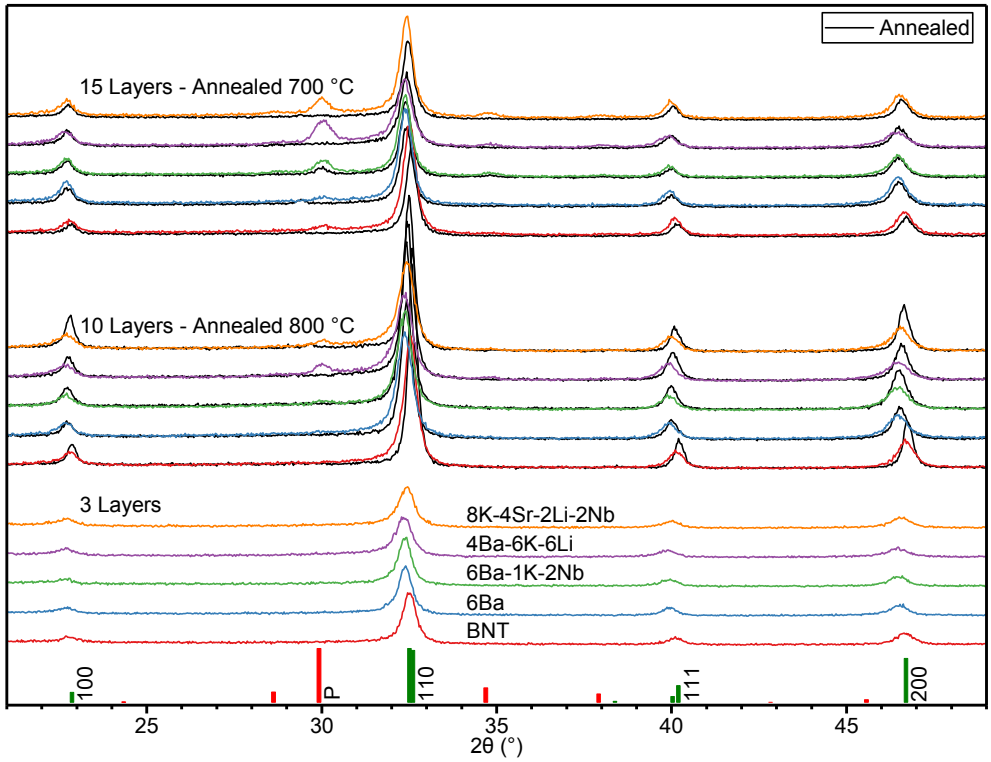

Figure 6.4 GIXRD patterns of thin films of different thicknesses and heat treatments. All layers of the films were pyrolized (colored) for 550 °C for 5 min before finally annealing (black) for 10 min. The 15 layer films of BNT and 6Ba were previously reported. [234]

Crystallinity due to A-site excess and heat treatment

Refined lattice parameters and crystallite sizes of both powders (same as Figure 6.3) and thin films are organized by batch rather than composition in Figure 6.5 in order to illustrate the effect of A-site excess and heat treatment. It can be seen that higher heat treatment temperatures appeared to cause smaller *a* and *c* parameters for all compositions. As expected, the crystallite sizes increased with increasing heat treatment temperature, and for as-pyrolized films the increased number of heat treatments with additional layers had the same effect. Interestingly, crystallite sizes were clearly larger for samples containing only Na excess and not Bi excess.

6.3.3 Microstructure of the thin films

Microstructures of cross-sections of thin films consisting of 15 layers deposited on Nb-doped $SrTiO_3$ (ST:Nb) substrates are shown in Figure 6.6. Homogeneous, dense, and defect free films were obtained for BNT, 6Ba, and 6Ba-1K-2Nb. The remaining two compositions demonstrated inflated bubbles between otherwise dense and homogenous layers. These were visible as ~500 nm wide and ~100 nm high topography bumps on the surface, and the cross-section SEM images showed that they were likely formed by gas development creating

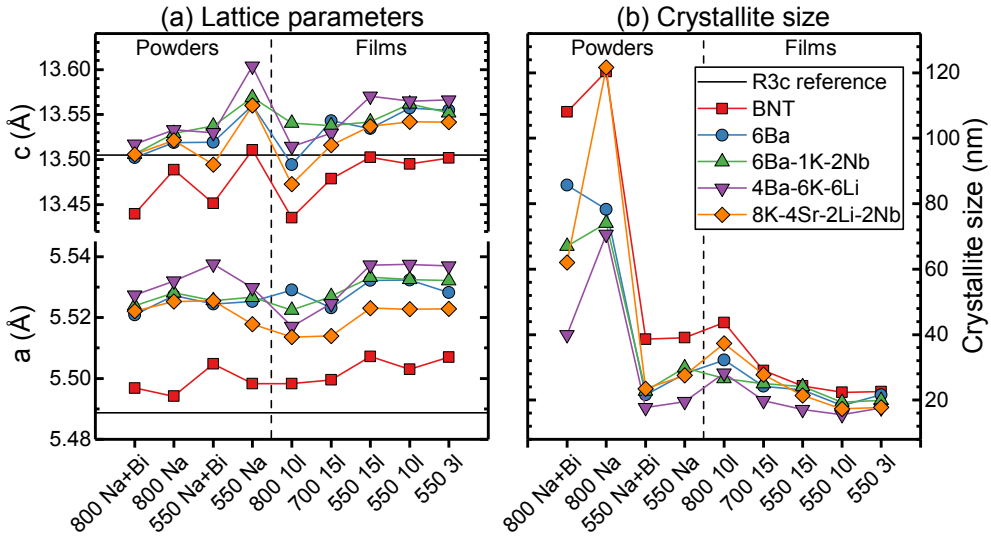

Figure 6.5 Lattice parameters and crystallite sizes organized by sample batches to illustrate the non-compositional influences. Batch notations indicate the number of layers for films and the A-site excess for powders. All films had Na excess.

inflated bubbles in an otherwise dense layer. The film thicknesses varied between 680 nm for 4Ba-6K-6Li and 780 nm for BNT. Only a small amount of porosity was visible between the layers, but near 100 % density was achieved after annealing (disregarding the inflated bubbles). The microstructure within the layers was not significantly influenced during annealing, in agreement with our previous study showing that grain growth is only significant for temperatures above 700 °C. [234]

SEM images of the surface microstructures before and after annealing are shown in Figure 6.7. A summary of various properties of the prepared samples, including approximate surface grain sizes are provided in Table 6.4. The compositions with the largest refined crystallite sizes (Figure 6.3 and 6.5) did not necessarily correspond to the compositions with the largest surface grains according to SEM, indicating that the average grain sizes may be significantly different than at the surface. This is not unexpected as the top layer has been exposed to shorter accumulated pyrolysis holding time than the average.

The surface morphology changed significantly during annealing. Approximately 100 nm pores or voids appeared in the top layer of all films. Considering the thickness of the films and the appearance of the voids, it is unlikely that they extended through the entire film thickness. The voids were more concentrated in particular areas on the micrometer scale and these areas were homogeneously distributed across the films. For 4Ba-6K-6Li and 8K-4Sr-2Li-2Nb, the areas of void formation appeared to be correlated with the locations of the inflated bubbles.

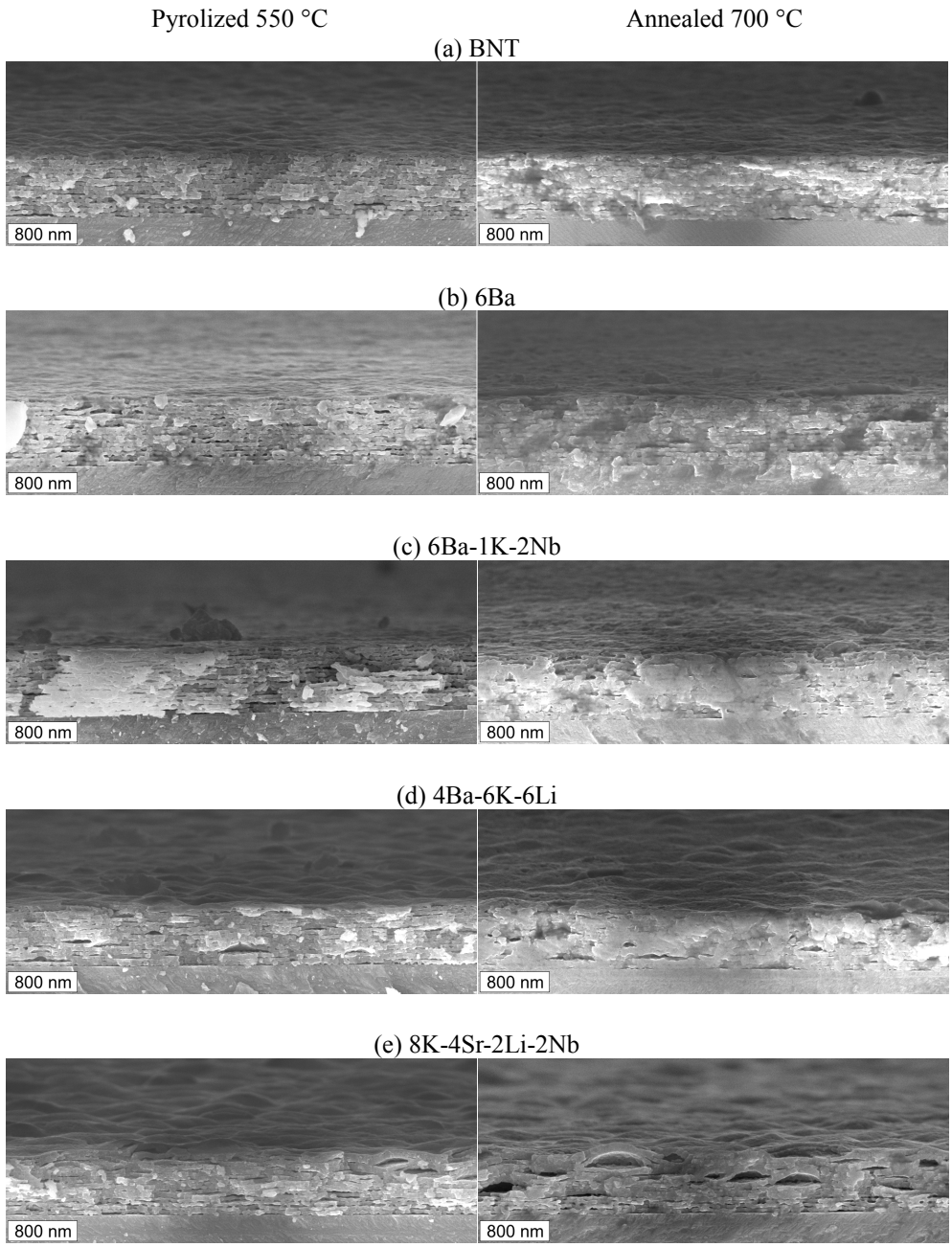

Figure 6.6 SEM images of BNT-based thin-film cross-sections. Samples pyrolized at 550 °C for 5 min (left) and finally annealed at 700 °C for 10 min (right). BNT and 6Ba samples were additionally reported in another work. [234]

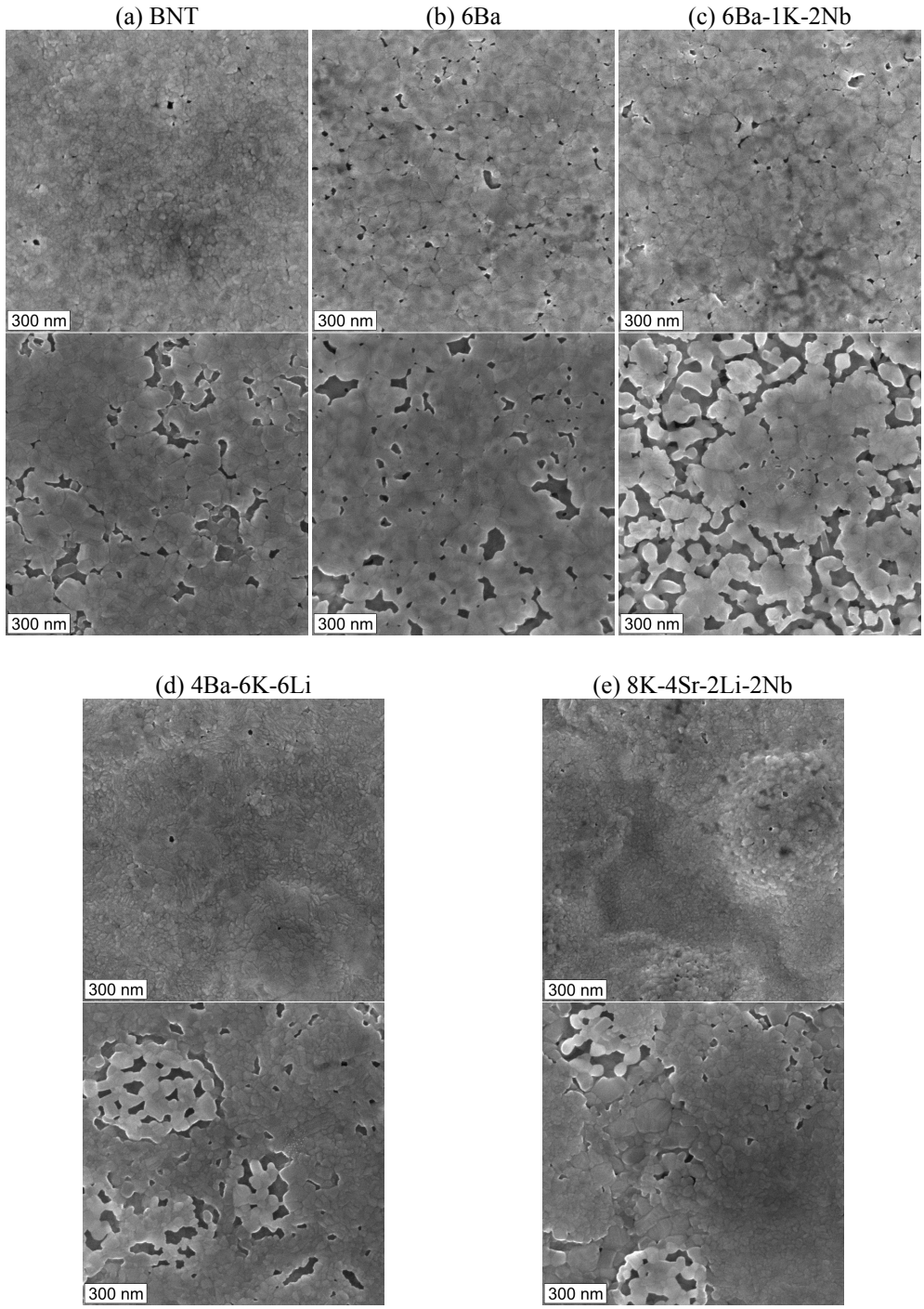

Figure 6.7 Top view SEM images of BNT-based thin films before (top) and after (bottom) annealing at 700 °C for 10 min. The thin films in (a, b) were previously reported. [234]

Table 6.4 Summary of selected powder and thin-film properties. The numbers in parenthesis denote relative severities.

		BNT	6Ba	6Ba-1K-2Nb	4Ba-6K-6Li	8K-4Sr-2Li-2Nb
Phase purity						
Powders		Pure	Pure	Pure	Pyrochlore (1) in 550 Na+Bi exc.	Pure
Films	**3 L As-pyr**	Pure	Pure	Pure	Pure	Pure
	10 L As-pyr	Pure	Pure	Pure	Pyrochlore (2)	Pyrochlore (1)
	10 L 800 °C	Pure	Pure	Pure	Pure	Pure
	15 L As-pyr	Pyrochlore (1)	Pyrochlore (1)	Pyrochlore (3)	Pyrochlore (5)	Pyrochlore (4)
	15 L 700 °C	Pure	Unknown (1)	Pyrochlore (1)	Pure	Pure
Lattice parameters and crystallite sizes (powders)						
***a* (Å) (800Na)**		5.494	5.527	5.528	5.532	5.525
***c* (Å) (800Na)**		13.489	13.519	13.529	13.533	13.521
Cryst. size (nm) (550Na)		39.1	28	29.9	19.5	27.5
Microstructure and morphology (15 layer films)						
Morphology		Good	Good	Good	Bubbles (1)	Bubbles (2)
Thickness (nm)		780	780	750	680	720
Grain size as-pyr (nm)		30	100	100	20	20
Grain size 700 °C (nm)		60	100	100	40	40

6.3.4 Electrical properties

Ferroelectric properties were measured for the 15-layer films deposited on ST:Nb substrates, and polarization-field loops are shown in Figure 6.8. At 500 Hz measurement frequency, all compositions demonstrated characteristic ferroelectric response comparable to that of BNT films prepared by other methods. [13, 143, 168] It is noted that no leakage current compensation or pre-polarization pulses were applied, and that only relatively limited leakage current was observed even at strong fields. Furthermore, none of the films experienced dielectric breakdown, demonstrating the high quality. At very strong fields, however, there was a noticeable contribution from leakage current in Figure 6.8 c and e.

The ferroelectric response was mechanically constricted by the substrate, and proper ferroelectric switching was not observed even at field strengths approaching 1500 kV/cm, approximately 30 times higher than the coercive field of bulk BNT. [15] The exact characteristic parameters (saturation polarization, remnant polarization and coercive field) and the effect of compositional engineering could therefore not be obtained. At the current conditions, variations in leakage current, microstructure, electrode size, and film thickness influenced the apparent ferroelectric properties more than the variation in composition.

Leakage current during stepwise increase of voltage is shown in Figure 6.9a. Leakage current measurements of this character are commonly reported for smaller electric fields, and the observed values are comparable to state of the art BNT thin films. [164] It is shown by the difference in initial and subsequent measurements that leakage currents were varying more due to history than composition. This change in electrical properties demonstrated that it was challenging to accurately determine properties such as remnant polarization from the P-E loops shown in Figure 6.8. Despite the varying properties, conductivity for negative bias was

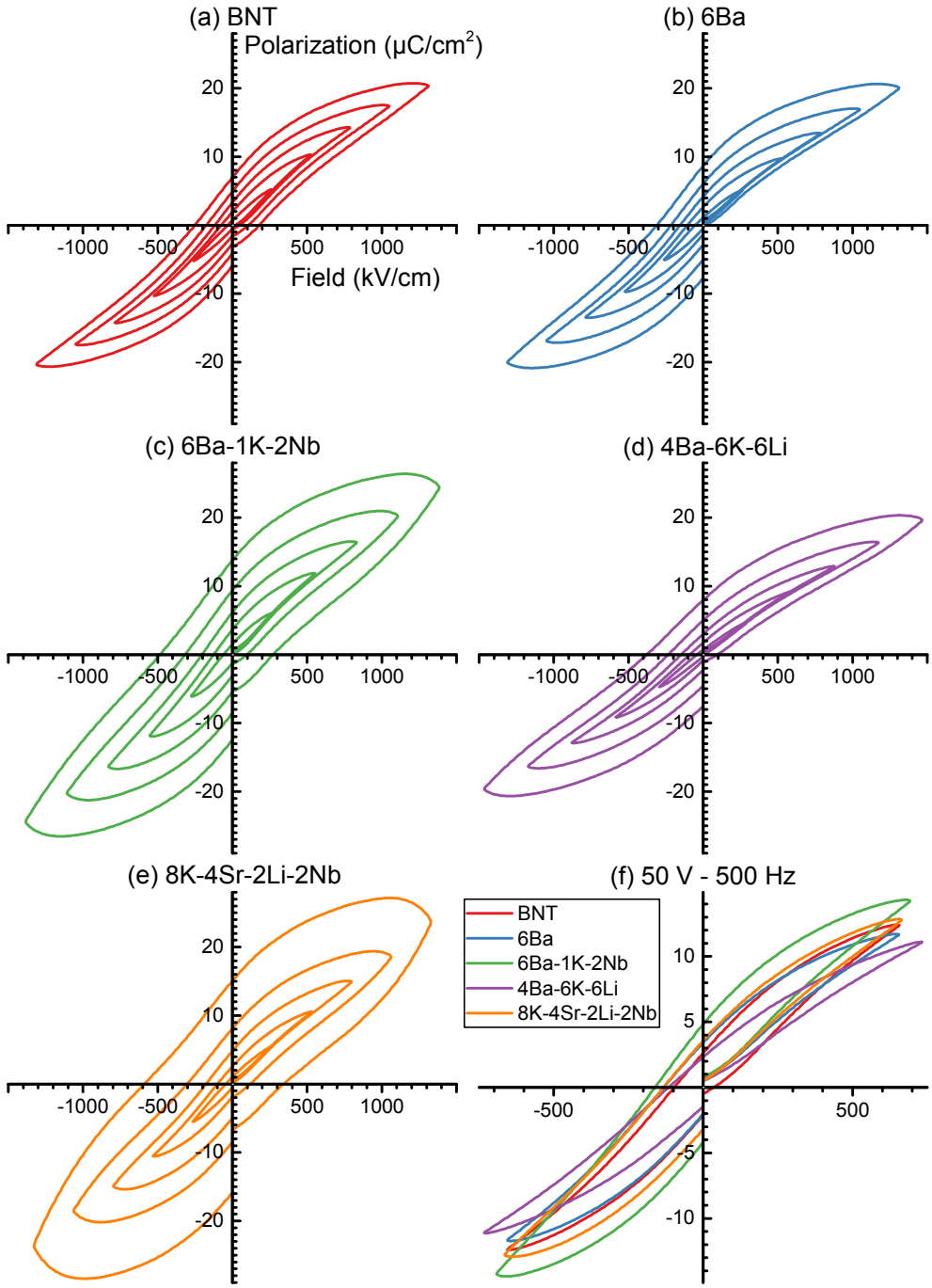

Figure 6.8 Polarization-field hysteresis loops for different voltage amplitudes and compositional engineering at 500 Hz linear cycling (a-e). (f) Comparison of different compositions for 50 V cycling amplitude. Properties of thin films in (a, b) were previously reported. [234]

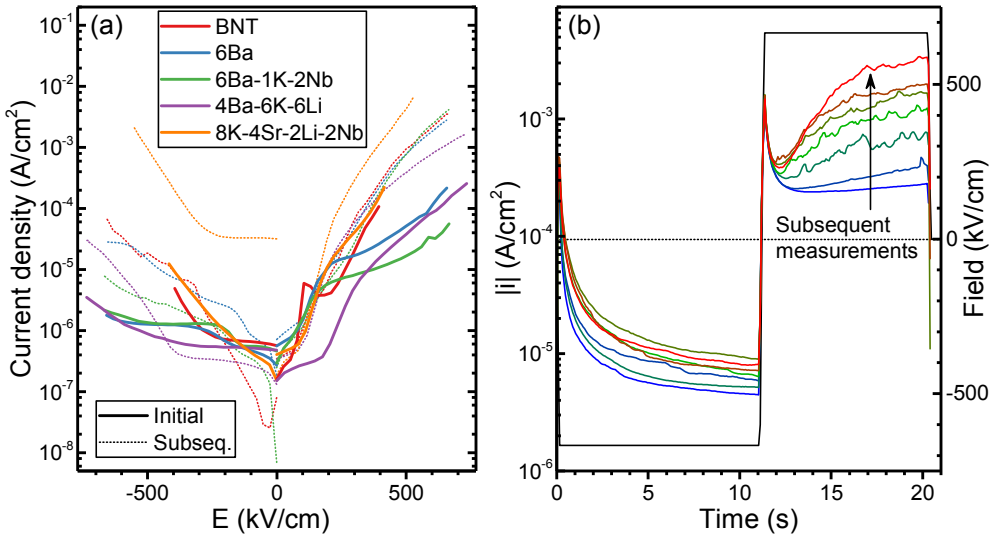

Figure 6.9 (a) Initial and subsequent leakage current of the BNT-based thin films measured repeatedly. Stepwise voltage increase, measuring during 1.4-1.8 s of each two-second step. (b) Absolute value of current density during constant voltage (50 V) and switching for 6Ba-1K-2Nb.

consistently orders of magnitude lower than for positive (relative to the top electrode). The current density during holding at constant bias (50 V) is shown for 6Ba-1K-2Nb in Figure 6.9b. The leakage current was clearly orders of magnitude larger for positive than for negative bias. Moreover, the current in positive direction was increasing with time and for subsequent measurements. The same behavior was observed for the other compositions.

The influence of leakage current on hysteresis measurements was investigated by plotting current density divided by frequency for polarization cycles of varying frequencies, shown in Figure 6.10. In general, dividing current density by the frequency normalizes the measurements to the same order of magnitude allowing direct comparison of properties for different frequencies. Ferroelectric or capacitive current density is proportional the cycling frequency, and normalizes to the same value when dividing by frequency. Leakage current, on the other hand, is independent on frequency and becomes negligible compared to the very high ferroelectric current at high frequencies. It was previously shown that the ferroelectric response time is on the order of 10^{-4} s for these films, and the observed response was therefore not limited by the ferroelectric switching speed with increasing frequency. [233, 234]

The peaks at approximately ±10 V in Figure 6.10 are attributed to the main ferroelectric switching signal. The wide character of these peaks and the remaining significant signal for further increasing bias demonstrate how commonly reported ferroelectric properties were poorly defined due to clamping from the substrate. For the individual compositions, a peak shift was observed upon increasing the frequency from 100 to 5000 Hz. This was most significant for 6Ba-1K-2Nb and least for undoped BNT, and signified the response time in the switching mechanism, indicating that domain wall motion may be slower for 6Ba-1K-2Nb.

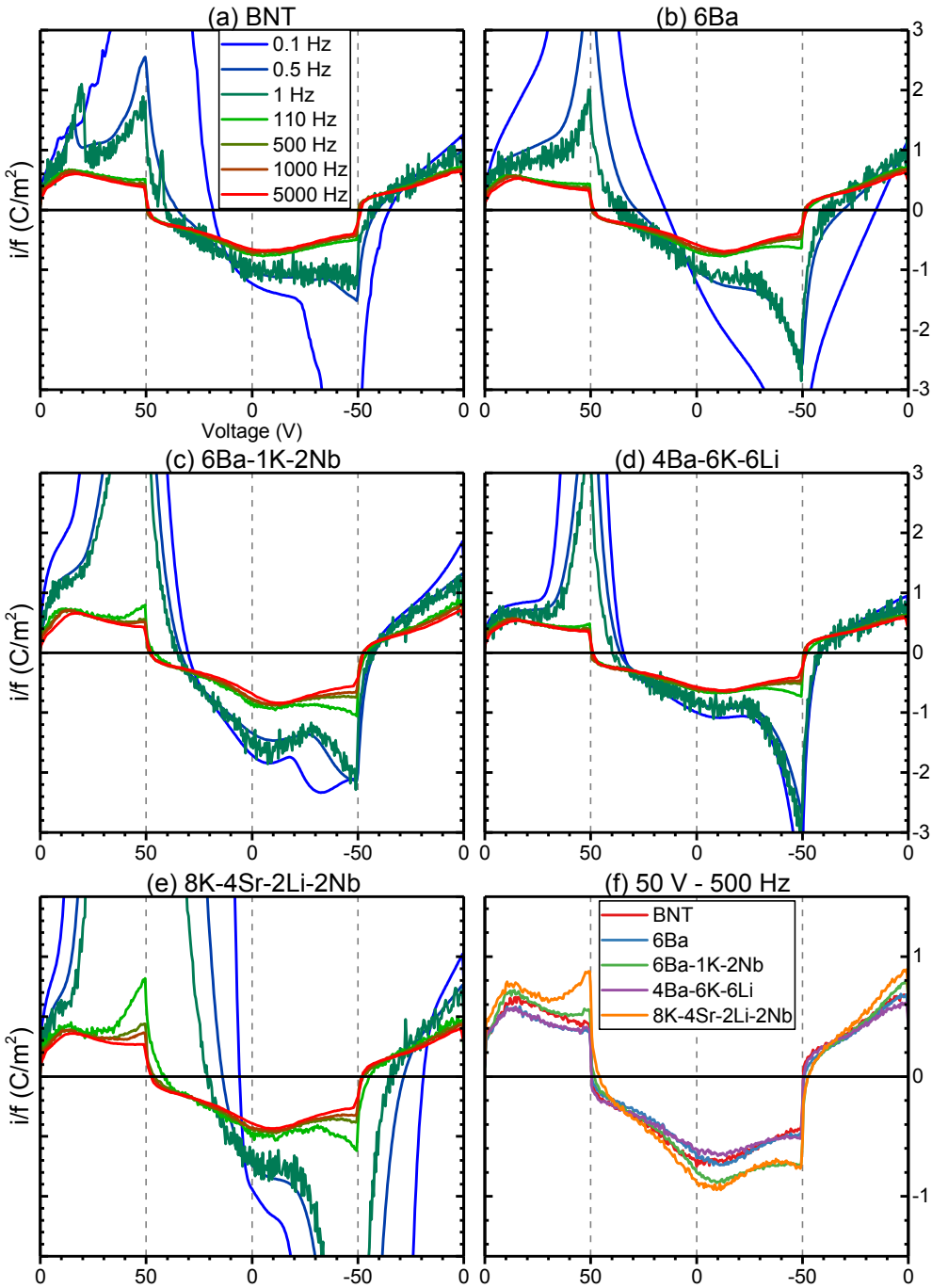

Figure 6.10 Current density divided by frequency as a function of voltage for different scan frequencies for BNT-based thin films (a-e). (f) Comparison of compositionally engineered BNT at 500 Hz. Properties of thin films in (a, b) were previously reported. [234]

The influence of leakage current on the P-E measurement is clearly visible in Figure 6.10. The similar responses of 500 Hz and 5 kHz demonstrate that the P-E hysteresis loops at 500 Hz were dominated by ferroelectric response and not leakage. By the deviation from 5 kHz it can be seen that leakage was relevant at different voltages for different frequencies. In Figure 6.10d, for example, the leakage contribution at low frequency initiated at ~30 V, while in Figure 6.10e, there was a threshold at 5-10 V. As was shown above, these thresholds decreased for all films with accumulated current exposure. Moreover, for 6Ba, 6Ba-1K-2Nb, and 4Ba-6K-Li, the high-frequency leakage was greater for negative bias than for positive, explaining the unclosed hysteresis loops in Figure 6.8.

Comparison of the compositionally engineered BNT thin films when cycling to 50 V at 500 Hz is shown in Figure 6.10f. The responses of the different compositions were remarkable similar, as the qualitative response of each sample was the same. The small variations in the values can be explained by non-compositional effects such as film thickness (voltage in relation to field), electrode size, and sample history. These results suggest that the different doping variants had only a limited effect on polarization properties for clamped films at these field strengths.

6.4 Discussion

6.4.1 Viability of the aqueous BNT CSD

The main result of this work was the demonstration that the aqueous chemical solution deposition (CSD) method could be adapted to compositionally engineered BNT. Large strain and temperature insensitive properties have been demonstrated for bulk materials of the prepared compositions. Ba, Sr, K, Li, and Nb in similar concentrations are also commonly reported for other BNT-based materials (Table 2.4, p. 50). The arguably most common BNT dopant not investigated here is Mn. However, stabilization of aqueous Mn by means of citric acid is known, and its successful introduction to the aqueous BNT CSD is therefore feasible. [101]

The strongest feature of this CSD method is the low degree of influence of the precursor of one cation on the precursors of the other cations. Bismuth, for example, is not stable in water without complexation, but Bi hydroxide will precipitate at pH greater than 0-1. In our previous work it was possible to prepare aqueous sols for BNT by stabilizing Bi^{3+} (aq) with low pH from HNO_3. [232] However, the high NO_3^- concentration from HNO_3 limits the stability of $Ba(NO_3)_2$ according to la Châtelier's principle. [235]

The most beneficial feature of the precursors used here is that they are all stable in water at conditions that are non-hazardous and compatible. The alkali cations (Li, Na, K) are added as hydroxides, which are highly soluble and do not have any secondary influence other than increasing the pH towards neutral (CA addition for other cations causes pH 1-2). Ba and Sr nitrates were used, and because these are the cations with the lowest nitrate solubility, NO_3^- anions will not cause precipitation of the other cations. Bi was added as BiCit, adding only citrate which is added intentionally for complexation of Ti/Ba/Sr. The Ti precursor used was TIP, yielding inert isopropanol upon hydrolysis and complexation with CA. Finally, the Nb precursor was Nb ammonium oxalate is water soluble and did not require additions. The acidity resulting from the high amount of CA was neutralized by ammonia. Thus, the chemistry of the precursors is highly compatible, and the individual precursors did not significantly decrease the solubility of the other.

The aqueous CSD method has therefore proved to be a robust framework suitable for fabrication of a range compositionally engineered BNT. Moreover, the method is cheap, environmentally friendly, safe, and very easily adapted and extended.

6.4.2 Phase purity

Loss of sodium

Intermediate pyrochlore phase has on several occasions been shown to pose challenges for thin-film fabrication of PZT [11] and BNT [232, 234]. The current thin films made by only a few layers were phase pure for all compositions. This demonstrates that the perovskite phase was formed at an early stage and that challenges with an intermediate/transient pyrochlore phase are not relevant. With the current pyrolysis scheme, the perovskite was the prevailing phase formed during deposition of an isolated layer. Only with introduction of changes to the

system from previous layers and heat treatment did the pyrochlore form and remain at the end of a pyrolysis step.

In our previous work, it was demonstrated that the pyrochlore phase is relatively poor in Na, and that its formation was related to the Na stoichiometry. [232, 234] Thus, the increasing content of pyrochlore with increasing film thickness is likely related to loss of Na. A larger degree of Na than Bi loss is also seen for alternative fabrication methods of BNT, as the applied excess of Na is commonly higher than for Bi. [147, 164, 168] Three apparent mechanisms for Na loss are (i) evaporation, (ii) dissolution of Na from the film by the sol itself, and (iii) diffusion into the substrate. These alternatives are treated in the following.

Evaporation of volatile constituents from perovskite oxides is well known, and Pb and Bi/Na are routinely added in excess for PZT and BNT, respectively. [11] The most common method to hinder evaporation is to use a sacrificial powder bed of the same material to increase the vapor pressure of the volatile species. [15, 39] However, bulk BNT is routinely sintered at temperatures as high as 1100 °C for several hours [15], and the powder samples prepared here were annealed at 800 °C for 2 h without the presence of pyrochlore. It is therefore unlikely that significant evaporation occurred for the thin films during pyrolysis at 550 °C for 5 min.

Dissolution of Na from the crystalline film by the sol during deposition of the next layer could cause Na deficiency in the film, and in our previous work it was demonstrated that pyrochlore formation was promoted by exposing the crystalline films to water in between depositions. [234] This effect would arguably be more significant for the outermost layers where the film is directly exposed to the sol. Because BNT thin films with three layers did not contain pyrochlore, Na dissolution does not sufficiently explain the increasing pyrochlore content with increasing number of layers.

Na deficiency due to diffusion into the substrate would cause increased formation of pyrochlore close to the substrate, explaining the observed trends well. Of the discussed mechanisms for loss of Na, it is suggested that diffusion was the most relevant. Na deficiency in the region close to the substrate may be compensated by adding increased amounts of Na in sols dedicated for deposition of early layers. The exact sol stoichiometry would have to be optimized depending on compositional engineering, selected heat treatment, and number of layers. Compositional engineering of the sol for deposition of individual layers is routinely done for PZT. [7, 97] Different diffusion barrier layers in the substrate stack such as SiO_2 in platinized silicon are also often applied. [12]

Na volatility and diffusion are well-known challenges in the semiconductor industry. The solubility and diffusion coefficient of Na in Si are relatively high at 10^{18} cm^{-3} and 7×10^{-8} cm^2/s at 550 °C, respectively. [197] This poses a potential stoichiometry and contamination control issue, particularly for deposition on platinized silicon substrates, and the Na stoichiometry should be a topic of care for BNT thin-film deposition.

Perovskite stability

There was a clear trend that the amount of pyrochlore changed with the overall composition of the BNT thin films. The same trend was observed in the previous work where higher Ba content clearly enhanced the formation of the pyrochlore. [234] In Table 6.4, lattice parameters are reported for powders calcined at 800 °C exclusively, because the isolated effect of composition on lattice parameters is most accurately determined for crystalline materials.

In the following, the compositional effect on structure (powders) is discussed in context with the observed phase purity and crystallite sizes of thin-film samples.

In general, the amount of the pyrochlore secondary phase in thin films was greatest for the compositions with the largest expansion of the unit cell. It is here suggested that the expansion of the unit cell was correlated to a slight increase in the Gibbs energy of the perovskite. In the final stage of the thermal decomposition of the gels, the amorphous oxide network may be transformed into perovskite, pyrochlore, or both. A marginal destabilization of the perovskite phase would render pyrochlore formation relatively more significant.

The lack of pyrochlore after deposition of three layers demonstrate that perovskite formation is the prevailing effect after 5 min pyrolysis for the principle system. With gradual change of the overall stoichiometry during several coating cycles (e.g. Na loss), the perovskite to pyrochlore formation balance would be shifted, explaining the appearance of pyrochlore with increasing number of layers.

In Figure 6.5 it was seen that Na excess consistently corresponded to larger crystallite sizes than for Na+Bi excess. This is suggested to be caused by a similar process. Because the pyrochlore phase is rich in Bi and poor in Na, increasing the Na/Bi ratio would destabilize the pyrochlore secondary phase according to Le Châtelier's principle. Formation of the pyrochlore phase suppresses the perovskite growth due to both segregation of cations and reduction of the driving force for perovskite formation (amorphous oxide to perovskite is more favorable than pyrochlore to perovskite. See Section 2.4.1, p. 45). Suppression of the pyrochlore would therefore enable more significant perovskite formation and growth.

Measures to reduce pyrochlore with increasing number of layers

Changes in stoichiometry are more easily accommodated in the amorphous oxide phase and the pyrochlore than in the perovskite. [97] Loss of Na from the perovskite implies reaction of perovskite into some other phase, because the maximum Na deficiency in BNT is minor. [46] For this reason, the reactivity of Na is decreased when the perovskite is formed, an Na-loss is therefore more likely before the perovskite is formed.

Thus, achieving phase pure perovskite for each coating may require smaller measures than those required for compensating for secondary phases that were allowed to remain initially. For Ba doped BNT films, pyrolizing at 600 rather than 550 °C provided increased phase purity, and increasing the pyrolysis temperature slightly may be effective in assuring the perovskite formation. [234] Counterintuitively, applying higher heat treatment temperatures is therefore predicted to reduce the level of evaporation, dissolution, and diffusion of Na. Alternatively, applying phase-purity promoting heat treatment steps (annealing) for every few layers could be equally efficient.

6.4.3 Refined structural parameters

Crystal structure

A first approach to predict the lattice expansion of chemically modified compositions can be estimated by the relative differences in ionic radii (Table 6.5). For example, 6 % Ba would replace 3 % Na and 3 % Bi, giving an expansion value (Å) of

$$0.03\times(1.61-1.17)+0.03\times(1.61-1.39)=0.020 \qquad (6.1)$$

Table 6.5 Ionic radii (Å) of cations in relevant coordination. (VIII) denotes that octahedral coordination is shown in absence of dodecahedral data. Data from Shannon. [236]

Coordination	Bi^{3+}	Na^{+}	Ba^{2+}	Sr^{2+}	K^{+}	Li^{+}	Ti^{4+}	Nb^{5+}
Dodecahedral	1.17 (VIII)	1.39	1.61	1.44	1.64	0.92 (VIII)		
Octahedral							0.74	0.74

Table 6.6 Refined lattice parameters normalized to undoped BNT for powders calcined at 800 °C (Table 6.4) compared to predicted expansion due to ionic radii.

	BNT	6Ba	6Ba-1K-2Nb	4Ba-6K-6Li	8K-4Sr-2Li-2Nb
			Refined lattice expansion		
a (Å)	0	0.033	0.034	0.038	0.031
c (Å)	0	0.030	0.040	0.044	0.033
			Predicted expansion		
Expansion value (Å)	0	0.020	0.025	0.000	0.019

This model relies on several assumptions, such as constant symmetry and oxygen stoichiometry. Performing the calculations for all compositions yielded the lattice expansions presented in Table 6.6. The refined lattice parameters are reprinted from Table 6.4 for direct comparison. This simple model was remarkable accurate, with the exception of 4Ba-6K-6Li. Either this deviation was due to the large concentration of Li with small radius and a non-trivial ionic radius to unit cell volume relationship, or there is another effect causing the large unit cell volume of this composition.

In general, both *a* and *c* parameters decreased with increasing heat treatment temperature in powders and films (Figure 6.5). This could be due to elimination of oxygen vacancies at, which generally cause lattice expansion, at higher temperatures. Reducing conditions during the decomposition process is likely, possibly resulting in higher concentration of oxygen vacancies directly after decomposition. [232] Moreover, assuming that Na loss is greater than the loss of Bi means that additional heat treatment would cause a relative increase in the Bi to Na ratio. According to Equation (6.4), this would also reduce the concentration of oxygen vacancies.

6.4.4 Microstructure

The microstructures of BNT, 6Ba and 6Ba-1K-2Nb were homogenous, dense, and defect free, while inflated bubbles in 4Ba-6K-6Li and 8K-4Sr-2Li-2Nb posed a challenge that needs to be solved (Figure 6.6). The bubbles were likely related to either water evaporation or development of CO_2 during pyrolysis. In either case, careful optimization of the process is suggested to remedy the situation efficiently, as was shown recently for undoped BNT. [234] If water evaporation was the main cause, higher temperature or longer drying time at the hot-plate could ensure that water is eliminated prior to subjecting the sample to vacuum and rapid ramp during the RTP.

The appearance of surface voids during annealing was discussed in [234], and it was suggested that the voids originated from detached grains during ramp to holding temperature, and that reducing the ramp rate might solve the issue. For the thin films expressing the inflated

bubbles (Figure 6.7), however, the surface voids seemed correlated to the locations of the bubbles. This correlation suggests that porosity between the layers were transformed to intergranular porosity upon annealing. Further experiments are required in order to fully understand the mechanism leading to the surface voids.

6.4.5 Electrical properties

Piezoelectric properties

The main finding of this work with respect to electrical properties was the demonstration that all compositions were ferroelectric. Moreover, the films could tolerate strong fields without experiencing dielectric breakdown. The coercive field of bulk BNT is typically around 50 kV/cm [15], at which point the polarization has a steep increase until saturation before 100 kV/cm. In the thin films produced here, the ferroelectric response was suppressed, and the clamping of in-plain strain suppressed the coupled out-of-plane polarization response. Saturation of polarization was still not observed at 1500 kV/cm. The characteristic properties associated with the compositional engineering, such as pinching of the hysteresis at low fields, was therefore not observed. For that reason, it was not possible to identify any difference in ferroelectric properties for the different BNT compositions prepared as thin films. The effect of clamping of PZT thin films by the Si substrate has been investigated systematically, and it was found that the dielectric permittivity of films increased multiple-fold by releasing the film from the substrate. [237] The clamping of the substrate was also found to significantly inhibit the ferroelectric domain wall motion and associated strain. [237]

In actuator devices such as cantilevers in micro electromechanical systems (MEMS), the effective substrate thickness is in the order of a few micrometers rather than the current 500 µm, and clamping will not be seen in the same magnitude. [7] For these devices, the expected properties would be much closer to what is seen for bulk. In order to probe the thin-film strain properties of the films prepared here, the actual cantilever devices would need to be prepared. An added benefit of removing the substrate clamping is that the required electric fields would be much smaller, and the leakage current seen at higher fields would not be relevant.

Conductivity

In general, conductivity in BNT is caused primarily by oxygen vacancies [164, 238], and the concentration of these can be reduced by donor doping [47] and by designated thermal annealing in O_2 atmosphere [111]. Furthermore, the mobility of the oxygen vacancies can be reduced by Mn doping, shifting the onset of ionic conductivity to higher fields. [26, 156, 164, 169, 178, 179, 212-215] The asymmetry of conductivity observed in the thin films produced here is characteristic of oxygen vacancy dominated conduction with changing concentration of vacancies throughout the film thickness. [164] The mechanisms controlling the concentrations of oxygen vacancies are treated in the following.

Oxygen vacancy formation must be charge compensated and is accompanied by one of several mechanisms. Loss of A-site cations due to evaporation, diffusion, or initial deficiency leads to vacancies according to:

$$2\mathrm{Na}_{\mathrm{Na}}^{\times} + \mathrm{O}_{\mathrm{O}}^{\times} \xrightarrow{\mathrm{BNT}} 2\mathrm{V}_{\mathrm{Na}}' + \mathrm{V}_{\mathrm{O}}^{\bullet\bullet} + 2\mathrm{Na(g)} + \tfrac{1}{2}\mathrm{O}_2\mathrm{(g)} \qquad (6.2)$$

$$2Bi_{Bi}^{\times} + 3O_O^{\times} \xrightarrow{BNT} 2V_{Bi}''' + 3V_O^{\bullet\bullet} + Bi_2O_3(g) \quad (6.3)$$

In Kröger-Vink notation, V denotes vacancies, subscripts denote the lattice site of the species, and $^{\times}$, $^{\bullet}$, and $'$ denote neutral, positive, and negative charges relative to that site, respectively. The effect of the above reactions is sufficient for significant change in conductivity, but the maximum vacancy concentration is low, and other mechanisms can counteract the effect of the vacancies. Secondary phases were observed to form already for less than 1 % A-site deficiency, limiting the vacancy concentration in the perovskite to the same value. [46] More influential on the oxygen vacancy concentration is the effect of acceptor or donor doping. Acceptor doping can occur as variation of the Na^+ to Bi^{3+} ratio

$$Na_2O + 2Bi_{Bi}^{\times} + 2O_O^{\times} \rightleftharpoons 2Na_{Bi}'' + 2V_O^{\bullet\bullet} + Bi_2O_3 \quad (6.4)$$

and donor doping is provided as the reverse reaction. Furthermore, donor doping may be achieved by introduction of other cations, such as Nb^{5+} on Ti^{4+} site:

$$Nb_2O_5 + V_O^{\bullet\bullet} + 2Ti_{Ti}^{\times} \xrightarrow{BNT} 2Nb_{Ti}^{\bullet} + O_O^{\times} + 2TiO_2 \quad (6.5)$$

Another possible charge compensating effect is that of changing valence states of transition metal cations such as Ti, Mn and Fe, illustrated for Mn here:

$$2Mn^{2+} + V_O^{\bullet\bullet} + \tfrac{1}{2}O_2(g) \rightleftharpoons 2Mn^{3+} + O_O^{\times} \quad (6.6)$$

$$2Mn^{3+} + V_O^{\bullet\bullet} + \tfrac{1}{2}O_2(g) \rightleftharpoons 2Mn^{4+} + O_O^{\times} \quad (6.7)$$

Furthermore, cations of varying valence state can contribute to electronic conductivity:

$$Mn^{4+} \rightleftharpoons Mn^{3+} + h^+ \quad (6.8)$$

$$Mn^{2+} \rightleftharpoons Mn^{3+} + e^- \quad (6.9)$$

For undoped BNT, however, the valence states of Na^+, Bi^{3+}, and Ti^{4+} are stable in air, and electronic conductivity and charge compensation is negligible compared to the effects of Equations (6.2)-(6.5). [215]

It has been demonstrated that various changes in the stoichiometry of BNT led to two discrete levels of conductivity, depending on the oxygen vacancy concentration of the materials. [45-47] The following discussion is based on the results of these references. Further intentional compositional modifications did not significantly influence the conductivity, as the low conductivity was limited by oxygen vacancy concentration approaching zero, and the high conductivity by maximum A-site vacancy concentration. Nominally stoichiometric BNT was in reality A-site deficient, and expressed high conductivity due to A-site deficiency (Eqs. (6.2) and (6.3)). Intentional Bi deficiency, causing Na acceptor doping on Bi-site, only marginally increased the conductivity relative to the virgin state. [46] Intentional 1 % Na deficiency, however, resulted in low conductivity, due to Bi donor doping on Na-site (reverse Eq. (6.4)) with stronger effect than that of Equation (6.2). This demonstrates that the intrinsic concentration of oxygen vacancies is limited by the ability of the perovskite to accommodate A-site vacancies, and that only minor intentional aliovalent doping may dominate the achieved conductivity level. For example, as little as 0.5 % Nb^{5+} doping was sufficient to obtain the low oxygen vacancy concentration, according to Equation (6.5). [47]

As discussed above, Na excess is required for phase purity considerations, and Equation (6.4) will be shifted to the right according to Le Châtelier's principle. This is an unwanted side effect of the Na excess, but its influence can be counteracted by intentional donor doping. The samples prepared in this work were nominally charge balanced, so that Nb^{5+} was coupled with monovalent A-site cations. By coupling Nb^{5+} doping with for example Ba^{2+} or Sr^{2+}, however, the donor doping character of Nb will emerge, while maintaining the beneficial Na to Bi ratio.

Dopants effect on conductivity

Upon increasing the complexity of the system by chemical modifications, the potential effects of small variations in stoichiometry on conductivity should be acknowledged. However, it was found that the conductivity of the films produced here was varying more for a single sample depending on sample history than between the compositions. This means that in order to investigate the effect of chemical modifications on conductivity, the effect of other parameters needs to be controlled. Nevertheless, the effect of chemical modifications on conductivity can be theoretically treated.

The cations introduced in this work have little potential for changes in valence state, and any influence on the defect chemistry would be of the sort in Equation (6.4). In undoped BNT, the potential effect of unintentional aliovalent doping is given by Na^{+} replacing Bi^{3+}, with associated change of -2 in site charge. If A^{+} was to replace A^{2+}, or if A^{2+} was to replace Bi^{3+}, the effect would be smaller than for undoped BNT. Thus, the effect on oxygen vacancy concentration through cation loss and Equation (6.4) is reduced or unchanged by the chemical modifications.

6.5 Conclusions

Aqueous chemical solution deposition of chemically modified BNT including the cations Ba, Sr, Li, K, and Nb was demonstrated. Thin films consisting of three deposited layers were phase pure after pyrolysis at 550 °C, while phase pure films made by 10-15 layers required further annealing. The films were all shown to be ferroelectric with leakage current characteristics comparable to state of the art BNT thin films synthesized by alternative methods. The low frequency leakage currents at large fields were significant, and it was argued that Nb doping introduced in this work can be exploited for increased properties. The microstructures of the films were homogeneous and dense for three compositions, while the films of 4Ba-6K-6Li and 8K-4Sr-2Li-2Nb require some further optimization to avoid formation of inflated bubbles. Increasing the number of layers showed a slight increase in the tendency for formation of the pyrochlore phase, which was proposed to be due to Na loss during deposition of several layers. The compositional engineering also influenced the occurrence of the pyrochlore phase, and it was suggested that dopants increasing the unit cell size simultaneously decreased the stability of the perovskite, suppressing its formation relative to pyrochlore.

Incompatibility of $Bi_{0.5}Na_{0.5}TiO_3$ thin films on platinized silicon and development of a $BaTiO_3$ diffusion barrier to avoid Bi-Pt reaction

Paper 4

Mads Christensen, Mari-Ann Einarsrud, Tor Grande

Manuscript not submitted.

Abstract

Platinized silicon (SiPt) has become the industry standard substrate for incorporation of oxide materials in micro electromechanical systems (MEMS). $Bi_{0.5}Na_{0.5}TiO_3$ based materials (BNT) on SiPt are promising for replacement of $Pb(Zr,Ti)O_3$ (PZT) in MEMS devices. Here, BNT thin films were deposited on SiPt by aqueous chemical solution deposition, and the morphology and microstructure of the BNT thin films were characterized by optical and scanning electron microscopy. The chemical and thermal compatibility of the BNT thin films and SiPt were investigated, and a reaction between Bi and Pt was identified. This led to weakening of the Pt-TiO_x interface of the SiPt substrate and delamination of the films. Introduction of a $BaTiO_3$ (BT) protective layer to spatially separate BNT and Pt was shown to reduce the challenges with the Bi-Pt reaction and allowed for deposition of thicker BNT thin films. It was demonstrated that BT has potential as a Bi diffusion barrier for deposition of BNT on SiPt.

7.1 Introduction

Micro electromechanical systems (MEMS) devices are commonly fabricated by means of Si wafer batch processing, a technology resulting from the development of electronic semiconductor devices. [3] Single crystal Si wafers are easily attainable, and fabrication methods such as lithography and etching allow for production of mechanical devices down to the µm scale. [196] Moreover, the semiconductor technology allows for integration of mechanical working parts and electrical circuits on the same unit. For most devices a bottom electrode is required, and for oxides such as $Pb(Zr,Ti)O_3$ (PZT) a metal electrode must not be susceptible to oxidation at the conditions during fabrication, allowing for only a few candidate electrode materials. Pt electrodes have been found to be chemically compatible with PZT, and it serves as an efficient nucleation surface for perovskite oxide materials. [11, 97] For this reason, platinized silicon (SiPt) has achieved the role of a reference substrate for deposition of electronic oxide materials. SiPt typically consists of 200-500 µm (100) oriented Si, coated by a 1 µm SiO_2 diffusion barrier, a ~20 nm partially oxidized Ti (TiO_x) adhesion layer, and ~50 nm (111) textured polycrystalline Pt. [239] Additional layers for diffusion control or strain compensation could also be employed. [12]

$Bi_{0.5}Na_{0.5}TiO_3$ based materials (BNT) are promising as a candidate for replacement of PZT in actuator applications. [15, 32, 66] Currently, piezoelectric devices are most often based on PZT, but lead-free alternatives are desirable due to the toxicity of lead. [2, 35, 36] A large strain response has been reported for bulk BNT, and BNT thin films have become an emerging research field with approximately 200 total publications by the end of 2016. [234] Often, the role of SiPt as the reference substrate is embraced, and SiPt is commonly used both for chemical solution deposition (CSD) [110, 146, 155, 157, 168] and physical deposition [238] of BNT. In our previous work, it was found that an interaction occurred between Bi and Pt for films deposited by an aqueous chemical solution method. [232] Similar reactivity of Bi and Pt have also been reported by other authors. [13, 230] However, to the best of our knowledge, the compatibility of BNT with SiPt is a topic that has not yet been treated systematically in literature. Different buffer layers for BNT deposited on Si have been reported, but the separation of BNT and Pt has not been the motivation or the focus of the investigations. Several authors have prepared BNT or similar materials on $LaNiO_3$ (LN) terminated Si substrates. The LN layer was deposited either on top of the Pt electrode for texture control of BNT [174], or instead of Pt as the bottom electrode [181, 240, 241]. $La_{0.7}Ca_{0.3}MnO_3$ has also been applied as a buffer layer on SiPt to promote (110) texture in BNT. [242]

In this work, the effect of a reaction between Pt and Bi from BNT on the Pt-TiO_x interface was investigated. BNT thin films on Pt were prepared by a previously reported aqueous CSD method. [232, 234, 243] A $BaTiO_3$ (BT) protective layer was introduced in order to spatially separate BNT and Pt, and different parameters for preparation of the BT layer were optimized. The BNT thin films were characterized by optical microscope, scanning electron microscope, and X-ray diffraction, with particular focus on how film quality developed with increasing number of layers.

7.2 Experimental

Aqueous BNT and BT sols were prepared by mixing stoichiometric amounts of individual precursor solutions. Starting chemicals and substrates with corresponding abbreviations are summarized in Table 7.1. The Ti precursor was prepared by adding TIP (0.6 M)[1] to a solution of CA (1.8 M) and stirring overnight at 70 °C. BiCit (1.0 M) was stabilized by EA (1.5 M) and ammonia for pH 8. Ba and Sr precursors were prepared as 0.2 M nitrate solutions by complexation with EDTA (0.2 M) and CA (0.4 M), and adjustment of the pH to neutral was obtained by addition of ammonia. NAmOx (0.5 M) and LiOH (1.0 M) were dissolved in water, and NaOH and KOH solutions were applied directly.

Undoped BNT was employed for the majority of this work, but compositionally engineered BNT was used in the final part (Table 7.2). BNT and 6Ba were prepared as reference compositions, while 6Ba-1K-2Nb, 4Ba-6K-6Li, and 8K-4Sr-2Li-2Nb were selected due to their promising properties for actuator applications in bulk BNT. [9, 10, 15] The BNT sols were adjusted to pH 7-10 by addition of ammonia and diluted to 0.3 M by water. The nominal stoichiometry of the BNT sols was adjusted to $A_{1.05}BO_3$ by Na excess. Preparation of the BNT sols and deposition on $SrTiO_3$ were described in detail in previous reports. [232, 234, 243] Long-term stable BT sols were obtained by mixing Ba and Ti precursor solutions, adjusting the pH to 7-10 by ammonia, and diluting with distilled water to 0.25 M.

Prior to film deposition, $SrTiO_3$ (ST) and platinized silicon (SiPt) substrates were heat treated at 550 °C to remove organic residues. The substrate surfaces were activated by oxygen plasma to enable wetting by the sol, and compressed air (clean room level ISO 7) was employed to remove any particles immediately before application of the sol. The sols were filtered through a 0.2 µm syringe filter during application, and promptly spin coated at 3000 rpm for 30 s, accelerating at 300 rpm/s. The films were dried by hot plate at 110 °C for 2 min. Pyrolysis was carried out by rapid thermal processing (RTP, Jipelec Jetfirst 200 mm, Semco Technologies, Montpellier, France) in O_2 atmosphere. The films were prepared in an ISO 7 level clean room.

Table 7.1 Summary of chemicals and substrates.

Abbr.	Name	Chem. formula	Supplier	Grade
TIP	Ti isopropoxide	$Ti(OCH(CH_3)_2)_4$	Sigma-Aldrich, SKU 87560	>97 %
CA	citric acid	$C_3H_5O(COOH)_3$	Sigma-Aldrich, SKU C0759	99 %
BiCit	Bi (III) citrate	$BiC_3H_5O(COO)_3$	Sigma-Aldrich, SKU 480746	99.99 %
EA	ethanolamine	$H_2N(CH_2)_2OH$	Sigma-Aldrich, SKU 411000	>99.5 %
ammonia	ammonia solution	NH_3 (aq)	Sigma-Aldrich, SKU 05002	33 wt.%
BaNit	Ba nitrate	$Ba(NO_3)_2$	Sigma-Aldrich, SKU 217581	>99 %
SrNit	Sr nitrate	$Sr(NO_3)_2$	Sigma-Aldrich, SKU 243426	>99 %
EDTA	ethylenediaminetetraacetic acid	$C_{10}H_{16}N_2O_8$	Sigma-Aldrich, SKU E9884	99.4-100.6 %
	Li hydroxide	LiOH	Sigma-Aldrich, SKU 62531	>99 %
NAmOx	Nb ammonium oxalate	$NH_4NbO(C_2O_4)_2$	Aldrich, SKU 525839	99.99 %
	Na hydroxide	NaOH	Sigma-Aldrich, SKU 35274	4.00 M
	K hydroxide	KOH	Sigma-Aldrich, SKU 35113	1.00 M
SiPt	platinized silicon	$Si_{100}\|TiO_{x,20nm}\|Pt_{111,40nm}$	MEMS Exchange	
ST	strontium titanate substrate	$SrTiO_3$	Crystal GmbH, Part No 1STO 101E	(100)

[1] Molarities in parenthesis correspond to the concentration after achieving the final solution volume.

Table 7.2 Overview of BNT compositions.

Sample notation	Nominal composition
BNT	$Bi_{0.5}Na_{0.55}TiO_3$
6Ba	$Bi_{0.47}Na_{0.52}Ba_{0.06}TiO_3$
6Ba-1K-2Nb	$Bi_{0.46}Na_{0.52}Ba_{0.06}K_{0.01}Ti_{0.98}Nb_{0.02}O_3$
4Ba-6K-6Li	$Bi_{0.48}Na_{0.41}Ba_{0.04}K_{0.06}Li_{0.06}TiO_3$
8K-4Sr-2Li-2Nb	$Bi_{0.47}Na_{0.44}Sr_{0.04}K_{0.08}Li_{0.02}Ti_{0.98}Nb_{0.02}O_3$

Table 7.3 Overview of BT protective layer notation scheme

Notation schemes for BT protective layers			
***x*BT550**	**1BT550+700**	**(*x*BT550)+700**	***x*(BT550+700)**
x layers BT pyrolized at 550 °C.	1 layer BT pyrolized at 550 °C and annealed at 700 °C.	*x* layers BT pyrolized at 550 °C. Annealed finally at 700 °C.	*x* layers BT pyrolized at 550 °C and annealed at 700 °C for each layer.

The pyrolysis process was the same for both BNT and BT, 5 min at 550 °C with a heating rate of 40 °C/s. In case of BNT, spin-coating and pyrolysis were repeated 1-20 times depending on the sample, and final annealing at 700 °C for 10 min (40 °C/s ramp rate) was employed for certain films. The BT protective layers were deposited by the same pyrolysis and annealing schemes, but the number of layers and level of annealing varied. BT films were either employed as-pyrolized, annealed after deposition of the final layer, or annealed for each layer. An overview of the BT notation convention is provided in Table 7.3, while Table 7.4 contains an overview of the prepared BT protective layer variants. The table is organized chronologically with short descriptions of the investigated topic of the batches/experiments, and the batch numbers correspond to headings in the Results chapter.

Films were characterized by grazing incidence X-ray diffraction (GIXRD, Bruker D8 Advance DaVinci with Lynxeye XE detector, Billerica, USA) with 0.03° step size and 7.7 s/step at 2° incidence angle. Microstructures were imaged by a scanning electron microscope (SEM) with a field emission electron gun, using the in-lens secondary electron detector (Zeiss Ultra 55 Limited Edition, Oberkochen, Germany). Optical microscope (OM) images were captured on a stereomicroscope with illumination from outside the lens (Nikon SMZ800). Because the incident illumination originated from outside the lens, perfectly flat surfaces did not reflect light into the lens, while small topographical features were enhanced.

Table 7.4 Overview of the batches/experiments, BT protective layers tested, and characterization techniques employed.

Batch #	Batch topic	1BT550	3BT550	1BT550+700	(3BT550)+700	2(BT550+700)	3(BT550+700)	10(BT550+700)	Characterization techniques
1	Introduction of BT protective layer. Influence on BNT	✓		✓	✓				OM, SEM, SEM, XRD
2	Characterization of BT (without BNT)	✓	✓	✓	✓				SEM (cross-section), SEM (top view), XRD
3	3 layers BT, thermal processing. Influence on BNT		✓		✓		✓		OM
4	Characterization of BT annealed each layer. (Without BNT)			✓		✓	✓	✓	SEM, XRD
5	Compositionally engineered BNT on the most promising BT protected SiPt						✓		Photograph, SEM, SEM/EDS, XRD

7.3 Results

No protective layer

OM images of BNT thin films deposited on ST and SiPt are displayed in Figure 7.1a. It is apparent that for otherwise identical processes, films on ST (left) demonstrated superior morphology relative to the films deposited on SiPt (right), which contained varying defects such as cracks and small delaminated areas. An OM image of the first BNT layer on SiPt is shown in Figure 7.1b. Already in the first deposited layer an uneven microstructure with tendencies of delamination was observed after pyrolysis. GIXRD patterns of the two films presented in Figure 7.1c demonstrate that the phase composition of the two BNT films was the same. Formation of a small amount of a pyrochlore secondary phase is evident in both films.

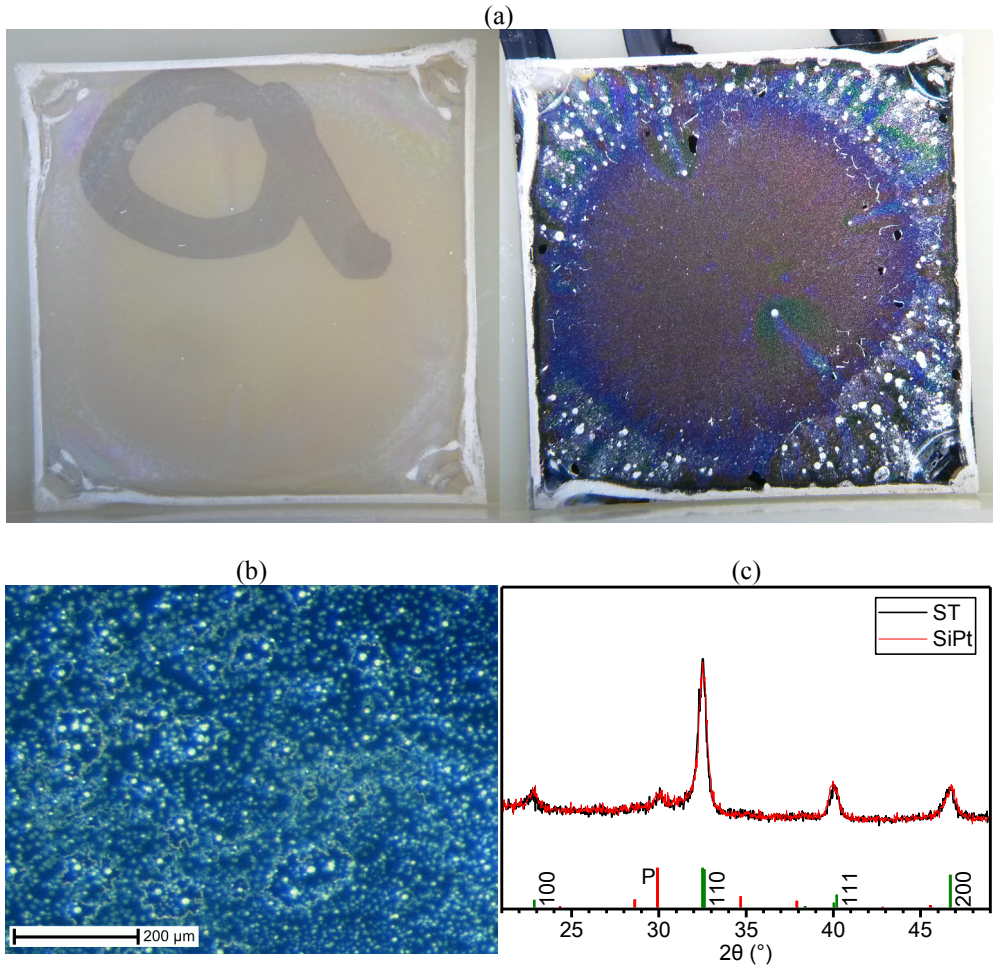

Figure 7.1 OM images of BNT thin films on 1×1 cm^2 substrates. (a) Comparison of 5 layers of BNT on ST (left) and SiPt (right). (b) Magnified OM image of a single layer of BNT on SiPt. (c) GIXRD patterns of the samples in (a). Reference patterns: R3c BNT with pseudocubic Miller indices [42] and pyrochlore [211].

Introduction of a BT protective layer

OM images of BNT deposited directly on SiPt or with different BT protective layers are shown in Figure 7.2 (refer to Table 7.3 for an overview of the BT notations). With increasing thickness of the BNT thin films due to successive layers, mm-scale delamination occurred for all films except the single layer BNT. The BNT film on 1BT550+700 delaminated after 6 BNT depositions, the film without BT after 8 depositions, and the film on 1BT550 failed after layer number 10. The BNT film on (3BT550)+700, however, did not delaminate until 20 depositions of BNT, and the delamination was limited to certain areas of the film. Additional films were prepared on substrates from another SiPt supplier, confirming the trend. A reference sample without BT and only one BNT layer did not delaminate or change surface morphology with the accumulated heat treatments.

The iridescence colors of the films in Figure 7.2 relate to the thicknesses and refractive indices of the films. The colors corresponded well to the expected trend according to the number of coatings. For example, yellow color was achieved at the fifth total layer regardless of the number of BT coatings.

It was confirmed by EDS that the debonding occurred between Pt and the TiO_x adhesive layer of SiPt in Figure 7.3. The figure shows the delaminated film on 1BT550, and Pt signal was not observed on the surface of the delaminated areas, while the bottom surface of the delaminated film showed a strong Pt signal. Moreover, the delaminated areas of the substrate appeared black to the naked eye, explained by the TiO_x layer which is known to turn dark blue as Ti is reduced. [244]

EDS mapping clearly identified the individual layers of Pt, BT, and BNT in the cross-section of the delaminated film on the (3BT550)+700 substrate with 20 BNT layers in Figure 7.4. BT and BNT layers were distinguishable by both EDS and by the morphology of the layers. The layer of BT consisted of grains as large as the BT thickness, approximately 100 nm, and some intergranular porosity was observed. The grains of BNT, however, were 20-50 nm in size, and the BNT film was dense. The phase content of this film was shown by GIXRD (Figure 7.5a) to be phase pure BNT perovskite after annealing, but some pyrochlore secondary phase was present prior to annealing.

GIXRD patterns demonstrating peak shift in a single layer of BNT deposited on 1BT550+700 are presented in Figure 7.5b. Shift of both BT and BNT reflections, relative to BT without BNT and BNT directly on SiPt, were observed. These shifts in the reflections demonstrate that the BT and BNT layers were in reality solid solutions of BNT-*x*BT. A reference pattern of BNT-9Ba (5 layers pyrolized 550 and finally annealed at 700 °C) is provided, and the shift of BNT reflections on the BT protective layer was even more severe, suggesting that the BNT layer contained more than 9 % Ba due to BT-BNT mixing.

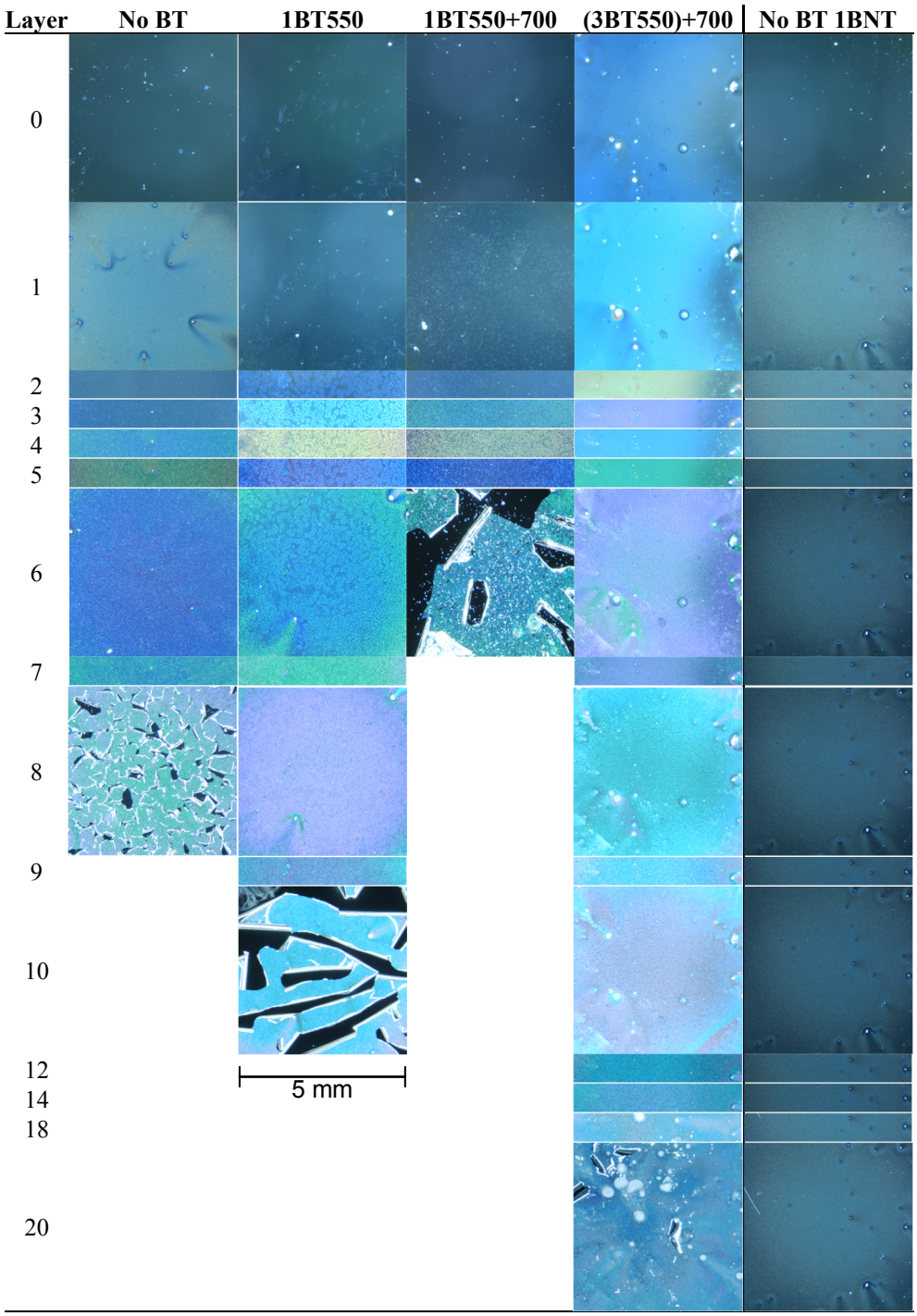

Figure 7.2 Optical microscope images of BNT thin films on BT protected platinized silicon with increasing number of coatings. Each column corresponds to a different BT protective layer, and each row to an additional BNT layer. 1BNT signifies that only 1 layer was deposited, but thermal processing was applied.

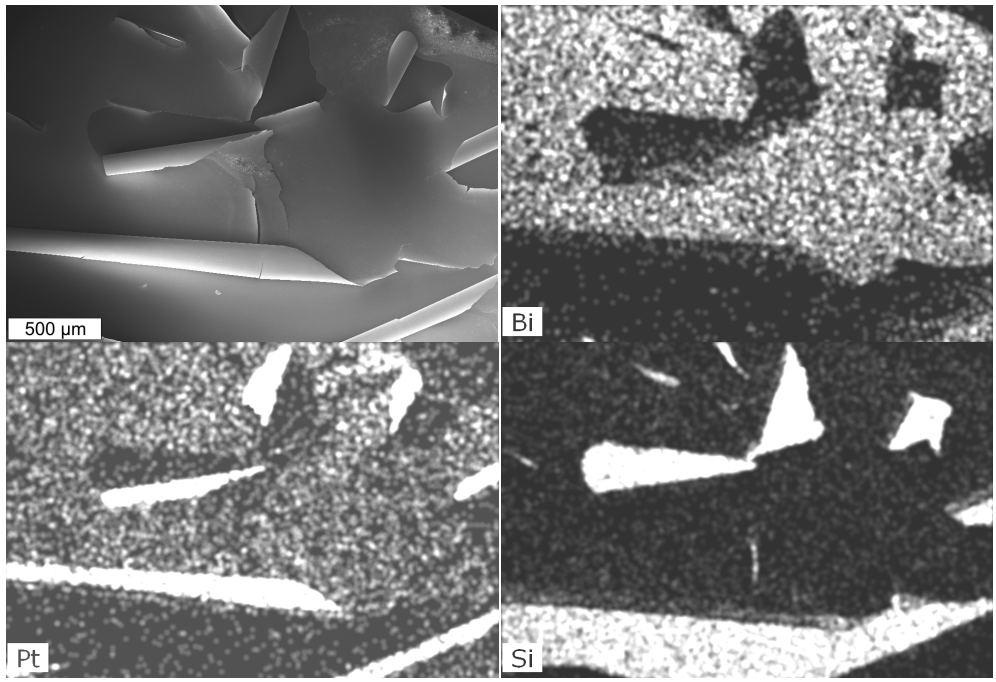

Figure 7.3 SEM image and EDS images of BNT deposited on 1BT550 in an area with delamination. The images show mm-scale sections of Pt-BT-BNT laminates that have curved away from the TiO_x surface.

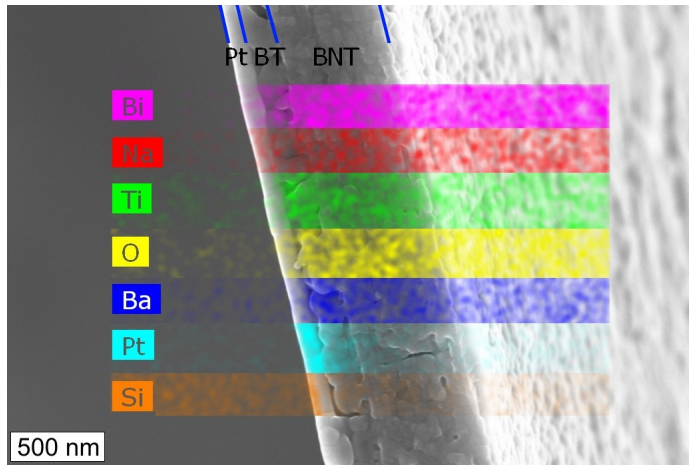

Figure 7.4 SEM image and EDS overlay of delaminated Pt-BT-BNT sequence bending out from the substrate. (3BT550)+700 with 20 layers of BNT, finally annealed at 800 °C. The bleeding EDS signal from other sections of the film is due to fundamental limitations in EDS resolution.

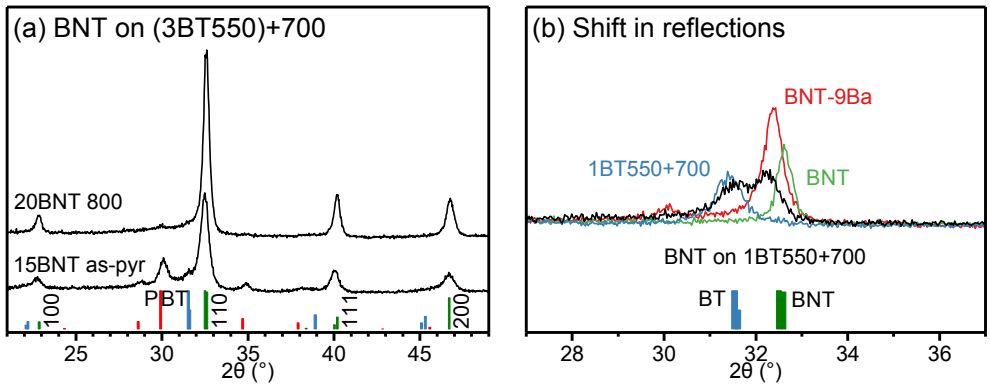

Figure 7.5 (a) GIXRD patterns before and after annealing of 15/20 layer BNT on (3BT550)+700. (b) Shift in BNT reflection on BT protective layer compared to BNT directly on SiPt, BNT doped with 9 % Ba (from [234]), and BT protective layer without BNT (from Figure 7.8). Reference patterns: BNT [42], BT [245], and pyrochlore [211].

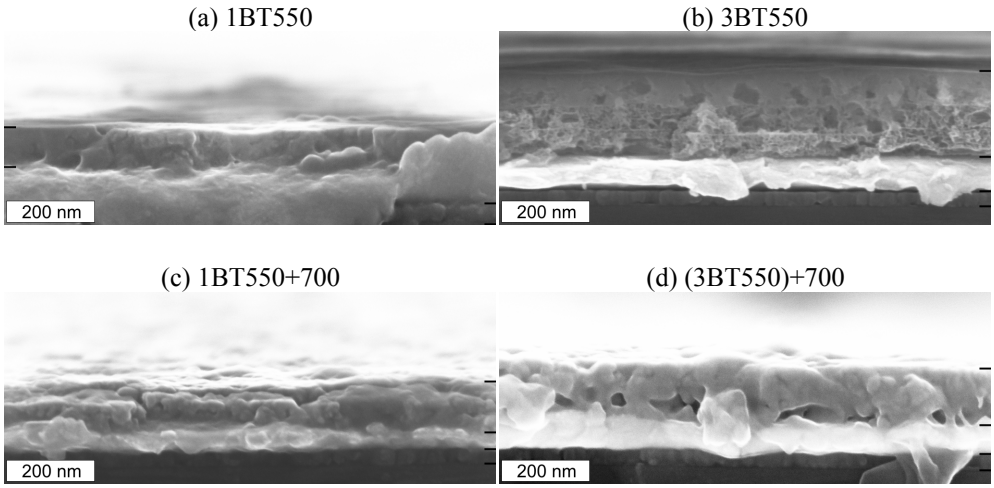

Figure 7.6 Cross-sectional SEM images of pure BT films on SiPt. Si-TiO_x-Pt-BT-air interfaces are marked.

Characterization of the BT protective layer without BNT

The microstructures of the BT thin films prior to BNT deposition are displayed as cross-sectional SEM images in Figure 7.6 and by top-view in Figure 7.7. The morphology of annealed films was significantly different from the as-pyrolized films. The as-pyrolized films lacked a clear grain structure, indicating that the films were still not crystalline. GIXRD patterns in Figure 7.8 confirmed the amorphous nature of the films. The thickness of the as-pyrolized films was also larger than for annealed films, indicating that the thermal decomposition and the accompanying weight loss giving rise to shrinkage was not completed. Moreover, the 3-layer thick annealed film contained significant porosity between the Pt electrode and the BT layer (Figure 7.6d), which most likely originated from gas evolution due

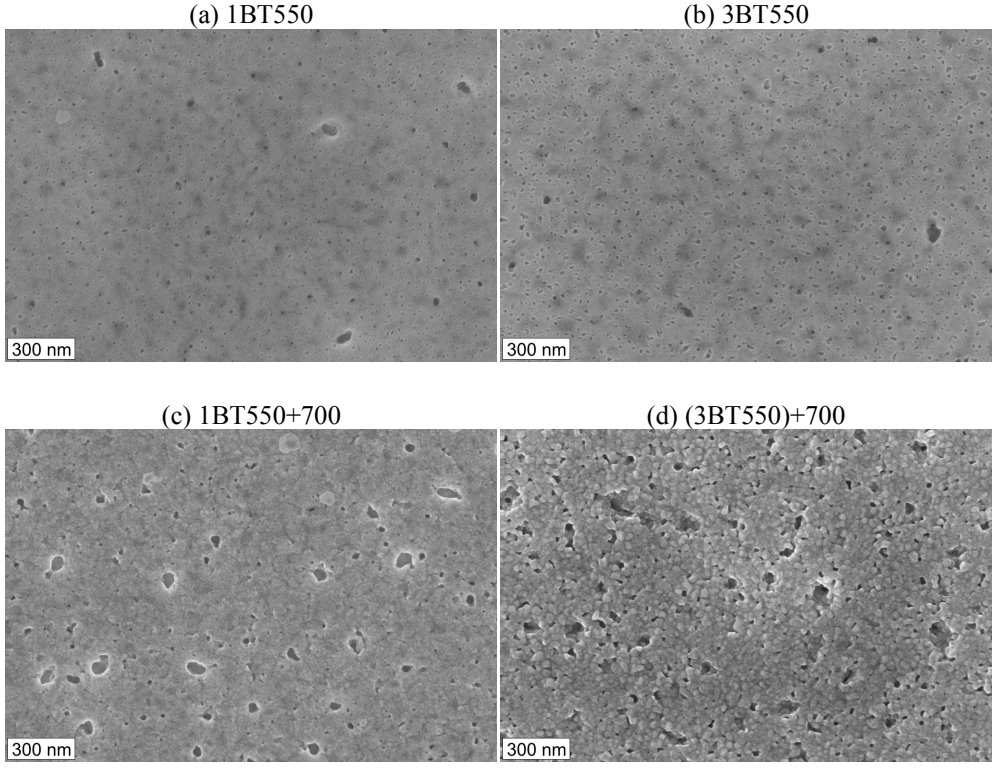

Figure 7.7 Top-view SEM images of BT films on SiPt without BNT.

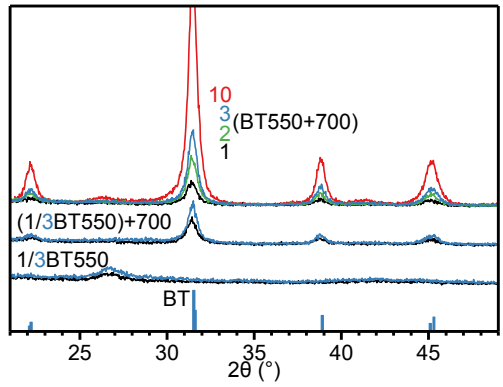

Figure 7.8 GIXRD patterns of BT thin films deposited on SiPt without BNT deposition.

to further decomposition after deposition of subsequent layers. Evenly distributed 100 nm pores are visible in otherwise dense microstructures for all films in the top-view images (Figure 7.7). In order to obtain films without pores extending through the coating, BT protective films consisting of 3 layers were studied further in the following.

Heat treatment of 3-layer BT films

The influence on film quality of the incomplete decomposition in 3-layer as-pyrolized BT films is shown by OM images in Figure 7.9. As-pyrolized and annealed BT films are compared and the morphologies of the BT and subsequent BNT thin films are shown. Defects on the μm scale visible as white spots appeared in the case where the second BT coating was deposited on an as-pyrolized previous layer. The defects remained after deposition of the third layer, and additional defects appeared. With deposition of BNT on as-pyrolized BT (3BT550), the topography of the film became uneven close to the initial BT defects. Varying topography on the film surface caused increased light intensity in the dark field OM images. The BNT on (3BT550)+700 did not develop this topography, due to the annealing step applied to the BT deposition process. When each BT layer was annealed at 700 °C, the resulting films were defect free, avoiding both the defects in the BT layer, and the topography in the BNT film. For comparison, deposition of BNT directly on Pt was still confirmed to cause defective films visible as inhomogeneous color/intensity and appearance of larger white spots. It is clear that annealing for each deposited BT layer yielded the superior film quality, and BT films of varying number of layers annealed for each deposition are characterized in the next section.

BT films with annealing of each layer

SEM images of the BT thin films of varying number of layers prepared by pyrolysis and thermal annealing at 700 °C of each layer are shown in Figure 7.10. Compared to thin films which were annealed only after the third layer (Figure 7.6), these films were denser without porosity trapped between the Pt bottom electrode and the BT film. The 100 nm pores previously observed on the surface occurred for this batch of films as well. All the annealed BT films were confirmed by GIXRD to be phase pure BT perovskite after annealing (Figure 7.8). A BT film consisting of 10 layers was also prepared, and the microstructure is presented in Figure 7.10d. The thicker BT film contained areas with a microstructure similar to the thinner BT films, but the majority of the film surface was covered by a porous microstructure.

Compositionally engineered BNT on 3(BT550+700)

3(BT550+700) was identified as the most promising BT protective layer above, and it was therefore selected for fabrication of compositionally engineered BNT thin films (BNT, 6Ba, 6Ba-1K-2Nb, 4Ba-6K-6Li, and 8K-4Sr-2Li-2Nb). These BNT compositions were previously investigated for deposition on ST, and defect free 15-layer films were successfully prepared in that case. [243] On BT protected SiPt substrates, however, the compositionally engineered BNT films delaminated upon deposition of BNT layer number 4 as seen in the photographs in Figure 7.11.

Prior to pyrolysis of BNT layer number 4, there was no visible difference between the films with the different BNT compositions. In the delaminated films in Figure 7.11, however, 1-2 mm circles of a brighter color are seen. These areas were found to correspond to nm-scale particles with relatively spherical morphology shown by SEM in Figure 7.12. EDS of the particles is presented in Figure 7.13, demonstrating that they were composed of Bi oxide. The EDS spectra clearly showed Pt signal from the electrode and Bi and O from the particle. It is suggested that these particles grew as liquid metallic Bi causing reactivity with Pt. Transient metallic Bi has been demonstrated for this synthesis method. [232] The O signal in EDS and the bright color (Bi_2O_3 is light yellow) suggest that the droplets/particles were later oxidized.

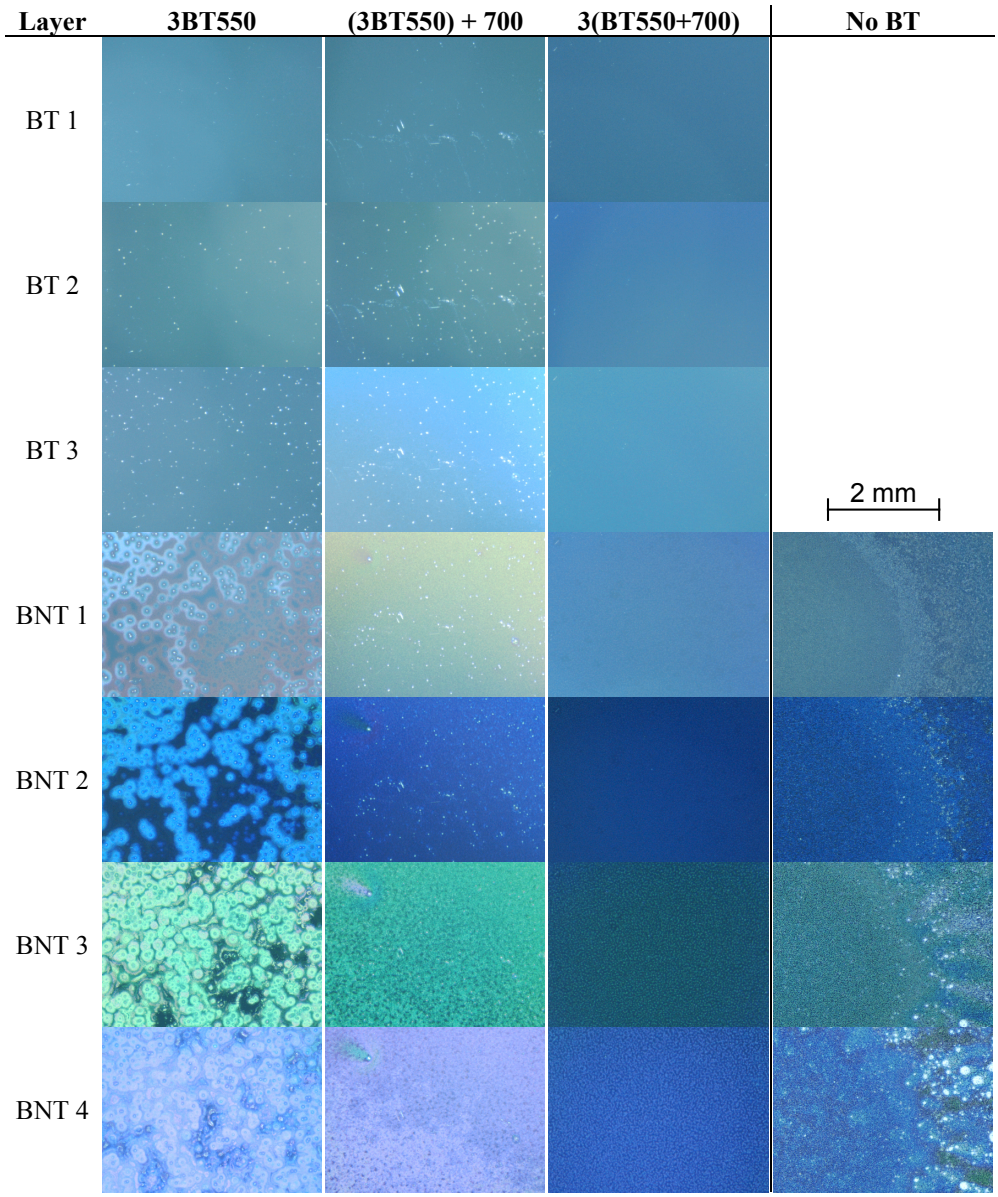

Figure 7.9 OM images demonstrating the effect of annealing the BT layers on the BT and BNT film qualities. As-pyrolized, finally annealed, and each layer annealed BT films are compared. BNT directly on SiPt is shown for reference. The columns correspond samples, and rows to additional layers.

GIXRD patterns of BNT, 6Ba-1K-2Nb, and 4Ba-6K-6Li films are presented in Figure 7.14. The undoped BNT showed distinct signatures of the perovskite BT and BNT, and a small amount of a pyrochlore secondary phase in accordance with observations in previous samples (Figure 7.5). Only a limited amount of BNT perovskite was observed in the doped BNT films, while there was a significant amount of the pyrochlore secondary phase. Furthermore, reflections due to formation of Bi_2O_3 were also evident by the reflection at 28°.

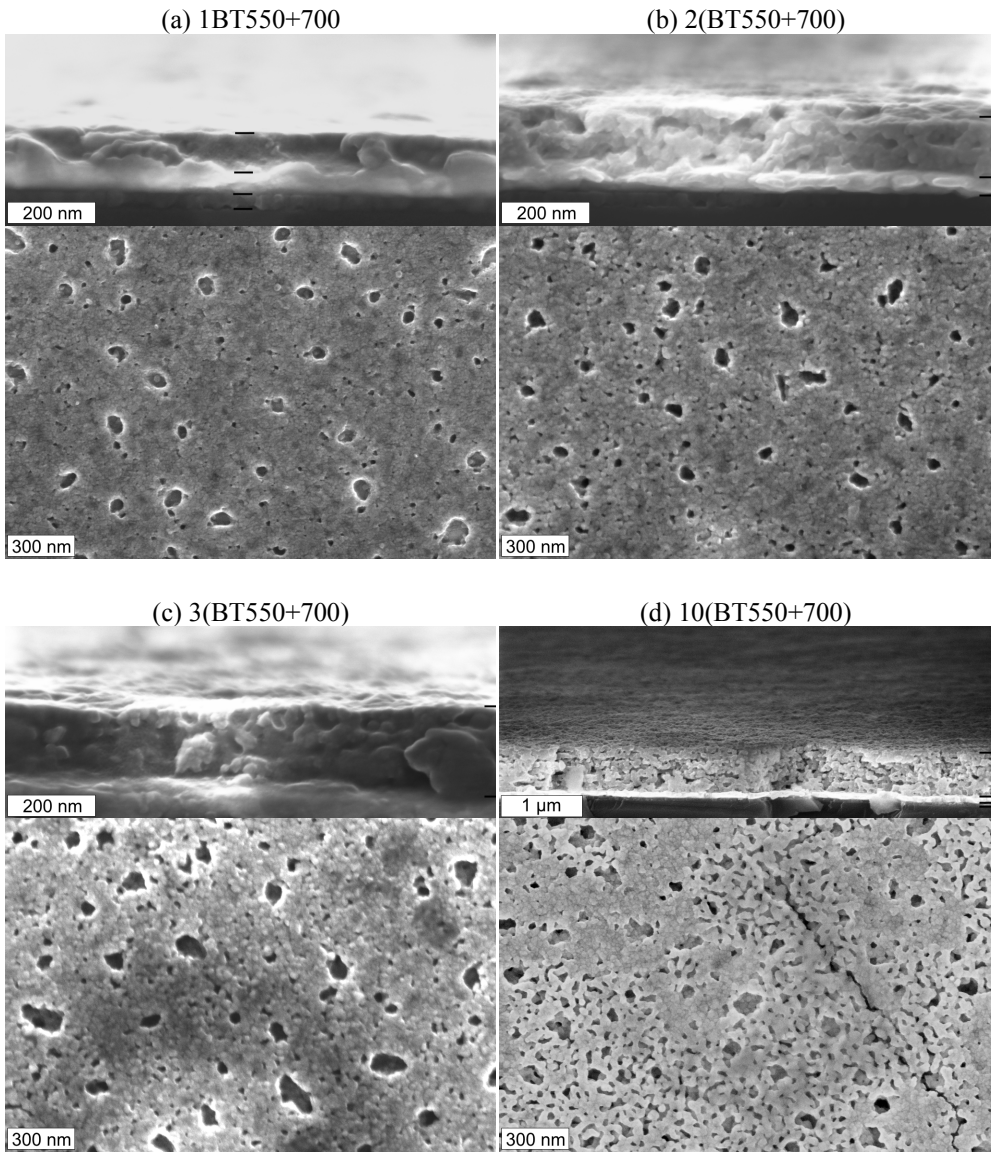

Figure 7.10 SEM images of BT protective layers prepared by pyrolizing and annealing each layer.

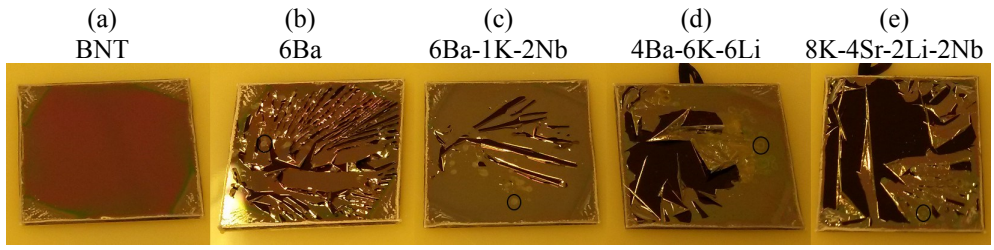

Figure 7.11 Delaminated films on 2×2 cm^2 BT protected SiPt (3(BT550+700)). Delamination occurred for BNT layer number 4. Black circles show examples of "circles of bright color" consisting of the droplet shaped particles in Figure 7.12.

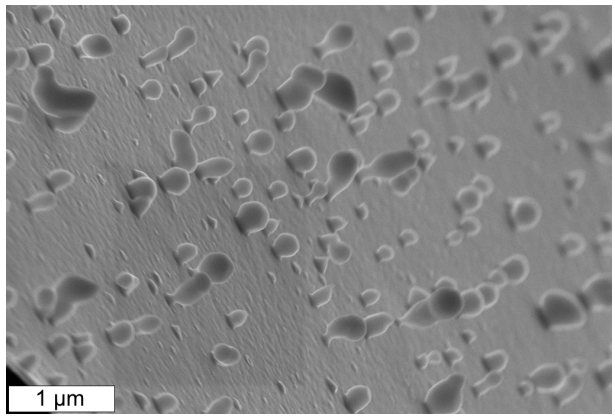

Figure 7.12 SEM image of the Pt bottom surface after delamination of the Pt-BT-BNT laminate. This is the film from Figure 7.11d.

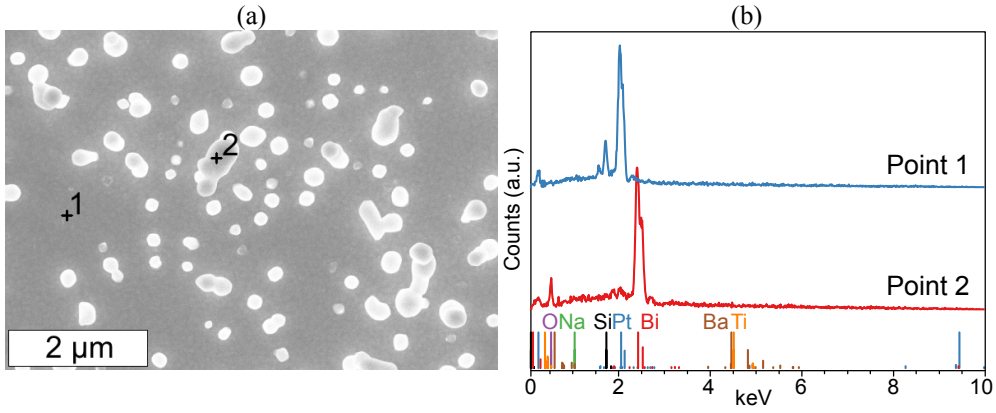

Figure 7.13 (a) SEM image of Bi droplets on the Pt bottom electrode. (b) EDS of points in (a).

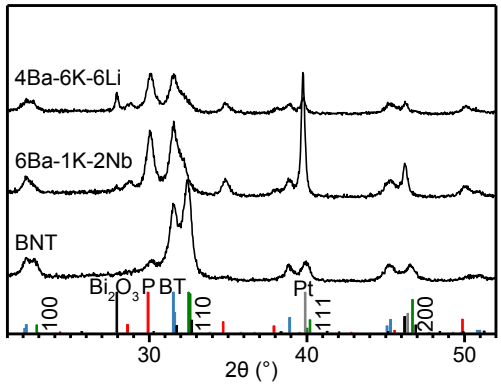

Figure 7.14 GIXRD patterns of films from Figure 7.11 (a, c, d) illustrating the phase composition of delaminated doped BNT films relative to the intact undoped BNT film. Reference patterns: BNT [42], BT [245], Pyrochlore [211], Bi_2O_3 and Pt.

7.4 Discussion

The reaction between Pt and Bi

It was apparent that direct contact between BNT and the Pt bottom electrode was central in weakening of the Pt electrode leading to delamination. No deterioration of the Pt electrode was observed even for 10-layer BT films annealed for each deposition. Moreover, with BT protective layers between the Pt bottom electrode and BNT, thicker BNT films could be obtained, and the morphology of the films was defect free, unlike when the BT protective layer was not employed.

During decomposition of the inorganic-organic BNT gel network, Bi is known to exist in a transient metallic state. [232] Bi and Pt metals are reactive, forming intermetallic phases (Bi_2Pt, BiPt) and alloys with melting temperatures ranging from 271 °C for pure Bi to 730 °C for 57 at% Pt. [216] In the intermediate range, solubility of Pt in the liquid phase increases gradually. [216] It is therefore concluded that the weakening of the Pt-TiO_x interface was a direct consequence of contact between the Pt bottom electrode and Bi from BNT.

It should be noted that a Bi-Pt reaction was identified in our previous work. Appearance of Pt reflections in GIXRD demonstrated that the Pt texture was lost with BNT deposition. [232] This was suggested to be caused by recrystallization of Pt, but debonding of Pt from TiO_x will cause severe reorientation of entire sections of the Pt electrode, explaining the appearance of Pt reflections equally well.

Despite the large improvement of the BNT film morphology when introducing the BT protective layer, delamination still occurred as the number of BNT layers increased. This suggests that the BT protective layers reduced the level of Bi-Pt reaction, but did not suppress the reaction entirely. The pores in the microstructure of the BT films and the solid solution of BNT and BT (peak shift in Figure 7.5) demonstrated that a partial contact of BNT and Pt was still relevant even for the densest BT protective layers produced in this work.

For even better protection of the Pt electrode the BT protective layer should be completely dense. Moreover, a superior material for the protective layer would be one that does not possess as good solubility in BNT, suppressing the mixing and Bi diffusion toward the Pt electrode.

Cause of delamination

The cause of the mm-scale delamination was clearly related to the BNT-Pt contact. However, the lack of delamination in the single layer of BNT deposited directly on SiPt demonstrates that BNT-Pt contact and heat treatment alone was not sufficient (Figure 7.2, right column). It is therefore suggested that the driving force for delamination increased with increasing BNT thickness.

Stress due to thermal expansion mismatch

For a thin film deposited on a thick substrate, the substrate can be treated as infinitely thick and un-strained. [205, 206] Imagine, for example, a 500-nm film on a 500-µm substrate, and that the two materials have different zero-strain dimensions. This causes tensile strain in one material and compressive in the other. Applying Hook's law and assuming that the film and substrate have equal Young's moduli yields that the substrate will be strained only 0.1 % of the strain experienced by the film. For this reason, the strain in the film will not change significantly with varying the film thickness. Such a strain occurs due to thermal expansion

mismatch upon cooling from a zero-strain crystallization temperature and is associated with a bilateral misfit stress, σ [205, 206]

$$\sigma = \frac{(\alpha_f - \alpha_s)(T_0 - T)E_f}{1 - \nu_f} \tag{7.1}$$

where α_f and α_s are the thermal expansion coefficients of film and substrate, respectively. T_0 is the initial temperature, T is the final temperature, E_f is the Young's modulus and ν_f is the Poisson ratio. Because the strain and stress are not influenced by the film thickness, additional layers will result in increased elastic energy.

The elastic energy represents the driving force for delamination, and the interfacial fracture energy, Γ (J/m^2), the resistance toward delamination. [205, 206] The empirical criterion for crack propagation in debonding of a thin film on an infinitely thick substrate is known as [205, 206]

$$\frac{E\Gamma}{(1-\nu^2)h\sigma^2} = 2 \tag{7.2}$$

where h is the film thickness. For debonding, the critical thickness of the film is then given by [205, 206]

$$h_c = \frac{2(1-\nu_f)\Gamma}{E_f \Delta\alpha^2 \Delta T^2} \tag{7.3}$$

Since the films here delaminated during the pyrolysis step, the highest applied temperature of 550 °C defines the zero-strain state. The thermal expansion of Si is 2.58×10^{-6} K^{-1} at room temperature [200], while the thermal expansion of perovskites such as BNT, PZT, and ST is approximately 9×10^{-6} K^{-1} [56, 201]. The Young's moduli of 6Ba and 6Ba-1K-2Nb have been reported to be approximately 57 GPa at RT. [207] The Poisson ratio was reported to be 0.25. [34] The interfacial fracture energy of Pt-TiO_x is not easily obtained, but one report suggested it to be as high as 12.36 J/m^2. [210] Calculating the critical thickness for delamination during cooling from 550 °C to room temperature using the above values yields 28.8 µm.

The above theoretical treatment yielded a critical BNT thickness for delamination which is a factor 100 larger than what was observed, indicating that one or more of the assumptions do not hold. The most obvious discrepancy is the interface energy of Pt-TiO_x which likely was significantly smaller for the substrates exposed to Bi. Larger Young's modulus and thermal expansion coefficient of the film will also reduce the estimated critical thickness.

It should be noted that another commonly observed mechanism of stress relief in strained films is that of cracking. The fact that this failure mechanism was not observed, but that the point of failure was in the substrate stack, demonstrates that the mechanical integrity and density of the BNT film itself were high.

Compositionally engineered versus undoped BNT

In our previous work, it was suggested that chemical modifications to BNT reduced the relative stability of the BNT perovskite, suppressing and delaying its formation slightly. [234, 243] On ST, however, phase pure perovskite phase was still obtained for these exact sols, while deposition on the BT protected SiPt yielded primarily the pyrochlore phase (Figure

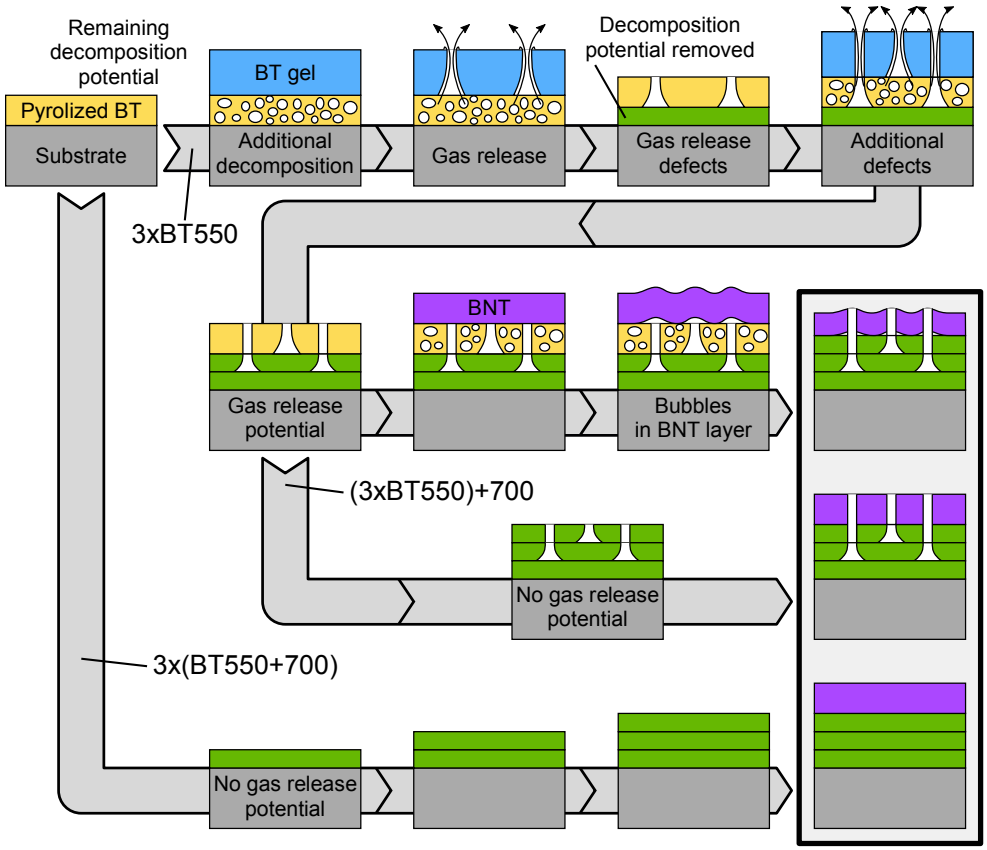

Figure 7.15 Illustration of the suggested mechanisms active during BT and BNT depositions. The yellow layer signifies a pyrolized BT layer with remaining potential for gas development. The blue layer signifies an early stage of the BT film during pyrolysis. The green layer signifies a BT layer without further potential for gas development.

7.14). [243] It is therefore suggested that the combined effect of the high concentration of Ba in the BT-BNT interface and the chemical modification of BNT caused a detrimental destabilization of the perovskite phase. This destabilization is further thought to have extended the time frame of the transient metallic state of Bi, leading to increased Bi-Pt reaction and ultimately delamination. Finally, the Bi droplets had grown large enough to be observed in SEM, and to remain as Bi oxide due to the too severe segregation.

BT film quality related to uncompleted decomposition

The different defects observed in the as-pyrolized BT films (Figure 7.9) provide an extensive insight into the decomposition processes of BT and BNT, and the homogeneity and density of the films throughout the pyrolysis. An illustration of the suggested mechanisms active during deposition of BT with different heat treatment and subsequent BNT deposition is provided in Figure 7.15. Despite the relatively porous structures of BT films, the appearance of defects in the second and third layers of BT demonstrates that these layers were too dense for gas release during pyrolysis. It is noted that the visible defects observed in Figure 7.9 and illustrated in Figure 7.15 were on the µm-scale, and separate mechanism to the 100-nm pores seen in SEM.

As films were deposited on top of layers which were not completely decomposed, gas evolving from this underlying layer pushed through the fresh layer, resulting in defects acting as chimneys. This likely occurred at 550 °C, because the underlying layer had already spent 5 min at 550 °C, and further decomposition at lower temperatures cannot have been significant.

Deposition of BNT on BT with further potential for gas evolution led to formation of bubbles perfectly correlated to the locations of the chimneys from the BT layers. This demonstrates that the BNT film during pyrolysis (likely at 550 °C) was more ductile than that of BT, allowing inflation and deformation of the film without releasing the evolved gas. With deposition of additional BNT layers, the bubbles remained, but the height difference decreased. Compare, for example, the homogeneity of the iridescence colors in layer 3 and 8 of BT550 in Figure 7.2. The bubbles in the BNT layer were avoided when the BT had been annealed at 700 °C, confirming that they were in fact caused by reactions in the BT layer.

7.5 Conclusions and further work

It was thoroughly demonstrated that a detrimental weakening of the Pt-TiO_x interface occurred when BNT was deposited directly onto the Pt electrode on SiPt. Combined with thermal expansion mismatch of Si and BNT, the accumulated elastic energy in the thin films led to complete delamination as the BNT thickness increased. The weakening of the Pt-TiO_x interface was concluded to be caused by a reaction between Bi and Pt. Introduction of a BT protective layer to spatially separate Bi from Pt increased the achievable thickness of BNT films without delamination. Depending on the density of the BT layer, however, Bi could still reach the Pt to a certain degree, and delamination occurred for films significantly thinner than what could be expected based on estimations takin into account the mismatch in thermal expansion. The BT films were not sufficiently dense and in case of compositionally engineered BNT films the presence of the BT layer destabilized the BNT perovskite phase resulting in droplet-shaped particles of Bi_2O_3 and a higher extent of Bi-Pt reaction.

While the detrimental nature of the Bi-Pt reaction was improved by introduction of a BT protective layer, further optimization is required for superior BNT films. The BT layers prepared were partly porous, and the solid solubility of BNT in BT also contributed to the Bi-Pt contact. Assuming that BT should still be the material of choice for the protective layer, care should be taken to achieve crystalline and dense films. Alternatively, one may also introduce alternative materials such as $SrTiO_3$ and $CaTiO_3$ as the reaction barrier. These materials could relatively easily be adapted to the aqueous CSD used in this study. Finally, replacing the Pt electrode must be acknowledged. Despite the technological relevance of the SiPt stack in commercial devices, alternative ceramic electrodes on Si such as $LaNiO_3$ [174, 178, 240] and $SrRuO_3$ [246] have also been reported.

Conclusions

Chapter 8

The motivation of this work was to replace the $Pb(Zr,Ti)O_3$ (PZT) actuator in the TLens with a lead-free alternative due to the health, environmental, and legislative concerns with PZT. To this end, the material system based on $Bi_{0.5}Na_{0.5}TiO_3$ (BNT) was selected as the superior lead-free candidate due to its large and temperature insensitive strain response. One of the overall goals of the Beat the Human Eye project was to make the TLens more environmentally friendly, and for this reason the selected fabrication method was aqueous chemical solution deposition (CSD). The main aim of this thesis work was therefore to develop the aqueous fabrication method of BNT thin films. It became clear in the early stage of the study that fundamental challenges in the fabrication method related to reproducibility, phase purity, microstructure, and compatibility with industrial application became the important sub-goals.

Aqueous CSD of BNT thin films was successfully achieved for the first time in this work. The precursor solution was a variant of the citrate CSD method, made by Ti isopropoxide stabilized by citric acid (CA), Bi citrate stabilized by ethanolamine, Ba and Sr nitrates stabilized by EDTA and CA, and ammonium niobate oxalate and alkali hydroxides which did not require complexation due to the high solubility in water. The method provided sols with long-term stability, requiring only simple preparation procedures while maintaining high reliability. Moreover, the sols consisted of environmentally friendly, cheap, and non-toxic chemicals.

Phase pure BNT powders were obtained by calcination of the gels at 550 °C for 2 h in air, while phase pure thin films prepared by spin coating was achieved on $SrTiO_3$ (ST) and platinized silicon (SiPt) by pyrolysis at 550 °C for 5 min in O_2. At lower pyrolysis temperatures, segregation of transient metallic Bi resulted in formation of a pyrochlore secondary phase. Addition of Na excess promoted the perovskite formation and suppressed the formation of the pyrochlore phase.

The CSD method was further developed for fabrication of BNT modified with Ba on A-site. Phase pure BNT-Ba perovskite with 0-9 % Ba could be obtained in the form of both powder and thin-film samples. With increasing Ba content in thin films, however, formation of the pyrochlore secondary phase was promoted, and phase purity required final annealing at 800 °C, pyrolysis at 600 °C, or addition of Na excess. The lattice parameters of BNT-Ba increased with the Ba content, reflecting the larger cation radius of Ba^{2+}. The electrical properties of thin-film BNT and BNT-6Ba were determined, and both compositions expressed polarization-field hysteresis loops characteristic of thin-film piezoelectrics. Strong fields of 1400 kV/cm could be applied without experiencing dielectric breakdown of the films, and at 500 Hz cycling frequency, the hysteresis loops were shown to be dominated by ferroelectric response. The effect of composition on electrical properties could not be determined due to the clamping effect of the substrate and the leakages current.

Next, the morphology and microstructure of BNT thin films were optimized. Homogeneous, dense, and defect free films were obtained on SiPt substrates by applying 40 °C/s ramp rate during pyrolysis. For films deposited on ST substrates, however, this rapid ramp led to formation of blisters, tears, and craters due to gas release during organic decomposition. Applying a slower ramp rate of 1.67 °C/s led to microstructures with low density and pores extending through the entire thickness of the film. Dense and homogeneous thin films of BNT on ST substrates were achieved by applying the slow ramp rate of 1.67 °C/s to 450 °C (temperature of perovskite nucleation) and rapid ramp of 40 °C/s from 450 to 550 °C.

The aqueous CSD was also extended to include additional chemical modifications to BNT. Stable sols containing Sr, Li, K, and Nb were developed, obtaining 0.3 M sols with long-term stability. Even more concentrated sols could be prepared by evaporation of the solvent, and sols of undoped BNT were long-term stable for 0.6 M. Phase pure perovskite powders were prepared by calcination at 550 °C. The thin films produced from the same sols were also phase pure after three depositions, demonstrating that the principle aqueous CSD method is viable for fabrication of BNT thin films with a range of chemical modifications. With increasing the number of coatings, however, an increasing amount of the pyrochlore secondary phase was present in the as-pyrolized films. The BNT and BNT-6Ba thin films were relatively phase pure after thermal annealing, while the films with 6Ba-1K-2Nb, 4Ba-6Li-6Nb, and 8K-4Sr-2Li-2Nb were not. Films of 10 layers turned phase pure upon annealing at 800 °C, while a small amount of secondary phases remained in two compositions after annealing 15-layer thick samples at 700 °C. The increasing amount of pyrochlore with subsequent depositions was argued to be caused by gradual change of the composition of the thin-films with accumulated heat treatment. Measures to obtain phase pure films on the μm scale were demonstrated. Electrical measurements were conducted, and the thin films were ferroelectric with properties comparable to state of the art BNT thin films produced by alternative methods. At strong fields and low frequency, the leakage current was significant and increasing with time. The leakage with positive bias to the top electrode was orders of magnitude larger than for negative bias, approaching 10^{-3} A/cm^2 at 500 kV/cm when holding at constant voltage for 2 s. The nature of the leakage and measures to suppress it were discussed.

The feasibility of deposition of BNT on SiPt substrates was the final part of the study. It was found that a weakening of the Pt-TiO_x interface occurred due to a reaction between Bi and the Pt bottom electrode. The effect of this reaction was apparent already with the first deposited BNT layer, where small-scale debonding and morphological irregularities were observed. With introduction of a $BaTiO_3$ (BT) protective layer to spatially separate Bi and Pt, BNT thin films of significantly better morphology were obtained. Despite the beneficial effect of the BT layer, complete delamination of large portions of the film still occurred with increasing thickness of the BNT thin film. This was due to a combination of the accumulated stress from thermal expansion mismatch of BNT and Si, and a weakening of the Pt-TiO_x interface as some Bi-Pt contact still occurred. Further investigation into protection of the Pt bottom electrode is therefore required.

Outlook

Chapter 9

Phase purity

Two sources of formation of the pyrochlore secondary phase were identified in this work. The first was the transient reduction of Bi^{3+} into metallic Bi with resulting long-range segregation when the heat treatment holding temperature was below 450-500 °C. This mechanism was identified and phase purity could be obtained by increasing the pyrolysis temperature. The second source of pyrochlore was related to destabilization of the perovskite phase upon chemical modification of the BNT compositions or fabrication of films with a large number of depositions. Certain aspects of this second source of pyrochlore retain topics for further optimization.

The formation of the pyrochlore secondary phase occurred when the BNT sol was modified by addition of Ba, Sr, K, Li, and Nb. In case of only a few deposited layers, the formation of the pyrochlore could be reversed, and phase purity was achieved by additional thermal annealing. Moreover, Na excess was demonstrated to promote phase purity. However, the amount of pyrochlore increased with increasing thickness of the thin films. 10-layer thick as-pyrolized films contained some pyrochlore that was removed by annealing, but two out of five compositions had a small amount of remaining secondary phase even after annealing of 15-layer thick films. This was explained by accumulated loss of Na during deposition of many layers.

The Na loss could occur due to evaporation, dissolution into the sol, or diffusion into the substrate, with the latter argued as being the most significant. In any case, applying sols with larger amount of Na excess for deposition of the first layers could be required for obtaining phase pure films with a large number of layers. The TLens and other cantilever actuators typically require films with thickness in the order of 1-2 μm, and multiple depositions is a

requirement for CSD. Another measure that could provide phase purity in thick films is to apply an annealing step for every few pyrolysis steps. The rationale behind this strategy is to ensure that the perovskite phase is formed to stabilize and reduce the activity of the principle oxides to suppress loss. A first approach to this could for example be to anneal at 700 °C for every 5-7 layers. Ensuring the perovskite formation could also be obtained by pyrolysis at higher temperature. Improved phase purity of BNT-6Ba by annealing at 600 °C rather than 550 °C was demonstrated. To limit the effect of evaporation of volatile constituents, sacrificial powder could also be utilized during pyrolysis and annealing of thin films. Finally, introducing barrier layers specifically designed for preventing diffusion of Na into the substrate stack would be of interest.

In general, the chemically modified BNT thin films synthesized in this work demonstrated an increasing challenge to obtain phase pure materials with increasing thickness or multiple coatings. Different strategies to ensure robust formation of the perovskite phase were demonstrated and discussed, but, with the exception of Na excess, the methods were not employed in actual thicker films. Preparation of these samples and clarifying the required measures (Na excess percentage, pyrolysis temperature, annealing steps, etc.) is necessary prior to production of devices, but the results may vary depending on composition, thickness, equipment, and other parameters.

Platinized silicon and the Pt-Bi reaction

Throughout the work, single crystal $SrTiO_3$ (ST) substrates were used as a chemically and mechanically inert reference point. ST is chemically stable in any conditions relevant for BNT, and the thermal expansion coefficient is similar to that of BNT, yielding only limited mechanical influence from the substrate on the BNT thin films. However, platinized silicon (SiPt) is the most relevant substrate for production of micro electromechanical systems. For this reason, the BNT films prepared by the CSD method should be compatible with SiPt substrates. It was found that a detrimental reaction occurred between Bi and the Pt bottom electrode, causing delamination of Pt from the TiO_x adhesive layer in the substrate stack. In order to remedy this problem, a $BaTiO_3$ (BT) protective layer was introduced to spatially separate Bi in BNT and Pt. This resulted in thin films with significantly improved quality, but the Bi-Pt reaction was not suppressed entirely, as delamination occurred when the films reached approximately 400 nm thickness. The driving force for this delamination was the thermal expansion mismatch of BNT and Si, leading to increasing mechanical force exerted on the Pt-TiO_x interface with increasing BNT thickness. Undamaged SiPt substrates should, based on theoretical considerations, be able to withstand this stress, and delamination was pursuant to a weakening of the interface due to Bi-Pt reactivity.

While the BT protective layers demonstrated a positive effect on thin film quality on SiPt, complete Bi impermeability was not achieved, leaving unresolved topics for further investigation. First, the BT layers contained porosity that left exposed areas of the Pt electrode. The BT deposition process should be optimized to ensure entirely dense BT films. For this goal, applying higher heat treatment temperatures is likely key, as densification processes are more active relative to coarsening at high temperatures. [247] Moreover, application of a higher number of BT layers should lead to denser films, as defects in one layer are covered by the next. In order to keep the thickness of the BT layer low relative to the functional BNT, it is suggested to reduce the concentration of the BT sol.

Two other materials are suggested as alternative perovskite protective layers. $CaTiO_3$ and $SrTiO_3$ (ST) are both chemically similar to BT, and strategies to prepare aqueous CSD sols for these cations were covered in the current work. Therefore, investigation of protective layers of these materials implies only marginal efforts when building on the experience already gained. Intermixing of BNT with the BT protective layer was also observed, and in order to achieve a superior Bi diffusion barrier, the protective layer should be of a material that is less soluble in BNT or which has a lesser tendency to dissolve BNT. Possible material systems in this regard were not discussed.

Replacing the Pt electrode in favor of a material more compatible with BNT is also an alternative. In literature, $LaNiO_3$ has been applied both as a seed layer on top of Pt [174], and instead of Pt on Si as the bottom electrode [181, 240, 241]. $SrRuO_3$ based bottom electrodes are also known from literature. [246] Relying on an oxide as the bottom electrode, however, represents an increased level of complexity, as the conductivity is not as predictable as for metals. Furthermore, the investment in developing the method would be greater than optimizing protective layers of Ti based perovskites, which have been established. Regardless, depending on the effectiveness of the measures discussed above, utilizing alternative substrates or bottom electrodes for production of MEMS devices is an alternative.

The value of stress developed due to thermal expansion mismatch of BNT and Si can be partially compensated for by other processes. For example, KNN thin films deposited on SiPt were shown to develop texture during cooling as a consequence of the thermal stress. [248] Introducing holding steps at intermediate temperatures during cooling of BNT thin films for intentional texturing or stress relief could reduce the risk of delamination.

Ferroelectric properties

All prepared compositions displayed polarization-field hysteresis loops characteristic of thin-film ferroelectric materials. However, due to the clamping effect of the substrate on the film and the strong electric fields applied, the effect of composition on electrical properties could not be determined. Furthermore, electromechanical properties of the BNT thin films were not measured. As for ferroelectric properties, it is expected that the clamping effect will dwarf the effect of composition on the piezoelectric properties. The characteristic properties of bulk BNT materials are generally visible at approximately 50 kV/cm, and 30× field strength was applied on the films in this work. For this reason, to assess the actuator properties of the thin films, actual devices should be prepared. With fabrication of cantilever devices with effective thinner substrate thicknesses (on the order of 10 μm), the properties of the thin films are expected to approach those of bulk materials. Fabrication of these devices would allow assessment of the actuating properties of the films and the influence of the chemical modifications.

The conductivity of the BNT thin films is another critical property. In this work, 500 Hz cycling frequency was applied, which yielded hysteresis loops dominated by true ferroelectric response even at the strongest fields applied (1500 kV/cm). This is on par with state of the art BNT thin films prepared by alternative methods. [13, 143, 168] With reduced cycling frequency, however, the accumulated leakage current became significant, causing resistive heating that may lead to dielectric breakdown of the films. Two main effects were identified for remedying too high conductivity in BNT thin films. The first is achieved naturally with preparation of devices. The high degree of clamping from the substrates dictates that strong

electric fields were required to observe hysteresis loops. With production of actual cantilever devices, however, the lower required field will naturally limit the leakage currents. Second, active measures to decrease the conductivity were discussed in Chapter 6. Donor doping of BNT has been shown to drastically decrease the conductivity. [164] In the current work, Nb^{5+} doping was already introduced, but its presence was charge balanced by alkali ions on A-site. By adding aliovalent Nb doping without intentional charge compensation, the oxygen vacancy concentration and conductivity are expected to decrease. Mn doping has also often been reported in literature as a measure to reduce the leakage in BNT. Its effect on conductivity is a slight increase at low field, but a significant reduction at high fields due to formation of Mn-V_O clusters reducing the mobility of the oxygen vacancies. A natural continuation of this work is to prepare BNT samples with Mn isovalent or Nb donor doping, and assess its influence on electric properties.

Additional topics for further investigation

Production of BNT thin film devices with thickness of a few µm requires in excess of 30 deposited layers using the present CSD method. This is comparable with alternative CSD methods, but increasing the efficiency of the deposition could significantly decrease the production time and cost. Combining CSD processes with a solid-state contribution has been demonstrated in literature for a 2-MOE based BNT sol-gel process with suspended KNN particles, achieving µm-scale thickness by a few coatings. [146] Including BNT particles as a dispersion could enable significantly more efficient production of BNT thin films on the µm scale. This would have benefits both in commercial considerations, but also with research and development where the production of BNT thin films can be time consuming. With the aqueous method developed here, a single layer amounted to approximately 50 nm thickness, and each layer required approximately 45 min for production. Samples of different compositions or substrates may be prepared in parallel with only marginally increased production time, but varying the heat treatment procedure implies another batch of samples. Preparing 2 µm films thus means 30 hours in the lab, and achieving thicker deposited layers is well worth the investment in the eyes of the researcher. Increasing the sol concentration would also result in thicker depositions. In the current work, sols of higher concentration were prepared, but only the undoped BNT showed long term stability with concentrations of 0.6 M or more. Nevertheless, employing the unstable sols of higher concentration may be worth the sacrifice for production of µm-scale thin films.

Bibliography

1. Haertling G.H., "Ferroelectric ceramics: history and technology", Journal of the American Ceramic Society, 1999 **82**(4) 797 doi: 10.1111/j.1151-2916.1999.tb01840.x.
2. Rödel J., Jo W., Seifert K.T.P., Anton E.-M., Granzow T., and Damjanovic D., "Perspective on the development of lead-free piezoceramics", Journal of the American Ceramic Society, 2009 **92**(6) 1153 doi: 10.1111/j.1551-2916.2009.03061.x.
3. Liu C., "Foundations of MEMS", 2 ed. 2012, Essex, England: Pearson Prentice Hall.
4. Rodel J., Webber K.G., Dittmer R., Jo W., Kimura M., and Damjanovic D., "Transferring lead-free piezoelectric ceramics into application", Journal of the European Ceramic Society, 2015 **35**(6) 1659 doi: 10.1016/j.jeurceramsoc.2014.12.013.
5. Henriksen L., "Deformable polymeric lens", 2014, Patent number: EP 2 781 939 A1.
6. Dumarest J. "Zero delay focus with poLight TLens", *Semicon Imaging Conference*. 2016 Grenoble.
7. Muralt P., "Recent progress in materials issues for piezoelectric MEMS", Journal of the American Ceramic Society, 2008 **91**(5) 1385 doi: 10.1111/j.1551-2916.2008.02421.x.
8. Muralt P., "PZT thin films for microsensors and actuators: where do we stand?", IEEE Transactions on Ultrasonics, Ferroelectrics, and Frequency Control, 2000 **47**(4) 903.
9. Yin D.-S., Zhao Z.-H., Dai Y.-J., et al., "Electrical properties and relaxor phase evolution of Li-modified BNT-BKT-BT lead-free ceramics", Journal of the American Ceramic Society, 2016 **99**(7) 2354 doi: 10.1111/jace.14247.
10. Malik R.A., Hussain A., Maqbool A., et al., "Temperature-insensitive high strain in lead-free $Bi_{0.5}(Na_{0.84}K_{0.16})_{0.5}TiO_3-0.04SrTiO_3$ ceramics for actuator applications", Journal of the American Ceramic Society, 2015 **98**(12) 3842 doi: 10.1111/jace.13722.
11. Schwartz R.W., Schneller T., and Waser R., "Chemical solution deposition of electronic oxide films", Comptes Rendus Chimie, 2004 **7**(5) 433 doi: 10.1016/j.crci.2004.01.007.
12. Bassiri-Gharb N., Bastani Y., and Bernal A., "Chemical solution growth of ferroelectric oxide thin films and nanostructures", Chemical Society Reviews, 2014 **43**(7) 2125 doi: 10.1039/c3cs60250h.
13. Alonso-Sanjose D., Jimenez R., Bretos I., and Calzada M.L., "Lead-free ferroelectric $(Na_{1/2}Bi_{1/2})TiO_3$-$BaTiO_3$ thin films in the morphotropic phase boundary composition: solution processing and properties", Journal of the American Ceramic Society, 2009 **92**(10) 2218 doi: 10.1111/j.1551-2916.2009.03229.x.
14. Jo W., Daniels J.E., Jones J.L., et al., "Evolving morphotropic phase boundary in lead-free $(Bi_{1/2}Na_{1/2})TiO_3$-$BaTiO_3$ piezoceramics", Journal of Applied Physics, 2011 **109**(1) 014110/1 doi: 10.1063/1.3530737.
15. Zhang S.T., Kounga A.B., Aulbach E., Ehrenberg H., and Rodel J., "Giant strain in lead-free piezoceramics $Bi_{0.5}Na_{0.5}TiO_3$-$BaTiO_3$-$K_{0.5}Na_{0.5}NbO_3$ system", Applied Physics Letters, 2007 **91**(11) 112906/1 doi: 10.1063/1.2783200.
16. Hofmann P., "Solid state physics: an introduction", 3 ed. 2008, Weinheim, Germany: Wiley-VCH Verlag & Co. KGaA.
17. Abrahams S.C., Kurtz S.K., and Jamieson P.B., "Atomic displacement relationship to Curie temperature and spontaneous polarization in displacive ferroelectrics", Physical Review, 1968 **172**(2) 551 doi: 10.1103/PhysRev.172.551.
18. Schreuer J. and Haussühl S., "A re-investigation of the quadratic electrostriction of alkali halides of rocksalt type", Journal of Physics D: Applied Physics, 1999 **32**(11) 1263 doi: 10.1088/0022-3727/32/11/313.

19. Vijaya M.S., "Piezoelectric materials and devices applications in engineering and medical sciences". 2012, Boca Raton: CRC Press, Taylor & Francis Group.
20. Izyumskaya N., Alivov Y.I., Cho S.J., Morkoç H., Lee H., and Kang Y.S., "Processing, structure, properties, and applications of PZT thin films", Critical Reviews in Solid State and Materials Sciences, 2007 **32**(3) 111 doi: 10.1080/10408430701707347.
21. Li G., Wu X.Q., Ren W., and Shi P., "Effect of excessive K and Na on the dielectric properties of (K,Na)NbO_3 thin films", Thin Solid Films, 2013 **548** 556 doi: 10.1016/j.tsf.2013.09.027.
22. Malič B., Koruza J., Hreščak J., et al., "Sintering of lead-free piezoelectric sodium potassium niobate ceramics", Materials, 2015 **8**(12) 8117 doi: 10.3390/ma8125449.
23. Villafuerte-Castrejón M., Morán E., Reyes-Montero A., et al., "Towards lead-free piezoceramics: facing a synthesis challenge", Materials, 2016 **9**(1) 21/1 doi: 10.3390/ma9010021.
24. Ahn C.W., Hong C.-H., Choi B.-Y., et al., "A brief review on relaxor ferroelectrics and selected issues in lead-free relaxors", Journal of the Korean Physical Society, 2016 **68**(12) 1481 doi: 10.3938/jkps.68.1481.
25. Bokov A.A. and Ye Z.G., "Recent progress in relaxor ferroelectrics with perovskite structure", Journal of Materials Science, 2006 **41**(1) 31 doi: 10.1007/s10853-005-5915-7.
26. Sapper E., Novak N., Jo W., Granzow T., and Rodel J., "Electric-field-temperature phase diagram of the ferroelectric relaxor system (1-x)$Bi_{1/2}Na_{1/2}TiO_3$-x$BaTiO_3$ doped with manganese", Journal of Applied Physics, 2014 **115**(19) 194104/1 doi: 10.1063/1.4876746.
27. Patterson E.A., Cann D.P., Pokorny J., and Reaney I.M., "Electromechanical strain in $Bi(Zn_{1/2}Ti_{1/2})O_3$-$(Bi_{1/2}Na_{1/2})TiO_3$-$(Bi_{1/2}K_{1/2})TiO_3$ solid solutions", Journal of Applied Physics, 2012 **111**(9) 094105/1 doi: 10.1063/1.4714346.
28. Guillemet-Fritsch S., Valdez-Nava Z., Tenailleau C., Lebey T., Durand B., and Chane-Ching J.Y., "Colossal permittivity in ultrafine grain size $BaTiO_{3-x}$ and $Ba_{0.95}La_{0.05}TiO_{3-x}$ materials", Advanced Materials, 2008 **20**(3) 551 doi: 10.1002/adma.200700245.
29. Karaki T., Yan K., Miyamoto T., and Adachi M., "Lead-free piezoelectric ceramics with large dielectric and piezoelectric constants manufactured from BaTiO3 nano-powder", Japanese Journal of Applied Physics, 2007 **46**(2L) L97 doi: 10.1143/JJAP.46.L97.
30. Panda P.K. and Sahoo B., "PZT to lead free piezo ceramics: a review", Ferroelectrics, 2015 **474**(1) 128 doi: 10.1080/00150193.2015.997146.
31. Aksel E. and Jones J.L., "Advances in lead-free piezoelectric materials for sensors and actuators", Sensors (Basel), 2010 **10**(3) 1935 doi: 10.3390/s100301935.
32. Jo W., Dittmer R., Acosta M., et al., "Giant electric-field-induced strains in lead-free ceramics for actuator applications - status and perspective", Journal of Electroceramics, 2012 **29**(1) 71 doi: 10.1007/s10832-012-9742-3.
33. Saito Y., Takao H., Tani T., et al., "Lead-free piezoceramics", Nature, 2004 **432**(7013) 84 doi: 10.1038/Nature03028.
34. Reichmann K., Feteira A., and Li M., "Bismuth sodium titanate based materials for piezoelectric actuators", Materials, 2015 **8**(12) 8467 doi: 10.3390/ma8125469.
35. EU, "EU-Directive 2002/95/EC: Restriction of the Use of Certain Hazardous Substances in Electrical and Electronic Equipment (RoHS)", The Official Journal of the European Union, 2003 **46**(L37) 19.

36. EU, "EU-Directive 2002/96/EC: Waste Electrical and Electronic Equipment(WEEE)", The Official Journal of the European Union, 2003 **46**(L37) 24.
37. Liu W. and Ren X., "Large piezoelectric effect in Pb-free ceramics", Physical Review Letters, 2009 **103**(25) 257602/1 doi: 10.1103/PhysRevLett.103.257602.
38. Li J.-F., Wang K., Zhu F.-Y., Cheng L.-Q., Yao F.-Z., and Green D.J., "(K,Na)NbO_3-based lead-free piezoceramics: fundamental aspects, processing technologies, and remaining challenges", Journal of the American Ceramic Society, 2013 **96**(12) 3677 doi: 10.1111/jace.12715.
39. Wefring E.T., Einarsrud M.-A., and Grande T., "Electrical conductivity and thermopower of (1-x)$BiFeO_3$ – x$Bi_{0.5}K_{0.5}TiO_3$ (x=0.1, 0.2) ceramics near the ferroelectric to paraelectric phase transition", Physical Chemistry Chemical Physics, 2015 **17**(14) 9420 doi: 10.1039/c5cp00266d.
40. Rojac T., Makarovic M., Walker J., Ursic H., Damjanovic D., and Kos T., "Piezoelectric response of $BiFeO_3$ ceramics at elevated temperatures", Applied Physics Letters, 2016 **109**(4) 042904 doi: 10.1063/1.4960103.
41. Smolenskii G.A., Isupov V.A., Agranovskaya A.I., and Krainik N.N., "New ferroelectrics with complex compounds. IV", Fizika Tverdogo Tela (Sankt-Peterburg), 1960 **2** 2982.
42. Jones G.O. and Thomas P.A., "Investigation of the structure and phase transitions in the novel A-site substituted distorted perovskite compound $Na_{0.5}Bi_{0.5}TiO_3$", Acta Crystallographica Section B: Structural Science, 2002 **58** 168 doi: 10.1107/S0108768101020845.
43. Xiao D.Q., Lin D.M., Zhu J.G., and Yu P., "Studies on new systems of BNT-based lead-free piezoelectric ceramics", Journal of Electroceramics, 2008 **21**(1-4) 34 doi: 10.1007/s10832-007-9087-5.
44. Ge W., Devreugd C.P., Phelan D., et al., "Lead-free and lead-based ABO_3 perovskite relaxors with mixed-valence A-site and B-site disorder: comparative neutron scattering structural study of ($Na_{1/2}Bi_{1/2}$)TiO_3 and Pb($Mg_{1/3}Nb_{2/3}$)O_3", Physical Review B, 2013 **88**(17) 174115/1 doi: 10.1103/PhysRevB.88.174115.
45. Li M., Pietrowski M.J., De Souza R.A., et al., "A family of oxide ion conductors based on the ferroelectric perovskite $Na_{0.5}Bi_{0.5}TiO_3$", Experimental Neurology, 2014 **13**(1) 31 doi: 10.1038/nmat3782.
46. Li M., Zhang H., Cook S.N., et al., "Dramatic influence of A-site nonstoichiometry on the electrical conductivity and conduction mechanisms in the perovskite oxide $Na_{0.5}Bi_{0.5}TiO_3$", Chemistry of Materials, 2015 **27**(2) 629 doi: 10.1021/cm504475k.
47. Li M., Li L., Zang J., and Sinclair D.C., "Donor-doping and reduced leakage current in Nb-doped $Na_{0.5}Bi_{0.5}TiO_3$", Applied Physics Letters, 2015 **106**(10) 102904/1 doi: 10.1063/1.4914509.
48. Aksel E., Forrester J.S., Jones J.L., Thomas P.A., Page K., and Suchomel M.R., "Monoclinic crystal structure of polycrystalline $Na_{0.5}Bi_{0.5}TiO_3$", Applied Physics Letters, 2011 **98**(15) 152901/1 doi: 10.1063/1.3573826.
49. Gorfman S., Glazer A.M., Noguchi Y., Miyayama M., Luo H., and Thomas P.A., "Observation of a low-symmetry phase in $Na_{0.5}Bi_{0.5}TiO_3$ crystals by optical birefringence microscopy", Journal of Applied Crystallography, 2012 **45**(3) 444 doi: 10.1107/S0021889812008217.
50. Gorfman S. and Thomas P.A., "Evidence for a non-rhombohedral average structure in the lead-free piezoelectric material $Na_{0.5}Bi_{0.5}TiO_3$", Journal of Applied Crystallography, 2010 **43** 1409 doi: 10.1107/s002188981003342x.

51. Groszewicz P.B., Breitzke H., Dittmer R., et al., "Nanoscale phase quantification in lead-free $(Bi_{1/2}Na_{1/2})TiO_3$-$BaTiO_3$ relaxor ferroelectrics by means of 23Na NMR", Physical Review B, Condensed Matter and Materials Physics, 2014 **90**(22) 220104/1 doi: 10.1103/PhysRevB.90.220104.
52. Levin I. and Reaney I.M., "Nano- and mesoscale structure of $Na_{1/2}Bi_{1/2}TiO_3$: a TEM perspective", Advanced Functional Materials, 2012 **22**(16) 3445 doi: 10.1002/adfm.201200282.
53. Levin I., Reaney I.M., Anton E.M., et al., "Local structure, pseudosymmetry, and phase transitions in $Na_{1/2}Bi_{1/2}TiO_3$-$K_{1/2}Bi_{1/2}TiO_3$ ceramics", Physical Review B, 2013 **87**(2) 024113/1 doi: 10.1103/Physrevb.87.024113.
54. Rao B.N. and Ranjan R., "Electric-field-driven monoclinic-to-rhombohedral transformation in $Na_{1/2}Bi_{1/2}TiO_3$", Physical Review B, 2012 **86**(13) 134103/1 doi: 10.1103/PhysRevB.86.134103.
55. Schneider D., Roedel J., Rytz D., and Granzow T., "Orientation-dependence of thermal depolarization and phase development in $Bi_{1/2}Na_{1/2}TiO_3$-$BaTiO_3$ single crystals", Journal of the American Ceramic Society, 2015 **98**(12) 3966 doi: 10.1111/jace.13843.
56. Suchanicz J., Stopa G., Kusz J., et al., "Structural, thermal expansion and heat capacity study of lead-free $[(1-x)(Na_{0.5}Bi_{0.5})-xBa]Zr_{1-y}Ti_yO_3$ ceramics", Journal of Materials Science, 2010 **45**(6) 1453 doi: 10.1007/s10853-009-4100-9.
57. Tanaka Y., Harigai T., Ueda M., Adachi H., and Fujii E., "Structural modification and large piezoelectricity of strained (Na, Bi)TiO_3-$BaTiO_3$ epitaxial thin films", Journal of the American Ceramic Society, 2012 **95**(11) 3547 doi: 10.1111/j.1551-2916.2012.05331.x.
58. Usher T.M., Forrester J.S., dela Cruz C.R., and Jones J.L., "Crystal structure of $0.96(Na_{0.5}Bi_{0.5}TiO_3)$-$0.04(BaTiO_3)$ from combined refinement of x-ray and neutron diffraction patterns", Applied Physics Letters, 2012 **101**(15) 152906/1 doi: 10.1063/1.4759117.
59. Zvirgzds J.A., Kapostin P.P., Zvirgzde J.V., and Kruzina T.V., "X-ray study of phase transitions in ferroelectric $Na_{0.5}Bi_{0.5}TiO_3$", Ferroelectrics, 1982 **40**(1) 75 doi: 10.1080/00150198208210600.
60. Rao B.N., Datta R., Chandrashekaran S.S., et al., "Local structural disorder and its influence on the average global structure and polar properties in $Na_{0.5}Bi_{0.5}TiO_3$", Physical Review B, 2013 **88**(22) 224103/1 doi: 10.1103/PhysRevB.88.224103.
61. Momma K. and Izumi F., "VESTA 3 for three-dimensional visualization of crystal, volumetric and morphology data", Journal of Applied Crystallography, 2011 **44** 1272 doi: 10.1107/S0021889811038970.
62. Dorcet V., Trolliard G., and Boullay P., "Reinvestigation of phase transitions in $Na_{0.5}Bi_{0.5}TiO_3$ by TEM. Part I: first order rhombohedral to orthorhombic phase transition", Chemistry of Materials, 2008 **20**(15) 5061 doi: 10.1021/cm8004634.
63. Dorcet V., Trolliard G., and Boullay P., "The structural origin of the antiferroelectric properties and relaxor behavior of $Na_{0.5}Bi_{0.5}TiO_3$", Journal of Magnetism and Magnetic Materials, 2009 **321**(11) 1758 doi: 10.1016/j.jmmm.2009.02.013.
64. Trolliard G. and Dorcet V., "Reinvestigation of phase transitions in $Na_{0.5}Bi_{0.5}TiO_3$ by TEM. Part II: second order orthorhombic to tetragonal phase transition", Chemistry of Materials, 2008 **20**(15) 5074 doi: 10.1021/cm800464d.
65. Takenaka T., Maruyama K., and Sakata K., "$(Bi_{1/2}Na_{1/2})TiO_3$-$BaTiO_3$ system for lead-free piezoelectric ceramics", Japanese Journal of Applied Physics, 1991 **30**(9B) 2236 doi: 10.1143/Jjap.30.2236.

66. Jo W., Granzow T., Aulbach E., Rodel J., and Damjanovic D., "Origin of the large strain response in $(K_{0.5}Na_{0.5})NbO_3$-modified $(Bi_{0.5}Na_{0.5})TiO_3$-$BaTiO_3$ lead-free piezoceramics", Journal of Applied Physics, 2009 **105**(9) 094102/1 doi: 10.1063/1.3121203.
67. Prasertpalichat S. and Cann D.P., "Hardening in non-stoichiometric $(1-x)Bi_{0.5}Na_{0.5}TiO_3$-$xBaTiO_3$ lead-free piezoelectric ceramics", Journal of Materials Science, 2016 **51**(1) 476 doi: 10.1007/s10853-015-9235-2.
68. Naderer M., Kainz T., Schuetz D., and Reichmann K., "The influence of Ti-nonstoichiometry in $Bi_{0.5}Na_{0.5}TiO_3$", Journal of the European Ceramic Society, 2014 **34**(3) 663 doi: 10.1016/j.jeurceramsoc.2013.10.010.
69. Aksel E., Forrester J.S., Foronda H.M., Dittmer R., Damjanovic D., and Jones J.L., "Structure and properties of La-modified $Na_{0.5}Bi_{0.5}TiO_3$ at ambient and elevated temperatures", Journal of Applied Physics, 2012 **112**(5) 054111/1 doi: 10.1063/1.4751357.
70. Glaum J., Zakhozheva M., Acosta M., et al., "Influence of B-Site disorder on the properties of unpoled $Bi_{1/2}Na_{1/2}TiO_3$-$0.06Ba(Zr_xTi_{1-x})O_3$ piezoceramics", Journal of the American Ceramic Society, 2016 **99**(8) 2801 doi: 10.1111/jace.14266.
71. Groh C., Franzbach D.J., Jo W., et al., "Relaxor/ferroelectric composites: a solution in the quest for practically viable lead-free incipient piezoceramics", Advanced Functional Materials, 2014 **24**(3) 356 doi: 10.1002/adfm.201302102.
72. Groh C., Jo W., and Rodel J., "Tailoring strain properties of $(0.94-x)Bi_{1/2}Na_{1/2}TiO_3$-$0.06BaTiO_3$-$xK_{0.5}Na_{0.5}NbO_3$ ferroelectric/relaxor composites", Journal of the American Ceramic Society, 2014 **97**(5) 1465 doi: 10.1111/Jace.12783.
73. Sumang R., Cann D.P., Kumar N., and Bongkarn T., "Large strain in lead-free piezoelectric $(1-x-y)Bi_{0.5}Na_{0.5}TiO_3$-$xBi_{0.5}K_{0.5}TiO_3$-$yBi_{0.5}Li_{0.5}TiO_3$ system near MPB prepared via the combustion technique", Ceramics International, 2015 **41**(Suppl._1) S127 doi: 10.1016/j.ceramint.2015.03.227.
74. Dislich H., "Sol-gel: science, processes and products", Journal of Non-Crystalline Solids, 1986 **80**(1) 115 doi: 10.1016/0022-3093(86)90384-4.
75. Brinker C.J., Keefer K.D., Schaefer D.W., Assink R.A., Kay B.D., and Ashley C.S., "Sol-gel transition in simple silicates II", Journal of Non-Crystalline Solids, 1984 **63**(1) 45 doi: 10.1016/0022-3093(84)90385-5.
76. Dey S.K., Budd K.D., and Payne D.A., "Thin-film ferroelectrics of PZT of sol-gel processing", IEEE Transactions on Ultrasonics, Ferroelectrics, and Frequency Control, 1988 **35**(1) 80 doi: 10.1109/58.4153.
77. Fukushima J., Kodaira K., and Matsushita T., "Preparation of ferroelectric PZT films by thermal decomposition of organometallic compounds", Journal of Materials Science, 1984 **19**(2) 595 doi: 10.1007/bf02403247.
78. Schwartz R.W., Reichert T.L., Clem P.G., Dimos D., and Liu D., "A comparison of diol and methanol-based chemical solution deposition routes for PZT thin film fabrication", Integrated Ferroelectrics, 1997 **18**(1-4) 275 doi: 10.1080/10584589708221705.
79. Livage J., Henry M., and Sanchez C., "Sol-gel chemistry of transition-metal oxides", Progress in Solid State Chemistry, 1988 **18**(4) 259 doi: 10.1016/0079-6786(88)90005-2.
80. Budd K.D., Dey S.K., and Payne D.A. "Sol-gel processing of $PbTiO_3$, $PbZrO_3$, PZT, and PLZT thin films", *British Ceramic Proceedings*. 1985: Inst of Ceramics.
81. Haertling G.H., "PLZT thin films prepared from acetate precursors", Ferroelectrics, 1991 **116**(1) 51 doi: 10.1080/00150199108007929.

82. Tu Y.-L., Calzada M.L., Phillips N.J., and Milne S.J., "Synthesis and electrical characterization of thin films of PT and PZT made from a diol-based sol-gel route", Journal of the American Ceramic Society, 1996 **79**(2) 441 doi: 10.1111/j.1151-2916.1996.tb08142.x.
83. Phillips N.J., Calzada M.L., and Milne S.J., "Sol-gel-derived lead titanate films", Journal of Non-Crystalline Solids, 1992 **147**(Supplement C) 285 doi: 10.1016/S0022-3093(05)80631-3.
84. Reaney I.M., Brooks K., Klissurska R., Pawlaczyk C., and Setter N., "Use of transmission electron microscopy for the characterization of rapid thermally annealed, solutioion-gel, lead zirconate titanate films", Journal of the American Ceramic Society, 1994 **77**(5) 1209 doi: 10.1111/j.1151-2916.1994.tb05394.x.
85. Malic B., Arcon I., Kodre A., and Kosec M., "Homogeneity of $Pb(Zr,Ti)O_3$ thin films by chemical solution deposition: Extended x-ray absorption fine structure spectroscopy study of zirconium local environment", Journal of Applied Physics, 2006 **100**(5) 051612 doi: 10.1063/1.2337079.
86. Wen J. and Wilkes G.L., "Organic/inorganic hybrid network materials by the sol−gel approach", Chemistry of Materials, 1996 **8**(8) 1667 doi: 10.1021/cm9601143.
87. Leaustic A., Babonneau F., and Livage J., "Structural investigation of the hydrolysis-condensation process of titanium alkoxides $Ti(OR)_4$ (OR=OPr-iso, OEt) modified by acetylacetone. 1. Study of the alkoxide modification", Chemistry of Materials, 1989 **1**(2) 240 doi: 10.1021/cm00002a015.
88. Chae H.K., Payne D.A., Xu Z., and Ma L., "Molecular structure of a new lead titanium bimetallic alkoxide complex $[PbTi_2(\mu_4\text{-}O)(OOCCH_3)(OCH_2CH_3)_7]_2$: evolution of structure on heat treatment and the formation of thin-layer dielectrics", Chemistry of Materials, 1994 **6**(10) 1589.
89. Boyle T.J. and Schwartz R.W., "An investigation of group (IV) alkoxides as property controlling reagents in the synthesis of ceramic materials", Comments on Inorganic Chemistry, 1994 **16**(5) 243.
90. Budd K., Dey S., and Payne D., "The effect of hydrolysis conditions on the characteristics of $PbTiO_3$ gels and thin films", MRS Online Proceedings Library Archive, 1986 **73** doi: 10.1557/PROC-73-711.
91. Vest R.W. and Jiejie X., "$PbTiO_3$ films from metalloorganic precursors", IEEE Transactions on Ultrasonics, Ferroelectrics, and Frequency Control, 1988 **35**(6) 711 doi: 10.1109/58.9327.
92. Ousi-Benomar W., Xue S., Lessard R., Singh A., Wu Z., and Kuo P., "Structural and optical characterization of $BaTiO_3$ thin films prepared by metal-organic deposition from barium 2-ethylhexanoate and titanium dimethoxy dineodecanoate", Journal of Materials Research, 1994 **9**(4) 970 doi: 10.1557/JMR.1994.0970.
93. Hoffmann S. and Waser R.M., "Dielectric properties, leakage behaviour, and resistance degradation of thin films of the solid solution series $Ba(Ti_{1-y}Zr_y)O_3$", Integrated Ferroelectrics, 1997 **17**(1-4) 141 doi: 10.1080/10584589708012989.
94. Yi G., Wu Z., and Sayer M., "Preparation of $Pb(Zr,Ti)O_3$ thin films by sol gel processing: electrical, optical, and electro-optic properties", Journal of Applied Physics, 1988 **64**(5) 2717 doi: 10.1063/1.341613.
95. Hennings D., Rosenstein G., and Schreinemacher H., "Hydrothermal preparation of barium titanate from barium-titanium acetate gel precursors", Journal of the European Ceramic Society, 1991 **8**(2) 107 doi: 10.1016/0955-2219(91)90116-H.

96. Sengupta S.S., Ma L., Adler D.L., and Payne D.A., "Extended x-ray absorption fine structure determination of local structure in sol-gel-derived lead titanate, lead zirconate, and lead zirconate titanate", Journal of Materials Research, 1995 **10**(6) 1345 doi: 10.1557/JMR.1995.1345.
97. Brennecka G.L., Ihlefeld J.F., Maria J.-P., Tuttle B.A., and Clem P.G., "Processing technologies for high-permittivity thin films in capacitor applications", Journal of the American Ceramic Society, 2010 **93**(12) 3935 doi: 10.1111/j.1551-2916.2010.04211.x.
98. Pechini M.P., "Barium titanium citrate, barium titanate and processes for producing same", 1966, Patent number: US3231328.
99. Deng Y.-F., Jiang Y.-Q., Hong Q.-M., and Zhou Z.-H., "Speciation of water-soluble titanium citrate: synthesis, structural, spectroscopic properties and biological relevance", Polyhedron, 2007 **26**(8) 1561 doi: 10.1016/j.poly.2006.08.017.
100. Sunde T.O.L., Grande T., and Einarsrud M.-A., "Modified pechini synthesis of oxide powders and thin films", in *Handbook of Sol-Gel Science and Technology*, Klein, Aparicio, and Jitianu, Editors. 2016, Springer International Publishing: Cham. p. 1.
101. Baythoun M.S.G. and Sale F.R., "Production of strontium-substituted lanthanum manganite perovskite powder by the amorphous citrate process", Journal of Materials Science, 1982 **17**(9) 2757 doi: 10.1007/bf00543914.
102. Van Bael M.K., Nelis D., Hardy A., et al., "Aqueous chemical solution deposition of ferroelectric thin films", Integrated Ferroelectrics, 2002 **45**(1) 113 doi: 10.1080/10584580215353.
103. Hardy A., Mondelaers D., van Bael M.K., et al., "Synthesis of $(Bi,La)_4Ti_3O_{12}$ by a new aqueous solution-gel route", Journal of the European Ceramic Society, 2004 **24**(6) 905 doi: 10.1016/s0955-2219(03)00420-5.
104. Haas D.E., Birnie D.P., Zecchino M.J., and Figueroa J.T., "The effect of radial position and spin speed on striation spacing in spin on glass coatings", Journal of Materials Science Letters, 2001 **20**(19) 1763 doi: 10.1023/A:1012522814442.
105. Birnie D.P., "Rational solvent selection strategies to combat striation formation during spin coating of thin films", Journal of Materials Research, 2001 **16**(4) 1145 doi: 10.1557/JMR.2001.0158.
106. Middleman S., "The effect of induced air-flow on the spin coating of viscous liquids", Journal of Applied Physics, 1987 **62**(6) 2530 doi: 10.1063/1.339465.
107. Scriven L.E., "Physics and applications of dip coating and spin coating", MRS Online Proceedings Library Archive, 1988 **121** doi: 10.1557/PROC-121-717.
108. Han J.-P., Gu J., and Ma T., "$SrBi_2Ta_2O_9$ (SBT) thin films prepared by electrostatic spray", Integrated Ferroelectrics, 1997 **14**(1-4) 229 doi: 10.1080/10584589708019996.
109. Huffman M., "Liquid source misted chemical deposition (LSMCD)–a critical review", Integrated Ferroelectrics, 1995 **10**(1-4) 39 doi: 10.1080/10584589508012262.
110. Kang G.Q., Yao K., and Wang J., "$0.90(Na_{0.5}Bi_{0.5}TiO_3)$-$0.06BaTiO_3$-$0.04K_{0.5}Na_{0.5}NbO_3$ ferroelectric thin films derived from chemical solutions", Journal of the American Ceramic Society, 2011 **94**(5) 1331 doi: 10.1111/j.1551-2916.2011.04478.x.
111. Yang C.H., Sui H.T., Wu H.T., Feng C., Geng F.J., and Yao Y.Y., "Enhanced ferroelectric and dielectric properties of Nb^{5+}-doped $Na_{0.5}Bi_{0.5}TiO_3$ thin film deposited under nitrogen annealing atmosphere", Ceramics International, 2015 **41**(8) 10272 doi: 10.1016/j.ceramint.2015.03.022.

112. Lakeman C.D.E., Xu Z., and Payne D.A., "On the evolution of structure and composition in sol-gel-derived lead zirconate titanate thin layers", Journal of Materials Research, 1995 **10**(8) 2042 doi: 10.1557/JMR.1995.2042.
113. Hasenkox U., Hoffmann S., and Waser R., "Influence of precursor chemistry on the formation of $MTiO_3$ (M = Ba, Sr) ceramic thin films", Journal of Sol-Gel Science and Technology, 1998 **12**(2) 67 doi: 10.1023/a:1026480027046.
114. Griswold E.M., Weaver L., Sayer M., and Calder I., "Phase transformations in rapid thermal processed lead zirconate titanate", Journal of Materials Research, 1995 **10**(12) 3149 doi: 10.1557/JMR.1995.3149.
115. Schwartz R.W., Voigt J.A., Tuttle B.A., Payne D.A., Reichert T.L., and DaSalla R.S., "Comments on the effects of solution precursor characteristics and thermal processing conditions on the crystallization behavior of sol-gel derived lead zirconate titanate thin films", Journal of Materials Research, 1997 **12**(2) 444 doi: 10.1557/JMR.1997.0066.
116. Roy R., "Gel route to homogeneous glass preparation", Journal of the American Ceramic Society, 1969 **52**(6) 344 doi: 10.1111/j.1151-2916.1969.tb11945.x.
117. Lange F.F., "Chemical solution routes to single-crystal thin films", Science, 1996 **273**(5277) 903.
118. Li W., Xu Z., Chu R., et al., "Enhanced dielectric and piezoelectric properties of (100) oriented $Bi_{0.5}Na_{0.5}TiO_3$-$BaTiO_3$-$SrTiO_3$ thin films", Journal of Materials Science: Materials in Electronics, 2016 **27**(9) 8911 doi: 10.1007/s10854-016-4918-2.
119. Golden S., Lange F., Clarke D., Chang L., and Necker C., "Metalorganic deposition of high critical current thin films in the Bi-Sr-Ca-Cu-O system on {100} $LaAlO_3$ substrates", Applied Physics Letters, 1992 **61**(3) 351 doi: 10.1063/1.107934.
120. Assink R.A. and Schwartz R.W., "Proton and carbon-13 NMR investigations of lead zirconate titanate ($Pb(Zr,Ti)O_3$) thin-film precursor solutions", Chemistry of Materials, 1993 **5**(4) 511 doi: 10.1021/cm00028a019.
121. Nam S.-M. and Tsurumi T., "In situ epitaxial growth of lead zirconate titanate films by bias sputtering at high RF power", Japanese Journal of Applied Physics, 2004 **43**(5R) 2672 doi: 10.1143/JJAP.43.2672.
122. Cho N.-H. and Kim H.-G., "Structure and electrical properties of $Pb(Zr,Ti)O_3$ thin films deposited by reactive sputtering using multi-targets", Thin Solid Films, 1995 **266**(2) 140 doi: 10.1016/0040-6090(95)06609-8.
123. Vilquin B., Bouregba R., Poullain G., Murray H., Dogheche E., and Remiens D., "Crystallographic and optical properties of epitaxial $Pb(Zr_{0.6},Ti_{0.4})O_3$ thin films grown on $LaAlO_3$ substrates", Journal of Applied Physics, 2003 **94**(8) 5167 doi: 10.1063/1.1610776.
124. Cattan E., Agius B., Achard H., Cheang Wong J., Ortega C., and Siejka J., "Physical properties of radio-frequency magnetron sputtered $Pb(Zr,Ti)O_3$ thin films: direct determination of oxygen composition by Rutherford backscattering spectroscopy and nuclear reaction analysis", Journal of Vacuum Science & Technology A: Vacuum, Surfaces, and Films, 1993 **11**(5) 2808 doi: 10.1116/1.578645.
125. Willmott P.R. and Huber J.R., "Pulsed laser vaporization and deposition", Reviews of Modern Physics, 2000 **72**(1) 315 doi: 10.1103/RevModPhys.72.315.
126. Abazari M., Safari A., Bharadwaja S.S.N., and Trolier-McKinstry S., "Dielectric and piezoelectric properties of lead-free $(Bi,Na)TiO_3$-based thin films", Applied Physics Letters, 2010 **96**(8) 082903 doi: 10.1063/1.3309706.

127. Kidoh H., Ogawa T., Morimoto A., and Shimizu T., "Ferroelectric properties of lead-zirconate-titanate films prepared by laser ablation", Applied Physics Letters, 1991 **58**(25) 2910 doi: 10.1063/1.104719.
128. Masuda A., Matsuda K., Yonezawa Y., Morimoto A., and Shimizu T., "Mechanism of stoichiometric deposition of volatile elements in multimetal-oxide films prepared by pulsed laser ablation", Japanese Journal of Applied Physics, 1996 **35**(2B) L237 doi: 10.1143/JJAP.35.L237.
129. Kwak B., Boyd E., and Erbil A., "Metalorganic chemical vapor deposition of $PbTiO_3$ thin films", Applied Physics Letters, 1988 **53**(18) 1702 doi: 10.1063/1.100471.
130. Asano G., Oikawa T., and Funakubo H., "Highly-reproducible preparation of $Pb(Zr,Ti)O_3$ films at low deposition temperature by metal organic chemical vapor deposition", Japanese Journal of Applied Physics, 2003 **42**(5R) 2801 doi: 10.1143/JJAP.42.2801.
131. Kim D.-H., Yang W.-Y., and Rhee S.-W., "Low temperature CVD of $Pb(Zr,Ti)O_3$ using $Pb(tmhd)_2$, $Zr(dmae)_4$, and $Ti(dmae)_4$", Journal of the Electrochemical Society, 2003 **150**(8) C516 doi: 10.1149/1.1584441.
132. Kim H.R., Jeong S., Jeon C.B., et al., "Metalorganic chemical vapor deposition of very thin $Pb(Zr,Ti)O_3$ thin films at low temperatures for high-density ferroelectric memory applications", Journal of Materials Research, 2001 **16**(12) 3583 doi: 10.1557/JMR.2001.0491.
133. Betts R. and Pitt C., "Growth of thin-film lithium niobate by molecular beam epitaxy", Electronics Letters, 1985 **21**(21) 960 doi: 10.1049/el:19850678.
134. Theis C.D. and Schlom D.G., "Epitaxial lead titanate grown by MBE", Journal of Crystal Growth, 1997 **174**(1-4) 473 doi: 10.1016/S0022-0248(96)01144-X.
135. Gu X., Izyumskaya N., Avrutin V., Morkoç H., Kang T.D., and Lee H., "High quality epitaxial growth of $PbTiO_3$ by molecular beam epitaxy using H_2O_2 as the oxygen source", Applied Physics Letters, 2006 **89**(12) 122912 doi: 10.1063/1.2354016.
136. Izyumskaya N., Avrutin V., Gu X., et al., "Growth of high-quality $Pb(Zr_xTi_{1-x})O_3$ films by peroxide MBE and their optical and structural characteristics", MRS Online Proceedings Library Archive, 2006 **966** doi: 10.1557/PROC-0966-T11-17.
137. Einarsrud M.A. and Grande T., "1D oxide nanostructures from chemical solutions", Chemical Society Reviews, 2014 **43**(7) 2187 doi: 10.1039/c3cs60219b.
138. Shimomura K., Tsurumi T., Ohba Y., and Daimon M., "Preparation of lead zirconate titanate thin film by hydrothermal method", Japanese Journal of Applied Physics, 1991 **30**(9S) 2174 doi: 10.1143/JJAP.30.2174.
139. Dalod A.R., Henriksen L., Grande T., and Einarsrud M.A., "Functionalized TiO_2 nanoparticles by single-step hydrothermal synthesis: the role of the silane coupling agents", Beilstein Journal of Nanotechnology, 2017 **8** 304 doi: 10.3762/bjnano.8.33.
140. Dalod A.R.M., Grendal O.G., Skjærvø S.L., et al., "Controlling oriented attachment and *in situ* functionalization of TiO_2 nanoparticles during hydrothermal synthesis with APTES", The Journal of Physical Chemistry C, 2017 **121**(21) 11897 doi: 10.1021/acs.jpcc.7b02604.
141. Wang S.F., Wang Y.R., Mahalingam T., Chu J.P., and Lin K.U., "Characterization of hydrothermally synthesized lead zirconate titanate (PZT) ceramics", Materials Chemistry and Physics, 2004 **87**(1) 53 doi: 10.1016/j.matchemphys.2004.04.009.
142. Su B., Button T., and Ponton C., "Control of the particle size and morphology of hydrothermally synthesised lead zirconate titanate powders", Journal of Materials Science, 2004 **39**(21) 6439 doi: 10.1023/B:JMSC.0000044881.35754.ea.

143. Zhou Z., Sun W., and Li J.-F., "Sol-gel synthesis of 0.94($Bi_{0.5}Na_{0.5}$)TiO_3-0.06$BaTiO_3$ lead-free piezoelectric films: effect of pyrolysis temperature on phase evolution and electrical properties", Journal of Sol-Gel Science and Technology, 2015 **77**(2) 423 doi: 10.1007/s10971-015-3870-6.
144. Remondiere F., Malic B., Kosec M., and Mercurio J.P., "Study of the crystallization pathway of $Na_{0.5}Bi_{0.5}TiO_3$ thin films obtained by chemical solution deposition", Journal of Sol-Gel Science and Technology, 2008 **46**(2) 117 doi: 10.1007/s10971-008-1717-0.
145. Peng J.F., Zheng X.J., Gong Y.Q., Zhan K., and Dai Z.H., "Effects of annealing temperature on the electric properties of 0.94($Na_{0.5}Bi_{0.5}$)TiO_3–0.06$BaTiO_3$ ferroelectric thin film", Journal of Electronic Materials, 2013 **43**(3) 724 doi: 10.1007/s11664-013-2912-5.
146. Ji H.F., Ren W., Wang L.Y., et al., "Enhanced structures and electrical properties of lead-free $K_{0.5}Na_{0.5}NbO_3$-$Bi_{0.5}Na_{0.5}TiO_3$ 0-3 composite ferroelectric thick films", Journal of the American Ceramic Society, 2011 **94**(10) 3425 doi: 10.1111/j.1551-2916.2011.04524.x.
147. Yao Y., Wu X., Ren W., Shi P., and Ye Z., "Preparation and electrical properties of (1−x)($Na_{0.5}Bi_{0.5}$)TiO_3–x$BiAlO_3$ thin films by a sol–gel process", Ceramics International, 2015 **41** S240 doi: 10.1016/j.ceramint.2015.03.270.
148. Sakamoto W., Makino N., Katayama T., Moriya M., and Yogo T., "Improvement of the ferroelectric properties of chemically synthesized $Bi_{1/2}Na_{1/2}TiO_3$ thin films via Mn doping", Ferroelectrics, 2015 **479**(1) 56 doi: 10.1080/00150193.2015.1011920.
149. Li W., Li P., Zeng H., Yue Z., and Zhai J., "The effect of stress on the piezoelectric properties of BNT-BT-ST thin films", Materials Letters, 2016 **162** 135 doi: 10.1016/j.matlet.2015.09.137.
150. Li W., Li P., Zeng H.R., Hao J.G., and Zhai J.W., "Orientation dependence on piezoelectric properties of $Bi_{0.5}Na_{0.5}TiO_3$-$BaTiO_3$-$SrTiO_3$ epitaxial thin films", Applied Physics Letters, 2014 **104**(17) 172903/1 doi: 10.1063/1.4874805.
151. Li P., Li W., Zeng H., Liu S., Wang W., and Zhai J., "Ferroelectric and piezoelectric properties of La-modified lead-free ($Bi_{0.5}Na_{0.5}$)TiO_3-($Bi_{0.5}K_{0.5}$)TiO_3-$SrTiO_3$ thin films", Ceramics International, 2015 **41** 4479 doi: 10.1016/j.ceramint.2014.11.140.
152. Sui H., Yang C., Geng F., and Feng C., "Effects of Zr doping content on microstructure, ferroelectric and dielectric properties of $Na_{0.5}Bi_{0.5}TiO_3$ thin film", Materials Letters, 2015 **139** 284 doi: 10.1016/j.matlet.2014.10.111.
153. Ojha K.S., "Structural optimization of bismuth sodium titanate thin films", Ferroelectrics, 2015 **474**(1) 163 doi: 10.1080/00150193.2015.997309.
154. Li P., Zhai J., Zeng H., Shen B., Li W., and Zhao K., "Crystallographic orientation dependence of piezoelectric and dielectric properties of BNT-based thin films", Journal of the European Ceramic Society, 2016 **36**(13) 3139 doi: 10.1016/j.jeurceramsoc.2016.05.019.
155. Cui W., Wang X., and Li L., "Large piezoelectric properties of (1 - x)$Na_{0.5}Bi_{0.5}TiO_3$-x$BaTiO_3$ thin films prepared by sol-gel method", Journal of Materials Science: Materials in Electronics, 2016 **27**(7) 7287 doi: 10.1007/s10854-016-4696-x.
156. Feng C., Yang C.H., Li S.X., et al., "Reduced leakage current and large polarization of $Na_{0.5}Bi_{0.5}Ti_{0.98}Mn_{0.02}O_3$ thin film annealed at low temperature", Ceramics International, 2015 **41**(10, Part B) 14179 doi: 10.1016/j.ceramint.2015.07.041.
157. Perez-Mezcua D., Sirera R., Bretos I., et al., "Morphotropic phase boundary in solution-derived $(Bi_{0.5}Na_{0.5})_{1-x}Ba_xTiO_3$ thin films: part I crystalline structure and

compositional depth profile", Journal of the American Ceramic Society, 2014 **97**(4) 1269 doi: 10.1111/jace.12753.

158. Acharya S.K., Lee S.-K., Hyung J.-H., Yang Y.-H., Kim B.-H., and Ahn B.-G., "Ferroelectric and piezoelectric properties of lead-free $BaTiO_3$ doped $Bi_{0.5}Na_{0.5}TiO_3$ thin films from metal-organic solution deposition", Journal of Alloys and Compounds, 2012 **540** 204 doi: 10.1016/j.jallcom.2012.06.071.
159. Acharya S.K., Ahn B.G., Hyung J.-H., and Lee S.-K., "Effect of Li doping on ferroelectric and piezoelectric properties of $Ba_{0.5}Na_{0.5}TiO_3$-$BaTiO_3$ (BNT-BT) thin films", Journal the of Korean Physical Society, 2013 **62**(5) 794 doi: 10.3938/jkps.62.794.
160. Acharya S.K., Ahn B.G., Jung C.U., Koh J.H., Choi I.H., and Lee S.K., "Effect of Rb doping on ferroelectric and piezoelectric properties of $Bi_{0.5}Na_{0.5}TiO_3$-$BaTiO_3$ thin films", Journal of Alloys and Compounds, 2014 **603** 248 doi: 10.1016/j.jallcom.2014.03.087.
161. Acharya S.K., Kim T.-M., Hyung J.-H., Ahn B.-G., and Lee S.-K., "Ferroelectric and piezoelectric properties of lead-free $Bi_{0.5}Na_{0.5}TiO_3$-$Bi_{0.5}K_{0.5}TiO_3$-$BaTiO_3$-thin films near the morphotropic phase boundary", Journal of Alloys and Compounds, 2014 **586** 549 doi: 10.1016/j.jallcom.2013.10.028.
162. Cernea M., Galca A.C., Cioangher M.C., Dragoi C., and Ioncea G., "Piezoelectric BNT-BT0.11 thin films processed by sol-gel technique", Journal of Materials Science, 2011 **46**(17) 5621 doi: 10.1007/s10853-011-5512-x.
163. Cernea M., Trupina L., Dragoi C., Galca A.C., and Trinca L., "Structural, optical, and electric properties of BNT-BT0.08 thin films processed by sol-gel technique", Journal of Materials Science, 2012 **47**(19) 6966 doi: 10.1007/s10853-012-6646-1.
164. Walenza-Slabe J. and Gibbons B.J., "Leakage current phenomena in Mn-doped Bi(Na,K)TiO_3-based ferroelectric thin films", Journal of Applied Physics, 2016 **120**(8) 084102/1 doi: 10.1063/1.4961428.
165. Jeon Y.H., Patterson E.A., Cann D.P., Mardilovich P., Stickel W., and Gibbons B.J., "Large piezoresponse and ferroelectric properties of $(Bi_{0.5}Na_{0.5})TiO_3$-$(Bi_{0.5}K_{0.5})TiO_3$-$Bi(Mg_{0.5}Ti_{0.5})O_3$ thin films prepared by chemical solution deposition", Journal of the American Ceramic Society, 2013 **96**(7) 2172 doi: 10.1111/jace.12279.
166. Kim C.Y., Sekino T., Yamamoto Y., and Niihara K., "The synthesis of lead-free ferroelectric $Bi_{1/2}Na_{1/2}TiO_3$ thin film by solution-sol-gel method", Journal of Sol-Gel Science and Technology, 2005 **33**(3) 307 doi: DOI 10.1007/s10971-005-6380-0.
167. Kim C.-Y., Sekino T., and Niihara K., "Optical, mechanical, and dielectric properties of $Bi_{1/2}Na_{1/2}TiO_3$ thin film synthesized by sol-gel method", Journal of Sol-Gel Science and Technology, 2010 **55**(3) 306 doi: 10.1007/s10971-010-2250-5.
168. Yao Y., Wu X., Shi P., and Ye Z.-G., "Effects of heat-treatment temperature on the properties of $(1-x)(Na_{0.5}Bi_{0.5})TiO_3$-$xBiAlO_3$ lead-free piezoelectric thin films", Journal of the American Ceramic Society, 2016 **99**(4) 1340 doi: 10.1111/jace.14116.
169. Sakamoto W., Makino N., Lee B.-Y., Iijima T., Moriya M., and Yogo T., "Influence of volatile element composition and Mn doping on the electrical properties of lead-free piezoelectric $(Bi_{0.5}Na_{0.5})TiO_3$ thin films", Sensors and Actuators A: Physical, 2013 **200** 60 doi: 10.1016/j.sna.2012.10.006.
170. Li W., Li P., Zeng H., Hao J., and Zhai J., "Enhanced dielectric and piezoelectric properties in lead-free $Bi_{0.5}Na_{0.5}TiO_3$-$BaTiO_3$-$SrTiO_3$ thin films with seed layer", Ceramics International, 2015 **41** S356 doi: 10.1016/j.ceramint.2015.03.178.

171. Li P., Li W., Liu S., Zhang Y., Zhai J., and Chen H., "Reduced leakage current, enhanced ferroelectric and dielectric properties of (La, Fe)-codoped $Bi_{0.5}Na_{0.5}TiO_3$-based thin films", Ceramics International, 2015 **41** S344 doi: 10.1016/j.ceramint.2015.03.177.
172. Li W., Li P., Zeng H., Hao J., Yue Z., and Zhai J., "Structural modification and piezoelectric properties in $Bi_{0.5}Na_{0.5}TiO_3$-$BaTiO_3$-$SrTiO_3$ thin films", Journal of Materials Science: Materials in Electronics, 2015 **27**(1) 215 doi: 10.1007/s10854-015-3740-6.
173. Li P., Zhai J., Zeng H., Zhao K., Shen B., and Chen H., "Effects of $LaNiO_3$ seeding layers on the crystal structure and electrical properties in $0.94(Bi_{0.5}Na_{0.5})TiO_3$-$0.06BaTiO_3$ thin films", Ceramics International, 2015 **41** 12980 doi: 10.1016/j.ceramint.2015.06.141.
174. Fang X.-l., Shen B., Zhai J.-w., and Yao X., "Preparation and ferroelectric properties of $(Na_{0.5}Bi_{0.5})_{0.94}Ba_{0.06}TiO_3$ thin films deposited on Pt electrodes using $LaNiO_3$ as buffer layer", Ceramics International, 2012 **38**(Suppl. 1) S83 doi: 10.1016/j.ceramint.2011.04.055.
175. Duk A., Schwarzkopf J., Kwasniewski A., Schmidbauer M., and Fornari R., "Impact of the crystallographic structure of epitaxially grown strained sodium-bismuth-titanate thin films on local piezo- and ferroelectric properties", Materials Research Bulletin, 2012 **47**(8) 2056 doi: 10.1016/j.materresbull.2012.04.004.
176. Daryapurkar A.S., Kolte J.T., and Gopalan P., "Growth and characterization of $Na_{0.5}Bi_{0.5}TiO_3$ thin films with $BaTiO_3$ buffer layer (study of Au/$Na_{0.5}Bi_{0.5}TiO_3$/$BaTiO_3$/Pt Capacitor)", Ferroelectrics, 2013 **447**(1) 46 doi: 10.1080/00150193.2013.821859.
177. Park J.S., Lee M.H., Kim D.J., et al., "Enhanced piezoelectric properties of lead-free $0.935(Bi_{0.5}Na_{0.5})TiO_3$-$0.065BaTiO_3$ thin films fabricated by using pulsed laser deposition", Journal of the Korean Physical Society, 2013 **62**(7) 1031 doi: 10.3938/jkps.62.1031.
178. Lin Q., Ding R., Li Q., et al., "Large piezoelectricity and ferroelectricity in Mn-doped $(Bi_{0.5}Na_{0.5})TiO_3$-$BaTiO_3$ thin film prepared by pulsed laser deposition", Journal of the American Ceramic Society, 2016 **99**(7) 2347 doi: 10.1111/jace.14227.
179. Hejazi M.M., Taghaddos E., and Safari A., "Reduced leakage current and enhanced ferroelectric properties in Mn-doped $Bi_{0.5}Na_{0.5}TiO_3$-based thin films", Journal of Materials Science, 2013 **48**(9) 3511 doi: 10.1007/s10853-013-7144-9.
180. Gallegos-Melgar A., Espinosa-Arbelaez D.G., Flores-Ruiz F.J., et al., "Ferroelectric properties of manganese doped $(Bi_{1/2}Na_{1/2})TiO_3$ and $(Bi_{1/2}Na_{1/2})TiO_3$-$BaTiO_3$ epitaxial thin films", Applied Surface Science, 2015 **359** 923 doi: 10.1016/j.apsusc.2015.09.175.
181. Yang K.-S., Choi M.-J., Choi J.-S., et al., "Lead-free $0.75(Bi_{0.5}Na_{0.5})TiO_3$-$0.25SrTiO_3$ (BNT-ST) epitaxial films grown on Si (001) substrates via pulsed laser deposition", Sensors and Actuators A: Physical, 2016 **243** 117 doi: 10.1016/j.sna.2016.03.018.
182. Harigai T., Tanaka Y., Adachi H., and Fujii E., "Piezoelectric properties of lead-free (Na,Bi)TiO_3-$BaTiO_3$ (001) epitaxial thin films around the morphotropic phase boundary", Applied Physics Express, 2010 **3**(11) 111501/1 doi: 10.1143/apex.3.111501.
183. Adachi H., Tanaka Y., Harigai T., Ueda M., and Fujii E., "Large transverse piezoelectricity in strained (Na,Bi)TiO_3-$BaTiO_3$ epitaxial thin films on MgO(110)", Applied Physics Express, 2011 **4**(5) 051501/1 doi: 10.1143/APEX.4.051501.

184. Quignon S., Soyer C., and Remiens D., "Synthesis and electrical properties of sputtered $(Na_{0.5}Bi_{0.5})TiO_3$ thin films on silicon substrate", Journal of the American Ceramic Society, 2012 **95**(10) 3180 doi: 10.1111/j.1551-2916.2012.05285.x.
185. Cui W., Wang X., Wu Y., Luo Y.-G., and Li L., "Investigation of thickness dependence of electric properties of sol-gel BNT-BT thin films with stepwise crystallization", Journal of the Ceramic Society of Japan, 2016 **124**(4) 464 doi: 10.2109/jcersj2.15315.
186. West D.L. and Payne D.A., "Preparation of $0.95Bi_{1/2}Na_{1/2}TiO_3{\cdot}0.05BaTiO_3$ ceramics by an aqueous citrate-gel route", Journal of the American Ceramic Society, 2003 **86**(1) 192 doi: 10.1111/j.1151-2916.2003.tb03303.x.
187. Kundu A. and Soukhojak A.N., "Ba-Zr codoped sodium bismuth titanate by novel alkoxyless wet chemical route: processing and electromechanical behavior", Applied Physics A, 2005 **82**(2) 309 doi: 10.1007/s00339-005-3295-0.
188. Xu Q., Chen S., Chen W., et al., "Synthesis and piezoelectric and ferroelectric properties of $(Na_{0.5}Bi_{0.5})_{1-x}Ba_xTiO_3$ ceramics", Materials Chemistry and Physics, 2005 **90**(1) 111 doi: 10.1016/j.matchemphys.2004.10.018.
189. Xu Q., Chen X.-L., Chen W., et al., "Effect of MnO addition on structure and electrical properties of $(Na_{0.5}Bi_{0.5})_{0.94}Ba_{0.06}TiO_3$ ceramics prepared by citrate method", Materials Science and Engineering: B, 2006 **130**(1-3) 94 doi: 10.1016/j.mseb.2006.02.051.
190. Xu Q., Chen X.-L., Chen W., Kim B.-H., Xu S.-L., and Chen M., "Structure and electrical properties of $(Na_{0.5}Bi_{0.5})_{1-x}Ba_xTiO_3$ ceramics made by a citrate method", Journal of Electroceramics, 2007 **21**(1-4) 617 doi: 10.1007/s10832-007-9281-5.
191. Mercadelli E., Galassi C., Costa A.L., Albonetti S., and Sanson A., "Sol–gel combustion synthesis of BNBT powders", Journal of Sol-Gel Science and Technology, 2008 **46**(1) 39 doi: 10.1007/s10971-008-1693-4.
192. Haugen A.B., Kumakiri I., Simon C., and Einarsrud M.-A., "TiO_2, TiO_2/Ag and TiO_2/Au photocatalysts prepared by spray pyrolysis", Journal of the European Ceramic Society, 2011 **31**(3) 291 doi: 10.1016/j.jeurceramsoc.2010.10.006.
193. Hardy A., Vanhoyland G., Van Bael M., Mullens J., and Van Poucke L., "A statistical approach to the identification of determinant factors in the preparation of phase pure $(Bi,La)_4Ti_3O_{12}$ from an aqueous citrate gel", Journal of the European Ceramic Society, 2004 **24**(9) 2575 doi: 10.1016/j.jeurceramsoc.2003.09.018.
194. Hardy A., Rul H., Bael M.K., and Mullens J., "Hyphenated thermal analysis for in situ study of $(Bi,Nd)_4Ti_3O_{12}$ formation from aqueous solution-gel synthesis", Journal of Thermal Analysis and Calorimetry, 2009 **96**(3) 955 doi: 10.1007/s10973-009-0051-2.
195. Perez-Rivero A., Ricote J., Bretos I., et al., "Morphotropic phase boundary in solution-derived $(Bi_{0.5}Na_{0.5})_{1-x}Ba_xTiO_3$ thin films: part II functional properties and phase stability", Journal of the American Ceramic Society, 2014 **97**(4) 1276 doi: 10.1111/jace.12752.
196. Muralt P., "Ferroelectric thin films for micro-sensors and actuators: a review", Journal of Micromechanics and Microengineering, 2000 **10**(2) 136 doi: 10.1088/0960-1317/10/2/307.
197. Švob L., "Solubility and diffusion coefficient of sodium and potassium in silicon", Solid-State Electronics, 1967 **10**(10) 991 doi: 10.1016/0038-1101(67)90148-7.
198. Aylward G.H. and Findlay T., "SI chemical Data", 6 ed. 2008, Milton: John Wiley & Sons Australia, Ltd.
199. Muralt P., "Piezoelectric thin films for MEMS", Integrated Ferroelectrics, 1997 **17**(1-4) 297 doi: 10.1080/10584589708013004.

200. Bergamin A., Cavagnero G., Mana G., and Zosi G., "Lattice parameter and thermal expansion of monocrystalline silicon", Journal of Applied Physics, 1997 **82**(11) 5396 doi: 10.1063/1.366308.
201. Moalla R., Vilquin B., Saint-Girons G., Sebald G., Baboux N., and Bachelet R., "Dramatic effect of thermal expansion mismatch on the structural, dielectric, ferroelectric and pyroelectric properties of low-cost epitaxial PZT films on $SrTiO_3$ and Si", CrystEngComm, 2016 **18**(11) 1887 doi: 10.1039/c5ce02311d.
202. Pavlic J., Malic B., and Rojac T., "Microstructural, structural, dielectric and piezoelectric properties of potassium sodium niobate thick films", Journal of the European Ceramic Society, 2014 **34**(2) 285 doi: 10.1016/j.jeurceramsoc.2013.09.001.
203. Sando D., Barthelemy A., and Bibes M., "$BiFeO_3$ epitaxial thin films and devices: past, present and future", Journal of Physics: Condensed Matter, 2014 **26**(47) 473201/1 doi: 10.1088/0953-8984/26/47/473201.
204. Davey W.P., "Precision measurements of the lattice constants of twelve common metals", Physical Review, 1925 **25**(6) 753 doi: 10.1103/PhysRev.25.753.
205. Hutchinson J.W. and Suo Z., "Mixed mode cracking in layered materials", Advances in Applied Mechanics, 1992 **29** 63.
206. Evans A.G. and Hutchinson J.W., "The thermomechanical integrity of thin films and multilayers", Acta Metallurgica et Materialia, 1995 **43**(7) 2507 doi: 10.1016/0956-7151(94)00444-M.
207. Dittmer R., Aulbach E., Jo W., Webber K.G., and Rödel J., "Large blocking force in $Bi_{1/2}Na_{1/2}TiO_3$-based lead-free piezoceramics", Scripta Materialia, 2012 **67**(1) 100 doi: 10.1016/j.scriptamat.2012.03.031.
208. Bhushan B. and Li X., "Micromechanical and tribological characterization of doped single-crystal silicon and polysilicon films for microelectromechanical systems devices", Journal of Materials Research, 1997 **12**(1) 54 doi: 10.1557/JMR.1997.0010.
209. Hess P., "Laser diagnostics of mechanical and elastic properties of silicon and carbon films", Applied Surface Science, 1996 **106** 429 doi: 10.1016/S0169-4332(96)00369-8.
210. Zheng J. and Sitaraman S.K. "In-process measurement of the interfacial fracture toughness for a sub-micron titanium thin film and silicon interface using a single-strip de-cohesion test", *Electronic Components and Technology Conference*. 2004: Institute of Electrical and Electronics Engineers doi: 10.1109/ECTC.2004.1319326.
211. Dong Q., Jiang H., Kumada N., Yonesaki Y., Takei T., and Kinomura N., "Preparation of a new pyrochlore-type compound $Na_{0.32}Bi_{1.68}Ti_2O_{6.46}(OH)_{0.44}$ by hydrothermal reaction", Journal of Solid State Chemistry, 2011 **184**(7) 1899 doi: 10.1016/j.jssc.2011.04.035.
212. Feng C., Yang C.H., Geng F.J., Lv P.P., and Yao Q., "Site engineering in chemical solution deposited $Na_{1/2}Bi_{1/2}TiO_3$ thin films using Mn acceptor", Materials Research Express, 2016 **3**(2) 026302/1 doi: 10.1088/2053-1591/3/2/026302.
213. Jin C.C., Wang F.F., Leung C.M., et al., "Growth and electric properties of (100)-oriented Mn-doped $(Bi_{0.5}Na_{0.5})TiO_3$-$BaTiO_3$ thin film by pulsed laser deposition", Applied Physics A, 2014 **115**(4) 1375 doi: 10.1007/s00339-013-8014-7.
214. Wu Y.Y., Wang X.H., Zhong C.F., and Li L.T., "Effect of anneal conditions on electrical properties of Mn-doped $(Na_{0.85}K_{0.15})_{0.5}Bi_{0.5}TiO_3$ thin films prepared by sol-gel method", Journal of the American Ceramic Society, 2011 **94**(6) 1843 doi: 10.1111/j.1551-2916.2010.04325.x.

215. Zhou X.Y., Gu H.S., Wang Y., Li W.Y., and Zhou T.S., "Piezoelectric properties of Mn-doped $(Na_{0.5}Bi_{0.5})_{0.92}Ba_{0.08}TiO_3$ ceramics", Materials Letters, 2005 **59**(13) 1649 doi: 10.1016/j.matlet.2005.01.034.
216. Okamoto H., "The Bi-Pt (bismuth-platinum) system", Journal of Phase Equilibria, 1991 **12**(2) 207 doi: 10.1007/BF02645718.
217. Ju J., Wang D., Lin J., et al., "Hydrothermal synthesis and structure of lead titanate pyrochlore compounds", Chemistry of Materials, 2003 **15**(18) 3530 doi: 10.1021/cm0301468.
218. Shrout T.R. and Zhang S.J., "Lead-free piezoelectric ceramics: alternatives for PZT?", Journal of Electroceramics, 2007 **19**(1) 113 doi: 10.1007/s10832-007-9047-0.
219. Takenaka T. and Nagata H., "Current status and prospects of lead-free piezoelectric ceramics", Journal of the European Ceramic Society, 2005 **25**(12) 2693 doi: 10.1016/j.jeurceramsoc.2005.03.125.
220. Takenaka T., Nagata H., and Hiruma Y., "Current developments and prospective of lead-free piezoelectric ceramics", Japanese Journal of Applied Physics, 2008 **47**(5) 3787 doi: 10.1143/Jjap.47.3787.
221. Schneller T., Griesche D., Malic B., et al., "Chemical solution deposition of functional oxide thin films". 2013, Wien: Springer-Verlag.
222. Kupec A. and Malic B., "Structural and dielectric properties of the lead-free $(1-x)K_{0.5}Na_{0.5}NbO_3$-$xSrTiO_3$ thin films from solutions", Journal of Alloys and Compounds, 2014 **596** 32 doi: 10.1016/j.jallcom.2014.01.193.
223. Lemoine C., Gilbert B., Michaux B., Pirard J.-P., and Lecloux A., "Synthesis of barium titanate by the sol-gel process", Journal of Non-Crystalline Solids, 1994 **175**(1) 1 doi: 10.1016/0022-3093(94)90309-3.
224. Chen M., Xu Q., Kim B.H., et al., "Structure and electrical properties of $(Na_{0.5}Bi_{0.5})_{1-x}Ba_xTiO_3$ piezoelectric ceramics", Journal of the European Ceramic Society, 2008 **28**(4) 843 doi: 10.1016/j.jeurceramsoc.2007.08.007.
225. Geguzina G.A., Shuvayev A.T., Vlasenko V.G., Shuvayeva E.T., and Shilkina L.A., "Synthesis and structure of new $A_{m-1}Bi_2B_mO_{3m+3}$ (m = 3) phases", Crystallography Reports, 2003 **48**(3) 406 doi: 10.1134/1.1578123.
226. Socrates G., "Infrared and raman characteristic group frequencies". 2001, Chichester, England: John Wiley & Sons Ltd.
227. Samajdar S., Becker F.F., and Banik B.K., "Surface-mediated highly efficient oxidation of alcohols by bismuth nitrate", Synthetic Communications, 2001 **31**(17) 2691 doi: 10.1081/scc-100105397.
228. Nelis D., van Werde K., Mondelaers D., et al., "Aqueous solution-gel synthesis of strontium bismuth niobate ($SrBi_2Nb_2O_9$)", Journal of Sol-Gel Science and Technology, 2003 **26** 1125 doi: 10.1023/A:1020771126807.
229. Li W., Zeng H., Zhao K., Hao J., and Zhai J., "Structural, dielectric and piezoelectric properties of $(Bi_{0.5}Na_{0.5})TiO_3$-$(Bi_{0.5}K_{0.5})TiO_3$-$Bi(Zn_{0.5}Ti_{0.5})O_3$ thin films prepared by sol-gel method", Ceramics International, 2014 **40**(6) 7947 doi: 10.1016/j.ceramint.2013.12.143.
230. Kim K., Jang G., Kim C., and Yoon D., "Ferroelectric properties of $Bi_{3.25}Nd_{0.75}Ti_3O_{12}$ thin films prepared by MOD process", Journal of Electroceramics, 2004 **13**(1/2/3) 77 doi: 10.1007/s10832-004-5079-x.
231. Muralt P. "Piezoelectric thin film devices", *Advances in Science and Technology*. 2010 doi: 10.4028/www.scientific.net/AST.67.64.

232. Christensen M., Einarsrud M.-A., and Grande T., "Fabrication of lead-free $Bi_{0.5}Na_{0.5}TiO_3$ thin films by aqueous chemical solution deposition", Materials, 2017 **10**(2) 213 doi: 10.3390/ma10020213.
233. Genenko Y.A., Zhukov S., Yampolskii S.V., et al., "Universal polarization switching behavior of disordered ferroelectrics", Advanced Functional Materials, 2012 **22**(10) 2058 doi: 10.1002/adfm.201102841.
234. Christensen M., Einarsrud M.-A., and Grande T., "Aqueous chemical solution deposition of phase pure Ba doped $Bi_{0.5}Na_{0.5}TiO_3$ thin films", Manuscript not submitted.
235. Greene C.H., "The solubility of barium nitrate in concentrated nitric acid", Journal of the American Chemical Society, 1937 **59**(7) 1186 doi: 10.1021/ja01286a008.
236. Shannon R.D., "Revised effective ionic-radii and systematic studies of interatomic distances in halides and chalcogenides", Acta Crystallographica Section A, 1976 **32** 751 doi: 10.1107/S0567739476001551.
237. Griggio F., Jesse S., Kumar A., et al., "Substrate clamping effects on irreversible domain wall dynamics in lead zirconate titanate thin films", Physical Review Letters, 2012 **108**(15) 157604/1 doi: 10.1103/PhysRevLett.108.157604.
238. Zhou Z.H., Xue J.M., Li W.Z., Wang J., Zhu H., and Miao J.M., "Leakage current and charge carriers in $(Na_{0.5}Bi_{0.5})TiO_3$ thin film", Journal of Physics D: Applied Physics, 2005 **38**(4) 642 doi: 10.1088/0022-3727/38/4/019.
239. Malic B. and Suzuki H., "Low-temperature processing of solution-derived ferroelectric thin films", Journal of the Ceramic Society of Japan, 2014 **121**(1421) 1 doi: 10.2109/jcersj2.122.1.
240. Qin W., Guo Y.P., Guo B., and Gu M.Y., "Dielectric and optical properties of $BiFeO_3$-$(Na_{0.5}Bi_{0.5})TiO_3$ thin films deposited on Si substrate using $LaNiO_3$ as buffer layer for photovoltaic devices", Journal of Alloys and Compounds, 2012 **513** 154 doi: 10.1016/j.jallcom.2011.10.011.
241. Shao F., Miao J., Wu S.Z., et al., "Improved electrical and ferroelectric properties of multiferroic $Na_{0.5}Bi_{0.5}TiO_3/Bi_{1.07}Nd_{0.03}FeO_3/Na_{0.5}Bi_{0.5}TiO_3$ sandwiched structure by a sol-gel process", Journal of Materials Science: Materials in Electronics, 2014 **25**(6) 2411 doi: 10.1007/s10854-014-1860-z.
242. Jin C.C., Wang F.F., Yao Q.R., Tang Y.X., Wang T., and Shi W.Z., "Enhanced ferroelectric and dielectric properties in $(La_{0.7}Ca_{0.3})MnO_3$-buffered $(Bi_{0.5}Na_{0.5})TiO_3$-based lead-free thin film by pulsed laser deposition", Journal of Alloys and Compounds, 2013 **553** 142 doi: 10.1016/j.jallcom.2012.11.095.
243. Christensen M., Einarsrud M.-A., and Grande T., "Chemical modification of $Bi_{0.5}Na_{0.5}TiO_3$ thin films prepared by aqueous chemical solution deposition", Manuscript not submitted.
244. Diebold U., "The surface science of titanium dioxide", Surface Science Reports, 2003 **48**(5) 53 doi: 10.1016/S0167-5729(02)00100-0.
245. Buttner R.H. and Maslen E.N., "Structural parameters and electron difference density in $BaTiO_3$", Applied Physics A, 1992 **48**(6) 764 doi: 10.1107/s010876819200510x.
246. Hejazi M., Jadidian B., and Safari A., "Lead-free $(Bi_{0.5}Na_{0.5})TiO_3$-based thin films by the pulsed laser deposition process", Ieee Transactions on Ultrasonics Ferroelectrics and Frequency Control, 2012 **59**(9) 1855 doi: 10.1109/tuffc.2012.2396.
247. German R.M., "Sintering theory and practice". Solar-Terrestrial Physics (Solnechno-zemnaya fizika). 1996, New York: John Wiley & Sons, Inc.

248. Kupec A., Malic B., Tellier J., Tchernychova E., Glinsek S., and Kosec M., "Lead-free ferroelectric potassium sodium niobate thin films from solution: composition and structure", Journal of the American Ceramic Society, 2012 **95**(2) 515 doi: 10.1111/j.1551-2916.2011.04892.x.